SCATTERING POLARIZATION WITH PASCHEN–BACK EFFECT AS A TOOL TO DIAGNOSE THE MAGNETIC STRUCTURING OF THE SOLAR ATMOSPHERE

A THESIS SUBMITTED TO
THE DEPARTMENT OF PHYSICS
PONDICHERRY UNIVERSITY

FOR THE AWARD OF THE DEGREE OF
DOCTOR OF PHILOSOPHY

CANDIDATE
K. SOWMYA

THESIS SUPERVISOR
PROF. K. N. NAGENDRA

INDIAN INSTITUTE OF ASTROPHYSICS
BENGALURU - 560 034 INDIA

MARCH 2016

DECLARATION

I hereby declare that the material presented in this thesis, submitted to the Department of Physics, Pondicherry University, for the award of Ph.D. degree, is the result of the investigations carried out by me, at the Indian Institute of Astrophysics, Bengaluru, under the supervision of Prof. K. N. Nagendra. The results reported in this thesis are new, and original, to the best of my knowledge, and have not been submitted in whole or part for a degree in any University. Whenever the work described is based on the findings of other investigators, due acknowledgment has been given. Any unintentional omission is sincerely regretted.

K. Sowmya
Ph.D. Candidate
Indian Institute of Astrophysics
Bengaluru 560 034
March 2016

CERTIFICATE

This is to certify that the work embodied in this thesis titled “Scattering polarization with Paschen–Back effect as a tool to diagnose the magnetic structuring of the solar atmosphere”, has been carried out by Ms. K. Sowmya, under my supervision and the same has not been submitted in whole or part for Degree, Diploma, Associateship Fellowship or other similar title to any University.

Prof. K. N. Nagendra
Thesis Supervisor
Indian Institute of Astrophysics
Bengaluru 560 034
March 2016

ACKNOWLEDGEMENTS

I sincerely thank my thesis supervisor, Prof. K. N. Nagendra, for his guidance and support. I am grateful to him for providing me with an opportunity to visit Istituto Ricerche Solari Locarno (IRSOL), Switzerland, and also for enabling my participation in national and international conferences. I thank Dr. M. Sampoorna for her guidance and scientific discussions which deepened my knowledge in the area of my research and Dr. L. S. Anusha for her timely help without which this thesis would not have been realized. Thanks are also due to Dr. B. Ravindra for his support and cooperation. I express my sincere gratitude to Dr. H. N. Smitha for delightful discussions, support in academic and administrative endeavors, to Prof. J. O. Stenflo for insightful discussions and guidance, and to Dr. M. Bianda for being a constant source of encouragement and for supporting my visit to IRSOL.

I thank the Director, Indian Institute of Astrophysics (IIA), the Dean and the Board of Graduate Studies, IIA, for providing the facilities to carry out the thesis work and aid in official matters. I acknowledge the use of HYDRA cluster facility at IIA for the computations related to the work presented in this thesis. I am grateful to IIA and the Department of Science & Technology for the financial assistance provided to participate in the conferences.

I extend my thanks to the doctoral committee members Prof. M. Srinivasa Rao, Prof. Dipankar Banerjee and Prof. G. Chandrasekaran, for evaluating the progress made and giving valuable suggestions. Special thanks are due to Prof. G. Chandrasekaran for guiding and supporting me through the administrative procedures in Pondicherry University (PU) at various stages during Ph.D. I also thank the Dean, School of Physical, Chemical & Applied Sciences, PU, the Head of the Department of Physics, PU, and the staff members of the Department of Physics, PU, for their cooperation in administrative matters.

I am thankful to Dr. Baba Varghese, Mr. Ashok, Mr. Anish Parwage, the computer center support team, the library staff, the administrative and canteen staff of IIA, and the staff members of Bhaskara hostel and guest house for their help and support.

I am indebted to my family, friends, teachers, and all those who directly or indirectly encouraged and helped me in the due course.

LIST OF PUBLICATIONS

In International Refereed Journals

1. *Polarized Scattering of Light for Arbitrary Magnetic Fields with Level-Crossings from the Combination of Hyperfine and Fine Structure Splittings*
   Sowmya, K., Nagendra, K. N., Sampoorna, M., & Stenflo J. O. 2015, ApJ, 814, 127

2. *Polarized Light Scattering with the Paschen–Back Effect, Level-Crossing of Fine Structure States, and Partial Frequency Redistribution*
   Sowmya, K., Nagendra, K. N., Sampoorna, M., & Stenflo J. O. 2014, ApJ, 793, 71

3. *Polarized Scattering with Paschen–Back Effect, Hyperfine Structure, and Partial Frequency Redistribution in Magnetized Stellar Atmospheres*
   Sowmya, K., Nagendra, K. N., Stenflo J. O., & Sampoorna, M. 2014, ApJ, 786, 150

4. *Polarized Line Transfer with F-State Interference in a Non-Magnetic Medium: Partial Frequency Redistribution Effects in the Collisionless Regime*
   Smitha, H. N., **Sowmya, K.**, Nagendra, K. N., Sampoorna, M., & Stenflo, J. O. 2012, ApJ, 758, 112

5. *Blend Lines in the Polarized Spectrum of the Sun*
   Sowmya, K., Nagendra, K. N., & Sampoorna, M. 2012, MNRAS, 423, 2949

In Refereed Conference Proceedings

1. *Paschen–Back Effect Involving Atomic Fine and Hyperfine Structure States*
   Sowmya, K., Nagendra, K. N., Sampoorna, M., & Stenflo J. O. 2015, in the Proceedings of the IAU Symposium No. 305, Polarimetry: From the Sun to Stars and Stellar Environments, ed. K. N. Nagendra et al., 154

2. *Intrinsically Polarized Blend Lines*
   Sowmya, K., Nagendra, K. N., & Sampoorna, M. 2014, in ASP Conf. Ser. 489, Solar Polarization 7, ed. K. N. Nagendra et al. (San Francisco, CA:ASP), 125

ABSTRACT

The Sun is a unique physical laboratory in which the various domains of physics inaccessible to laboratories on earth can be studied in great detail. Its proximity allows us to understand it in great depths. George Ellery Hale, in 1908, discovered the magnetic fields in sunspots through his observations of the Zeeman effect (splitting of atomic lines in the presence of a magnetic field). Advancements in observational techniques, and instrumentation since then enabled us to see the Sun with a high resolution. This revealed that the magnetic fields are present everywhere on the Sun and they govern its structure and dynamics. The terrestrial environment is now known to be influenced by the solar magnetic fields. This is one of the reasons why their study is of great importance.

One of the methods to study and measure these magnetic fields is to analyze the polarization of the light emitted by the Sun. The traditionally observed intensity spectrum of the Sun called the first solar spectrum gives substantial information about the structure and composition of the solar surface layers (photosphere, chromosphere, transition region, and corona). However, more detailed information like the strength and spatial distribution of the solar magnetic fields can be obtained from the polarized light emitted by the Sun.

The line polarization arises due to the magnetic fields and the coherent scattering processes taking place due to anisotropic illumination of the radiating atoms by the limb darkened radiation. The linearly polarized solar spectrum produced by coherent scattering mechanisms is called the 'second solar spectrum'. Magnetic fields generate polarization via Zeeman effect and also modify the scattering polarization (via the Hanle effect). The fingerprints of the magnetic fields are encoded in the polarization signals. The analysis of these fingerprints is of high scientific interest, since they can be suitably exploited to investigate the magnetic fields present in the solar atmosphere.

The most commonly used technique for the magnetic field diagnostics is the Zeeman effect in which case the spectral lines are split by the external magnetic field. However, if the magnetic field is very weak then Zeeman effect cannot be used for diagnosing the field because it is practically difficult to measure extremely small splitting by instruments with finite spectral resolution. Also, the Zeeman effect is blind to mixed polarity fields

within the resolution element of the telescope. These drawbacks can be overcome by the Hanle effect which refers to the modification of the non-magnetic scattering polarization by the magnetic fields. The Hanle effect can help to detect the fields that are either weak or turbulent. Thus, it acts as a complementary diagnostic tool to the Zeeman effect.

In some situations, the magnetic field is so strong that it produces a splitting whose pattern is very different from that expected for the Zeeman effect. Apart from completely splitting the atomic lines, it also causes the magnetic substates of different atomic states belonging to a given term to interfere. Such an effect of the magnetic field is called Paschen–Back effect. It acts in those domains of field strength that are not accessible through the standard techniques based on the Zeeman effect. Due to the different magnetic field strength regimes in which they operate, the Hanle, Zeeman, and Paschen–Back effects complement one another. The role played by the Paschen–Back effect in shaping the polarization profiles of the spectral lines needs to be understood in order to explore the possibility of using the Paschen–Back effect as a diagnostic tool for magnetic fields. To this end, in this thesis, we develop the scattering theory of Paschen–Back effect in atomic states by accounting for the redistribution in the frequencies of the photons due to Doppler shift and apply it to analyze the polarization profiles of diagnostically important solar spectral lines. This study is an important step forward in understanding the effects of strong magnetic fields and their manifestation in the polarized line radiation emerging from the solar (or stellar) atmosphere.

We have divided the thesis into two parts. The first part (Chapters 2 and 3) concerns the problem of line radiative transfer in the presence of polarized blend lines and a polarized continuum. Polarizing blend lines are known to influence the polarization of the spectral lines as well as the polarized background continuum. The theoretical modeling of any spectral line in the second solar spectrum requires a proper treatment of these blend lines. With this motivation, in Chapter 2, we develop a formalism to include a blend line resulting from transition in a two-level atom, having a non-zero intrinsic polarization, formed under non-local thermodynamic equilibrium conditions, in the polarized radiative transfer equation in the presence of a weak magnetic field (the Hanle effect). Considering one-dimensional isothermal atmosphere, we study in detail its influence on the main spectral line of interest, also resulting from the transition in a two-level atom.

In Chapter 3, we extend the formalism developed in Chapter 2 to incorporate multiple blend lines in the polarized transfer equation. This is important because generally more than one blend line will be present in the wings of the main spectral line. Our formalism can treat any number of blend lines, however, for the sake of simplicity, we present the results of our study involving only two polarized blend lines. In this case we find that the

blend line effects are important and needs to be considered when it is lying very close to the main line and is relatively strong. As mentioned earlier, this study becomes important while modeling the spectral lines in the second solar spectrum in order to extract the physical quantities related to the magnetic field and the solar atmosphere.

In the second part of the thesis (Chapters 4, 5, 6, and 7), we develop the scattering theory of Paschen–Back effect using the Kramers–Heisenberg scattering matrix approach. We study the problem of quantum interfere (interference between the scattering amplitudes of transitions) in the presence of a magnetic field of arbitrary strength with a particular interest in the Paschen–Back effect regime. The second solar spectrum hosts many spectral lines which are governed by the quantum interference effects. The polarization features of such lines can be explained only when interference effects are consistently accounted for. The quantum interference occurring between the atomic states gets modified in the presence of a magnetic field. We identify and study the signatures imprinted in the polarization profiles by the quantum interference taking place in the presence of a magnetic field.

In Chapter 4, we develop the scattering theory of Paschen–Back effect in hyperfine structure states by considering a two-level atom which undergoes hyperfine structure splitting because of the interaction between the total angular momentum of the electron and the nuclear spin. We consider frequency coherent scattering of the photons in the atom's rest frame and account for the partial frequency redistribution effects in the laboratory frame that arise due to Doppler motions of the atoms. We test this theory by taking example of the Na I D_2 line for which observable effects from the Paschen–Back regime are expected for the magnetic fields present on the Sun. Since our aim is to identify and study the fingerprints of Paschen–Back effect on polarization, we consider only a single scattering of the incident unpolarized radiation by the Na atom, avoiding the complications due to radiative transfer.

We then formulate the theory of quantum interference between the fine structure states in a two-term atom in the presence of arbitrarily strong magnetic fields (including the Paschen–Back regime) by accounting for the effects due to partial frequency redistribution. We present the theoretical formulation as well as the results of the tests performed in a single scattering on the Li I D_1 & D_2 lines in Chapter 5. This is the only line system which is sensitive to Paschen–Back effect for the field strengths that are seen in the Sun (the magnetic field strength required to see Paschen–Back effect in fine structure states for other lines is much higher than those present in the Sun). For this line system, the effects from the Paschen–Back regime are seen for field strengths typically present in sunspots. We identify the various signatures of the level-crossings and avoided-crossings that take place in the Paschen–Back regime.

We also develop a more general scattering theory in Chapter 6 which accounts for fine and hyperfine structure interference simultaneously in the presence of arbitrary strength magnetic fields, for a two-term atom with hyperfine structure. We account for the effects due to partial frequency redistribution. Due to the relevance to solar applications, we again consider the Li I D_1 & D_2 lines to test this theory in a single scattering of the unpolarized incident radiation. We find that Paschen–Back effect results in net circular polarization value (which is not seen in the case of Zeeman effect) and that this value has a particular pattern of variation with an increase in the magnetic field strength. This net circular polarization could serve as a diagnostic tool for solar magnetic fields.

In Chapter 7 we describe our efforts to model the lithium lines using the last scattering approximation method and the theory developed in Chapter 6. We consider two levels of approximations of the last scattering method originally developed for non-magnetic and weak field cases and extend it to include the effects due to strong magnetic fields. We end the thesis by summarizing the results and indicating the possible directions for future work in Chapter 8 and provide the additional details in the appendices.

List of Abbreviations

The following is a list of abbreviations used in this thesis, along with their expansions.

ZIMPOL	Zurich IMaging POLarimeter
LTE	Local Thermodynamic Equilibrium
NLTE	Non-LTE
CRD	Complete frequency ReDistribution
RM	Redistribution Matrix
PRD	Partial frequency ReDistribution
MS	Magnetic Splitting
PBE	Paschen–Back Effect
PB	Paschen–Back
1D	One-Dimensional
ALI	Approximate Lambda Iteration
PALI	Polarized ALI
DELO	Diagonal Element Lambda Operator
DELOPAR	DELO with PARabolic accuracy
LSA	Last Scattering Approximation
FBF	Frequency-By-Frequency
SEM	Scattering Expansion Method
2D	Two-Dimensional
HFS	HyperFine structure Splitting
NCP	Net Circular Polarization
FS	Fine structure Splitting

PSS . . . . . Principle of Spectroscopic Stability

A-O . . . . . Alignment-to-Orientation

CLV . . . . . Center to Limb Variation

CONTENTS

1

INTRODUCTION

In this chapter, we introduce the basic concepts and terminology that will be used in the present thesis which are essential for understanding its contents. We qualitatively describe the relevant physical effects without going into detailed mathematical derivation except when it is needed.

1.1 Representation of Polarized Radiation

The state of polarization of an electromagnetic radiation is completely specified by the four Stokes parameters $I, Q, U,$ and V. They were first defined by Sir George Gabriel Stokes in 1852 as a mathematically convenient way of representing the partially polarized light and later introduced in the astrophysical context by Chandrasekhar (1950). I is the total intensity, Q is a measure of the degree of linear polarization, U gives the orientation of the plane of polarization, and V gives a measure of circular polarization.

Following the monograph by Stenflo (1994), we describe below, the mathematical framework that will be used in this thesis, to determine the state of polarization of a radiation. For a more detailed description of the polarized light we refer the reader to this monograph. When a polarized light travels through a medium, because of its interaction with matter, its characteristics change. This interaction can be calculated in a number of ways. The simplest one is the Jones formalism, introduced in 1941 by R. Clark Jones (see Shurcliff, 1961; Collett, 1993; Clarke, 2010, for more details), where the electric vector $\boldsymbol{E}$ is decomposed into two mutually orthogonal directions $\boldsymbol{e}_1$ and $\boldsymbol{e}_2$, as

$$\boldsymbol{E} = \mathrm{Re}(E_1\boldsymbol{e}_1 + E_2\boldsymbol{e}_2)\ , \tag{1.1}$$

and the Jones vector $\boldsymbol{J}$ is constructed using E_1 and E_2, as

$$\boldsymbol{J} = \begin{pmatrix} E_1 \\ E_2 \end{pmatrix} . \tag{1.2}$$

The complex amplitude and phase information are contained in E_1 and E_2. The interaction of the polarized light with the medium is then represented by a 2×2 Jones matrix $\boldsymbol{w}$ as

$$\boldsymbol{J} = \boldsymbol{w}\boldsymbol{J}' . \tag{1.3}$$

Here, $\boldsymbol{J}'$ is the Jones vector of the light entering the medium and $\boldsymbol{J}$ is that of the light leaving the medium after interaction. It is important to note that the Jones formalism assumes that the waves propagate in the orthogonal directions maintaining the same phase or the same phase difference. This refers to radiation beams which are perfectly coherent and perfectly polarized. In a statistical ensemble of uncorrelated photons (produced by independent processes) with different state of polarization, partial polarization arises due to incoherent superposition. In order to deal with this, we use the coherency matrix $\boldsymbol{D}$ which is formed from the Jones vector as

$$\boldsymbol{D} = \boldsymbol{J}\boldsymbol{J}^{\dagger} , \tag{1.4}$$

where $\boldsymbol{J}^{\dagger}$ denotes the adjoint of $\boldsymbol{J}$ (transposition and complex conjugation of $\boldsymbol{J}$). The coherency matrix then transforms as

$$\boldsymbol{D} = \boldsymbol{w}\boldsymbol{D}'\boldsymbol{w}^{\dagger} . \tag{1.5}$$

The polarized light is represented by a four component Stokes vector of the form

$$\boldsymbol{I} = [I, Q, U, V]^T , \tag{1.6}$$

and is related to coherency matrix through the expression

$$\boldsymbol{I} = \mathrm{Tr}(\boldsymbol{\sigma}\boldsymbol{D}) . \tag{1.7}$$

Here, Tr stands for trace which is the sum of all the diagonal elements and $\boldsymbol{\sigma}$ are the Pauli spin matrices. The Stokes vector in a medium transforms according to

$$\boldsymbol{I} = \mathrm{M}\boldsymbol{I}' , \tag{1.8}$$

where $\mathbf{M}$ is the Mueller matrix which describes how an incident Stokes vector gets transformed in a medium. It is defined as

$$\mathbf{M} = \mathbf{T}\mathbf{W}\mathbf{T}^{-1} \,, \tag{1.9}$$

where

$$\mathbf{W} = \boldsymbol{w} \otimes \boldsymbol{w}^* = \begin{pmatrix} w_{11}w_{11}^* & w_{11}w_{12}^* & w_{12}w_{11}^* & w_{12}w_{12}^* \\ w_{11}w_{21}^* & w_{11}w_{22}^* & w_{12}w_{21}^* & w_{12}w_{22}^* \\ w_{21}w_{11}^* & w_{21}w_{12}^* & w_{22}w_{11}^* & w_{22}w_{12}^* \\ w_{21}w_{21}^* & w_{21}w_{22}^* & w_{22}w_{21}^* & w_{22}w_{22}^* \end{pmatrix} . \tag{1.10}$$

The symbols $\otimes$ and $*$ denote tensor product and complex conjugation, respectively. $\mathbf{T}$ and $\mathbf{T}^{-1}$ are the purely mathematical transformation matrices having the form

$$\mathbf{T} = \begin{pmatrix} 1 & 0 & 0 & 1 \\ 1 & 0 & 0 & -1 \\ 0 & 1 & 1 & 0 \\ 0 & -i & i & 0 \end{pmatrix} \; ; \quad \mathbf{T}^{-1} = \frac{1}{2} \begin{pmatrix} 1 & 1 & 0 & 0 \\ 0 & 0 & 1 & i \\ 0 & 0 & 1 & -i \\ 1 & -1 & 0 & 0 \end{pmatrix} . \tag{1.11}$$

The formalism based on the Mueller matrix accounts for the partially polarized light. Mueller matrix is an important tool in the measurement of polarized light (for more details, see, for example, del Toro Iniesta, 2004). In this thesis, we use the coherency matrix formalism, following the approach developed by Stenflo (1994, 1998).

1.2 Solar Polarization and Blend Lines

The criterion for radiation to get polarized is breaking of the spatial symmetry. In the solar atmosphere this is met when there is an anisotropic illumination of the atoms or when there is a magnetic or electric field present. The source of anisotropy is the limb darkening, because of which a scattering atom receives more radiation from the vertical (radial) direction, than from the horizontal (lateral) direction. When an atom is illuminated by such an anisotropic radiation, population imbalances and coherences are introduced among the magnetic substates. In other words, the atom gets polarized. This 'atomic polarization' is transferred to the scattered photon in a coherent scattering event. Thus, there exist definite phase correlations between the incident and scattered photons in such coherent processes. The linear polarization gets generated in the scattering processes which are coherent. In the incoherent processes, due to collisions the atom loses its memory of how it was excited, and hence there exists no phase relation between the incident and scattered photons. Therefore,

the scattered photon is unpolarized in an incoherent scattering event.

The degree of polarization depends on the degree of anisotropy that prevails in the layers from where the photons are emitted. The degree of anisotropy is small in the solar atmosphere and hence the degree of polarization is of the order of just a few percent. With spectropolarimeters like ZIMPOL (Zurich Imaging POLarimeter, see, for example, Povel, 1995), it is possible to measure such weak signals. Maximum polarization is measured in the limb observations and minimum in the disk center because of the axial symmetry of the radiation field.

Magnetic fields play an important role in shaping the polarization profiles of the spectral lines, as scattering polarization signals are sensitive to their presence. They modify the polarization generated in non-magnetic coherent scattering events and give rise to observable signatures in the polarization through a series of interesting physical mechanisms. The analysis of these signatures is of high scientific interest, since they can be suitably exploited to investigate the magnetic fields present in the solar atmosphere (or in other astrophysical plasma). See Section 1.7 for more details on the solar magnetic fields and the various techniques used to determine them.

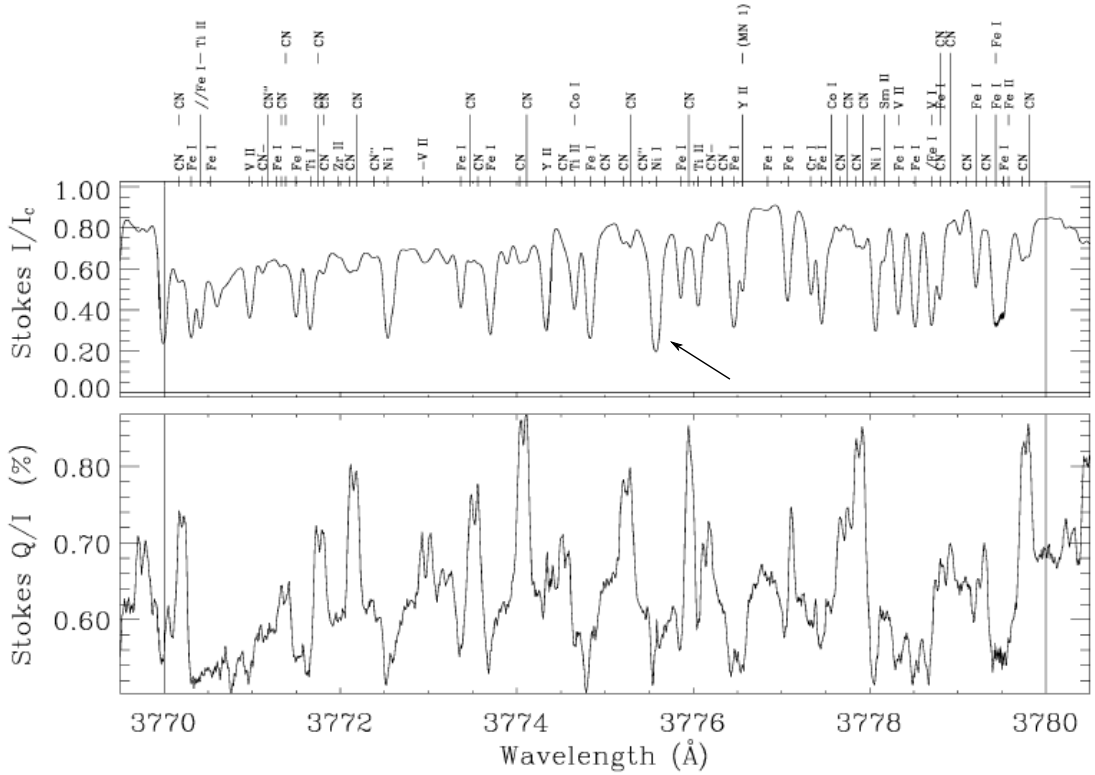

Figure 1.1: The second solar spectrum in the range $3770 - 3780$ Å (Gandorfer, 2005b).

1.2.1 The Second Solar Spectrum

A record of the linear polarization resulting from the coherent scattering processes in the Sun as a function of wavelength is called the 'second solar spectrum' (see Gandorfer, 2000, 2002, 2005a). In Figure 1.1, we show the second solar spectrum (Q/I panel) recorded in the wavelength range $3770 - 3780$ Å (Gandorfer, 2005b), along with the regular intensity spectrum which is called the first solar spectrum. As we can see from this figure, Q/I spectrum is very different from the intensity spectrum and hence the name second solar spectrum (Ivanov, 1991; Stenflo & Keller, 1997). It contains a wealth of information about the various physical processes governing the structure and dynamics of the solar atmosphere. It is highly structured and is characterized by a polarized background continuum on which the spectral lines superpose. The physical mechanisms generating it are different from the ones which give rise to the intensity spectrum. To explain these mechanisms, scattering theories were formulated based on the principles of quantum mechanics. Using these theoretical formulations, it is possible to characterize the layers in the solar atmosphere from where the polarization is generated. This opened a previously unexplored window to study the solar atmosphere (see, for example, Stenflo, 2009a,b, 2011).

1.2.2 The Blend Lines

As mentioned in Section 1.2.1, the second solar spectrum is characterized by numerous spectral lines which are formed at different heights in the solar atmosphere. Modeling their polarization profiles is one of the ways to map the variation of different physical quantities within the atmosphere. This requires a proper treatment of the blend lines which are known to affect the polarization of these spectral lines of interest. In Figure 1.1, if we consider the spectral line marked by an arrow in the intensity panel as the main line of our interest, then we refer to all the other lines present in this wavelength window as blend lines. The blend lines can arise from the transitions in the same atomic species as the main line or from different atomic species. For simplicity, they are generally assumed to be formed in a medium under local thermodynamic equilibrium (LTE[1]) condition and are also assumed to be unpolarized. The background continuum radiation is polarized by Rayleigh scattering on neutral hydrogen and Thomson scattering on free electrons. The intrinsically unpolarized spectral lines dilute the polarized continuum photons and depolarize the continuum. Blend lines, in reality, can be either polarizing or depolarizing.

[1] The LTE represents the transfer of radiation in a denser medium, where the collision processes dominate. The absorption and emission processes are sufficient to define the local source function, which at a given point in the medium is given simply by the Planck function at the local temperature. In the solar atmosphere, LTE is a good approximation in the deeper photospheric layers.

In polarization measurements and modeling of a spectral line, determining the absolute zero level of polarization is very important but remains a challenge (see Stenflo et al., 1998) because of the instrumental polarization. One of the ways to arrive at the absolute scale for the polarization measurements is to use the blend lines. Stenflo (2005) presented the method of using the blend lines for this purpose. Smitha et al. (2014) used the blend lines to determine the zero level of polarization in their efforts to model the Sc II 4247 Å line. In Part I of this thesis, we present a formalism to treat both polarizing and depolarizing blend lines formed in non-LTE (NLTE[2]) conditions, and the ways to use them for modeling main line polarization.

1.3 Frequency and Angular Redistribution in Scattering Events

In scattering processes, the frequencies, polarization and directions of the photons get redistributed. By considering a two-level atom (a simple atomic configuration having only a lower and an upper level between which the transitions occur), in this section, we describe the various types of redistribution that occurs in the atom's rest frame. We refer the reader to Mihalas (1978) and Hubeny & Mihalas (2015) for detailed discussions on this topic.

Type I: This is an idealized situation where we consider both the levels of the two-level atom to be infinitely sharp. In this case, there is no redistribution in the atom's frame. Type I redistribution does not apply to any real line, however, it is useful in understanding the redistribution which occurs due to Doppler motion as seen by an observer in the laboratory frame.

Type II: In this case, we assume that the lower level is infinitely sharp and the upper level is only radiatively broadened because of Heisenberg's uncertainty principle. Further, we assume that there are no additional perturbations (such as collisions) to the upper level so that when the atom de-excites, it emits a photon of the same frequency as was absorbed. No redistribution occurs in the atom's frame. This applies to a resonance line (for which the lower level is an infinitely long lived ground state) formed in low density layers where collisions are negligible.

Type III: We consider the lower level to be infinitely sharp as before but the upper level is now both radiatively and collisionally broadened. Because of collisions, the excited elec-

[2] The NLTE represents the transfer of radiation in a rarefied medium, where the scattering processes dominate. The source function at a given point is decoupled from the local temperature and is controlled by the photons arriving from other points within the medium. NLTE prevails in the low density layers of the solar atmosphere, namely, the upper photosphere and the chromosphere.

trons get reshuffled within the broadened upper level before the de-excitation occurs. The atom therefore emits photon which will have no correlation with the incident photon. There will be complete frequency redistribution (CRD) in the atom's frame. This is applicable to lines formed in high density layers dominated by collisions.

Type IV: In this situation, we assume both the lower and upper levels to be having finite width. The absorption and emission occurs between the radiatively broadened levels. This picture is suitable to describe the redistribution in subordinate lines.

The description of all these types of redistribution as seen by an observer in the laboratory frame are given in Hummer (1962). Heinzel (1981) derived the expression for the type IV redistribution in the laboratory frame. This function is called the type V function. See also Hubený (1982) and Heinzel & Hubený (1982) for non-coherent scattering in subordinate lines. In this thesis, we use both angle averaged and angle dependent forms of Hummer's functions.

1.3.1 Redistribution Matrix

In the scattering theory as applied to the astrophysical problems, the functions which describe the correlations between the frequencies and angles of the absorbed and emitted photons are called the redistribution functions. The polarization correlations are described by the matrices called the phase matrices. In the simpler non-magnetic case, the product of the two is referred to as the scattering matrix or the redistribution matrix (RM). In the magnetic case, the angle, frequency, and polarization correlations in general cannot be factorized. They can at most be expressed as combinations of these correlation functions. For atoms under the influence of a magnetic field, the RM is generally denoted as $\boldsymbol{R}(x, x', \boldsymbol{n}, \boldsymbol{n}'; \boldsymbol{B})$ where x' and $\boldsymbol{n}'$ are the frequency and direction of the absorbed photon, and x and $\boldsymbol{n}$ are the corresponding quantities for the emitted photon. $\boldsymbol{B}$ is the vector magnetic field whose strength is B, inclination is θ_B, and azimuth is χ_B with respect to the atmospheric reference frame, which is the frame fixed to the star, with the z-axis being normal to the atmosphere. RM contains the atomic physics of scattering and is a very important tool in understanding the generation and transfer of polarized radiation field.

For resonance lines, the scattering events that occur can be expressed as a mixture of the type II and type III processes. The resulting spectral lines will show the effects due to both perfectly frequency coherent and incoherent scattering events. Therefore, one has to use the RM for both these types of scattering and combine them appropriately using the branching ratios which depend on the parameters that account for the radiative and collisional processes. This is referred to as the partial frequency redistribution (PRD). In

Part I of the thesis, we deal with both type II and type III scattering processes. In Part II, we consider only the type II processes in the atom's rest frame and derive the RM (or the PRD matrix) in the laboratory frame accounting for the redistribution which occurs due to the Doppler shift. We consider atomic systems which are more complex compared to the simple two-level atom model. To achieve this task, we make use of the coherency matrix formalism presented in Section 1.1 along with the Kramers–Heisenberg formula. This formula gives the scattering amplitude for a general $a \rightarrow b \rightarrow f$ type transition where $a, b,$ and f are the initial, intermediate, and final states. It was derived by Kramers & Heisenberg (1925) based on the correspondence principle applied to the classical dispersion relation for light. A quantum mechanical derivation of the Kramers–Heisenberg formula was given by Dirac (1927a,b).

1.3.2 A Brief History of PRD

In PRD, there exists a correlation between the frequencies and angles of the absorbed and scattered photons. It is now known that the PRD mechanism plays a crucial role in shaping the polarization profiles of the spectral lines, particularly the resonance lines. PRD affects both the intensity and polarization and gives rise to a characteristic triple peak structure (see, for example, Mihalas, 1978; Rees & Saliba, 1982).

PRD was first introduced to explain the linear polarization profiles of resonance lines by Zanstra (1941a,b). Its first quantum electrodynamical treatment was given by Omont et al. (1972) for the non-magnetic case which was later extended to include the magnetic fields by Omont et al. (1973). The functional forms of the RMs of Omont et al. (1972) for practical applications were provided by Domke & Hubeny (1988). Using the approach based on the quantum electrodynamics, Bommier (1997a,b) formulated the matrices for the non-magnetic and magnetic cases, properly taking account of the collisional redistribution. A modern approach for the atomic frame RM based on the classical oscillator model was given by Stenflo (1994, 1998) and later extended by Bommier & Stenflo (1999) to include the effects of collisions. Based on the density matrix approach, using the concept of metalevels, Landi Degl'Innocenti et al. (1997) derived the RMs for coherent scattering in the atom's rest frame in the absence of collisions. Sampoorna et al. (2013) presented a heuristic theoretical approach to the problem of polarized line formation in multi-level atoms taking into account the effects of PRD and a weak magnetic field. See the review by Frisch (1996) for more details.

There are more recent formulations of PRD matrices for more general physical mechanisms. For example, Sampoorna et al. (2007a) derived the Hanle-Zeeman PRD matrix for

the simpler case of a normal Zeeman effect (see Section 1.7.1) and for a coordinate system in which the z-axis is along the magnetic field. Sampoorna (2011a) generalized the PRD theory of Sampoorna et al. (2007a) to other types of transitions with arbitrary quantum numbers. This theory accounts for the quantum interference (see Section 1.6) between the magnetic substates of a given atomic state. Smitha et al. (2011b) developed the PRD theory of quantum interference between the fine structure states of an atom by considering the upper states to be only radiatively broadened and in a later paper (Smitha et al., 2013a) developed a heuristic approach to include the effects of elastic collisions. Smitha et al. (2012b) formulated the PRD theory for the quantum interference taking place between the hyperfine structure states in the absence of magnetic fields and collisions. Recently, Casini et al. (2014) developed an approach based on the Feynman diagrams representing atom-photon interaction and presented the generalized frequency redistribution functions for arbitrary magnetic fields. In this thesis, we extend the PRD theories of Smitha et al. (2011b) and Smitha et al. (2012b) to include the effects of magnetic fields of arbitrary strength and also formulate a more general theory which can treat the quantum interference among the fine and hyperfine structure states, simultaneously (see Part II of the thesis for more details). See the review articles by Nagendra (2014, 2015) for discussions on the role played by PRD in scattering.

1.4 Atomic Configurations

In this section, we discuss the various atomic configurations that we consider in our studies. We assume that the lower level is infinitely sharp and unpolarized throughout. For simplicity, we show only the atomic configurations in the absence of magnetic fields when the magnetic substates are degenerate. All the atomic transitions considered in this thesis are of electric dipole type.

1.4.1 Two-Term Atom without Hyperfine Structure

An atomic term is characterized by the orbital angular momentum quantum number L and spin quantum number S of the electron, under the approximation that the atom undergoes spin-orbit coupling. The $L-S$ coupling results in states labeled by the total electronic angular momentum quantum number J. The term symbol generally followed in spectroscopy is given by ${}^{(2S+1)}L_J$. In the two-term atom that we deal with in this thesis, the lower term is ^{2}S ($L=0, S=1/2$) and the upper term is ^{2}P ($L=1, S=1/2$). The $L-S$ coupling gives rise to ${}^2\mathrm{S}_{1/2}$ state in the lower term, and ${}^2\mathrm{P}_{1/2}$ and ${}^2\mathrm{P}_{3/2}$ states in the upper term,

according to $J = |L - S|...L + S$. In Figure 1.2, we show the two-term configuration in

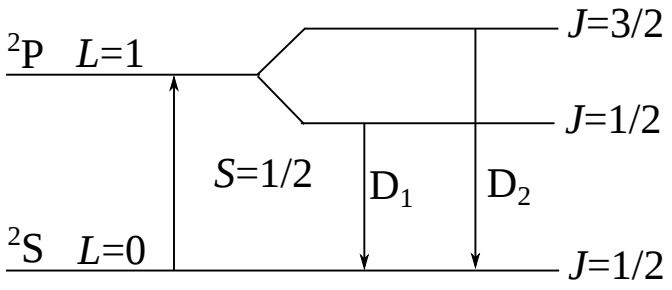

Figure 1.2: A two-term configuration taking example of Li I $D_{1,2}$ doublet. The splittings are not to the scale.

Li atom. We study the effects of a magnetic field on this system in Chapter 5. The dipole type transitions in a two-term atom follow the selection rules $\Delta L = 0, \pm 1$ ($L = 0 \nrightarrow 0$), $\Delta S = 0$, and $\Delta J = 0, \pm 1$ ($J = 0 \nrightarrow 0$). When a magnetic field is applied, the degeneracy of the magnetic substates is lifted and the transitions occurring between these states obey $\Delta\mu = 0, \pm 1$, with μ being the magnetic quantum number labeling the magnetic substates of the J states.

1.4.2 Two-Level Atom with Hyperfine Structure

The two-level atom that we consider has two J states belonging to two different terms. When the atomic nucleus possesses a spin I_s (Pauli, 1924), the coupling between J and I_s results in hyperfine structure states labeled by the total angular momentum quantum number F so that $\boldsymbol{F} = \boldsymbol{J} + \boldsymbol{I}_s$. The F states are given by the vector addition formula

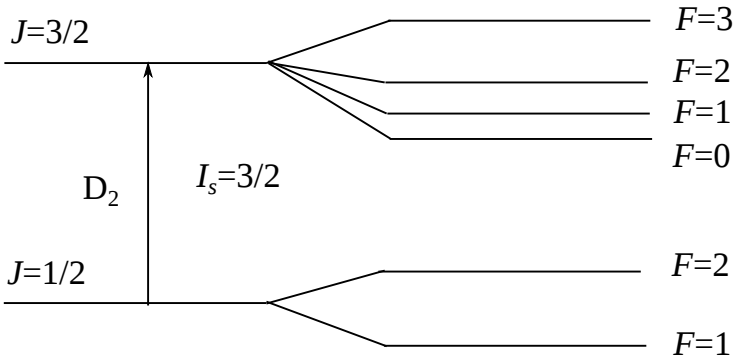

Figure 1.3: A two-level atom with hyperfine structure taking the example of Na I D_2 line. The splittings are not to the scale.

$F = |J - I_s|, ..., J + I_s$. The number of F states into which a given J state splits is

given by $min(2J+1,\ 2I_s+1)$. For electric dipole transitions between the F states the selection rules are $\Delta J = 0, \pm 1$ ($J = 0 \nrightarrow 0$), $\Delta F = 0, \pm 1$ ($F = 0 \nrightarrow 0$), and $\Delta\mu = 0, \pm 1$. Here, μ denotes the magnetic substates of the F states. The electric dipole nature of the interaction does not permit transitions among F states of a given J state. Figure 1.3 shows the configuration of Na atom which we deal with in Chapter 4. In Part I of the thesis, a two-level atom model without hyperfine structure is considered.

1.4.3 Two-Term Atom with Hyperfine Structure

In Section 1.4.1, we did not account for the hyperfine structure states that results because of the coupling between J and I_s. Certain spectral lines in the second solar spectrum are

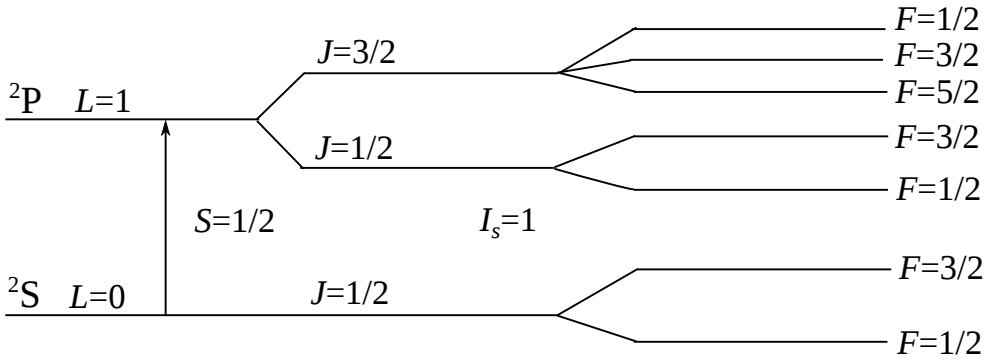

Figure 1.4: A two-term atom with hyperfine structure taking the example of D_1 and D_2 lines of ^{6}Li. The splittings are not to the scale.

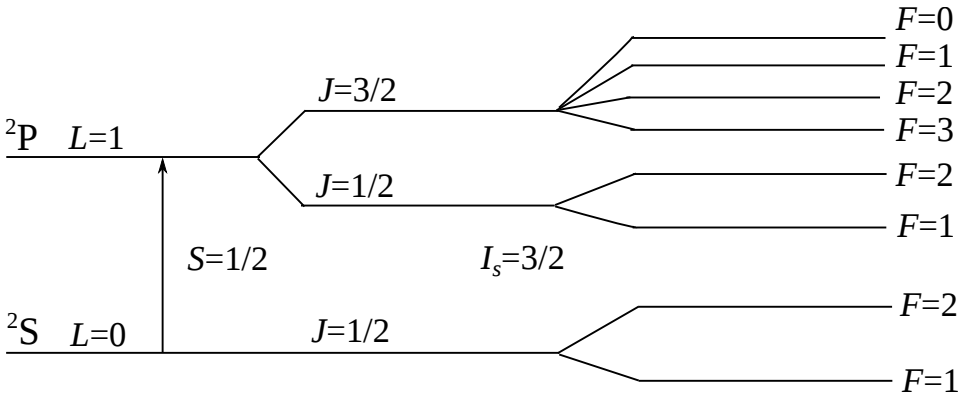

Figure 1.5: A two-term atom with hyperfine structure taking the example of D_1 and D_2 lines of ^{7}Li. The splittings are not to the scale.

known to be influenced by both fine and hyperfine structure. To study such lines, one has

to deal with two-term atom with hyperfine structure. In Chapters 6 and 7, we treat the lines resulting from transitions between the ^{2}S and ^{2}P terms of two stable isotopes ^{6}Li and ^{7}Li (see Figures 1.4 and 1.5). The selection rules for the electric dipole transitions are the same as the ones discussed in Sections 1.4.1 and 1.4.2.

Throughout this thesis, we denote the levels from which the absorptions occur with subscripts a, the levels to which the absorptions take place with subscripts b, and the levels to which the emissions happen with subscripts f.

1.5 Theory of Fine and Hyperfine Structure in Atoms

In this section, we briefly introduce the derivation of the expressions for the fine and hyperfine structure interaction Hamiltonians which will be used in Part II of the thesis. We follow Condon & Shortley (1935); Corney (1977) and Woodgate (1992) for this purpose and recall their expressions here, for the sake of completeness.

1.5.1 Fine Structure Hamiltonian

The fine structure states arise due to the energy change produced by the interaction between the spin moment and the magnetic moment generated because of the orbital motion of the electron (see Section 1.4). In this thesis, we consider only the spin-orbit coupling arising from the relativistic orbital motion of electrons possessing spin in an electric field produced by the nuclear charge.

For a single electron system, this interaction can be represented by the spin-orbit Hamiltonian

$$\mathcal{H}_{\rm fs} = -\boldsymbol{\mu}_s \cdot \boldsymbol{B}_l \ , \tag{1.12}$$

where the spin magnetic moment of the electron $\boldsymbol{\mu}_s$ is given by

$$\boldsymbol{\mu}_s = -g_s \mu_B \boldsymbol{s} \ . \tag{1.13}$$

Here, the spin-g factor $g_s = 2$ and $\mu_B = e\hbar/2m_e$ is the Bohr magneton where m_e is the mass of the electron, e is its charge and $\hbar = h/2\pi$ (h is the Planck constant). In Equation (1.12), $\boldsymbol{B}_l$ is the magnetic field generated at the electron because of its orbital motion and is given by

$$\boldsymbol{B}_l = -\frac{\boldsymbol{v} \times \boldsymbol{E}}{c^2} \ , \tag{1.14}$$

where c is the speed of light, $\boldsymbol{v}$ is the velocity of the electron and $\boldsymbol{E}$ is the electric field generated by the nucleus. Using the fact that $\boldsymbol{E}$ is radial and the momentum $\boldsymbol{p} = m_e \boldsymbol{v}$, we

can rewrite Equation (1.14) as

$$\boldsymbol{B}_l = \frac{\boldsymbol{r} \times \boldsymbol{p}}{m_e c^2} \frac{E}{r} \,. \tag{1.15}$$

We know that,

$$\boldsymbol{l} = \frac{\boldsymbol{r} \times \boldsymbol{p}}{\hbar}; \quad E = \frac{1}{e}\frac{\mathrm{d}V(r)}{\mathrm{d}r}; \quad V(r) = -\frac{Ze^2}{4\pi\epsilon_0 r} \,. \tag{1.16}$$

Using these in Equation (1.15) we get

$$\boldsymbol{B}_l = \frac{\hbar}{m_e e c^2}\frac{1}{r}\frac{\mathrm{d}V(r)}{\mathrm{d}r}\boldsymbol{l} \,. \tag{1.17}$$

The Hamiltonian in Equation (1.12) now becomes

$$\mathcal{H}_{\mathrm{fs}} = \frac{\hbar^2}{2m_e^2 c^2}\frac{Ze^2}{4\pi\epsilon_0 r^3}\boldsymbol{s}\cdot\boldsymbol{l} \,, \tag{1.18}$$

whose expectation value gives the first order energy shift E_{fs}, arising from the spin-orbit interaction. The extra factor $1/2$ comes because of the relativistic corrections.

From the vector model of the atom, we know that $\boldsymbol{j} = \boldsymbol{l} + \boldsymbol{s}$. Also, $\boldsymbol{s}\cdot\boldsymbol{l}$ commutes with $\boldsymbol{l}^2, \boldsymbol{s}^2, \boldsymbol{j}^2$ and j_z which have a common eigenvector $|lsj\mu\rangle$ where μ is the eigenvalue of the operator j_z. We can now compute E_{fs} as

$$E_{\mathrm{fs}} = \langle lsj\mu|\xi\boldsymbol{s}\cdot\boldsymbol{l}|lsj\mu\rangle \,, \tag{1.19}$$

where

$$\xi = \frac{\hbar^2}{2m_e^2 c^2}\frac{Ze^2}{4\pi\epsilon_0}\langle r^{-3}\rangle \,. \tag{1.20}$$

We can express $\boldsymbol{s}\cdot\boldsymbol{l}$ as follows

$$\boldsymbol{j}^2 = \boldsymbol{j}\cdot\boldsymbol{j} = (\boldsymbol{l}+\boldsymbol{s})\cdot(\boldsymbol{l}+\boldsymbol{s}) = \boldsymbol{l}^2 + \boldsymbol{s}^2 + 2\boldsymbol{s}\cdot\boldsymbol{l} \,, \tag{1.21}$$

from which we can write

$$\boldsymbol{s}\cdot\boldsymbol{l} = \frac{1}{2}[\boldsymbol{j}^2 - \boldsymbol{l}^2 - \boldsymbol{s}^2] \,. \tag{1.22}$$

Using Equation (1.22) in Equation (1.19) and using the expectation values of the operators $\boldsymbol{j}^2, \boldsymbol{l}^2$, and $\boldsymbol{s}^2$, we arrive at

$$E_{\mathrm{fs}} = \frac{\xi}{2}[j(j+1) - l(l+1) - s(s+1)] \,, \tag{1.23}$$

which is the energy shift produced by the spin-orbit interaction for a single electron system.

For a multi-electron system, we can generalize the spin-orbit Hamiltonian as

$$\mathcal{H}_{\rm fs} = \sum_i \xi(r_i) \boldsymbol{l}_i \cdot \boldsymbol{s}_i \ , \tag{1.24}$$

and the various angular momenta as

$$\boldsymbol{L} = \sum_i \boldsymbol{l}_i; \quad \boldsymbol{S} = \sum_i \boldsymbol{s}_i; \quad \boldsymbol{J} = \boldsymbol{L} + \boldsymbol{S} \ . \tag{1.25}$$

Here, $i = 1, 2, ...n$ with n being the total number of electrons. The Hamiltonian is now given by

$$\mathcal{H}_{\rm fs} = \zeta(LS) \boldsymbol{L} \cdot \boldsymbol{S} \ , \tag{1.26}$$

and $\mathcal{H}_{\rm fs}$ commutes with $\boldsymbol{J}^2, \boldsymbol{L}^2, \boldsymbol{S}^2$, and J_z. With the basis vector $|LSJ\mu\rangle$ (where $\mu = J_z$) we arrive at

$$E_{\rm fs} = \frac{\zeta(LS)}{2}[J(J+1) - L(L+1) - S(S+1)] \ , \tag{1.27}$$

where $\zeta(LS)$ includes the ξ for each electron and has the dimension of energy. We make use of Equation (1.27) to calculate the energies of the fine structure states in Chapters 5, 6, and 7.

1.5.2 Hyperfine Structure Hamiltonian

Hyperfine structure is due to the interaction between the electromagnetic multipole moments of the nucleus with the electromagnetic field generated at the nucleus by the electrons. The largest contributions to the hyperfine structure come from the interaction of nuclear magnetic dipole moment with an electronic magnetic field and of nuclear electric quadrupole moment with a gradient of the electronic electric field. The contributions from other terms in the multipolar expansion are either negligible compared to these two terms or vanish because of the parity and time-reversal symmetries.

Magnetic dipole interaction: The interaction of the nuclear magnetic moment $\boldsymbol{\mu}_{I_s}$ with the magnetic field $\boldsymbol{B}_{\rm el}$ produced at the nucleus by the electrons is described by the Hamiltonian

$$\mathcal{H}_D = -\boldsymbol{\mu}_{I_s} \cdot \boldsymbol{B}_{\rm el} \ . \tag{1.28}$$

We assume that the unperturbed Hamiltonian contains the central field, the electrostatic repulsion terms between electrons, and the spin-orbit interaction so that we have to consider only those states labeled by (LSJ). This approximation is in analogy with the $L - S$

coupling and is called $I_s - J$ coupling. This allows one to write

$$\boldsymbol{\mu}_{I_s} = g_{I_s}\mu_N \boldsymbol{I}_s \ , \tag{1.29}$$

where g_{I_s} is the nuclear g factor, $\mu_N = e\hbar/2M$ is the nuclear magneton and M is the mass of the proton. Since we assume that $\boldsymbol{\mu}_{I_s}$ depends only on the nuclear coordinates and $\boldsymbol{B}_{\rm el}$ only on the electronic coordinates, we can write, using the $I_s - J$ coupling approximation

$$\boldsymbol{B}_{\rm el} \propto \boldsymbol{J} \ , \tag{1.30}$$

and therefore

$$\mathcal{H}_D = \mathcal{A}_J \boldsymbol{I}_s \cdot \boldsymbol{J} \ . \tag{1.31}$$

Here, $\mathcal{A}_J$ is the magnetic dipole interaction constant. To the first order the energy shift of a state J because of the magnetic dipole interaction is given by the expectation value of the Hamiltonian $\mathcal{H}_D$

$$E_D = \langle J I_s F \mu | \mathcal{A}_J \boldsymbol{I}_s \cdot \boldsymbol{J} | J I_s F \mu \rangle = \frac{\mathcal{A}_J}{2}\mathcal{K} \ , \tag{1.32}$$

where $\mathcal{K} = [F(F+1) - J(J+1) - I_s(I_s+1)]$ and μ is the eigenvalue of F_z. We have used $\boldsymbol{F} = \boldsymbol{I}_s + \boldsymbol{J}$ from the vector model of the atom.

Electric quadrupole interaction: The electrostatic interaction between a proton of charge e at the point $\boldsymbol{r}_n$ and an electron of charge $-e$ at the point $\boldsymbol{r}_e$ is given by

$$\mathcal{H}_Q = -\frac{e^2}{4\pi\epsilon_0 |\boldsymbol{r}_e - \boldsymbol{r}_n|} \ , \tag{1.33}$$

where the origin of the coordinates is the center of mass of the nucleus. To account for the finite extent of the nuclear charge distribution, we assume $r_e > r_n$ and expand $\mathcal{H}_Q$ in ascending powers of r_n/r_e as

$$\begin{aligned} \mathcal{H}_Q &= -\frac{e^2}{4\pi\epsilon_0}(r_e^2 + r_n^2 - 2 r_e r_n \cos\theta_{en})^{-1/2} \ , \\ &= -\frac{e^2}{4\pi\epsilon_0}\sum_k \frac{r_n^k}{r_e^{k+1}} P_k(\cos\theta_{en}) \ , \end{aligned} \tag{1.34}$$

where $P_k(\cos\theta_{en})$ is the Legendre polynomial of order k and θ_{en} is the angle between $\boldsymbol{r}_e$ and $\boldsymbol{r}_n$.

The first term in Equation (1.34) represents a monopole interaction. As discussed earlier, the moments of odd k vanish because of the parity and time-reversal symmetry. We

can now separate the electric and nuclear coordinates in Equation (1.34) by applying the spherical harmonic addition theorem as

$$P_k(\cos\theta_{en}) = \frac{4\pi}{2k+1}\sum_{q=-k}^{k}(-1)^q Y_k^{-q}(\theta_n,\chi_n)Y_k^q(\theta_e,\chi_e)\;, \tag{1.35}$$

where Y_k^q is the q^{th} component of the spherical harmonic of order k and the spherical coordinates (θ,χ) are measured with respect to an arbitrary z-axis. For $k=2$, $\mathcal{H}_Q$ takes the form

$$\begin{aligned}
\mathcal{H}_Q &= -\frac{e^2}{4\pi\epsilon_0}\frac{r_n^2}{r_e^3}P_2(\cos\theta_{en})\;,\\
&= -\frac{e^2 r_n^2}{4\pi\epsilon_0 r_e^3}\frac{4\pi}{5}\sum_{q=-2}^{2}(-1)^q Y_2^{-q}(\theta_n,\chi_n)Y_2^q(\theta_e,\chi_e)\;,\\
&= \sum_{q=-2}^{2}(-1)^q\left\{\sqrt{\frac{4\pi}{5}}e r_n^2 Y_2^{-q}(n)\right\}\left\{\sqrt{\frac{4\pi}{5}}\left(\frac{-e}{4\pi\epsilon_0 r_e^3}\right)Y_2^q(e)\right\}\;,\\
&= \sum_q (-1)^q Q_2^{-q}(n)F_2^q(e)\;.
\end{aligned} \tag{1.36}$$

When summed over all the protons and electrons, this equation gives the complete electric quadrupole interaction. It can be simplified by defining the nuclear quadrupole moment and the average gradient of the electric field produced by the electrons. It finally leads us to the Hamiltonian

$$\mathcal{H}_Q = \frac{\mathcal{B}_J}{2I_s(2I_s-1)J(2J-1)}\left\{3(\boldsymbol{I}_s\cdot\boldsymbol{J})^2+\frac{3}{2}(\boldsymbol{I}_s\cdot\boldsymbol{J})-I_s(I_s+1)J(J+1)\right\}\;, \tag{1.37}$$

and its expectation value gives the energy shift due to electric quadrupole interaction as

$$E_Q = \frac{\mathcal{B}_J}{8I_s(2I_s-1)J(2J-1)}\{3\mathcal{K}(\mathcal{K}+1)-4J(J+1)I_s(I_s+1)\}\;, \tag{1.38}$$

where $\mathcal{B}_J$ is the electric quadrupole interaction constant. In Chapters 4, 6, and 7, we use the expressions for E_D and E_Q to obtain the energies of the F states.

1.6 Quantum Interference Phenomena

The transitions in a two-term atom (see Section 1.4) give rise to multiplets. The spectral lines constituting the multiplets interact with each other and give rise to interesting sig-

natures in the second solar spectrum. One such feature observed is the crossover in Q/I between the Ca II H and K lines. Figure 1.6 shows the non-magnetic observations of the linear polarization in this doublet obtained near the solar limb. In such observations the only source of polarization is the coherent scattering in lines. A simple two-level atom model for the doublet without fine structure interaction could not explain the crossover effect.

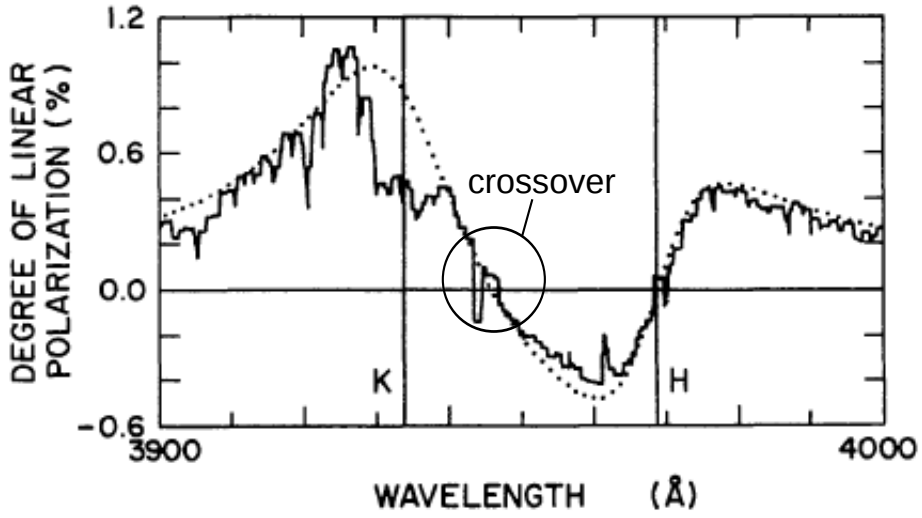

Figure 1.6: Observed (solid line) and theoretical (dotted) profiles of the Ca II H and K lines given in Stenflo (1980). Notice the crossover between the K and H lines.

Stenflo (1980) showed that this signature is a result of the quantum mechanical interference that always occurs between the scattering transitions belonging to a multiplet. Ca II H and K lines result from the transitions in a two-term atom like the one shown in Figure 1.2. $J = 1/2 \rightarrow 1/2$ transition gives rise to H line, and $J = 3/2 \rightarrow 1/2$ to the K line. The S-shaped profile seen in the observations is attributed to the quantum interference between the upper $J = 1/2$ and $J = 3/2$ states. This means that the scattered photons arise due to a joint probability of transitions from both the upper J states to the lower J state. This is analogous to the probability of a photon passing through both the slits simultaneously in the double-slit experiment. The photons scattered on the calcium ions do not choose whether to scatter via H or K line. In fact, they have a joint probability of scattering in both the lines at the same time.

Mathematically this arises due to the fact that the wave function ψ of an atomic state can be expressed as a superposition of n substates as $\psi = \sum_n c_n \phi_n$ and the probability of

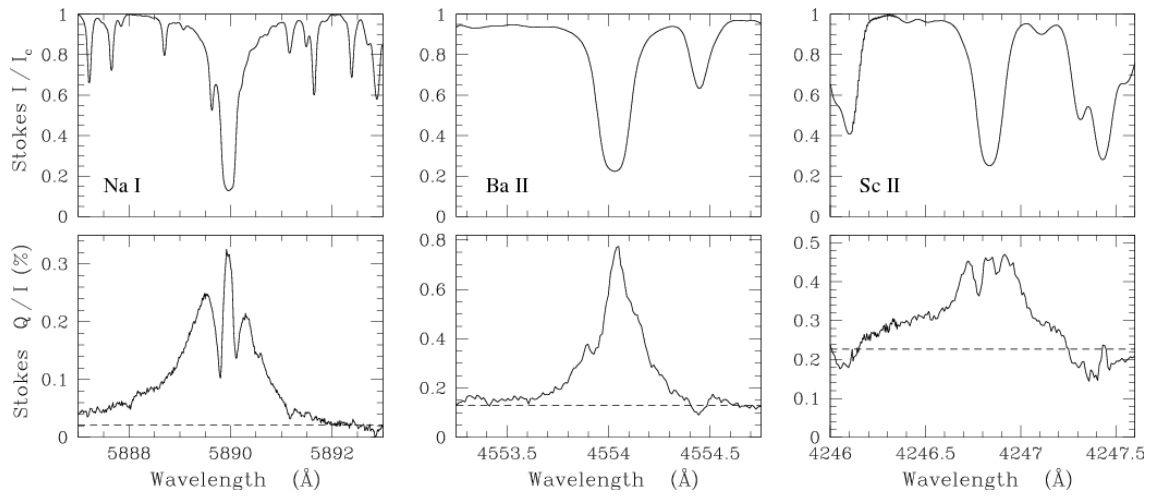

Figure 1.7: Examples of the spectral lines showing effects due to F-state interference. This figure is taken from Belluzzi (2009). The observations of the Na and Ba lines presented here were first reported by Stenflo & Keller (1997). The upper panels show the intensity and the lower panels the degree of linear polarization.

finding the system to be in a given state is

$$|\psi|^2 = |\sum_n c_n \phi_n|^2 \,, \tag{1.39}$$

and not

$$|\psi|^2 = \sum_n |c_n \phi_n|^2 \,. \tag{1.40}$$

Equation (1.39) involves cross products which represent interference in addition to the terms given by Equation (1.40). From this it can be clearly understood that the scattering amplitude resulting from the calcium ions is a linear superposition of the scattering amplitudes for the H and K transitions (Stenflo, 1980, 2009a). This type of quantum interference taking place between the J states is called J-state interference. The interference which occurs between the F states is called F-state interference. We study the effect of a magnetic field on these types of interference, in Part II. The interference between the magnetic substates of a given J or F state is called as m-state interference where m is the magnetic quantum number (see Stenflo, 1994; Sampoorna, 2011a)[3]. Figure 1.7 shows some of the other examples of the spectral lines which are influenced by the interference phenomena.

[3]See also Bommier (1997a,b)

1.7 A Brief Introduction to Magnetic Fields on the Sun

The existence of magnetic fields on the Sun (in sunspots) was first discovered by George Ellery Hale in 1908 through the observations of Zeeman effect (Hale, 1908a,b). Soon after it was observed that the magnetic fields are also present in the regions other than sunspots. Since then a lot of advancement has taken place in understanding the mechanisms generating these fields, their nature and distribution. See the review article by Stenflo (2015a) for the history of solar magnetic fields since the time of their discovery by Hale.

Sun is the only star for which we have the possibility to resolve and study in detail the interaction between the magnetic fields and matter. With the help of several ground and space based observations, we now know that the Sun is a highly magnetized sphere. Magnetic fields, whose strengths vary from a few gauss to a few kilogauss, govern the structure and dynamics of the Sun. They contribute to the heating of the corona, which is a long standing problem in the field of solar physics which is not yet completely understood. They give rise to energetic phenomena like flares, prominences, coronal mass ejections etc. (see, for example, Howard, 1971; Kundu et al., 1989; Wilson, 1999). The coronal mass ejections drive the solar winds which govern the space weather. The magnetic fields in the solar winds interact with the earth's magnetosphere and directly influence the terrestrial environment. Therefore, the study of the solar magnetic fields is of profound importance.

The rapidly varying solar magnetic fields can be studied in numerous ways (Beckers, 1971; Stenflo, 1978b; Landi Degl'Innocenti, 1985, 1992). Measurements based on the polarization of the electromagnetic radiation involves methods which use Zeeman effect, Hanle effect, gyro-synchrotron radiation (radio observations), and Faraday rotation. A few methods use magnetohydrodynamics effects on the solar atmosphere like alignment of the structures, local changes in the temperature and pressure, Alfven velocity, prominence oscillations etc. Theoretical considerations involve force-free potential field calculations and equipartition of magnetic and kinetic energies. In-situ measurements in the solar wind region and using the information on the primordial magnetic fields contained in the meteorites are among the other methods to study the solar magnetic fields.

1.7.1 The Zeeman Effect

Splitting of a spectral line into differently polarized components by the magnetic field present in the region of line formation is termed as the Zeeman effect. It was discovered by Pieter Zeeman in 1896 (Zeeman, 1897). The amount of splitting is proportional to the magnetic field strength, the square of the line center wavelength and the Landé factor

which depends on the quantum numbers of the levels involved in the transition. Since the discovery of magnetic fields on the Sun by Hale, Zeeman effect has been the main tool for their diagnostics.

In the case of normal Zeeman effect ($J = 0 \rightarrow 1 \rightarrow 0$ transition), three components result: one unshifted π component and two oppositely shifted σ components (see Figure 1.8). The π component vanishes when the magnetic field is parallel to the line of sight (longitudinal Zeeman effect) and the two σ components are left and right circularly polarized. When the magnetic field is perpendicular to the line of sight (transverse Zeeman effect), all the three components are present. The strength of the π component equals the sum of the two σ components. Essentially, the linear polarization responds to the transverse Zeeman effect and the circular polarization to the longitudinal Zeeman effect. Therefore, in principle, it is possible to derive the strength and geometry of the magnetic field by the simultaneous measurement of the Stokes parameters (see Stenflo, 1978b).

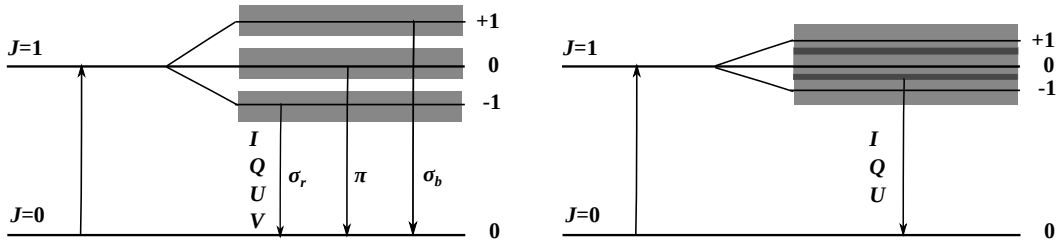

Figure 1.8: Quantum mechanical picture of the Zeeman (left) and Hanle (right) effects. The splittings are not to the scale in the illustration.

Zeeman effect depends on the ratio of the magnetic splitting (MS), and the Doppler width (which is substantially larger than the natural width of the line). Thus, the Zeeman effect is relatively insensitive to weak fields. Zeeman effect vanishes if the fields are turbulent and tangled within the resolution element because the polarization from the opposite polarities cancel out due to symmetry. Therefore, it is much suited for studying resolved strong fields which are unbalanced in the resolution element of the telescope.

1.7.2 The Hanle Effect

Scattering in a spectral line in the absence of a magnetic field produces linear polarization. This is called as Rayleigh scattering or resonance scattering in spectral lines. Hanle effect refers to the modification by the magnetic field, of the scattering polarization generated by resonance scattering in the line. The magnetic field rotates the plane of polarization, and leads to a decrease in the degree of linear polarization in the line core. This means

that the Stokes U signal is generated and the magnitude of the Stokes Q is reduced (as compared to its value in the non-magnetic case). These signatures help in the measurement of magnetic fields. Therefore, in recent years, Hanle effect has emerged as a diagnostic tool complementary to the Zeeman effect.

When the magnetic substates are not completely split by the magnetic field, the scattering transitions take place from the overlapping substates, as shown in Figure 1.8. This type of interference was first discovered in resonance lines by Rayleigh (1922) in his light scattering experiment with mercury vapor in the absence of magnetic fields (however, the Earth's magnetic field was not shielded). Wood & Ellet (1923) studied the depolarization caused by weak applied magnetic fields. Hanle (1923, 1924) performed an experiment with weak applied magnetic fields, and observed for the first time, the so called 'Hanle depolarization', and a rotation of the plane of polarization. He also gave a correct explanation for this phenomena and hence the effect is named after him as Hanle effect. Hanle effect played a fundamental role in the development of quantum mechanics in clarifying the concept of linear superposition of stationary states in atoms. For a variety of applications of Hanle effect in the main land of physics and also astrophysics, see Moruzzi & Strumia (1991).

Hanle effect depends on the natural width of the levels and the amount of splitting caused by the magnetic field and does not depend on the Doppler width of the spectral lines. It is, therefore, sensitive to oriented fields that are weak, and also to the fields of mixed polarity within the resolution element (which are not accessible by the Zeeman effect, see Stenflo, 1978b, 2002, 2015a). The Hanle sensitivity regime varies depending on the spectral line under consideration. Trujillo Bueno (2001) showed that for typical solar lines in the optical domain, the upper level Hanle effect sensitivity is in the range 1 to 100 gauss, while that for the lower level is between 10^{-3} and 1 gauss. The Hanle and Zeeman effects therefore complement each other in a rather ideal way in terms of field strength regime.

In recent years, Hanle effect has found many applications in the determination of magnetic fields. Its first application in astrophysics was by Leroy et al. (1977, see also Leroy 1985; Bommier et al. 1985) to determine the magnetic fields in the prominences. Hanle effect in turbulent and oriented fields were also observed by Stenflo (1982). Indeed the diagnostic potential of Hanle effect to detect turbulent fields was clearly demonstrated by Stenflo in his paper (1982). Faurobert-Scholl et al. (1995) used the Hanle effect to determine the turbulent magnetic field strength in the solar photosphere and Faurobert-Scholl (1996) addressed the problem of the diagnostics of weak magnetic fields in the solar photosphere and chromosphere by means of their Hanle effect in some selected absorption lines. Faurobert (2000) showed how the Hanle effect may be used for the diagnos-

tics of magnetic canopies in the chromosphere (see also Faurobert, 2003). Some of the other studies related to the measurement of weak magnetic fields using the Hanle effect can be found in the papers Stenflo (2002); Trujillo Bueno (2003a); Trujillo Bueno et al. (2005, 2006) and Faurobert (2012). See the monograph by Stenflo (1994) and the book by Landi Degl'Innocenti & Landolfi (2004) for full theoretical details.

1.7.3 The Paschen–Back Effect

When the magnetic field is strong enough to produce a splitting which is comparable to or greater than the separation between the atomic states of a given term in the absence of the magnetic field, the magnetic substates belonging to different atomic states interfere. This effect is called the Paschen–Back effect (PBE). The magnetic field influences the coupling between the orbital and spin angular momenta, leading to a splitting pattern different from that of the Zeeman effect. This effect was discovered by Friedrich Paschen and Ernst Back in 1912 (Paschen & Back, 1912).

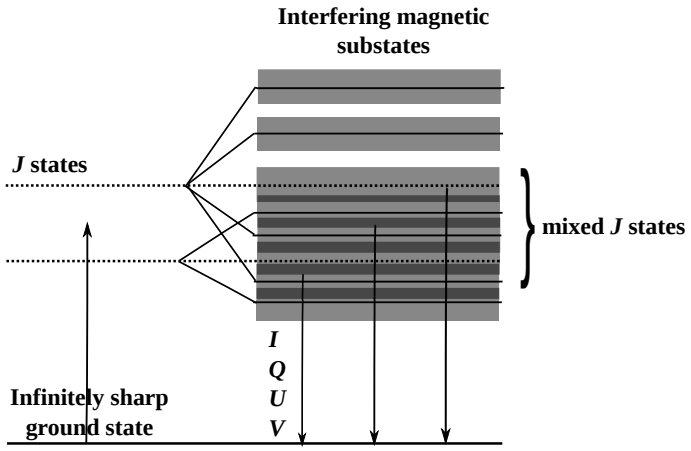

Figure 1.9: Illustration of the atomic level mixing in the PB regime for fine structure. The splittings are not to the scale.

PBE depends on the ratio of MS to the atomic (fine or hyperfine structure) splitting. If the ratio is less than 1, then the effects are still described by the Zeeman effect. We enter a regime called the incomplete Paschen–Back (PB) regime when the ratio is close to 1. This regime is characterized by nonlinear MS. When the ratio of the splittings is much greater than 1, we see the effects due to complete PBE. In this regime, MS is linear like in the Zeeman effect. The spectral lines formed in the PB regime violate the ordinary selection rules as a result of which the spectral lines will compose of the previously forbidden transitions. This comes as a consequence of the mixing of the atomic states due to which

the quantum numbers cannot be precisely defined for these mixed states (see, for example, Condon & Shortley, 1935). In Figure 1.9, we illustrate the mixing of fine structure states in the PB regime. More details on the effects of such a mixing are provide in Part II of the thesis.

PBE in molecules is of great significance in the stellar astrophysics because of its potential as a tool in diagnosing magnetic fields present in the stars. Over the last few years, the theoretical formulations for PBE in molecules have been developed and applied for magnetic field diagnostics. Berdyugina et al. (2005) formulated the theory of molecular PBE which is valid for terms of any multiplicity and accounts for interactions of all rotational levels in a molecular electronic state (see also Berdyugina et al., 2006b). This formulation was employed by Asensio Ramos et al. (2005) to model the polarization profiles produced by PBE in CN molecules, by Berdyugina et al. (2006a) to model the PBE in CaH transitions, and by Shapiro et al. (2006, 2007) for developing the theory of molecular Hanle effect in the PB regime. Asensio Ramos (2006) also presented the theory of molecular PBE neglecting interactions between the rotational levels. Further, Kuzmychov & Berdyugina (2013) examined the potential of PBE in CrH molecule for magnetic field measurements on stars, brown dwarfs, and hot exoplanets.

Many atomic spectral lines formed in the solar atmosphere are sensitive to PBE for the magnetic field strengths encountered on the Sun. PBE in atomic lines is also of great importance because the signatures of it in the polarization of these spectral lines can serve as diagnostic tools for magnetic fields, in a complementary way to the Zeeman and Hanle effects. However, the scattering theory of atomic spectral line formation with PBE needed for this purpose is still not completely formulated. Bommier (1980) discussed the effect of level-crossings and anti-level-crossings (see Part II) that occur in the PB regime on the polarization of the D_3 helium line of solar prominences considering the case of CRD (see also Landi Degl'Innocenti, 1982; Socas-Navarro et al., 2004). Based on the concept of metalevels, Landi Degl'Innocenti et al. (1997) presented a formalism to include the effects of a magnetic field of arbitrary strength including the effects of PRD. A formalism based on the density matrix approach is able to account for PBE (Landi Degl'Innocenti & Landolfi, 2004; Casini & Manso Sainz, 2005) but is limited to CRD. Using this density matrix theory Trujillo Bueno et al. (2002) and Belluzzi et al. (2007) explored the sensitivity of polarization in Na I D lines and Ba II D lines, respectively, to the magnetic fields in the PB regime. Based on the approach of Feynman diagrams for scattering, Casini et al. (2014) presented generalized frequency redistribution function for a two-term atom including PBE which was extended recently to the case of lambda-type multi-term atom by Casini & Manso Sainz (2016). Our aim in this thesis is to develop the scattering the-

ory of PBE including the effects of PRD, using an alternative approach starting from the Kramers–Heisenberg formula. The RM derived in this approach can then be incorporated in the transfer equation and used for modeling different spectral lines to analyze the magnetic sensitivity of the solar lines in the PB regime. More details are given in Part II of the thesis.

1.8 The Transfer of Polarized Radiation

The photons emitted by the atom traverse through the media, like solar or stellar atmosphere before reaching the observer. Thus, they undergo multiple scattering before escaping from the stellar atmosphere. This transport is described by the radiative transfer equation (which is an energy balance equation) containing the absorption and emission terms. In Part I of the thesis, we deal with the polarized transfer equation in the absence and presence of weak magnetic fields and in Chapter 7, with the transfer in the presence of strong magnetic fields.

1.8.1 The Polarized Radiative Transfer Equation

In this thesis, we consider the formation and transfer of spectral lines in a one-dimensional (1D) plane-parallel atmosphere under NLTE conditions (see Section 1.2.2). In Chapters 2 and 3, we consider isothermal atmospheres while in Chapter 7, we deal with realistic solar model atmospheres (Fontenla et al., 1990, 1991, 1993; Avrett, 1995) which mimic the conditions prevailing on the Sun. The polarized radiative transfer equation in the presence of a magnetic field of arbitrary strength (Stenflo, 1994; Landi Degl'Innocenti & Landolfi, 2004) is given by

$$\mu \frac{\partial \boldsymbol{I}(\tau, \lambda, \boldsymbol{n})}{\partial \tau} = \mathbf{K}\boldsymbol{I}(\tau, \lambda, \boldsymbol{n}) - \boldsymbol{S}(\tau, \lambda, \boldsymbol{n}) \, , \tag{1.41}$$

where the Stokes vector $\boldsymbol{I} = [I, Q, U, V]^T$, τ is the optical depth, λ is the wavelength, $\mathbf{K}$ is the 4×4 total absorption matrix and $\boldsymbol{S}$ is the total source vector (see Chapter 7 for its explicit forms). $\mu = \cos\theta$, with colatitude θ which is the angle between the normal to the atmosphere and the line of sight (see left panel of Figure 1.10). $\boldsymbol{n}$ represents the direction of the scattered ray (see right panel of Figure 1.10). We follow the convention that the direction for positive Q corresponds to the linear polarization perpendicular to the solar limb.

When the magnetic field is weak (such that the magnetic splitting is comparable to the radiative width), the anisotropic absorption by the atom can be neglected. In such a case, the off-diagonal elements of the absorption matrix $\mathbf{K}$ can be ignored and only the diagonal elements (scalar absorption coefficient) can be retained. Thus, we replace the $\mathbf{K}$

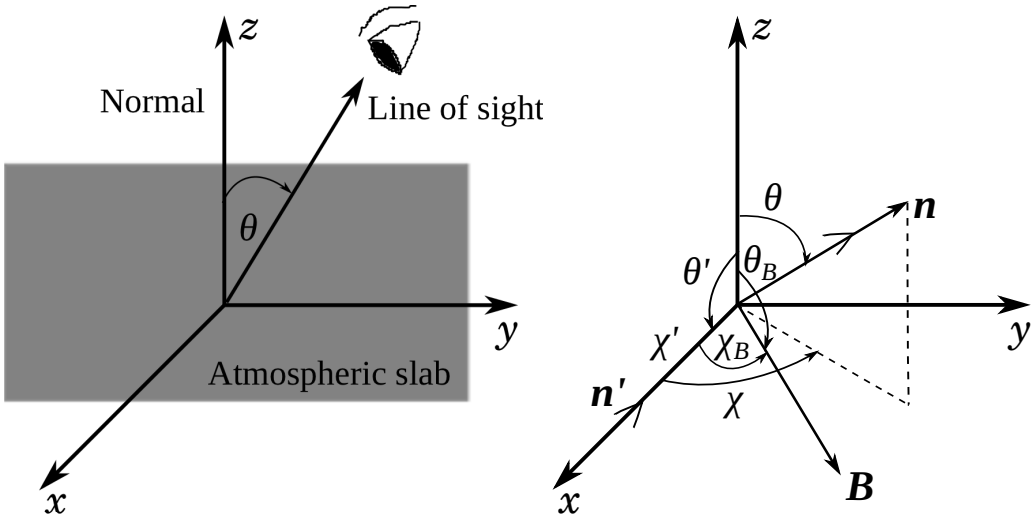

Figure 1.10: A 1D plane-parallel atmospheric slab with z being the normal to the atmosphere (left). Scattering geometry with the atom at the origin and incident ray ($\boldsymbol{n}'$) along the x-axis (right). The scattered ray is along $\boldsymbol{n}$. The angles θ' and θ are the colatitudes for the incident and the scattered rays, respectively, measured with respect to the normal. The angles χ' and χ are the azimuths of the incident and scattered rays respectively, measured with respect to the x-axis. In the figure shown, $\chi' = 0°$. $\boldsymbol{B}$ is the vector magnetic field whose strength is given by B, inclination by θ_B, and azimuth by χ_B.

in Equation (1.41) with $k_{\rm tot}$ which is the principal diagonal element of $\mathbf{K}$, and obtain the transfer equation for the weak field Hanle effect as

$$\mu \frac{\partial \boldsymbol{I}(\tau, \lambda, \boldsymbol{n})}{\partial \tau} = -k_{\rm tot} \left[\boldsymbol{I}(\tau, \lambda, \boldsymbol{n}) - \boldsymbol{S}(\tau, \lambda, \boldsymbol{n}) \right] , \tag{1.42}$$

where, now, $\boldsymbol{I} = [I, Q, U]^T$ and $k_{\rm tot} = \phi(\lambda) + r$ is the total absorption coefficient with $\phi(\lambda)$ being the line profile function and r the ratio of the continuum to the line averaged absorption coefficients. In case of the weak field Hanle effect, the circular polarization (Stokes V) gets completely decoupled from the linear polarization and hence it suffices to describe the radiation field by $\boldsymbol{I} = [I, Q, U]^T$. Stokes V does not get generated unless there is an input circular polarization. In the absence of magnetic fields, $\boldsymbol{I} = [I, Q]^T$ in Equation (1.42). The RM and the contribution from the polarized continuum are contained in the total source vector (see Chapters 2 and 3).

1.8.2 Numerical Methods

Many methods have been developed over the past several decades to solve the transfer equations. To solve the scalar NLTE transfer equation, we use approximate lambda itera-

tion (ALI) technique. It is a fast numerical method developed by Olson et al. (1986) based on the concept of operator splitting (Cannon, 1985). For an overview of the ALI method for scalar transfer see Hubeny (1992, 2003). In order to solve the polarized transfer equation of the type presented in Section 1.8.1, the ALI method was extended and called polarized ALI (PALI) method by Faurobert-Scholl et al. (1997) for the case of CRD in the absence of magnetic fields. PRD was included in a later paper by Paletou & Faurobert-Scholl (1997).

For the case of Hanle effect with CRD Nagendra et al. (1998) developed the PALI method which was extended to the case of PRD by Nagendra et al. (1999, 2000); Fluri et al. (2003) and Sampoorna et al. (2008a). For a review on the numerical methods used to solve the polarized transfer equation see Trujillo Bueno (2003b); Nagendra et al. (2003); Nagendra (2003) and Nagendra & Sampoorna (2009). The PALI method described in all these papers are for the case of a two-level atom. Smitha et al. (2011a, 2013a) developed the PALI method for a two-term atom for non-magnetic and weak field Hanle cases. Smitha et al. (2012b) developed the PALI method for a two-level atom with hyperfine structure in the absence of magnetic fields. A heuristic approach to solve the polarized line transfer equation with PRD in a multi-level atom, without lower level polarization, in the presence of a weak magnetic field is presented in Sampoorna et al. (2013).

In the presence of an external magnetic field, the radiation field is non-axisymmetric. For the case of weak fields, Nagendra et al. (1998) and Frisch (2007) showed that the non-axisymmetry can be removed by expressing the Stokes vector in terms of a 6-component irreducible vector which is cylindrically symmetric. The original PALI methods were developed for the transfer equation written in terms of these irreducible vectors. Thus, the transfer problem is solved in its axisymmetric form, and the solution is later converted to the Stokes vector, which is actually non-axisymmetric. It is necessary to perform this transformation because Stokes parameters are actually the observed quantities. The decomposition described above was actually performed only for the case of angle averaged PRD functions. However, when solving the problems with angle dependent PRD functions, the above mentioned decomposition leads to irreducible vectors which still retain the non-axisymmetry. In Faurobert (1987, 1988) and Nagendra et al. (2002), the angle dependent PRD problems in the non-magnetic and the Hanle scattering cases were solved, respectively, in the Stokes vector basis itself, which is computationally expensive. They showed the differences in the Stokes profiles between the angle averaged and angle dependent cases, for atmospheric slabs of different properties.

Frisch (2009, 2010) Fourier expanded the angle dependent PRD functions, over the azimuth angle, and succeeded in further reducing the non-axisymmetry of the irreducible intensity vector. The PALI methods developed later (Sampoorna et al., 2011; Sampoorna,

2011b; Nagendra & Sampoorna, 2011; Supriya et al., 2013a) were based on this technique to solve the angle dependent transfer problems. This technique is numerically very efficient. A detailed review of these methods is given in Sampoorna (2014). Supriya et al. (2013b) performed the non-magnetic angle dependent PRD calculations for a two-term atom, and a two-level atom with hyperfine structure including the effects due to quantum interference. They showed that for all practical purposes, the angle averaged redistribution can be considered to a good approximation in the non-magnetic case.

A method to solve vector transfer equation in the presence of magnetic fields where the polarization is generated only by the Zeeman effect (called the Zeeman line transfer) in NLTE media was first proposed by Auer et al. (1977) based on the method of Feautrier (1964). Other techniques involve discrete space method (Nagendra & Peraiah, 1985a,b), a faster diagonal element lambda operator (DELO) method (Rees et al., 1989) and DELO parabolic (DELOPAR: Trujillo Bueno, 2003b), which is an extension of the scalar short-characteristics method of Kunasz & Auer (1988) to handle polarization. See Landi Degl'Innocenti & Landolfi (2004) for more details on the Zeeman line transfer. The methods mentioned above treat only the incoherent (CRD) scattering. Stenflo (1994) formulated the polarized transfer equation including both the coherent scattering (in PRD) and the Zeeman effect. To solve this transfer equation for strong magnetic fields which includes both the absorption matrix and the RM, given in Equation (1.41), a method was devised by Sampoorna et al. (2008b) based on the DELOPAR formal solver. Such a general method is necessary to solve the vector transfer equation with the PRD scattering matrices and PB absorption matrix derived in Part II of the thesis.

1.9 An Overview of the Thesis

In this thesis, we propose a formalism to include the intrinsically polarized blend lines in the line transfer calculations to model any given spectral line in the second solar spectrum. We derive the RMs for the quantum interference taking place between the atomic states in the presence of arbitrary magnetic fields (covering the Hanle, Zeeman and PB regimes). We test the correctness of our formalism by reproducing the known benchmarks. We explore the possibility of using the PBE as a tool to diagnose magnetic fields. We divide the thesis into two parts. The first part consists of two chapters and the second part consists of four chapters.

In Part I of the thesis, we deal with the formation of blend lines, their transfer through the medium and highlight the role played by them in shaping the polarization profiles of the spectral lines. For our purpose, we consider the simple case of a line formed in a two-

level atom and its transfer through an isothermal constant property medium. In Chapter 2, we treat a single blend line interacting with the main spectral line and carry out a detailed parametric analysis. We extend this formalism to include the effects of more than one blend line in Chapter 3. We find that the influence of the blend lines cannot be neglected in the modeling efforts when they are strong and lie very close to the main spectral line of interest.

In Part II, we take up the more difficult problems of line formation in a two-level atom with hyperfine structure, and a two-term atom without and with hyperfine structure, under the influence of a magnetic field of arbitrary strength. In such cases, the level-crossing, avoided crossing and quantum interference effects come into picture. We develop the theoretical formulations which treat these phenomena. We restrict our attention to the single scattering case and try to identify the various signatures of the PBE on the Stokes profiles. In Chapter 4, we focus our attention on the F-state interference taking place in a two-level atom with hyperfine structure. We derive the necessary RM for this problem and test it taking Na I (neutral sodium) D_2 line as an example. The RM for the J-state interference phenomenon in the case of a two-term atom without hyperfine structure is derived in Chapter 5. We apply this theory to the case of Li I (neutral lithium) D lines at 6708 Å and identify the signatures of the magnetic field in the PB regime. In Chapter 6, we develop a theory to treat the combined F- and J-state interference phenomena (two-term atom with hyperfine structure). We once again take the Li I D lines at 6708 Å as an example and study the characteristics of the RM derived. We attempt to model these lines using the last scattering approximation (LSA) method and present the developments in this regard in Chapter 7.

In Chapter 8, we summarize the work carried out in this thesis and present the possible future applications of this work. We add a few appendices at the end of the thesis for presenting those details which could not be accommodated without affecting the flow of discussions in the main chapters.

PART I

POLARIZED LINE TRANSFER WITH BLEND LINES

2

POLARIZED BLEND LINES

This chapter is based on:
Sowmya, K., Nagendra, K. N., & Sampoorna, M. 2012, MNRAS, 423, 2949

Outline

Blend lines, as discussed in Section 1.2.2, form an integral part of the theoretical analysis and modeling of the polarized spectrum of the Sun. Their interaction with other spectral lines needs to be explored and understood before we can properly use the main spectral lines to diagnose the Sun. Blend lines are known to cause a decrease in the polarization in the wings of the main line on which they superpose, or in the polarization of the background continuum, when they are assumed to be formed either under the LTE conditions, or when they do not have non-zero intrinsic polarization. In this chapter, we describe the theoretical framework to include a blend line formed under NLTE conditions, in the radiative transfer equation, and the numerical techniques to solve it. We discuss the properties of a blend line having an intrinsic polarization of its own and its interaction with the main line. The results of our analysis show that the influence of the blend line on the main spectral lines, though small for the parameters considered, is important and needs to be accounted when interpreting the polarized spectral lines in the second solar spectrum.

2.1 Introduction

A survey of the linear polarization arising due to the coherent scattering processes, carried out by Stenflo et al. (1983) over the wavelength range $3165 - 4230$ Å of the solar spectrum,

revealed the nature and influence of the blend lines on the second solar spectrum (the polarized solar spectrum that is produced by scattering processes, see Section 1.2.1). They introduced an empirical relation between the intensity and polarization profiles of intrinsically unpolarized lines. Based on this model, they could obtain a good determination of both the zero-point of the polarization scale and the level of the continuum polarization, and could further use the model to remove the effect of the depolarizing blend lines and the continuum polarization to bring out the intrinsic polarization of the spectral lines in the second solar spectrum. The high resolution recording of the second solar spectrum by Stenflo & Keller (1996, 1997) and the atlas of Gandorfer (2000, 2002, 2005a) also explicitly showed the importance of blend lines and the polarizing continuum.

The highly structured second solar spectrum is characterized by a polarized background continuum on which both intrinsically polarizing and depolarizing blend lines are superposed. While a relative polarimetric precision of 10^{-5} can routinely be achieved in current imaging Stokes polarimetry, a direct observational determination of the zero-point of the polarization scale is not possible with comparable accuracy. Instead, the zero-point, which is needed to convert the observed relative polarizations to absolute polarizations, has to be determined by theoretical considerations based on the expected polarization shapes of the depolarizing blend lines. For this reason, the blend lines are of fundamental importance for all observational and theoretical work with the second solar spectrum. The blend line model that was proposed in Stenflo et al. (1983) was later applied in a somewhat extended way in Stenflo (2005) for the empirical determination of the polarization of the continuous spectrum based on the Gandorfer's atlas.

The theoretical modeling of the line polarization in the second solar spectrum is always associated with incorporating the depolarizing blend lines, as they invariably affect the shapes of the polarized main lines. Blend lines are usually treated by assuming that they are formed in LTE conditions, thereby ignoring their own intrinsic polarization. When blend lines are treated in LTE, polarized line and continuum photons are removed due to larger absorption within the line, causing a depolarization of the main line and the continuum (see Fluri & Stenflo, 1999, 2001). A theoretical study by Fluri & Stenflo (1999) on the depolarizing blend lines in the visible solar spectrum showed that the relative intensity and relative polarization profiles defined with respect to the continuum, are approximately proportional to each other, with a proportionality constant that varies with angle, wavelength, and line strength.

The blend lines can be treated in LTE if their height of formation corresponds to collision-dominated layers. If they are formed in low density layers, it may be necessary to treat them as being formed under NLTE. Analysis by Fluri & Stenflo (2003) also

showed that the depolarization of the continuum by absorbing blend lines rapidly decreases with increasing height of formation, while the depolarization by scattering blend lines increases with height of formation. These calculations were performed with realistic model atmospheres, and hypothetical or real line profiles formed in these atmospheres. Although the blend lines were treated in NLTE, their intrinsic polarizability factor was assumed to be zero (namely the blend lines do not have linear polarization of their own). When they have a non-zero polarizability factor, it may also become necessary to treat their intrinsic polarization, to represent their contribution to the polarization profile of the main line (depolarization or repolarization).

In this chapter, we consider a blend line with intrinsic polarization, which occurs in the wings of the main lines. The number density of strongly polarizing lines is modest in the visible part of the second solar spectrum. Therefore, the conditions that we have imposed in this chapter (namely the proximity of polarizing main and blend lines) is not often realized. However, as we go down in the UV, the second solar spectrum gets increasingly more crowded with strongly polarizing lines. There we can find several good examples of polarizing blend lines (see the UV atlas of Gandorfer, 2005a). Therefore, the theoretical studies presented in this chapter become relevant in the analysis of the scattering polarization of the lines in the UV region of the second solar spectrum.

Blend lines belonging to different elements 'interact' with the main line of interest through radiative transfer effects (i.e., they couple to the main line through the opacity distribution and multiple scattering). The strength of this interaction depends on their wavelength separation. This interaction is an example of incoherent superposition of the lines. On the other hand, the interaction between the line components of multiplets like Ca II H&K, Na I D_1&D_2, Cr I $5204 - 5208$ Å multiplet etc. represents coherent superposition of lines. These interactions between the lines arise due to the quantum interference between fine structure states or hyperfine structure states of an atom (Stenflo, 1997; Smitha et al., 2011b, 2012b).

In Section 2.2, we describe the formulation of the relevant transfer equation. In Section 2.3, we discuss the numerical methods used to solve the transfer equation. In Section 2.4, we present the results of this line transfer with resonance and Hanle scattering and present the concluding remarks in Section 2.5.

2.2 Formulation of the Transfer Equation

Line polarization arises from resonance scattering processes (both in the main and the blend lines). In the presence of magnetic fields, this polarization is modified by the Hanle effect

(see Section 1.7.2). It is sufficient to describe the radiation field by the Stokes vector $\boldsymbol{I} = (I, Q, U)^T$ because we limit our attention to linear polarization, which, for the weak-field Hanle effect, is fully decoupled from circular polarization. We consider only one polarizing blend line in the wings of the main line, formed in a 1D, plane-parallel, static, isothermal atmosphere with homogeneous layers. In the presence of a vector magnetic field ($\boldsymbol{B}$) and the blend line polarization, the total source vector in the Stokes vector basis can be written as

$$\boldsymbol{S}(\tau,\lambda,\boldsymbol{n}) = \frac{k_l\phi_l(\lambda)\boldsymbol{S}_l(\tau,\lambda,\boldsymbol{n}) + k_c B(\lambda)\boldsymbol{U}}{k_l\phi_l(\lambda)+k_b\phi_b(\lambda)+\sigma_{sc}+k_c} + \frac{k_b\phi_b(\lambda)\boldsymbol{S}_b(\tau,\lambda,\boldsymbol{n}) + \sigma_{sc}\boldsymbol{S}_{sc}(\tau,\lambda,\boldsymbol{n})}{k_l\phi_l(\lambda)+k_b\phi_b(\lambda)+\sigma_{sc}+k_c}\,, \tag{2.1}$$

where k_l and k_b are the frequency-integrated main and blend line absorption coefficients, respectively. σ_{sc} and k_c are the continuum scattering and absorption coefficients. ϕ_l and ϕ_b denote the absorption profiles for the main and the blend lines. Throughout this chapter, the symbols 'l' and 'b' stand for the 'main' line and the 'blend' line, respectively. τ is the total optical depth scale defined by

$$d\tau = -[k_l\phi_l(\lambda) + k_b\phi_b(\lambda) + \sigma_{sc} + k_c]\, dz\,. \tag{2.2}$$

The ray direction $\boldsymbol{n}$ is defined by its polar angles (θ,χ) with respect to the atmospheric normal (see Figure 1.10). In Equation (2.1), $\boldsymbol{U} = (1,0,0)^T$. The line source vectors for the main and the blend lines are $\boldsymbol{S}_l$ and $\boldsymbol{S}_b$. The continuum scattering source vector is denoted as $\boldsymbol{S}_{sc}$. They are given by

$$\boldsymbol{S}_l(\tau,\lambda,\boldsymbol{n}) = \epsilon_l B(\lambda)\boldsymbol{U} + (1-\epsilon_l)\oint\frac{d\boldsymbol{n}'}{4\pi}\int_0^\infty d\lambda'\frac{\boldsymbol{R}^l(\lambda,\lambda',\boldsymbol{n},\boldsymbol{n}';\boldsymbol{B})}{\phi_l(\lambda)}\boldsymbol{I}(\tau,\lambda',\boldsymbol{n}')\,,$$

$$\boldsymbol{S}_b(\tau,\lambda,\boldsymbol{n}) = \epsilon_b B(\lambda)\boldsymbol{U} + (1-\epsilon_b)\oint\frac{d\boldsymbol{n}'}{4\pi}\int_0^\infty d\lambda'\frac{\boldsymbol{R}^b(\lambda,\lambda',\boldsymbol{n},\boldsymbol{n}';\boldsymbol{B})}{\phi_b(\lambda)}\boldsymbol{I}(\tau,\lambda',\boldsymbol{n}')\,,$$

and

$$\boldsymbol{S}_{sc}(\tau,\lambda,\boldsymbol{n}) = \oint\frac{d\boldsymbol{n}'}{4\pi}\int_0^\infty d\lambda'\boldsymbol{P}(\boldsymbol{n},\boldsymbol{n}')\boldsymbol{I}(\tau,\lambda',\boldsymbol{n}')\delta(\lambda-\lambda')\,, \tag{2.3}$$

where ϵ_l and ϵ_b are the thermalization parameters for the main and blend lines respectively, and $B(\lambda)$ is the Planck function. For simplicity, $B(\lambda)$ is taken as the same for both the main and the blend lines. The continuum is assumed to be scattering coherently through Rayleigh

and Thomson scattering. $\boldsymbol{P}(\boldsymbol{n},\boldsymbol{n}')$ is the Rayleigh phase matrix (see e.g. Chandrasekhar, 1950). The RM $\boldsymbol{R}(\lambda,\lambda',\boldsymbol{n},\boldsymbol{n}';\boldsymbol{B})$ is factorized in the form

$$\boldsymbol{R}(\lambda,\lambda',\boldsymbol{n},\boldsymbol{n}';\boldsymbol{B}) = R(\lambda,\lambda')\ \boldsymbol{P}(\boldsymbol{n},\boldsymbol{n}';\boldsymbol{B})\ , \tag{2.4}$$

where $\boldsymbol{B}$ is the vector magnetic field and $\boldsymbol{n'}$ is the direction of incidence. $R(\lambda,\lambda')$ is the angle averaged redistribution function of Hummer (1962). $\boldsymbol{P}(\boldsymbol{n},\boldsymbol{n}';\boldsymbol{B})$ is the Hanle phase matrix (see Stenflo, 1978a; Landi Degl'Innocenti & Landi Degl'Innocenti, 1988). For clarity, we present the equations for a simple version of the RM $\boldsymbol{R}$. In particular, we neglect depolarizing elastic collisions and consider only pure type II scattering in the main line. The blend line is assumed to be scattering according to either PRD or CRD. An exact treatment of collisions according to the Approximation level III of Bommier (1997b) can easily be incorporated into the present formalism. Calculations using such physically realistic RM are presented in Section 2.4.8.

For isothermal slab models, we introduce the parameters

$$\beta_c = \frac{k_l}{k_c}; \qquad \beta_b = \frac{k_b}{k_c}; \qquad \beta_{sc} = \frac{\sigma_{sc}}{k_c}\ . \tag{2.5}$$

Further, we work in the irreducible basis (see Frisch, 2007), where the source vector depends only on τ and λ. In this basis, using the Hanle phase matrix elements in the atmospheric reference frame, it is easy to show that the total and the line source vectors have the form:

$$\boldsymbol{\mathcal{S}}(\tau,\lambda) = \frac{[\beta_c\phi_l(\lambda)+\beta_b\phi_b(\lambda)+\beta_{sc}]\boldsymbol{\mathcal{S}}_L(\tau,\lambda)+B(\lambda)\boldsymbol{\mathcal{U}}}{\beta_c\phi_l(\lambda)+\beta_b\phi_b(\lambda)+\beta_{sc}+1}\ , \tag{2.6}$$

and

$$\begin{aligned}\boldsymbol{\mathcal{S}}_L(\tau,\lambda) &= \frac{\beta_c\phi_l(\lambda)\epsilon_l+\beta_b\phi_b(\lambda)\epsilon_b}{\beta_c\phi_l(\lambda)+\beta_b\phi_b(\lambda)+\beta_{sc}}B(\lambda)\boldsymbol{\mathcal{U}}\\ &+\int_{-1}^{+1}\frac{d\mu'}{2}\int_0^\infty d\lambda'\Bigg[\frac{\boldsymbol{\mathcal{N}}^l(\boldsymbol{B})\beta_c(1-\epsilon_l)\boldsymbol{W}^lR^l(\lambda,\lambda')}{\beta_c\phi_l(\lambda)+\beta_b\phi_b(\lambda)+\beta_{sc}}\\ &+\frac{\boldsymbol{\mathcal{N}}^b(\boldsymbol{B})\beta_b(1-\epsilon_b)\boldsymbol{W}^bR^b(\lambda,\lambda')+\boldsymbol{\mathcal{E}}\beta_{sc}\delta(\lambda-\lambda')}{\beta_c\phi_l(\lambda)+\beta_b\phi_b(\lambda)+\beta_{sc}}\Bigg]\boldsymbol{\Psi}(\mu')\boldsymbol{\mathcal{I}}(\tau,\lambda',\mu')\ .\end{aligned} \tag{2.7}$$

Here, $\boldsymbol{\mathcal{U}} = (1,0,0,0,0,0)^T$, $R^b(\lambda,\lambda')$ is either given by $R^b_{\rm II}(\lambda,\lambda')$ or CRD. Note that we have combined the line source vectors for both the main and the blend lines, as well as the continuum scattering source vector, in a single expression. This allows us to apply the ALI method of solution based on the frequency by frequency (FBF) technique to compute the line source vector corrections. $\boldsymbol{\Psi}(\mu')$ is the Rayleigh phase matrix in the irreducible basis.

$\boldsymbol{\mathcal{N}}^l(\boldsymbol{B})$ and $\boldsymbol{\mathcal{N}}^b(\boldsymbol{B})$ are the Hanle phase matrices in the irreducible basis for the main and blend lines, respectively. Expressions for these can be found in Frisch (2007). Hanle phase matrices for the two lines could be different as they can form at different heights in the atmosphere, with different strength and geometry of the magnetic fields. In the absence of magnetic fields $\boldsymbol{\mathcal{N}}^l(\boldsymbol{B})$ and $\boldsymbol{\mathcal{N}}^b(\boldsymbol{B})$ matrices reduce to unity matrix $\boldsymbol{\mathcal{E}}$. The matrices $\boldsymbol{W}^l$ and $\boldsymbol{W}^b$ are diagonal, with $W^{l,b}_{00} = 1$ and $W^{l,b}_{kk} = W^{l,b}_2$ where $k = 1, 2, 3, 4, 5$. Here, W_2 are called polarizability factors. They depend on the angular momentum quantum numbers of the upper and lower levels. For a normal Zeeman triplet transition ($J = 0 \rightarrow 1 \rightarrow 0$), this factor is unity.

The 1D line transfer equation (see Section 1.8.1 for the transfer equation in the Stokes vector basis) for polarized Hanle scattering problem in the irreducible basis is then given by

$$\mu \frac{\partial \boldsymbol{\mathcal{I}}(\tau, \lambda, \mu)}{\partial \tau} = \boldsymbol{\mathcal{I}}(\tau, \lambda, \mu) - \boldsymbol{\mathcal{S}}(\tau, \lambda) \; . \tag{2.8}$$

$\boldsymbol{\mathcal{I}}$ is the formal 6-component vector. Our task is to solve this transfer equation to obtain the Stokes profiles $I, Q/I$, and U/I. For this purpose we use the scattering expansion method (SEM) proposed by Frisch et al. (2009). See Section 1.8.2 for a short summary of the various methods used to solve the polarized radiative transfer equation.

2.3 Numerical Solution of the Transfer Equation

The solution of the polarized radiative transfer equation by the commonly used PALI method (see Nagendra et al., 1999) with the FBF technique is computationally expensive (see e.g. Sampoorna et al., 2008a). Therefore, we opt for SEM which is a faster approximate method. It is based on Neumann series expansion of the polarized component of the source vector. We apply this method presented in Frisch et al. (2009) to the problem at hand. In this method, we first write the source vector components in the irreducible basis as

$$\begin{aligned} S^K_{Q,L}(\tau, \lambda) &= \frac{\beta_c \phi_l(\lambda) \epsilon_l + \beta_b \phi_b(\lambda) \epsilon_b}{\phi(\lambda)} \, B(\lambda) \delta_{K0} \delta_{Q0} \\ &+ \int_{-1}^{+1} \frac{d\mu'}{2} \int_0^\infty d\lambda' \sum_{Q'} \frac{R^K_{QQ'}}{\phi(\lambda)} \sum_{K'} \Psi^{KK'}_{\mathrm{Q'}}(\mu') I^{K'}_{\mathrm{Q'}}(\tau, \lambda', \mu') \; , \end{aligned} \tag{2.9}$$

where

$$\phi(\lambda) = \beta_c \phi_l(\lambda) + \beta_b \phi_b(\lambda) + \beta_{sc} \; , \tag{2.10}$$

and

$$R^K_{QQ'} = \frac{\beta_c(1-\epsilon_l)R^l(\lambda,\lambda')W^l_K}{\phi(\lambda)}\, N^{K,l}_{QQ'}(\boldsymbol{B}) + \frac{\beta_b(1-\epsilon_b)R^b(\lambda,\lambda')W^b_K}{\phi(\lambda)}\, N^{K,b}_{QQ'}(\boldsymbol{B}) + \frac{\beta_{sc}\delta(\lambda-\lambda')}{\phi(\lambda)}\,\delta_{QQ'}\delta_{Q'0}\,. \tag{2.11}$$

In the solar atmosphere, the degree of anisotropy is of the order of a few percent. Thus, the degree of linear polarization that arises due to Rayleigh scattering is small. In other words, for the calculation of Stokes I, one can neglect the contribution from the linear polarization (Q,U) to I to a good approximation. Therefore, the dominant contribution to Stokes I comes from the component I^0_0. The corresponding source vector component neglecting the $K \neq 0$ terms is given by

$$\tilde{S}^0_0 \simeq \frac{\beta_c\phi_l(\lambda)\epsilon_l + \beta_b\phi_b(\lambda)\epsilon_b}{\phi(\lambda)}\, B(\lambda) + \int_{-1}^{+1}\frac{d\mu'}{2}\int_0^\infty d\lambda' \frac{R^0_{00}}{\phi(\lambda)} I^0_0(\tau,\lambda',\mu')\,. \tag{2.12}$$

Here, $\tilde{S}^0_0$ stands for approximate value of S^0_0. It represents the solution of a NLTE unpolarized radiative transfer equation. We calculate it using the ALI method of solution with the FBF technique (see Paletou & Auer, 1995).

Retaining only the contribution from $\tilde{I}^0_0$ on the RHS of $K = 2$ component of $S^K_{Q,L}$ in Equation (2.9), we obtain the single scattering approximation for each component $S^2_{Q,L}$ as

$$[\tilde{S}^2_{Q,L}(\tau,\lambda)]^{(1)} \simeq \int_{-1}^{+1}\frac{d\mu'}{2}\int_0^\infty d\lambda' \frac{R^2_{Q0}}{\phi(\lambda)}\Psi^{20}_0(\mu')\tilde{I}^0_0(\tau,\lambda',\mu')\,. \tag{2.13}$$

The superscript (1) stands for single scattering. The single scattered polarized radiation field $[\tilde{I}^2_Q]^{(1)}$ is calculated using a formal solver. This solution is used as a starting point to calculate the higher order scattering terms. Thus the iterative sequence at order n is

$$[\tilde{S}^2_{Q,L}(\tau,\lambda)]^{(n)} \simeq [\tilde{S}^2_{Q,L}(\tau,\lambda)]^{(1)} + \int_{-1}^{+1}\frac{d\mu'}{2}\int_0^\infty d\lambda' \times \sum_{Q'}\frac{R^2_{QQ'}}{\phi(\lambda)}\Psi^{22}_{Q'}(\mu')[\tilde{I}^2_{Q'}(\tau,\lambda',\mu')]^{(n-1)}\,. \tag{2.14}$$

The iteration is continued until the maximum relative change in surface polarization becomes less than the convergence criteria of 10^{-8}.

2.4 Results

When modeling the specific lines of the second solar spectrum, the blend lines are generally treated in LTE. In that case, the blend usually depolarizes the main line polarization. In this section we consider a polarizing blend line that is formed due to a transition in a two-level atom with $J = 0$ and 1 for the lower and upper levels, respectively, both in the presence and absence of magnetic fields. We present the dependence of the main line polarization on the blend line polarizability, its separation from the main line and its strength. We consider the effects of variation of T – the optical thickness of the isothermal slab, ϵ_b – the thermalization parameter of the blend line and $\tilde{\beta}_c$ – the ratio of the background absorbing continuum opacity to the main line opacity, on the main line polarization. We also discuss the role played by the Hanle effect and collisions. Finally, we present a brief discussion on the behavior of the scattering continuum.

Standard model: In the case of an isothermal atmosphere, the emergent intensity and polarization spectra resemble closely the realistic situation, for the following model parameters. A self-emitting slab of optical thickness $T = 10^8$. The ratio of background absorbing continuum opacity to the main line opacity $\tilde{\beta}_c = 10^{-7}$, the main line strength $\beta_c = 10^7$, the blend line strength $\beta_b = 5 \times 10^2$, and the continuum scattering coefficient $\beta_{sc} = 0$. The thermalization parameters are $\epsilon_l = 10^{-4}$ and $\epsilon_b = 5 \times 10^{-2}$. The damping parameters of the main and blend lines are 2×10^{-3} and 10^{-4}, respectively. Both the lines scatter according to pure $R_{\rm II}$ in the absence of magnetic fields. The main and the blend lines are assumed to be resulting from the $J = 0 \rightarrow 1 \rightarrow 0$ transitions in a two-level atom. W_2 of both the lines are therefore unity. The main line is centered at 5000 Å and the blend line at 5001 Å. The Doppler width is 0.025 Å for both the lines. We refer to this model as the 'standard model' and the Stokes profiles for this model are represented by the solid lines in most of the figures. The vertical dotted lines represent the wavelength positions of the main and blend lines.

2.4.1 Influence of the Blend Line Polarizability Factor

Figure 2.1 shows the emergent intensity and polarization profiles. Initially we treat the blend line to be depolarizing ($W_2^b = 0$) and gradually increase the value of W_2^b until it becomes completely polarizing ($W_2^b = 1$). The variation in W_2^b causes a very little or no change in the intensity. As expected, PRD triple peaks in Q/I are clearly visible in the case of the main line. The PRD peaks of the blend line are not seen, since the blend line is assumed to be weaker than the main line. If the blend line has zero intrinsic polarization

(see the dotted line in the inset), then the wing polarization of the main line is reduced at the core position of the blend line. The extent of depolarization depends on the blend line strength. In the case presented in Figure 2.1 (where the blend line is not too strong), we

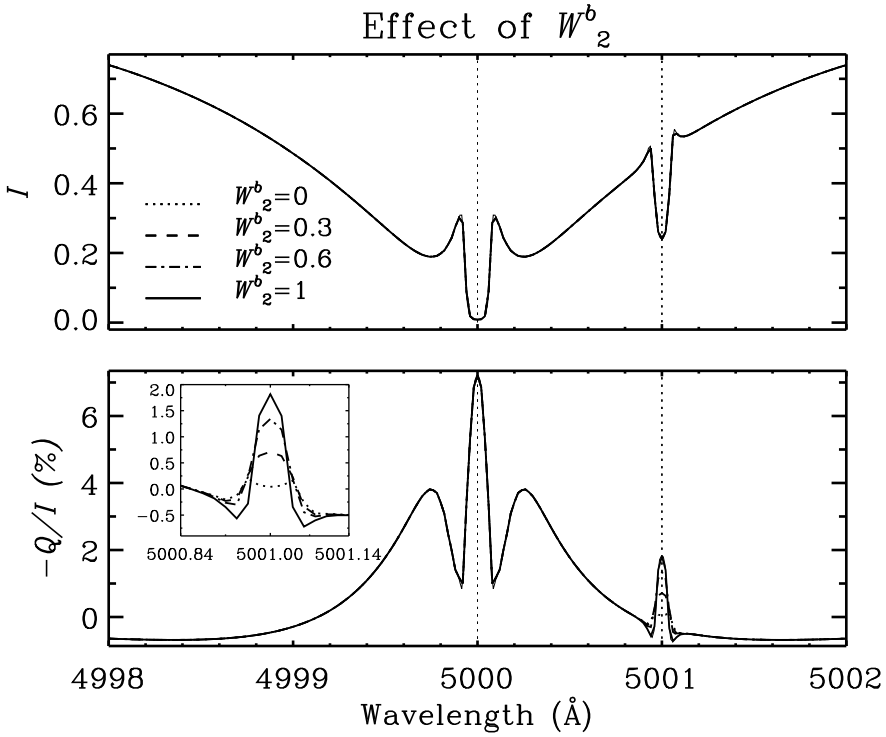

Figure 2.1: Effect of variation of the polarizability factor of the blend line. The 'standard model' parameters defined in Section 2.4 are used. Emergent Stokes profiles are shown for a line of sight $\mu = 0.05$, where $\mu = \cos\theta$.

still see a significant depolarization at the blend line core. When the blend line has a non-zero intrinsic polarizability, a peak at the wavelength position of the blend line is observed. As expected, with an increase in W_2^b the polarization of the blend line increases from $0\,\%$ (when $W_2^b = 0$) to nearly $2\,\%$ (when $W_2^b = 1$). Since the blend line is very weak, the polarization of the main line is insensitive to the changes in the polarizability factor of the blend line outside the narrow core region of the blend line.

2.4.2 Influence of the Separation From the Main Line

The relevant results are shown in Figure 2.2. The main line is kept fixed at $5000\,$Å and the position of the blend line is varied. The influence of the blend line on the main line remains limited to the core region and the immediate surroundings of the blend line, as it does not have a significant wing opacity due to its weakness. The ratio of the blend line opacity to the main line opacity increases as the blend line is shifted away from the

main line center (because the main line opacity is relatively small in the far wings). This change in the opacity ratio makes the blend line intensity profile more and more deep, along with corresponding increase in Q/I, at the wavelength positions of the blend line. As the

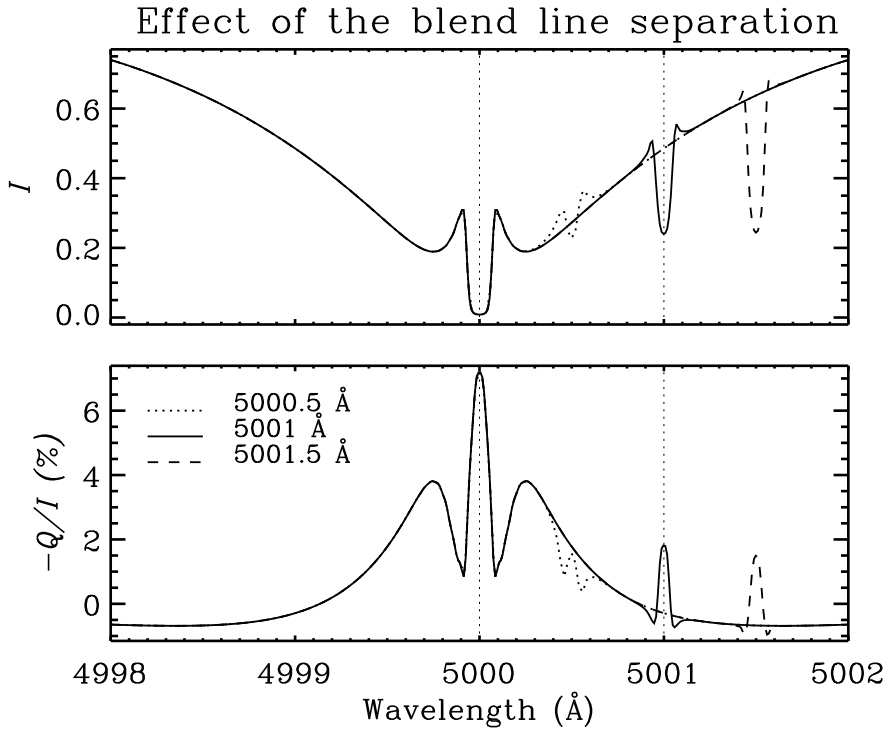

Figure 2.2: Effect of wavelength separation between the main and the blend line. The 'standard model' parameters are used. The W_2^b factor of the blend line is set to unity. The line of sight is represented by $\mu = 0.05$. The wavelength separation is shown by different line types.

line separation increases, the two lines are weakly coupled by transfer effects, eventually becoming completely independent. The profiles computed by treating the blend line in PRD or in CRD are similar because the blend line is assumed to be weak.

2.4.3 Influence of the Blend Line Strength

The strength of the blend line is varied from $\beta_b = 5 \times 10^2$ to $\beta_b = 5 \times 10^4$. The blend line is positioned 1 Å away from the main line. The emergent intensity and polarization profiles are shown in Figure 2.3. As β_b increases, the blend line optical thickness increases resulting in relatively larger heights of the blend line PRD wing peaks in intensity. In the Q/I panel, the PRD peaks of the blend line become more and more prominent as its strength increases. This occurs because of the enhanced scattering opacity as a result of which the near wing polarization of the blend line increases. The Stokes profiles computed treating the blend

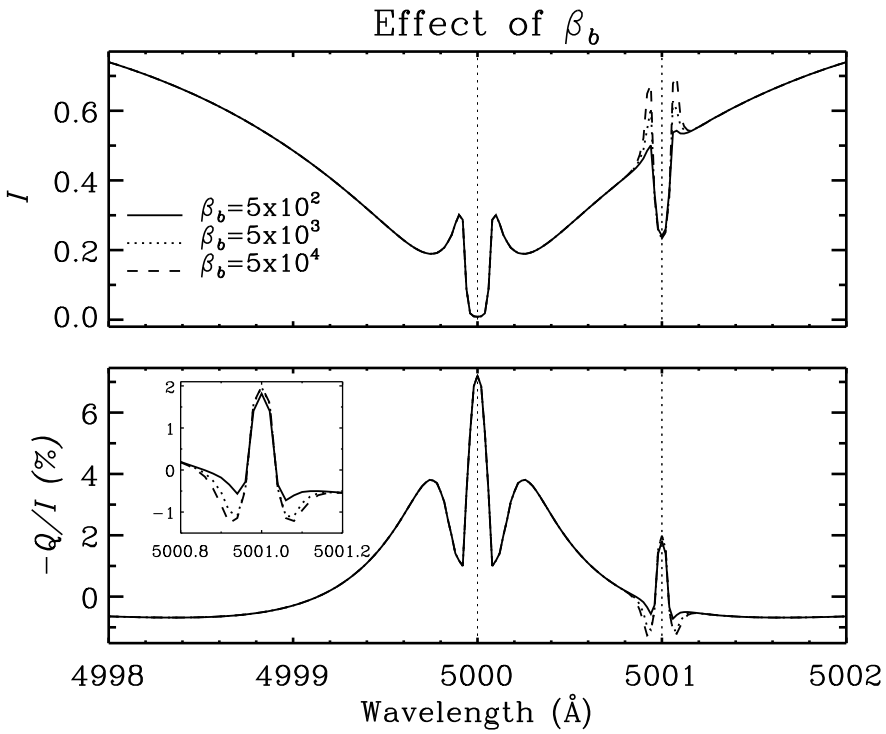

Figure 2.3: Effect of the blend line strength β_b. The 'standard model' parameters are used. The line of sight is $\mu = 0.05$. The line types are given in the top panel.

line in CRD are not significantly different from those computed using PRD as the blend line strength continues to be smaller than the main line strength.

2.4.4 Influence of the Optical Thickness of the Slab

The effect of a polarizing blend line on the main line polarization profile with the variation in the total optical thickness T of the isothermal slab is shown in Figure 2.4. The blend line is much weaker than the main line and scatters according to pure $R_{\rm II}$. As T increases, the main line changes from a self-reversed emission line to an absorption line (see the intensity panel in Figure 2.4). As the main line core is already saturated, the effect of increase in T is felt only in the line wings. As for the blend line, when $T = 10^5$, a weak line is formed because of the smaller number of main line photons available for scattering. As T increases, the blend line starts to show up prominently in intensity.

The main line polarization profile shows a typical triple peak structure (due to PRD mechanism) when $T = 10^5$. However, the main line near wing PRD peak changes over from negative maxima to positive maxima, as T increases. This has a direct correlation with the behavior of the Stokes I profile in the region of near wing maxima. The change in sign is indicative of a switchover from limb brightening to the limb darkening of the

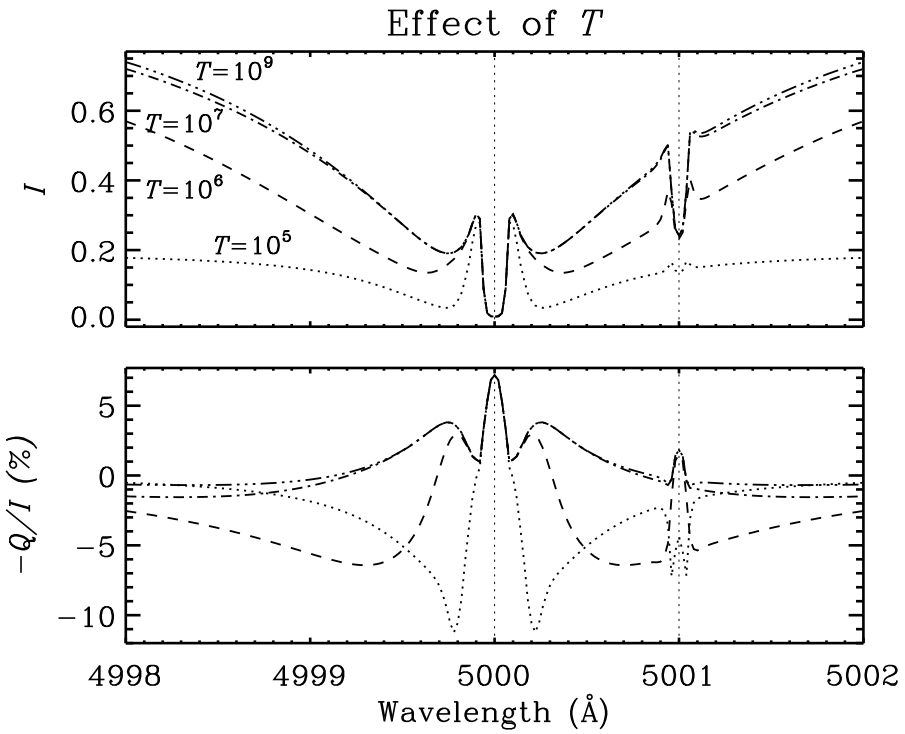

Figure 2.4: Effect of polarizing blend line on the main line polarization with variation in the isothermal slab optical thickness T. The 'standard model' parameters are used. The line of sight is represented by $\mu = 0.05$.

radiation field at heights where the monochromatic optical depths corresponding to the near wing maxima are unity. When $T = 10^5$ the blend line shows a double-peak structure in Q/I, although it is weaker in intensity. The polarization is quite strong, as the blend line is assumed to be polarizing with $W_2^b = 1$. As T increases, the double-peak structure changes over to a single-peak structure. Away from the blend line center, the Q/I profiles of the blend line smoothly merge with the main line polarization profiles.

2.4.5 Influence of the Continuum Absorption Parameter

The ratio of the background continuum absorption opacity to the main line opacity, $\tilde{\beta}_c$, is varied from 10^{-3} to 10^{-9} (see Figure 2.5). The main line strength ($1/\tilde{\beta}_c$) correspondingly changes. This variation of $\tilde{\beta}_c$ influences the Stokes profiles of both the lines. The intensity profiles become narrow and shallow with the increase in the value of $\tilde{\beta}_c$. This is because the continuum progressively influences the inner parts of the main line profile as $\tilde{\beta}_c$ increases. The main line which was a pure absorption line when $\tilde{\beta}_c = 10^{-3}$ (the dotted line) becomes a self reversed emission line when $\tilde{\beta}_c = 10^{-9}$ (dot-dashed line). The decrease in wing intensity is due to a decrease in the continuum optical thickness ($T^C = \tilde{\beta}_c T$) as $\tilde{\beta}_c$ varies

from 10^{-3} to 10^{-9}. The blend line intensity profile also changes from a strong absorption line to a weak emission line as $\tilde{\beta}_c$ changes from 10^{-3} to 10^{-9}.

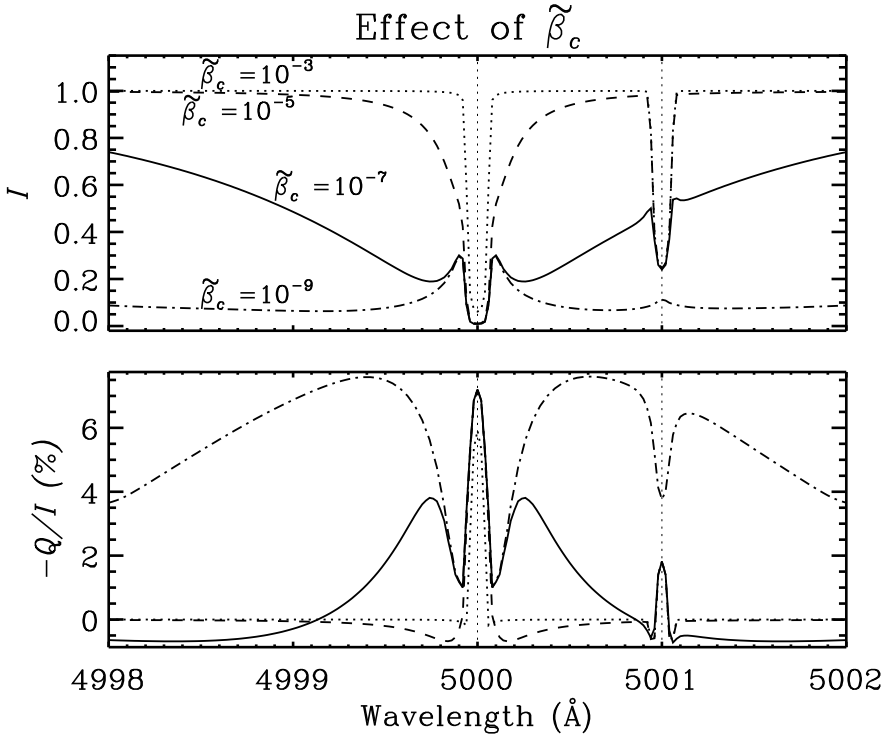

Figure 2.5: Effect of polarizing blend line on the main line polarization with variation in $\tilde{\beta}_c$. The 'standard model' parameters are used. The line of sight is represented by $\mu = 0.05$.

The main line Q/I core amplitude is not very sensitive to $\tilde{\beta}_c$ unless $\tilde{\beta}_c$ is sufficiently large (see the dotted line). The main line near wing PRD peak, as well as far wing polarization, decreases in magnitude as $\tilde{\beta}_c$ increases, due to the predominance of the unpolarized continuum. The Q/I profiles at the core of the blend line nearly coincide for $\tilde{\beta}_c = 10^{-3}, 10^{-5}$, and 10^{-7}. However, when $\tilde{\beta}_c = 10^{-9}$, the blend line acts like a depolarizing line in the wing of the main line, in spite of W_2^b being unity. This is possibly because the blend line in this case is a weak emission line, whose polarization profiles are characteristically different from those of absorption lines.

2.4.6 Influence of the Photon Destruction Probability

For the 'standard model' considered in this study, the variation in ϵ_b (the photon destruction probability) does not produce significant changes in the $(I, Q/I)$ profiles of the main line as can be seen from Figure 2.6. With a decrease in the value of ϵ_b, the blend line depth increases (going from LTE-like to NLTE-like expected behavior), which saturates for $\epsilon_b < 10^{-3}$ (figure not shown). In Q/I, the blend line core peak increases with the decrease in

ϵ_b, as the blend line becomes more and more scattering dominated. Further, for $\epsilon_b < 10^{-3}$,

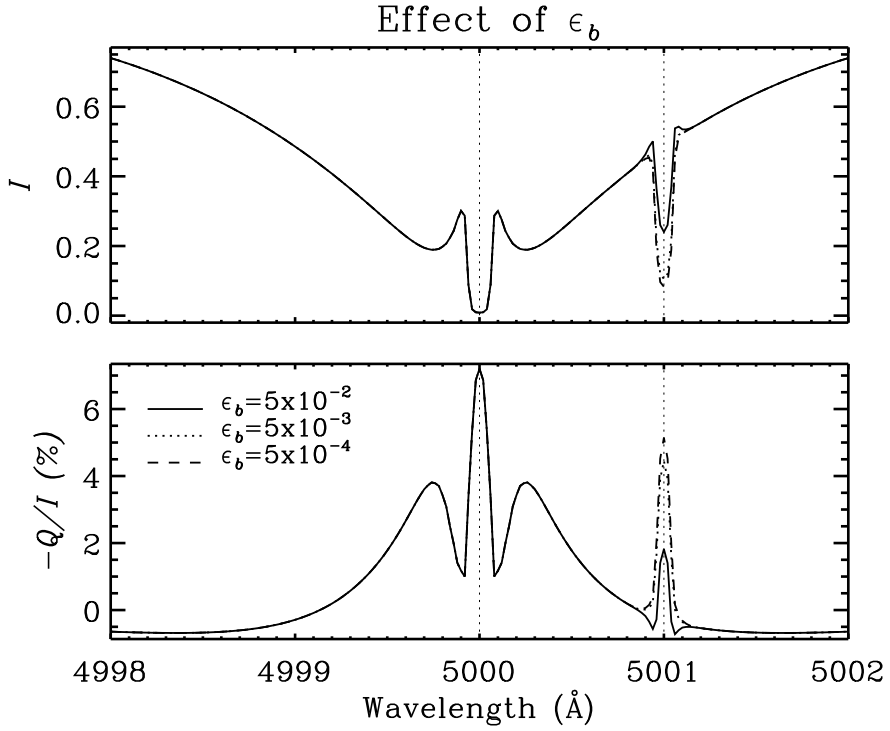

Figure 2.6: Effect of polarizing blend line on the main line polarization with variation in ϵ_b. The 'standard model' parameters are used. The line of sight is represented by $\mu = 0.05$.

the blend line core peak in Q/I saturates, an effect discussed in Faurobert (1988) for the single line case.

2.4.7 Influence of the Magnetic Fields

The vector magnetic field $\boldsymbol{B}$ is parametrized through $(\gamma_B, \theta_B, \chi_B)$, with $\gamma_B = \mathrm{g}_J \omega_L / \Gamma_R$, where g_J is the upper level Landé factor, ω_L the Larmor precession frequency, and Γ_R the damping rate (inverse life time) of the excited state (see e.g. Stenflo, 1994). The magnetic field orientation represented by θ_B and χ_B are defined with respect to the atmospheric normal (see Figure 1.10). The γ_B for the main line is fixed as unity. The γ_B of the blend line is varied from 0 to 10.

Figure 2.7 shows the profiles for the two-line system in the presence of magnetic fields. The blend line shows similar effects on the main line both in the presence and absence of magnetic fields, for the model parameters used in this section. The main and blend line intensities are unaffected. The magnitude of Q/I in the central peak of the blend line reduces with an increase in the value of its γ_B. This is the typical effect of magnetic fields, namely, the Hanle effect which is operative in the core regions of the two lines. Stokes U

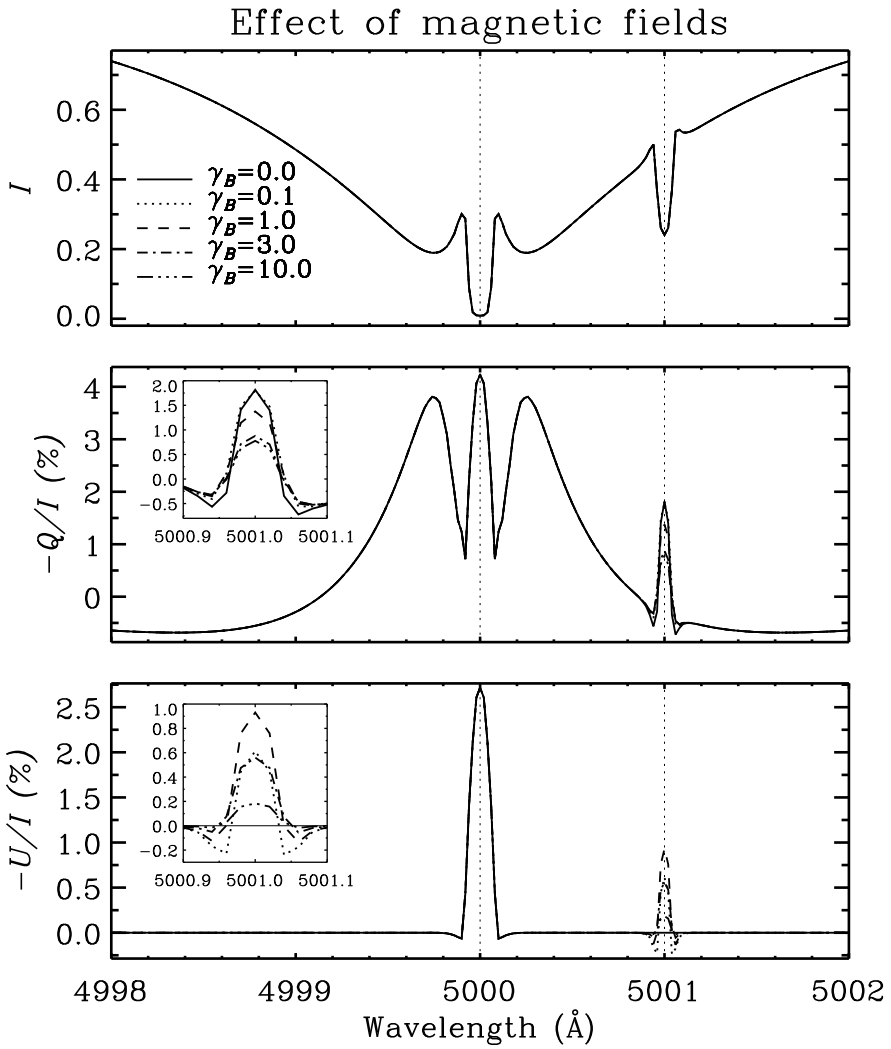

Figure 2.7: Illustration of the effect of a blend line on the scattering polarization of the main line in the presence of magnetic fields. The 'standard model' parameters are used. The magnetic field parameters are $(\gamma_B, \theta_B, \chi_B) = (1, 30°, 0°)$ for the main line and $(\theta_B, \chi_B) = (30°, 0°)$ with γ_B as free parameter for the blend line.

which was zero for Rayleigh case is generated by the Hanle effect and hence characteristic core peaks are seen in the U/I panel. The depolarization in the core region of the blend line due to Hanle effect causes a corresponding increase in U/I.

2.4.8 Influence of the Elastic Collisions

It is well known that the Hanle effect operates efficiently in the line core (within a few Doppler widths) and disappears in the line wings (Omont et al., 1973). The functional form of this frequency dependence of the Hanle effect is presented in Stenflo (1998). To account for this frequency dependence of the Hanle effect in numerical computations, we introduce

the 1D cut-off approximation. Figure 2.7 presented in Section 2.4.7 was computed using the

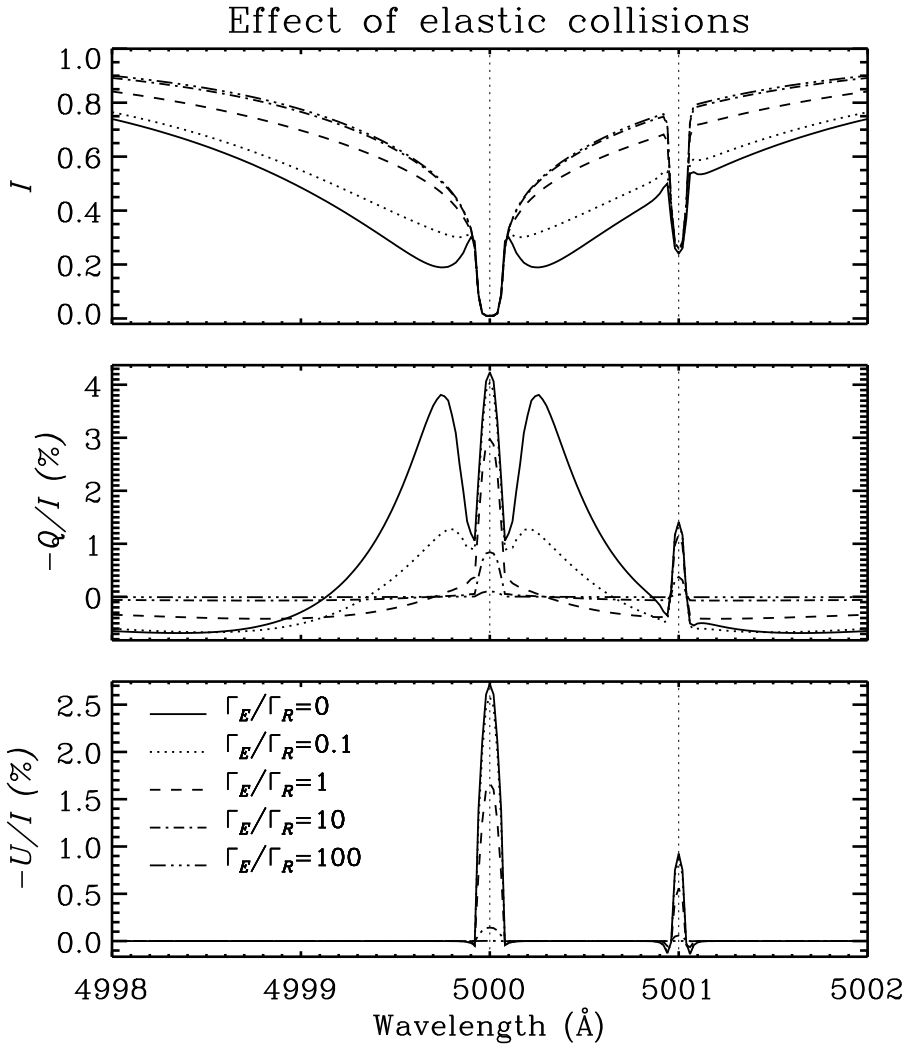

Figure 2.8: The effect of depolarizing elastic collisions. The magnetic field parameters are $(\gamma_B, \theta_B, \chi_B) = (1, 30°, 0°)$ for both the lines. Other model parameters are the same as in the 'standard model'.

1D cut-off approximation, which implies the use of Hanle phase matrix up to, say, $|x| \sim 3.5$ and the Rayleigh phase matrix elsewhere. x is the non-dimensional frequency expressed in Doppler width units. In the present section, we use the so called 'two-dimensional (2D) frequency domains', which refer to a distribution of the domains in the (x, x') space. These so called 'domains' are nothing but piecewise continuous functions of x and x' marking the switchover from Hanle to the Rayleigh-like phase matrices. The exact collisional PRD theory of Hanle effect as well as the approximations leading to these 2D domain based PRD formulation are developed by Bommier (1997a,b). It is rather straightforward to extend the formulation presented in Section 2.2 to include the 2D frequency domains using the domain

logic given in Bommier (1997b).

The strength of elastic collisions is specified through Γ_E/Γ_R, where Γ_E denotes the elastic collisional rate and Γ_R the radiative de-excitation rate. The values of Γ_E/Γ_R chosen by us cover the situations ranging from the absence of elastic collisions (pure $R_{\rm II}$) to the presence of strong elastic collisions. Depolarizing collision rates are given by $D^{(2)} = c\Gamma_E$ with $c = 0.5$ (see Stenflo, 1994). The emergent Stokes profiles are shown in Figure 2.8. They refer to the cases where Γ_E/Γ_R of both the lines are taken as equal and varied in the same fashion. In all these cases we see that the elastic collisions do not modify the intensities in the cores of the two lines. This is because in the line core $R_{\rm II}$ behaves more like CRD. In the wings of the two lines, the PRD-like intensity profiles gradually approach the CRD-like behavior (true absorption line), with an increase in the elastic collision rate Γ_E/Γ_R. As in the single line case, the Q/I profiles show a simultaneous decrease in magnitude at all wavelength points in the line profile, with an increase in Γ_E/Γ_R. For large values of $\Gamma_E/\Gamma_R(= 100)$, the line polarization approaches zero (dash-triple-dotted line) throughout the line profiles. U/I profiles also show similar behavior as the Q/I profiles in both the lines.

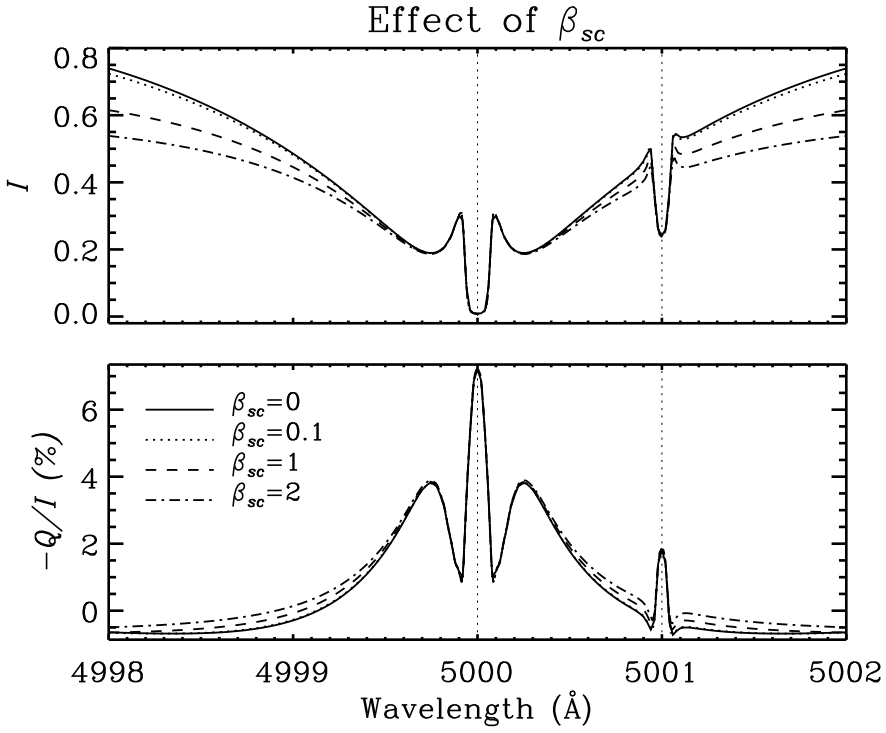

Figure 2.9: Effect of continuum polarization. Figure shows the change in the shape of the wing polarization profiles when a background polarizing continuum radiation is present. The 'standard model' is used to compute these profiles.

2.4.9 Influence of the Continuum Polarization

Figure 2.9 shows the effect of continuum polarization on the blend and the main line polarization. The continuum polarization arises due to Thomson scattering on electrons and Rayleigh scattering on atoms and molecules. It is included here through the parameter β_{sc}.

The continuum polarization is generally small in magnitude except in the UV region of the spectrum. Also, it has a weak wavelength dependence in the visible region of the spectrum. It affects the intensity and polarization throughout the line wings through the addition of a spectrally flat polarizing opacity across the line, while the line cores remain unaffected, because there the line opacity always dominates over the continuum opacity.

2.5 Conclusions

In this chapter, we presented our detailed studies on the effects of a blend line (polarizing or depolarizing) present in the wings of a main line. Our particular interest is the linear polarization profiles of the main line. We showed how theoretically the total source function can be generalized to include a blend line. The same formalism can be extended to deal with the cases where there is more than one blend line. We formulated the radiative transfer equation in the irreducible tensorial basis. We solved this transfer equation by computing the scalar intensity with the standard FBF iterative technique, and the polarization by a faster, promising method called SEM. The SEM involves expanding the polarized component of the source vector in Neumann series, computing the single scattered solution at first, and then using this solution for calculating the higher order scattering terms. We explored the dependence of the blend line intensity and polarization effects on various parameters like polarizability factor, distance from the main line core, blend line strength, isothermal slab optical thickness, continuum opacity and polarization, magnetic field, and elastic collision rate.

The blend lines in the linearly polarized spectrum of the Sun invariably affect the main spectral lines. A knowledge of the way in which this interaction takes place plays an important role in the interpretation of the second solar spectrum. The insight that we have gained through our theoretical studies using isothermal slab models is a first step towards realistic modeling of the second solar spectrum. Such calculations become necessary in a fine analysis of the solar spectrum, and help in our studies of the solar atmosphere. The studies carried out by Anusha et al. (2010, 2011b) and Smitha et al. (2012a) form the basis for the inclusion of intrinsically polarized blend lines in modeling the second solar spectrum.

3

RADIATIVE TRANSFER WITH MULTIPLE BLEND LINES

This chapter is based on:
Sowmya, K., Nagendra, K. N., & Sampoorna, M. 2014, in ASP Conf. Ser. 489, Solar Polarization 7, 125

Outline

The second solar spectrum formed by coherent scattering processes in the Sun, is highly structured. It is characterized by numerous blend lines, both intrinsically polarizing and depolarizing, superposed on the background continuum. These blend lines play an important role in the interpretation of the second solar spectrum. In the previous chapter, we studied the way in which a blend line affects the shape of the neighboring spectral line. In reality, a spectral line of interest gets influenced by several closely lying blend lines. All these blend lines have to be treated carefully while modeling the spectral line of interest. An understanding of the influence of the blend lines on the polarization of the spectral lines leads to a proper determination of the zero-point of the polarization scale, which otherwise is very difficult to measure. With this motivation, in this chapter, we extend the framework developed in the previous chapter to include many blend lines, both depolarizing and polarizing, formed under NLTE conditions, in the radiative transfer equation. For the sake of simplicity, we present the results for the particular case of two blend lines situated on either side of the main spectral line.

3.1 Introduction

In the second solar spectrum, the spectral lines superpose on the background continuum. To correctly estimate the line polarization, a knowledge of the continuum polarization is therefore essential. Blend lines serve as a tool in fixing the zero point of the polarization scale (Stenflo, 2005). It is not possible to directly determine the absolute polarization scale with a precision that comes close to the polarimetric precision of the relative polarization scale. The depolarizing blend lines can be used to obtain a good estimate of the zero point of the polarization scale. Due to this fact the depolarizing blend lines are of profound importance for all observational works on the second solar spectrum. The problem of blend lines is of considerable interest due to its relevance to the measurement and interpretation of the polarized solar spectrum.

In the theoretical modeling of the line polarization in the second solar spectrum, we have to incorporate the numerous blend lines in the vicinity of the line of interest, as they are known to affect the shape of the polarized main line. In all the efforts to model the second solar spectrum, the blend lines in the wavelength range of interest are assumed to be depolarizing and formed under LTE conditions (see, for example, Fluri & Stenflo, 1999, 2001). This assumption fails when the blend lines are formed in low density layers which demands the use of NLTE formulations. In Chapter 2, we showed the importance of the blend lines having non-zero intrinsic polarization and developed a framework to include in the polarized line transfer equation an intrinsically polarized blend line formed under NLTE conditions (see Sowmya et al., 2012).

In this chapter, we extend the formalism developed in Chapter 2 for a single polarized blend line, to treat many blend lines with intrinsic polarization that occur in the wings of the main lines. They interact with the main line through radiative transfer effects. As explained in Chapter 2, the formulation presented in this chapter becomes relevant in the analysis of the scattering polarization of the lines in the UV region of the second solar spectrum. In Section 3.2, we develop the transfer equation in the absence of magnetic fields and present its numerical solution in Section 3.3. In Section 3.4, we present the results of this so called 'multiline transfer' with resonance scattering and conclusions in Section 3.5.

3.2 The Transfer Equation

The main and the blend lines are considered to be formed in a 1D, plane-parallel, static, isothermal atmosphere. Throughout this chapter the symbols 'l' and 'b_a' stand for the 'main' line and the 'blend' lines respectively, where the subscript 'a' takes values 1 to n,

with n being the number of blend lines considered. In the absence of a magnetic field, the total source vector in the Stokes vector basis may be written as

$$\boldsymbol{S}(\tau,\lambda,\mu) = \frac{1}{k_{\rm tot}(\lambda)}\Bigg\{ \beta_c\phi_l(\lambda)\boldsymbol{S}_l(\tau,\lambda,\mu) + \sum_{a=1}^{n}\beta_{b_a}\phi_{b_a}(\lambda)\boldsymbol{S}_{b_a}(\tau,\lambda,\mu) + \beta_{sc}\boldsymbol{S}_{sc}(\tau,\lambda,\mu) + B(\lambda)\boldsymbol{U}\Bigg\}\,, \tag{3.1}$$

where $\mu = \cos\theta$, with θ being the colatitude, and

$$k_{\rm tot}(\lambda) = \beta_c\phi_l(\lambda) + \sum_{a=1}^{n}\beta_{b_a}\phi_{b_a}(\lambda) + \beta_{sc} + 1\,, \tag{3.2}$$

with

$$\beta_c = \frac{k_l}{k_c}; \qquad \beta_{b_a} = \frac{k_{b_a}}{k_c}; \qquad \beta_{sc} = \frac{\sigma_{sc}}{k_c}\,. \tag{3.3}$$

Here, k_l and k_{b_a} are the frequency integrated main and blend line absorption coefficients, respectively. σ_{sc} and k_c are the continuum scattering and absorption coefficients. ϕ_l and ϕ_{b_a} denote the absorption profiles for the main and the blend lines. The total optical depth scale τ is defined by $d\tau = -k_{\rm tot}(\lambda)k_c dz$. In Equation (3.1), $\boldsymbol{U} = (1,0)^T$. The source vectors for the main and the blend lines $\boldsymbol{S}_l$ and $\boldsymbol{S}_{b_a}$, and the continuum scattering source vector $\boldsymbol{S}_{sc}$ are given, respectively, by

$$\boldsymbol{S}_l(\tau,\lambda,\mu) = \epsilon_l B(\lambda)\boldsymbol{U} + (1-\epsilon_l)\int_{-1}^{+1}\frac{d\mu'}{2}\int_0^\infty d\lambda'\frac{\boldsymbol{R}^l(\lambda,\lambda',\mu,\mu')}{\phi_l(\lambda)}\boldsymbol{I}(\tau,\lambda',\mu')\,, \tag{3.4}$$

$$\boldsymbol{S}_{b_a}(\tau,\lambda,\mu) = \epsilon_{b_a}B(\lambda)\boldsymbol{U} + (1-\epsilon_{b_a})\int_{-1}^{+1}\frac{d\mu'}{2}\int_0^\infty d\lambda'\frac{\boldsymbol{R}^{b_a}(\lambda,\lambda',\mu,\mu')}{\phi_{b_a}(\lambda)}\boldsymbol{I}(\tau,\lambda',\mu')\,, \tag{3.5}$$

and

$$\boldsymbol{S}_{sc}(\tau,\lambda,\mu) = \int_{-1}^{+1}\frac{d\mu'}{2}\int_0^\infty d\lambda'\boldsymbol{P}(\mu,\mu')\boldsymbol{I}(\tau,\lambda',\mu')\delta(\lambda-\lambda')\,, \tag{3.6}$$

where ϵ_l and ϵ_{b_a} are the thermalization parameters for the main and blend lines, respectively, $\boldsymbol{I} = [I,Q]^T$, and $B(\lambda)$ is the Planck function. $B(\lambda)$ is taken as the same for both the main and the blend lines. The continuum is assumed to scatter coherently through Rayleigh and Thomson scattering. $\boldsymbol{P}(\mu,\mu')$ is the Rayleigh phase matrix (see e.g., Chandrasekhar, 1950). The RM $\boldsymbol{R}(\lambda,\lambda',\mu,\mu')$ contains the physics of scattering. For simplicity, here we

consider the factorized form of the RM, given by

$$\boldsymbol{R}(\lambda, \lambda', \mu, \mu') = R(\lambda, \lambda')\ \boldsymbol{P}(\mu, \mu')\ , \tag{3.7}$$

where $R(\lambda, \lambda')$, as mentioned in Chapter 2, is the angle averaged redistribution function of Hummer (1962) which contains only the frequency correlations between the incident and scattered photons. The Rayleigh phase matrix is now only a function of θ and not $\boldsymbol{n}$. This is due to the fact that in the absence of a magnetic field, the radiation field is assumed to be azimuthally symmetric.

The angular dependency of the source vectors are eliminated by working in the irreducible basis (see Frisch, 2007). In this basis, the total and the line source vectors have the form:

$$\boldsymbol{\mathcal{S}}(\tau, \lambda) = \frac{k_L(\lambda)\boldsymbol{\mathcal{S}}_L(\tau, \lambda)\ +\ B(\lambda)\boldsymbol{\mathcal{U}}}{k_{\rm tot}(\lambda)}\ , \tag{3.8}$$

and

$$\begin{aligned}\boldsymbol{\mathcal{S}}_L(\tau, \lambda) = &\frac{1}{k_L(\lambda)}\left[\beta_c\phi_l(\lambda)\epsilon_l + \sum_{a=1}^{n}\beta_{b_a}\phi_{b_a}(\lambda)\epsilon_{b_a}\right]B(\lambda)\boldsymbol{\mathcal{U}}\\ &+ \frac{1}{k_L(\lambda)}\int_{-1}^{+1}\frac{d\mu'}{2}\int_0^{\infty}d\lambda'\Bigg[\beta_c(1-\epsilon_l)R^l(\lambda, \lambda')\boldsymbol{W}^l\\ &+ \sum_{a=1}^{n}\beta_{b_a}(1-\epsilon_{b_a})R^{b_a}(\lambda, \lambda')\boldsymbol{W}^{b_a} +\ \beta_{sc}\delta(\lambda-\lambda')\boldsymbol{\mathcal{E}}\Bigg]\ \boldsymbol{\Psi}(\mu')\boldsymbol{\mathcal{I}}(\tau, \lambda', \mu')\ ,\end{aligned} \tag{3.9}$$

where $k_L(\lambda) = \beta_c\phi_l(\lambda)\ +\ \sum_{a=1}^{n}\beta_{b_a}\phi_{b_a}(\lambda)\ +\ \beta_{sc}$. Here, $\boldsymbol{\mathcal{U}} = (1, 0)^T$, $\boldsymbol{\mathcal{E}}$ denotes the 2×2 unity matrix, and $R^{b_a}(\lambda, \lambda')$ is given by the type II redistribution function ($R^{b_a}_{\rm II}(\lambda, \lambda')$) of Hummer (1962). $\boldsymbol{\Psi}(\mu')$ is the 2×2 Rayleigh phase matrix in the irreducible basis. The matrices $\boldsymbol{W}$ are given by

$$\begin{pmatrix} 1 & 0\\ 0 & W_2\end{pmatrix}\ , \tag{3.10}$$

where W_2 are polarizability factors. They depend on the angular momentum quantum numbers of the upper and lower levels. For a normal Zeeman triplet transition ($J = 0 \rightarrow 1 \rightarrow 0$), this factor is unity.

The 1D polarized line transfer equation in the irreducible basis is then given by

$$\mu\frac{\partial\boldsymbol{\mathcal{I}}(\tau, \lambda, \mu)}{\partial\tau} = \boldsymbol{\mathcal{I}}(\tau, \lambda, \mu) - \boldsymbol{\mathcal{S}}(\tau, \lambda)\ , \tag{3.11}$$

where $\boldsymbol{\mathcal{I}}$ is the irreducible intensity vector. To solve this transfer equation we use SEM

proposed by Frisch et al. (2009).

3.3 Numerical Method of Solution

SEM is based on the Neumann series expansion of the polarized component of the source vector. Single scattered solution is computed at first, and this solution is then used for calculating the higher order scattering terms.

In the absence of a magnetic field, the source vector components in the irreducible basis can be written as

$$\begin{aligned} S^K_{0,L}(\tau,\lambda) &= \frac{1}{k_L(\lambda)}\left[\,\beta_c\phi_l(\lambda)\epsilon_l + \sum_{a=1}^{n}\beta_{b_a}\phi_{b_a}(\lambda)\epsilon_{b_a}\right]B(\lambda)\delta_{K0} \\ &+ \frac{1}{k_L(\lambda)}\int_{-1}^{+1}\frac{d\mu'}{2}\int_0^\infty d\lambda'\left[\,\beta_c(1-\epsilon_l)R^l(\lambda,\lambda')W^l_K\right. \\ &\left.+\sum_{a=1}^{n}\beta_{b_a}(1-\epsilon_{b_a})R^{b_a}(\lambda,\lambda')W^{b_a}_K + \beta_{sc}\delta(\lambda-\lambda')\,\right] \\ &\times\sum_{K'=0,2}\Psi_0^{KK'}(\mu')I_0^{K'}(\tau,\lambda',\mu')\,, \end{aligned} \tag{3.12}$$

where $\Psi_0^{KK'}$ are the elements of the $\mathbf{\Psi}$ matrix with $K, K' = 0, 2$. For the calculation of Stokes I, one can neglect the contribution from the linear polarization Q to a good approximation because the linear polarization resulting from Rayleigh scattering in the solar atmosphere is small. Therefore, the dominant contribution to Stokes I comes from the component I^0_0. The corresponding source vector component, neglecting the $K \neq 0$ terms, is given by

$$\begin{aligned} \tilde{S}^0_0 &\simeq \frac{1}{k_L(\lambda)}\left[\,\beta_c\phi_l(\lambda)\epsilon_l + \sum_{a=1}^{n}\beta_{b_a}\phi_{b_a}(\lambda)\epsilon_{b_a}\right]B(\lambda) + \frac{1}{k_L(\lambda)}\int_{-1}^{+1}\frac{d\mu'}{2}\int_0^\infty d\lambda' \\ &\times\left[\,\beta_c(1-\epsilon_l)R^l(\lambda,\lambda') + \sum_{a=1}^{n}\beta_{b_a}(1-\epsilon_{b_a})R^{b_a}(\lambda,\lambda') + \beta_{sc}\delta(\lambda-\lambda')\,\right] \\ &\times I^0_0(\tau,\lambda',\mu')\,. \end{aligned} \tag{3.13}$$

Here, $\tilde{S}^0_0$ stands for approximate value of S^0_0. We calculate it using the ALI method of solution with the FBF technique (see Paletou & Auer, 1995).

Retaining only the contribution from $\tilde{I}^0_0$ on the RHS of $K = 2$ component of $S^K_{0,L}$ in

Equation (3.12), we obtain the single scattering approximation as

$$\left[\tilde{S}^2_{0,L}(\tau,\lambda)\right]^{(1)} \simeq \frac{1}{k_L(\lambda)}\int_{-1}^{+1}\frac{d\mu'}{2}\int_0^{\infty}d\lambda'\left[\beta_c(1-\epsilon_l)R^l(\lambda,\lambda')W_2^l + \sum_{a=1}^{n}\beta_{b_a}(1-\epsilon_{b_a})R^{b_a}(\lambda,\lambda')W_2^{b_a} + \beta_{sc}\delta(\lambda-\lambda')\right]\Psi_0^{20}(\mu')\tilde{I}_0^0(\tau,\lambda',\mu') \,. \quad (3.14)$$

The superscript (1) stands for single scattering. The single scattered polarized radiation field $\left[\tilde{I}^2_0\right]^{(1)}$ is calculated using a formal solver. This solution is used as a starting point to calculate the higher order scattering terms. Thus the iterative sequence at order n is

$$\left[\tilde{S}^2_{0,L}(\tau,\lambda)\right]^{(n)} \simeq \left[\tilde{S}^2_{0,L}(\tau,\lambda)\right]^{(1)} + \frac{1}{k_L(\lambda)}\int_{-1}^{+1}\frac{d\mu'}{2}\int_0^{\infty}d\lambda'\left[\beta_c(1-\epsilon_l)R^l(\lambda,\lambda')W_2^l + \sum_{a=1}^{n}\beta_{b_a}(1-\epsilon_{b_a})R^{b_a}(\lambda,\lambda')W_2^{b_a} + \beta_{sc}\delta(\lambda-\lambda')\right]\Psi_0^{22}(\mu')\left[\tilde{I}^2_0(\tau,\lambda',\mu')\right]^{(n-1)} \,. \quad (3.15)$$

We impose the convergence criteria of 10^{-8} and continue the iteration until the maximum relative change in the surface polarization becomes less than the convergence criteria.

3.4 Results

In this section, we present the effects of polarizing blends on the main line of interest. For illustration, we consider two blends located to the left (denoted b_1) and to the right (denoted b_2) of the main line. A detailed parametric study involving only one polarizing blend line is presented in Chapter 2.

We consider a self-emitting isothermal atmospheric slab characterized by the parameters $(T, r, B) = (10^8, 10^{-5}, 1)$. The grids used in the computations have the resolution given by $(N_d, N_x, N_\mu) = (5, 401, 5)$. N_d is the number of depth points in a decade of the logarithmically spaced τ grid with the first point being 10^{-2}. N_x is the total number of points in the equally spaced wavelength grid with a separation of $5\,$mÅ. N_μ is the colatitude grid represented by a 5-point Gaussian quadrature formula. The main line strength $\beta_c = 10^5$ and the continuum scattering coefficient $\beta_{sc} = 0$. $r = 1/\beta_c$ is the ratio of continuum to the main line opacity. The photon destruction probabilities are given by $\epsilon_l = 10^{-4}$ and $\epsilon_{b_a} = 5 \times 10^{-2}$. The damping parameters for the three lines are $a_l = 2 \times 10^{-3}$ and $a_{b_a} = 10^{-4}$. The main line is centered at $5000\,$Å. The two blends are placed $20\,$mÅ away on either side of the main line. The Doppler widths of all the lines are $25\,$mÅ unless specified otherwise.

The Stokes profiles obtained from this multiline transfer are presented in Figure 3.1. The positive Q corresponds to the vibrations of the electric vector perpendicular to the limb. In panels (a), (b), and (c), dotted lines represent $(I, Q/I)$ profiles computed without

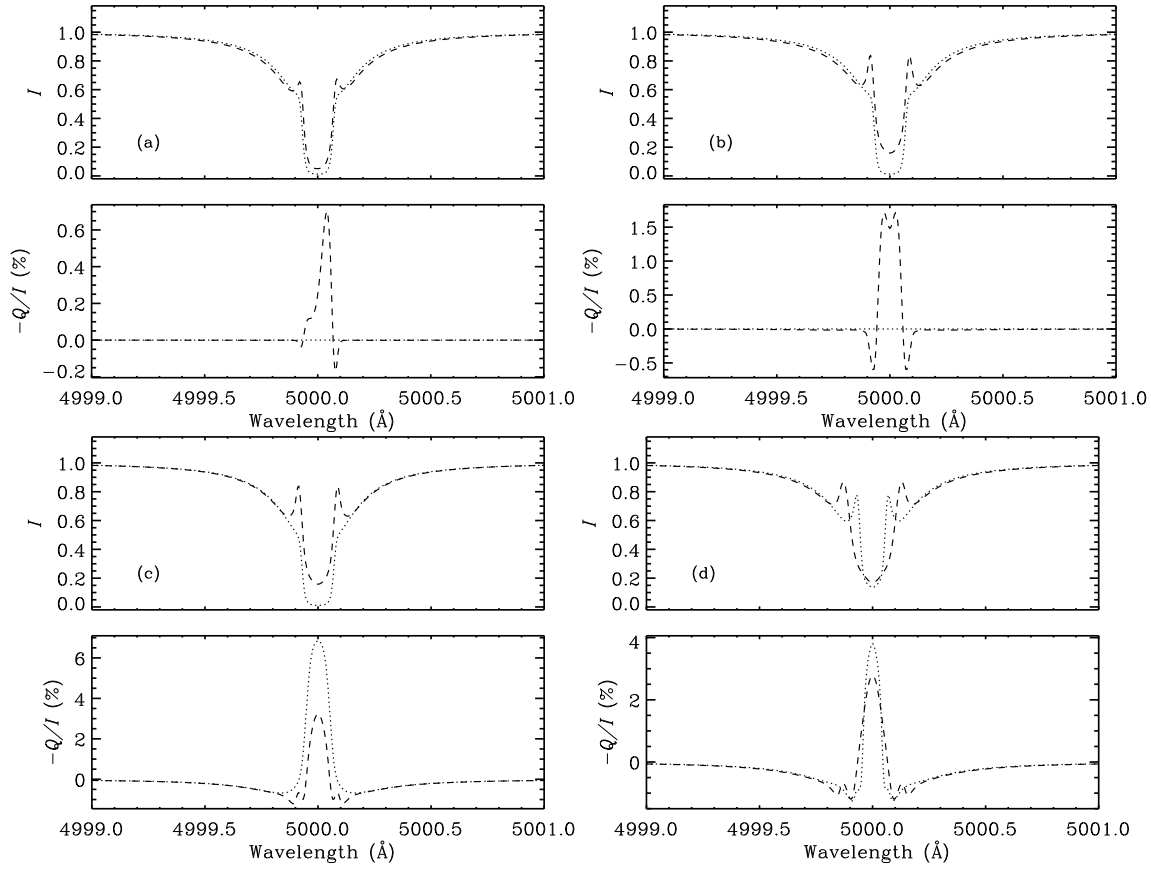

Figure 3.1: Emergent Stokes profiles in the presence of two blend lines for a line of sight $\mu = 0.047$. See Section 3.4 for details on the cases presented and parameters used for the computations of the profiles presented in panels (a), (b), (c) and (d).

blends, while dashed lines represent those computed with blends. In panels (a) and (b), we show the effects of polarizing blends ($W_2^{b_a} = 1$) on the intrinsically unpolarized main line ($W_2^l = 0$). Blends of unequal strength are considered in panel (a), while in panel (b), they are of equal strength. In panel (a), the blend at 4999.98 Å has a strength of $\beta_{b_1} = 5 \times 10^2$ and the one at 5000.02 Å has a strength of $\beta_{b_2} = 5 \times 10^3$. Blends make the main line core in I relatively narrow and less deep (compare dotted and dashed lines in Figure 3.1(a)). In Q/I, the main line does not produce any signal in the absence of blends as expected (see dotted line). The blends show triple peak structure (not all peaks are seen here) due to the PRD scattering mechanism. The wing peaks of the blends differ in amplitude because of the difference in their relative strengths. The main line polarization which should have

been zero according to the expectations ($W_2^l = 0$) is now clearly non-zero (see dashed line in Figure 3.1(a)). This is an effect of the proximity of the polarizing blends. The central and the wing PRD peaks of the two blends combine so as to give a distorted signal in Q/I. It appear as though the Q/I signal that we are seeing is due to the main line. One has to be therefore careful in identifying these effects in the process of modeling.

The parameters used to compute the Stokes profiles in panel (b) are similar to those used in panel (a) but for blend lines of equal strengths ($\beta_{b_a} = 5 \times 10^4$). We see, as before, a shallow and narrow absorption line in Stokes I when blends are included (see dashed line) compared to the case when they are neglected (see dotted line). Since both the blends are of equal strength, the Q/I profile is symmetric and shows a double peak structure with a dip at the main line center ($5000\,$Å). The increase in the percentage of polarization compared to panel (a) is attributed to the increase in the blend line strengths.

The case in which all the three lines are strongly polarizing ($W_2^l = W_2^{b_a} = 1$) is presented in panel (c). The blend lines have equal strengths ($\beta_{b_a} = 5 \times 10^4$). The dotted line corresponds to the main line case without blends. In this case, the main line appears as a pure absorption line in intensity and shows a strong polarization of about $7\,\%$ at main line center. When the blends are included, they bring down the line center polarization of the main line to nearly $4\,\%$ (see dashed line). The short peaks on either side of the main line core correspond to blend line peaks. The signs of the Q/I at the main line center and at the blend lines centers are opposite. This is indicative of a switchover from limb brightening to the limb darkening of the radiation field.

The effect of variation of the Doppler width is shown in panel (d). Here, the dotted and dashed lines represent the cases where the Doppler widths for the blends are $15\,$mÅ and $40\,$mÅ, respectively. The Doppler width of the main line is $25\,$mÅ in both the cases. The strength of the blends continues to be 5×10^4. All the three lines have an intrinsic polarizability factor $W_2 = 1$. The intensity I profile becomes broad in the main line core, with an increase in the the Doppler width of the blends. Magnitude of Q/I in the main line core decreases with an increase in the blend line width.

3.5 Conclusions

In this chapter, we have shown theoretically how the total source vector can be generalized to include many blend lines (see Sowmya et al., 2014a). Blend lines are generally present in the wings of the main spectral line. For the cases considered in this chapter, blend lines lie in the core of the main line. In practice, it is possible to have such situations where the blend lines are placed very close to the main line, thereby showing a considerable effect.

We showed in our studies that the blends affect the main line polarization significantly when they lie closer to the main line. Including these effects helps to achieve a better modeling of a given spectral line. These studies are essential in a fine analysis of the second solar spectrum, and help in our understanding of the solar atmosphere.

PART II

POLARIZED LINE FORMATION WITH MAGNETIC FIELDS

4

PBE IN A TWO-LEVEL ATOM WITH HYPERFINE STRUCTURE

This chapter is based on:
Sowmya, K., Nagendra, K. N., Stenflo J. O., & Sampoorna, M. 2014, ApJ, 786, 150

Outline

In this chapter, we consider the quantum interference (Section 1.6) in a two-level atom with hyperfine structure (Section 1.4.2) under the influence of a magnetic field. We derive the PRD matrix (Sections 1.3 and 1.3.1) that includes interference between the upper F states and neglect the interference between the lower F states. We apply the theory to the Na I D_2 line that is produced by the transition between the lower $J = 1/2$ and upper $J = 3/2$ states which split into F states because of the coupling with the nuclear spin $I_s = 3/2$. We explore the properties of the PRD matrix for the single scattering case, in particular, the effects of the magnetic field in the PB regime and their usefulness as a tool for the diagnostics of solar magnetic fields.

4.1 Introduction

The atomic energy levels are split into magnetic substates in the presence of a magnetic field. When MS is much smaller than the hyperfine structure splitting (HFS), then we are in the Zeeman effect (see Section 1.7.1) regime. In this regime, the energy shift produced by the magnetic field varies linearly with the field strength. On the other hand, if the MS

is comparable to or larger than the HFS then the magnetic field effects are described by the PBE (Section 1.7.3) in which the MS varies nonlinearly with the magnetic field strength, leading to level-crossing interference effects. The Hanle effect represents a modification of the resonance scattering polarization by the magnetic field. In this chapter, we are concerned with the Hanle effect involving F states. This leads to several interesting phenomena related to level-crossing interferences.

PBE in molecules gives signatures in the Stokes profiles, which serve as a promising tool for diagnosis of solar and stellar magnetic fields (see, for example, Berdyugina et al., 2005, 2006a,b; Shapiro et al., 2006, 2007; Asensio Ramos, 2006). Like PBE in molecular lines, PBE in atomic lines could also serve as a diagnostic tool for measuring the magnetic fields. With this motivation, people have studied the influence of PBE on emergent profiles of atomic lines such as the He I 10830 Å multiplet (Bommier, 1980), Fe II multiplet, Si II, Si III etc. (see, for example, Sasso et al., 2006; Stift et al., 2008; Stift & Leone, 2008; Khalack & Landstreet, 2012).

Landi Degl'Innocenti (1975) formulated the transfer equation for a line with hyperfine structure in the presence of a magnetic field, both in LTE and NLTE. He also presented expressions for the strengths and shifts of the magnetic components of the lines formed due to transitions between the F states. In a later paper, he provided a Fortran program to compute these strengths and magnetic shifts (see Landi Degl'Innocenti, 1978). We use this computer program to calculate the eigenvalues and expansion coefficients discussed in Section 4.3. López Ariste et al. (2002, 2003) discussed the net circular polarization (NCP) induced by the hyperfine structure and its usefulness as a tool for the diagnosis of solar magnetic fields in the quiet photosphere and plages.

The F-state interference phenomenon plays a significant role in modifying the shapes of the emergent Stokes profiles. Stenflo (1997) developed a scattering theory of quantum interference phenomena which explains the effect of F-state interference on coherently scattered lines. Landi Degl'Innocenti & Landolfi (2004) developed a QED theory to handle F-state interference phenomenon in the PB regime for scattering on a multilevel atom under the approximation of CRD. Casini & Manso Sainz (2005) discuss the same problem but for scattering on a multi-term atom that includes both J-state and F-state interference phenomena again under the approximation of CRD. Using the theory of Landi Degl'Innocenti & Landolfi (2004), Belluzzi et al. (2007) and Belluzzi (2009) investigated the effects of magnetic field on lines resulting from transitions between hyperfine structure states of odd isotope of Ba and Sc II, respectively.

A scattering theory of F-state interference based on a metalevel approach was developed by Landi Degl'Innocenti et al. (1997). This theory takes into account PRD in the

collisionless regime. In Smitha et al. (2012b), we presented the PRD matrix for the F-state interference phenomenon in the absence of magnetic fields and in the collisionless regime. This PRD theory was applied in Smitha et al. (2013b) to illustrate the importance of PRD, hyperfine structure, isotopic shifts, and radiative transfer in modeling the observed non-magnetic linear polarization profiles of Ba II D_2 $4554\,$Å line. In this chapter, we derive the PRD matrix for a two-level atom with hyperfine structure in the presence of a magnetic field of arbitrary strength. A straightforward extension of the J-state RM presented in Smitha et al. (2011b) to the case of F-state interference in the PB regime is not possible because the RM derived in that paper is valid only in the linear Zeeman regime. Therefore, in this chapter, we formulate the theory of F-state interference in the PB regime and derive an expression for the RM including PRD in the absence of collisions. We assume the lower levels to be infinitely sharp and unpolarized. For the sake of clarity, in Section 4.2 we describe the atomic system on which the magnetic field acts. We discuss the atom-radiation interaction in the presence of a magnetic field of arbitrary strength quantitatively in Section 4.3. In Section 4.4 we present the characteristics of the RM derived in Section 4.3 and give our concluding remarks in Section 4.5.

4.2 The Interaction Hamiltonian

The hyperfine structure of an element has dominant contributions from the magnetic dipole and electric quadrupole interactions (see Corney, 1977; Woodgate, 1992). The Hamiltonian $\mathcal{H}_D$ describing the interaction of the nuclear magnetic moment with the magnetic field produced at the nucleus by the valence electrons can be written as

$$\mathcal{H}_D = \mathcal{A}_J \boldsymbol{I}_s \cdot \boldsymbol{J} \ , \tag{4.1}$$

where $\mathcal{A}_J$ is the magnetic dipole hyperfine structure constant and is mostly determined from experiments. The Hamiltonian $\mathcal{H}_Q$ for the electric quadrupole interaction between the protons and electrons due to the finite extent of the nuclear charge distribution is given by

$$\mathcal{H}_Q = \frac{\mathcal{B}_J}{2I_s(2I_s-1)J(2J-1)}\left\{3(\boldsymbol{I}_s\cdot\boldsymbol{J})^2+\frac{3}{2}(\boldsymbol{I}_s\cdot\boldsymbol{J})-I_s(I_s+1)J(J+1)\right\}\ , \tag{4.2}$$

where $\mathcal{B}_J$ is the electric quadrupole hyperfine structure constant which is also in most cases determined by experimental measurements. $\mathcal{B}=0$ when $I_s=1/2$ because the nuclear charge distribution is spherically symmetric. Also, $\mathcal{B}_J$ vanishes when $J=0,1/2$ because

of the spherical symmetry of the electron charge distribution.

The total Hamiltonian for the atomic system in the presence of an external magnetic field is written as

$$\mathcal{H} = \mathcal{H}_0 + \mathcal{H}_{\rm hfs} + \mathcal{H}_B \ , \tag{4.3}$$

where $\mathcal{H}_0$ is the Hamiltonian describing the atomic structure excluding hyperfine structure, $\mathcal{H}_{\rm hfs}$ is the Hamiltonian for the hyperfine structure interaction which, is the sum of $\mathcal{H}_D$ and $\mathcal{H}_Q$.

In the absence of an external magnetic field, the hyperfine interaction energy $E_{\rm hfs}$ is given by

$$E_{\rm hfs} = \frac{1}{2}\mathcal{A}_J\mathcal{K} + \frac{\mathcal{B}_J}{8I_s(2I_s-1)J(2J-1)}\{3\mathcal{K}(\mathcal{K}+1) - 4J(J+1)I_s(I_s+1)\} \ , \tag{4.4}$$

where $\mathcal{K} = F(F+1) - J(J+1) - I_s(I_s+1)$. $E_{\rm hfs}$ is the energy of the F state measured from the parent J state. See Section 1.5.2 for more details.

In the limit of $\mathcal{B}_J \ll \mathcal{A}_J$, the spacing between the F states is given by the so called hyperfine structure interval rule

$$\Delta E = E_F - E_{F-1} = \mathcal{A}_J F \ . \tag{4.5}$$

In cases where $\mathcal{B}_J$ is finite, an additional energy shift is produced.

The magnetic Hamiltonian $\mathcal{H}_B$ in Equation (4.3) has the form

$$\mathcal{H}_B = \mu_0(\boldsymbol{L} + 2\boldsymbol{S})\cdot\boldsymbol{B} = \mu_0 B(J_z + S_z) \ , \tag{4.6}$$

where μ_0 is the Bohr magneton. B is the strength of the vector magnetic field $\boldsymbol{B}$. The z-axis of the coordinate system is assumed to be along the magnetic field direction. In the PB regime, the magnetic field produces a splitting comparable with the separation between the F states (HFS). In such cases, the magnetic substates of a given F state can superpose on the magnetic substates of another F state. This leads to a mixing of F states. Such a mixing of states can occur even for very small values of field strengths. Our purpose is to derive an expression for the PRD matrix representing the F-state interference process in the PB regime.

4.3 PRD Matrix

As mentioned in Chapter 1, in the scattering theory approach, the physics of atom radiation interaction is described through the RM. In this section, we derive the general form of the RM for the F-state interference process and present its forms in a few special cases.

4.3.1 RM in the PB Regime

The PB regime is reached when the Zeeman splitting of the magnetic substates μ belonging to a given F state becomes comparable to the energy separation between the F states themselves. This is generally referred to as the incomplete PBE. In such a situation, the magnetic field can no longer be treated as a perturbation to the atom-radiation interaction, and one has to carry out a simultaneous diagonalization of the hyperfine interaction and magnetic Hamiltonians. In the complete PB regime, the Zeeman splitting is very large compared to the separation between the F states.

The Kramers–Heisenberg formula (Kramers & Heisenberg, 1925) gives the complex probability amplitudes for scattering from an initial magnetic substate a to a final substate f through intermediate states b and is written as

$$w_{\alpha\beta} \sim \sum_b \frac{\langle f|\mathbf{r}\cdot\mathbf{e}_\alpha|b\rangle\langle b|\mathbf{r}\cdot\mathbf{e}_\beta|a\rangle}{\omega_{bf}-\omega-\mathrm{i}\gamma/2} \ . \tag{4.7}$$

Here, $\omega = 2\pi\xi$ is the circular frequency of the scattered radiation. $\hbar\omega_{bf}$ is the energy difference between the excited and final levels, and γ is the damping constant.

The coherency matrix (Section 1.1) for this scattering process $a \to b \to f$ is given by

$$\mathbf{W} = \sum_a \sum_f \boldsymbol{w}\otimes\boldsymbol{w}^* \ . \tag{4.8}$$

The incoherent summation is taken over the initial and final levels (see Stenflo, 1998). Here, $\boldsymbol{w}$ is the Jones matrix, and its elements are given by Equation (4.7).

We first identify the basis vectors $|a\rangle, |b\rangle$, and $|f\rangle$ in the PB regime as

$$|a\rangle = |J_a I_s i_a \mu_a\rangle \ , \tag{4.9}$$

with similar forms for $|b\rangle$ and $|f\rangle$. We then expand these PB regime basis vectors in terms

of basis vectors $|JI_sF\mu\rangle$ of the Zeeman regime as

$$|J_aI_si_a\mu_a\rangle = \sum_{F_a} C^{i_a}_{F_a}(J_aI_s,\mu_a)\,|J_aI_sF_a\mu_a\rangle\ , \tag{4.10}$$

with similar expansions carried out for the intermediate and final state vectors. The C coefficients appearing in the above equation are given by

$$C^i_F(JI_s,\mu) = \langle JI_sF\mu|JI_si\mu\rangle\ , \tag{4.11}$$

which can be assumed to be real because the total Hamiltonian is real.

Using Equation (4.10) in the Kramers–Heisenberg formula and noting that $J_f = J_a$, the dipole matrix elements can be expanded using the Wigner–Eckart theorem (see Equations (2.96) and (2.108) of Landi Degl'Innocenti & Landolfi, 2004) to obtain

$$\begin{aligned} w_{\alpha\beta} \sim & \sum_{i_b\mu_b}\sum_{F_aF_fF_bF_{b''}}\sum_{qq''}(-1)^{q-q''}C^{i_f}_{F_f}(J_aI_s,\mu_f)C^{i_a}_{F_a}(J_aI_s,\mu_a) \\ & \times C^{i_b}_{F_b}(J_bI_s,\mu_b)C^{i_b}_{F_{b''}}(J_bI_s,\mu_b)(2J_a+1)\sqrt{(2F_a+1)(2F_f+1)(2F_b+1)(2F_{b''}+1)} \\ & \times \begin{pmatrix} F_b & F_f & 1 \\ -\mu_b & \mu_f & -q \end{pmatrix}\begin{pmatrix} F_{b''} & F_a & 1 \\ -\mu_b & \mu_a & -q'' \end{pmatrix}\begin{Bmatrix} J_a & J_b & 1 \\ F_b & F_f & I_s \end{Bmatrix}\begin{Bmatrix} J_a & J_b & 1 \\ F_{b''} & F_a & I_s \end{Bmatrix} \\ & \times \varepsilon^{\alpha^*}_q\varepsilon^{\beta}_{q''}\,\Phi_\gamma(\nu_{i_b\mu_bi_f\mu_f}-\xi)\ . \end{aligned} \tag{4.12}$$

Here, ε are the spherical vector components of the polarization unit vectors with α and β referring to the scattered and incident rays, respectively. $\Phi_\gamma(\nu_{i_b\mu_bi_f\mu_f}-\xi)$ is the frequency-normalized profile function given by

$$\Phi_\gamma(\nu_{i_b\mu_bi_f\mu_f}-\xi) = \frac{1/\pi\mathrm{i}}{\nu_{i_b\mu_bi_f\mu_f}-\xi-\mathrm{i}\gamma/4\pi}\ , \tag{4.13}$$

where we have used an abbreviation

$$\nu_{i_b\mu_bi_f\mu_f} = \nu_{J_bI_si_b\mu_b,J_aI_si_f\mu_f} = \nu_{J_bJ_a} + \frac{E_{i_b}(J_bI_s,\mu_b)-E_{i_f}(J_aI_s,\mu_f)}{h}\ , \tag{4.14}$$

with h being the Planck constant. The energy eigenvalues E and the expansion coefficients C are obtained by diagonalizing the total Hamiltonian given in Equation (4.3, see Landi Degl'Innocenti 1978).

We take the bilinear product of the matrix elements $w_{\alpha\beta}$, which involves performing coherent summation over the intermediate substates b. Furthermore, we perform inco-

herent summations over initial (a) and final (f) substates to form the coherency matrix and transform it to the laboratory frame, following the steps described in Section 2.2 of Sampoorna et al. (2007a). With the help of Equation (3.84) of Stenflo (1994) and the steps given in Appendix C of Sampoorna et al. (2007b), we express the coherency matrix in terms of irreducible spherical tensors $\mathcal{T}^K_Q(i,\boldsymbol{n})$ introduced to polarimetry by Landi Degl'Innocenti (1984). Here, $i = 0,1,2,3$ refer to the Stokes parameters, $K = 0,1,2$, with Q taking $(2K+1)$ values, and $\boldsymbol{n}$ is the direction of the scattered ray. We then transform the coherency matrix to Stokes vector basis following the steps in Appendix C of Sampoorna et al. (2007b) to obtain

$$\boldsymbol{I}_i = \sum_{j=0}^{3} \boldsymbol{R}^{\rm II}_{ij}(x,\boldsymbol{n},x',\boldsymbol{n}';\boldsymbol{B})\boldsymbol{I}'_j \,, \tag{4.15}$$

where $\boldsymbol{I}_i$ and $\boldsymbol{I}'_j$ are the Stokes vectors for the scattered and incident rays, respectively, $\boldsymbol{R}^{\rm II}_{ij}$ is the normalized RM for type II scattering in the laboratory frame given by

$$\begin{aligned}
\boldsymbol{R}^{\rm II}_{ij}(x,\boldsymbol{n},x',\boldsymbol{n}';\boldsymbol{B}) &= \frac{3(2J_b+1)}{(2I_s+1)} \sum_{KK'Q} \sum_{i_a\mu_a i_f\mu_f i_b\mu_b i_{b'}\mu_{b'}} \sum_{F_aF_{a'}F_fF_{f'}F_bF_{b'}F_{b''}F_{b'''}} \\
&\times \sum_{qq'q''q'''} (-1)^{q-q'''+Q} \sqrt{(2K+1)(2K'+1)}\cos\beta_{i_{b'}\mu_{b'}i_b\mu_b} \mathrm{e}^{\mathrm{i}\beta_{i_{b'}\mu_{b'}i_b\mu_b}} \\
&\times [(h^{\rm II}_{i_b\mu_b,i_{b'}\mu_{b'}})_{i_a\mu_a i_f\mu_f} + \mathrm{i}(f^{\rm II}_{i_b\mu_b,i_{b'}\mu_{b'}})_{i_a\mu_a i_f\mu_f}] C^{i_f}_{F_f}(J_aI_s,\mu_f) C^{i_a}_{F_a}(J_aI_s,\mu_a) C^{i_b}_{F_b}(J_bI_s,\mu_b) \\
&\times C^{i_b}_{F_{b''}}(J_bI_s,\mu_b) C^{i_f}_{F_{f'}}(J_aI_s,\mu_f) C^{i_a}_{F_{a'}}(J_aI_s,\mu_a) C^{i_{b'}}_{F_{b'}}(J_bI_s,\mu_{b'}) C^{i_{b'}}_{F_{b'''}}(J_bI_s,\mu_{b'}) \\
&\times \sqrt{(2F_a+1)(2F_f+1)(2F_{a'}+1)(2F_{f'}+1)(2F_b+1)(2F_{b'}+1)(2F_{b''}+1)(2F_{b'''}+1)} \\
&\times \begin{pmatrix} F_b & F_f & 1 \\ -\mu_b & \mu_f & -q \end{pmatrix} \begin{pmatrix} F_{b'} & F_{f'} & 1 \\ -\mu_{b'} & \mu_f & -q' \end{pmatrix} \begin{pmatrix} F_{b''} & F_a & 1 \\ -\mu_b & \mu_a & -q'' \end{pmatrix} \\
&\times \begin{pmatrix} F_{b'''} & F_{a'} & 1 \\ -\mu_{b'} & \mu_a & -q''' \end{pmatrix} \begin{pmatrix} 1 & 1 & K \\ q & -q' & -Q \end{pmatrix} \begin{pmatrix} 1 & 1 & K' \\ q''' & -q'' & Q \end{pmatrix} \\
&\times \begin{Bmatrix} J_a & J_b & 1 \\ F_b & F_f & I_s \end{Bmatrix} \begin{Bmatrix} J_a & J_b & 1 \\ F_{b'} & F_{f'} & I_s \end{Bmatrix} \begin{Bmatrix} J_a & J_b & 1 \\ F_{b''} & F_a & I_s \end{Bmatrix} \begin{Bmatrix} J_a & J_b & 1 \\ F_{b'''} & F_{a'} & I_s \end{Bmatrix} \\
&\times (-1)^Q \mathcal{T}^K_{-Q}(i,\boldsymbol{n}) \mathcal{T}^{K'}_{Q}(j,\boldsymbol{n}') \,.
\end{aligned} \tag{4.16}$$

Equation (4.16) represents the PRD matrix for hyperfine interaction in the PB regime. This equation, when written in the atomic rest frame, can be directly obtained from Equation (12) of Landi Degl'Innocenti et al. (1997) by introducing the spherical tensors and by assuming that the lower levels are unpolarized. The PRD matrix derived in this sec-

tion satisfies the symmetry relations described in detail in Bommier (1997b). In the above expression, $\boldsymbol{n}'$ represents the direction of the incident ray and the so called Hanle angle $\beta_{i_{b'}\mu_{b'}i_b\mu_b}$ is given by

$$\tan\beta_{i_{b'}\mu_{b'}i_b\mu_b} = \frac{\nu_{i_{b'}\mu_{b'}i_a\mu_a} - \nu_{i_b\mu_b i_a\mu_a}}{\gamma/2\pi} \,. \tag{4.17}$$

The auxiliary functions $h^{\rm II}$ and $f^{\rm II}$ appearing in Equation (4.16) have the form

$$(h^{\rm II}_{i_b\mu_b,i_{b'}\mu_{b'}})_{i_a\mu_a i_f\mu_f} = \frac{1}{2}[R^{\rm II,H}_{i_b\mu_b i_a\mu_a i_f\mu_f} + R^{\rm II,H}_{i_{b'}\mu_{b'}i_a\mu_a i_f\mu_f}] \,, \tag{4.18}$$

and

$$(f^{\rm II}_{i_b\mu_b,i_{b'}\mu_{b'}})_{i_a\mu_a i_f\mu_f} = \frac{1}{2}[R^{\rm II,F}_{i_{b'}\mu_{b'}i_a\mu_a i_f\mu_f} - R^{\rm II,F}_{i_b\mu_b i_a\mu_a i_f\mu_f}] \,, \tag{4.19}$$

where the magnetic redistribution functions of type II are defined as

$$\begin{aligned} R^{\rm II,H}_{i_b\mu_b i_a\mu_a i_f\mu_f}(x_{ba}, x'_{ba}, \Theta) = \frac{1}{\pi\sin\Theta}\exp\left\{ -\left[\frac{x_{ba} - x'_{ba} + x_{i_a\mu_a i_f\mu_f}}{2\sin(\Theta/2)}\right]^2\right\} \\ \times H\left(\frac{a}{\cos(\Theta/2)}, \frac{x_{ba} + x'_{ba} + x_{i_a\mu_a i_f\mu_f}}{2\cos(\Theta/2)}\right) \,, \end{aligned} \tag{4.20}$$

and

$$\begin{aligned} R^{\rm II,F}_{i_b\mu_b i_a\mu_a i_f\mu_f}(x_{ba}, x'_{ba}, \Theta) = \frac{1}{\pi\sin\Theta}\exp\left\{ -\left[\frac{x_{ba} - x'_{ba} + x_{i_a\mu_a i_f\mu_f}}{2\sin(\Theta/2)}\right]^2\right\} \\ \times 2F\left(\frac{a}{\cos(\Theta/2)}, \frac{x_{ba} + x'_{ba} + x_{i_a\mu_a i_f\mu_f}}{2\cos(\Theta/2)}\right) \,. \end{aligned} \tag{4.21}$$

Here, Θ is the scattering angle, the functions H and F are the Voigt and Faraday–Voigt functions (see Equation (18) of Smitha et al., 2011b). The quantities appearing in the expressions for the type II redistribution functions have the following definitions:

$$\begin{aligned} x_{ba} &= \frac{\nu_{i_b\mu_b i_a\mu_a} - \nu}{\Delta\nu_{\rm D}} \;;\;\; x'_{ba} = \frac{\nu_{i_b\mu_b i_a\mu_a} - \nu'}{\Delta\nu_{\rm D}} \,, \\ x_{i_a\mu_a i_f\mu_f} &= \frac{\nu_{i_a\mu_a i_f\mu_f}}{\Delta\nu_{\rm D}} \;;\;\; a = \frac{\gamma}{4\pi\Delta\nu_{\rm D}} \,, \end{aligned} \tag{4.22}$$

where x_{ba} is the emission frequency, a is the damping parameter, and $\Delta\nu_{\rm D}$ is the Doppler width.

We remark that the PRD matrix in the PB regime presented in this section can also be obtained by an alternative approach based on the transition amplitudes (Shapiro et al., 2007) that avoids the use of statistical tensors $\mathcal{T}^K_Q$. See Appendix A for more details.

4.3.2 Special Cases

The PB theory and the relevant RM derived in Section 4.3.1 gives exact PRD matrix for the problem at hand. However, it is possible, under limiting cases, to derive simple expressions for practical applications. One example of this is the so called Zeeman regime. In this regime, the magnetic field is so weak that it produces a splitting which is much smaller than the energy differences between the F states. In such a case, the magnetic Hamiltonian can be diagonalized analytically using the perturbation theory.

In the Zeeman regime where the basis vector is $|JI_sF\mu\rangle$ in which F is a good quantum number, the RM in Equation (4.16) takes the form

$$\begin{aligned}
\boldsymbol{R}^{\mathrm{II}}_{ij}(x,\boldsymbol{n},x',\boldsymbol{n}';\boldsymbol{B}) &= \frac{3(2J_b+1)}{2I_s+1} \sum_{KK'Qqq'q''q'''F_a\mu_aF_f\mu_fF_b\mu_bF_{b'}\mu_{b'}} (-1)^{q-q'''+Q} \\
&\times \cos\beta_{F_{b'}\mu_{b'}F_b\mu_b} \mathrm{e}^{\mathrm{i}\beta_{F_{b'}\mu_{b'}F_b\mu_b}} \left[(h^{\mathrm{II}}_{F_b\mu_b,F_{b'}\mu_{b'}})_{F_a\mu_aF_f\mu_f} + \mathrm{i}(f^{\mathrm{II}}_{F_b\mu_b,F_{b'}\mu_{b'}})_{F_a\mu_aF_f\mu_f} \right] \\
&\times (2F_a+1)(2F_f+1)(2F_b+1)(2F_{b'}+1)\sqrt{(2K+1)(2K'+1)} \\
&\times \left\{ \begin{array}{ccc} J_a & J_b & 1 \\ F_b & F_f & I_s \end{array} \right\} \left\{ \begin{array}{ccc} J_a & J_b & 1 \\ F_b & F_a & I_s \end{array} \right\} \left\{ \begin{array}{ccc} J_a & J_b & 1 \\ F_{b'} & F_f & I_s \end{array} \right\} \left\{ \begin{array}{ccc} J_a & J_b & 1 \\ F_{b'} & F_a & I_s \end{array} \right\} \\
&\times \left(\begin{array}{ccc} F_b & F_a & 1 \\ -\mu_b & \mu_a & -q'' \end{array} \right) \left(\begin{array}{ccc} F_b & F_f & 1 \\ -\mu_b & \mu_f & -q \end{array} \right) \left(\begin{array}{ccc} F_{b'} & F_a & 1 \\ -\mu_{b'} & \mu_a & -q''' \end{array} \right) \\
&\times \left(\begin{array}{ccc} F_{b'} & F_f & 1 \\ -\mu_{b'} & \mu_f & -q' \end{array} \right) \left(\begin{array}{ccc} 1 & 1 & K \\ q & -q' & -Q \end{array} \right) \left(\begin{array}{ccc} 1 & 1 & K' \\ q''' & -q'' & Q \end{array} \right) \\
&\times (-1)^Q \mathcal{T}^K_{-Q}(i,\boldsymbol{n}) \mathcal{T}^{K'}_{Q}(j,\boldsymbol{n}') \, . \qquad (4.23)
\end{aligned}$$

The Hanle angle $\beta_{F_{b'}\mu_{b'}F_b\mu_b}$ is given by

$$\tan\beta_{F_{b'}\mu_{b'}F_b\mu_b} = \frac{\omega_{F_{b'}F_b} + (\mathrm{g}_{F_{b'}}\mu_{b'} - \mathrm{g}_{F_b}\mu_b)\omega_L}{\gamma} \, , \qquad (4.24)$$

where ω_L is the Larmour frequency associated with the applied magnetic field. The Landé factors g_F appearing in the above equation are defined as

$$\mathrm{g}_F = \mathrm{g}_J \, \frac{1}{2} \frac{F(F+1) + J(J+1) - I_s(I_s+1)}{F(F+1)} \, , \qquad (4.25)$$

for $F \neq 0$. Here, g_J is the $L-S$ coupling Landé factor given by

$$\mathrm{g}_J = 1 + \frac{1}{2} \frac{J(J+1) - L(L+1) + S(S+1)}{J(J+1)} \, . \qquad (4.26)$$

Equation (4.23) has a formal resemblance to Equation (25) derived in Smitha et al. (2011b) for the case of J-state interference. Indeed, the F-state interference RM in the Zeeman regime can be obtained from the corresponding J-state interference RM through the replacement of (J, L, S) by (F, J, I_s) in the latter RM. When the magnetic field is set to zero in Equation (4.23), it takes the same form as Equation (2) of Smitha et al. (2012b).

4.4 Redistribution in Single Scattering

To study the behavior of the RM derived in Section 4.3.1 for arbitrary field strengths, we consider the atomic line with the following configuration, namely, the Na I D_2 line resulting from the transition between $J_a = 1/2$ and $J_b = 3/2$ (see Figures 1.3 and 1.7). The wavelength in air corresponding to this transition is $\lambda_0 = 5889.95095$ Å. The nuclear spin $I_s = 3/2$. The $J - I_s$ coupling results in the hyperfine structure states $F_b = 0, 1, 2, 3$ for the upper state J_b and $F_a = 1, 2$ for the lower state J_a. The energies of these F states are taken from Steck (2003). When the degeneracy of the magnetic substates of the F states is lifted by the magnetic field, 68 allowed transitions take place between them in the PB regime. The hyperfine structure constants have the values $\mathcal{A}_{1/2} = 885.81$ MHz, $\mathcal{B}_{1/2} = 0$, $\mathcal{A}_{3/2} = 18.534$ MHz, and $\mathcal{B}_{3/2} = 2.724$ MHz (see Steck, 2003). The Einstein A coefficient for the $J_b = 3/2$ state is taken to be 6.3×10^7 s^{-1}. The Doppler width $\Delta\lambda_D = 25$ mÅ and the damping parameter $a = 0.00227$ (a value obtained after using $\gamma = 6.3 \times 10^7$ s^{-1} in Equation (4.22), where a is defined) for all the components. The system that we have considered obeys the spacing rule described in Section 4.2. For the case of $I_s = 3/2$ considered here, the spacing between the F states is predicted to be

$$E_2 - E_1 = 2\mathcal{A}_{1/2} \, ,$$

for the lower $J = 1/2$ state and

$$\begin{aligned} E_3 - E_2 &= 3\mathcal{A}_{3/2} + \mathcal{B}_{3/2} \, , \\ E_2 - E_1 &= 2\mathcal{A}_{3/2} - \mathcal{B}_{3/2} \, , \\ E_1 - E_0 &= \mathcal{A}_{3/2} - \mathcal{B}_{3/2} \, , \end{aligned}$$

for the upper $J = 3/2$ state. We study the results of a single $90°$ scattering event in which the unpolarized spectrally flat incident beam is scattered by this atomic system in a direction perpendicular to the incident beam. We show the results obtained by considering the Li I D_2 lines in Appendix B.

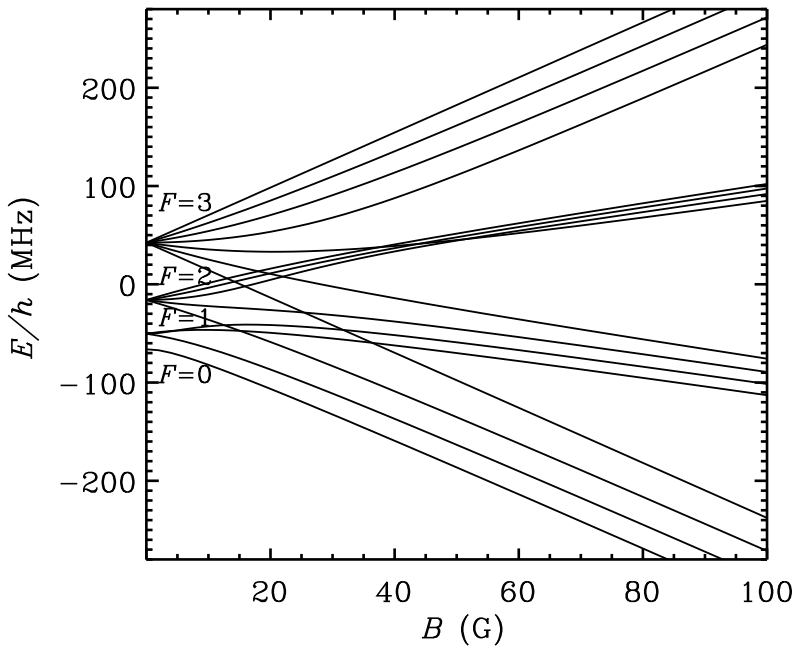

Figure 4.1: Energies of the magnetic substates of the F states as a function of the magnetic field strength B in G.

4.4.1 Polarization Diagram

Figure 4.1 shows the energies of the magnetic substates of the upper F states as a function of the magnetic field strength B. This figure is similar to the one presented in Figure 3.11 of Landi Degl'Innocenti & Landolfi (2004). It is apparent from the figure that the MS is nonlinear. This nonlinear behavior of the energies of the magnetic substates starts as soon as $B \neq 0$. We also notice several level-crossings occurring at different field strengths. For the atomic system under consideration, the magnetic field strengths (in G) for which the level-crossings occur are tabulated in Table 4.1. These level-crossings show up as loops in the polarization diagrams (plots of Q/I vs U/I) and significantly influence the scattered Stokes profiles.

The scattering geometry used for the calculation of the polarization diagrams in the present section is shown in Figure 4.2. This geometry is identical to the one considered in Figure 5.11 of Landi Degl'Innocenti & Landolfi (2004). To explore the effects of the magnetic field in the PB regime on the linear polarization, we present in Figure 4.3 polarization diagrams computed at different distances from the line center. To construct these diagrams, we first compute the elements of the RM for a given value of B and integrate the first column of the RM over incident wavelengths.

The solid curve for $\beta = 0°$ (magnetic field parallel to the scattered beam) in Figure 4.3

$F_b \diagdown F_{b'}$		2	3	3	3
	$\mu_b \diagdown \mu_{b'}$	-2	-3	-2	-1
1	0	**12.7**	31.3	...	...
1	$+1$	15	36	...	...
2	-1	...	**25.1**	...	...
2	0	...	16.3	**22**	52
2	$+1$	...	14	20	**44.5**
2	$+2$	...	13.3	18	37.8

Table 4.1: Magnetic field strengths (approximate values in G) for which the magnetic substates of the F states cross. For instance, the crossing between $\mu_b = 0$ of $F_b = 1$ and $\mu_{b'} = -2$ of $F_{b'} = 2$ occurs at $B \sim 12.7\,\mathrm{G}$. The numbers highlighted in boldface correspond to the field strength values for which level-crossings occur when one considers the geometry given in Figure 4.2, i.e., the level-crossings corresponding to $\Delta\mu = \mu_{b'} - \mu_b = \pm 2$.

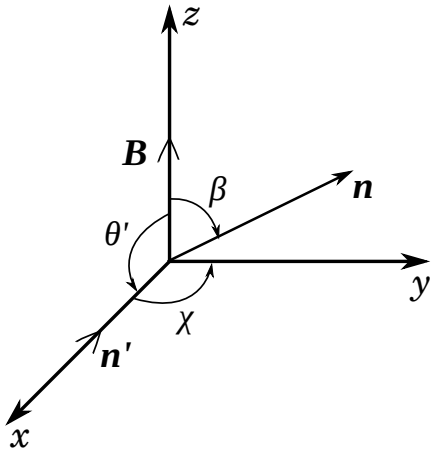

Figure 4.2: Geometry considered for polarization diagrams. β is the angle between the magnetic field vector and the scattered beam. The incident radiation is characterized by $(\theta', \chi') = (90°, 0°)$ and the scattered radiation by $(\theta, \chi) = (\beta, 90°)$. The magnetic field inclination $\theta_B = 0°$ and its azimuth $\chi_B = 0°$ (magnetic reference frame).

matches with Figure 10.30 of Landi Degl'Innocenti & Landolfi (2004). As discussed in Landi Degl'Innocenti & Landolfi (2004), the loops seen in the polarization diagram arise due to the level-crossings that occur in the PB regime (see Figure 4.1). For the geometry considered, level-crossings take place only between magnetic substates with $|\Delta\mu| = 2$. The magnetic field values for which these crossings occur are highlighted in boldface in Table 4.1. The coherence between the overlapping substates increases around these values of field strengths. This leads to an increase in the scattering polarization toward its non-magnetic value, resulting in the formation of loops.

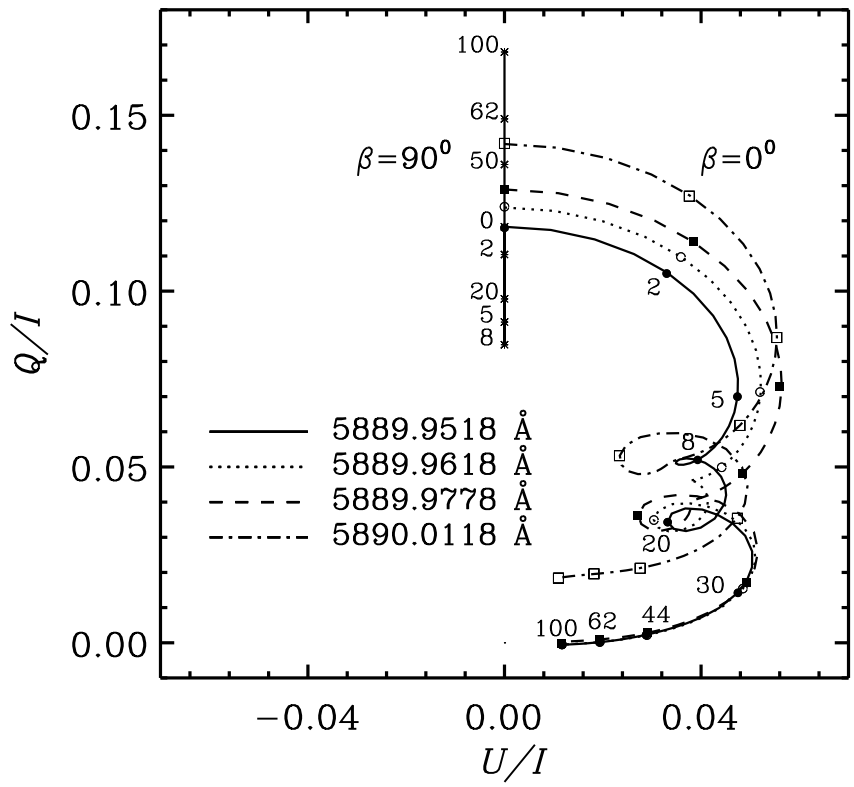

Figure 4.3: Polarization diagrams obtained for $\beta = 0°$ at different distances from the line center as indicated in the figure. The solid vertical line represents the $\beta = 90°$ case corresponding to the line center wavelength. The numbers along the solid curves represent the value of magnetic field strength B in G. The symbols on the other curves mark the same values of B as indicated for the solid curve for $\beta = 0°$. The zero field point is the same for the two cases represented by solid lines.

We see from the figure an overall increase in Q/I and U/I as we move away from the line center when $\beta = 0°$. Furthermore, the upper loop (near $8\,$G) seen in the solid line case disappears for wavelengths away from the line center. On the other hand, the lower loop (near $20\,$G) becomes bigger in size. In the far wings of the line, the polarization diagram becomes a point corresponding to the Rayleigh case at $Q/I = 0.428$ and $U/I = 0$.

In Figure 4.3, we also present the case of $\beta = 90°$ (magnetic field perpendicular to the scattering plane). In this case, the Hanle effect in a two-level atom with hyperfine structure shows an interesting phenomenon (see the vertical solid line) called anti-level-crossing, which has been extensively studied and characterized in the case of CRD (Bommier, 1980; Landi Degl'Innocenti & Landolfi, 2004). We see that the Q/I initially decreases from 0.118 at $B = 0$ to nearly 0.0847 for $B = 8\,$G. With further increase in B, the Q/I starts

increasing and exceeds its value at $B = 0$. Thus, we see that

$$\left(\frac{Q}{I}\right)_{B=0}^{I_s\neq 0} < \left(\frac{Q}{I}\right)_{B\to\infty}^{I_s\neq 0}. \tag{4.27}$$

This occurs due to the basis transformation of the energy eigenstates in the complete PB regime. The basis transformation takes place when the field strength increases from incomplete PB regime to the complete PB regime. In the incomplete PB regime, the energy eigenstates are given by $|JI_s i\mu\rangle$, whereas in the complete PB regime they are given by $|J\mu_J I_s \mu_{I_s}\rangle$. Anti-level-crossing is also known as avoided crossing, in which, due to the strong coupling of the J and I_s to the magnetic field, the magnetic substates instead of crossing, repel each other. Due to the geometry of the problem, U/I is zero.

4.4.2 Scattered Stokes Profiles

In this section, we present the Stokes profiles computed with PRD in the PB regime. Sections 4.4.2.1, 4.4.2.2, and 4.4.2.3 show the Stokes profiles obtained for various magnetic field configurations. The magnetic field orientations are discussed in the text and strengths are indicated in the figures. The incident radiation is characterized by $(\cos\theta', \chi') = (0, 0°)$ and the scattered ray by $(\cos\theta, \chi) = (0, 90°)$. For the computation of the Stokes profiles, we use a wavelength grid having 376 finely spaced points covering a bandwidth of 2 Å. The separation between the F states in the absence of a magnetic field is of the order of mÅ. In the presence of a magnetic field, the magnetic components are shifted away from the line center and the wavelength grid that we have considered is good enough and covers all the components shifted by the magnetic field.

4.4.2.1 Vertical Field Perpendicular to the Line of Sight

In Figure 4.4, we show the Stokes profiles obtained for different strengths of a vertical magnetic field ($\theta_B = 0°$ and $\chi_B = 0°$). We see that the intensity increases slightly with increasing field strength. Q/I profiles show a decrease in amplitude up to 8 G (see short dashed line). For stronger fields (greater than 8 G), the Q/I amplitude increases (see also Figure 4.3). This is the signature of anti-level-crossing effect which occurs because of the repulsion between the magnetic substates. As discussed earlier, as a result of this effect, the Q/I line core value, when considered as a function of the field strength, initially decreases and then increases beyond its non-magnetic value. Transverse Zeeman effect signatures show up prominently for fields stronger than 100 G. Because of the geometry considered, U/I is zero.

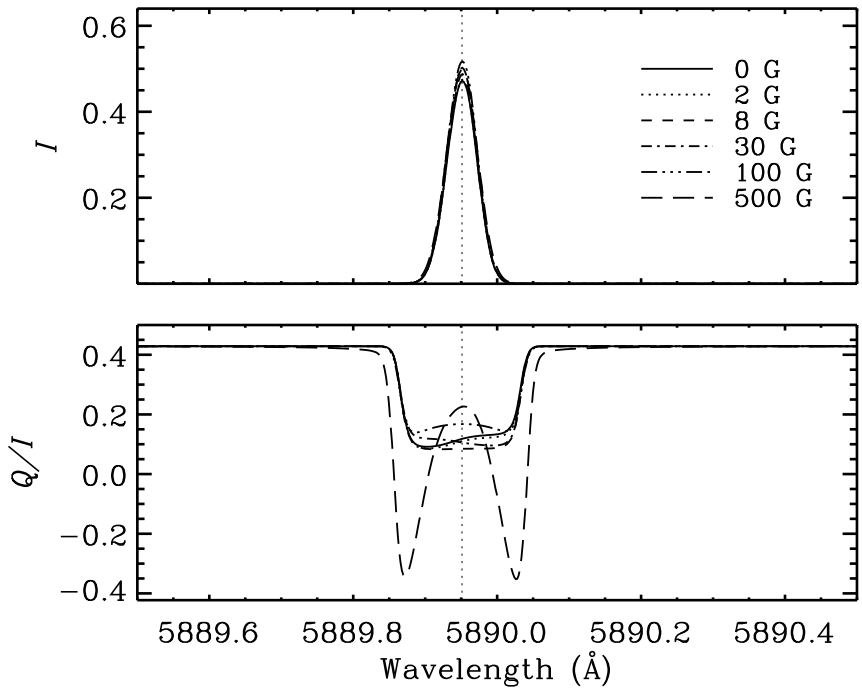

Figure 4.4: Stokes profiles computed for the case of a vertical magnetic field. Vertical dotted line marks the wavelength position of the Na I D_2 line.

4.4.2.2 Horizontal Field Perpendicular to the Line of Sight

The case of a horizontal field perpendicular to the line of sight ($\theta_B = 90°$ and $\chi_B = 0°$) is shown in Figure 4.5. We see that the intensity decreases monotonically with field strength. Q/I profiles show an increase in amplitude from their Rayleigh scattered values with an increase in the field strength. For fields of the order of $100\,\mathrm{G}$ and larger, we see three lobed profiles in Q/I due to transverse Zeeman effect. Once again, U/I is zero due to the geometry.

4.4.2.3 Horizontal Field Parallel to the Line of Sight

For this geometry of the magnetic field ($\theta_B = 90°$ and $\chi_B = 90°$), the intensity profiles behave in the same way as in the case of a horizontal field perpendicular to the line of sight (see Figure 4.6). The depolarization in the line core due to the Hanle effect is clearly visible in the Q/I panel. The U/I signal is now generated because of Hanle rotation. There is an increase in U/I amplitude for weaker fields and then a decrease for stronger fields, which is a typical signature of the Hanle effect. We notice that the V/I profiles are asymmetric in the incomplete PB regime (for fields up to $200\,\mathrm{G}$) while it is perfectly anti-symmetric in the complete PB regime (for fields greater than $200\,\mathrm{G}$). This is because

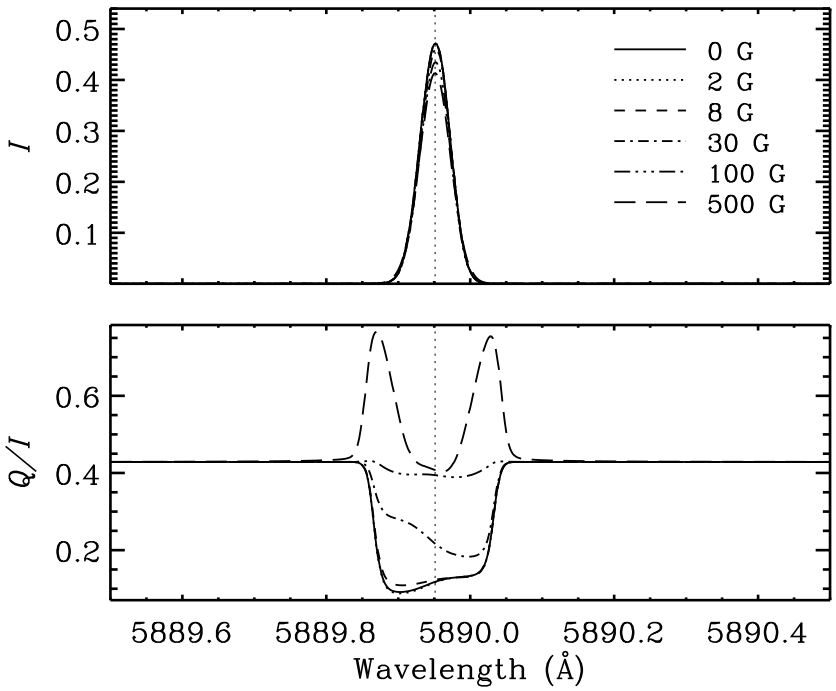

Figure 4.5: Stokes profiles computed for the case of a horizontal magnetic field perpendicular to the line of sight. Vertical dotted line marks the wavelength position of the Na I D_2 line.

incomplete PBE shifts the magnetic components asymmetrically about the line center and causes differential strengths for these components. Because of this asymmetry, the NCP, defined as $\int V\, d\lambda$ (where the integration is done over the full line profile), is non-zero (the NCP would be zero if the splitting produced by the magnetic field is symmetric). For the atomic line under consideration, NCP remains non-zero up to 200 G.

4.5 Conclusions

Landi Degl'Innocenti & Landolfi (2004) incorporated the PBE on the hyperfine structure states in the polarization studies under the assumption of CRD. They assumed that the incident radiation is independent of frequency in an interval larger than the frequency shifts and inverse lifetimes of the hyperfine structure substates involved in the transitions (flat-spectrum approximation). In this chapter, we considered the same problem, but for the case of PRD. This allows us to handle the frequency dependence of the incident radiation field (relaxation of flat-spectrum approximation). In this way, the Stokes profile shapes can be properly calculated by including the effects of PRD. We derived the PRD matrix for F-state interference process, in the collisionless regime, in the presence of magnetic fields

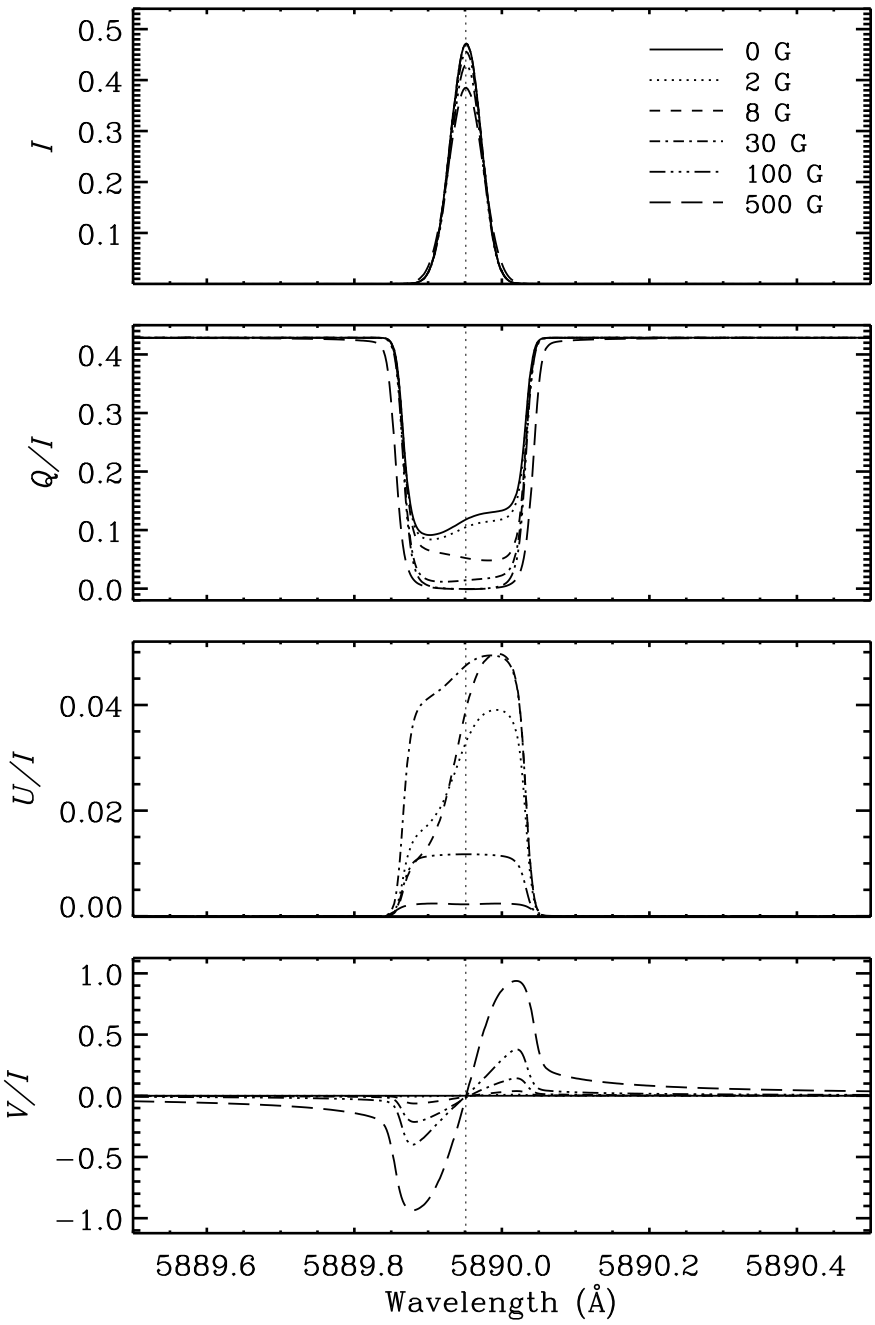

Figure 4.6: Stokes profiles computed for the case of a horizontal magnetic field parallel to the line of sight. Vertical dotted line marks the wavelength position of the Na I D_2 line.

of arbitrary strengths.

Through the polarization diagrams computed at different scattered wavelengths, we showed the dependence on wavelength of the loops which are characteristics of the level-crossings that occur in the PB regime. With the help of the Stokes profiles computed for

the case of a vertical magnetic field, we also demonstrated the anti-level-crossing effect, discussed for the case of CRD by Bommier (1980) and Landi Degl'Innocenti & Landolfi (2004). Based on the formulation described in this chapter, it is possible to explore the diagnostic potential of PBE with PRD, in a complementary way with the Zeeman effect, to determine the strengths and geometry of the magnetic fields in the solar atmosphere.

5

PBE IN A TWO-TERM ATOM WITHOUT HYPERFINE STRUCTURE

This chapter is based on:
Sowmya, K., Nagendra, K. N., Sampoorna, M., & Stenflo J. O. 2014, ApJ, 793, 71

Outline

In Chapter 4, we dealt with the problem of quantum interference between the F states in a two-level atom with hyperfine structure. In this chapter, we study the quantum interference between the fine structure states of an atom which modifies the shapes of the emergent Stokes profiles in the second solar spectrum. This phenomenon has been studied in great detail both in the presence and absence of magnetic fields. By assuming a flat-spectrum for the incident radiation, the signatures of this effect have been explored for arbitrary field strengths. Even though the theory which takes into account the frequency dependence of the incident radiation is well developed, it is restricted to the regime in which MS is much smaller than the separation between the fine structure states. In this chapter, we carry out a generalization of our scattering matrix formalism including the effects of PRD for arbitrary magnetic fields. We test the formalism by using available benchmarks for special cases. In particular, we apply it to the Li I $6708\,\text{Å}$ D_1 and D_2 line system (see Figure 1.2), for which observable effects from the PB regime are expected in the Sun's spectrum.

5.1 Introduction

The magnetic substates belonging to the J states are degenerate in the absence of a magnetic field. When a magnetic field is applied, the degeneracy is lifted and the energies of these magnetic substates are modified. With an increase in the field strength, the magnetic substates belonging to different J states of a given term begin to overlap, leading to a mixing of the J states, and therefore J no longer remains a good quantum number. The PBE occurs when the splitting produced by the magnetic field is comparable to the fine structure splitting (FS). In this chapter, we address the problem of PBE on a two-term atom without hyperfine structure (Section 1.4.1) taking into account the effects of PRD. In other words, we study the J-state interference phenomenon in the presence of a magnetic field of arbitrary strength. In particular, we derive the PRD matrix for the problem at hand and present the results obtained for the single scattering case.

Bommier (1980) developed a density matrix formalism to handle J-state interference in the presence of a magnetic field of arbitrary strength (including both the Zeeman and PB regimes). Her formalism was limited to CRD in scattering. A quantum theory of J-state interference phenomenon for the case of frequency coherent scattering was formulated by Stenflo (1980, 1994, 1997). Landi Degl'Innocenti & Landolfi (2004), under the flat-spectrum approximation, developed a QED theory for the J-state interference phenomenon in a multi-term atom and in the presence of magnetic fields of arbitrary strengths. Assuming CRD, Casini & Manso Sainz (2005) considered the problem of PBE in a multi-term atom with hyperfine structure involving the interferences among both the J and F states. In the linear Zeeman regime where FS is larger than the splitting produced by the magnetic field, Smitha et al. (2011b, 2013a) developed a theory for the interference between the fine structure states taking into account the effects of PRD. In this chapter, we generalize the RM derived by Smitha et al. (2011b) in the absence of collisions to include the PBE. In other words, we present a general form of the RM which holds true in the Hanle, Zeeman, and PB regimes.

PBE is of great interest to the stellar community as well as the solar community because it serves as an effective tool to diagnose vector magnetic fields. The emergent spectral line polarization depends sensitively on the magnetic field. PBE in molecules has proven to be a good diagnostic tool in recent years for magnetic field measurements. Since the FS in molecules is smaller than those for atoms, the PBE becomes operative for relatively lower field strengths in molecules. Attempts have been made to develop a theoretical framework for this problem and to identify and understand the signatures of this effect in the emergent line polarization (see, for example, Asensio Ramos & Trujillo Bueno, 2006;

Berdyugina et al., 2005, 2006a,b; Shapiro et al., 2006, 2007). An important step in doing a similar study with atoms is to set up the Hamiltonian in the right form and diagonalize it to obtain the energy eigenvalues and eigenvectors, which can be used later in the computations of the Stokes parameters. To this end, in our work concerned with PBE in atoms, we use the diagonalization code of Landi Degl'Innocenti (1978). This is a computer program written for the simultaneous diagonalization of the magnetic and hyperfine structure Hamiltonian. We modify this program suitably for the problem of our interest.

In Chapter 4, we derived the PRD matrix for PBE on hyperfine structure states of a two-level atom (see Sowmya et al., 2014c). Furthermore, we studied the characteristics of the RM in a single $90°$ scattering event. The same framework can also be developed for the case of PBE on fine structure states through the straightforward replacement of the quantum numbers which we discuss in Section 5.3. In Section 5.2, we set up the total Hamiltonian for PBE in a two-term atom. The Hamiltonian in this case has non-zero, non-diagonal elements which represent the mixing of the J states. We present the general form of the RM in terms of the irreducible spherical tensors, derived assuming the lower levels to be unpolarized and infinitely sharp, in Section 5.3. We discuss the results for the single scattering case in Section 5.4 considering the fine structure states of the lithium D_1 and D_2 lines as an example. In the solar case, the Li I 6708 Å doublet, which has the same fine structure configuration as the D_1 and D_2 lines of Na I and Ba II, but for which the FS is only 0.15 Å, serves as a good candidate for application of the theory developed in this chapter. Spectropolarimetric observations of this Li I doublet have been published in Stenflo (2011). The theoretical work on the same spectral line system has been presented by Belluzzi et al. (2009) in the limit of microturbulent fields and for the non-magnetic case. In Section 5.5 we give our concluding remarks.

5.2 The Total Hamiltonian

We consider a two-term atom described by the $L-S$ coupling scheme. Under the $L-S$ coupling approximation, the fine structure Hamiltonian (see Section 1.5.1) is given by

$$\mathcal{H}_{\rm fs} = \zeta(L_k S)\boldsymbol{L}_k \cdot \boldsymbol{S} \,, \tag{5.1}$$

where $\zeta(L_k S)$ has the dimensions of energy and is given by the "Landé-interval" rule as

$$\zeta(L_k S) = \frac{E(J_k) - E(J_k - 1)}{J_k} \,. \tag{5.2}$$

Here, $k = a$ (lower term) or b (upper term). The energy shift due to spin-orbit coupling can be obtained from Hund's rule (3) as

$$E_{L_kS}(J_k) = \frac{1}{2}\zeta(L_kS)[J_k(J_k+1) - L_k(L_k+1) - S(S+1)] \; . \tag{5.3}$$

If an external magnetic field is applied, then its interaction with the atomic system is described by the Hamiltonian

$$\mathcal{H}_B = \mu_0(\boldsymbol{L}_k + 2\boldsymbol{S}) \cdot \boldsymbol{B} \; . \tag{5.4}$$

If the applied magnetic field produces a splitting comparable to the FS, then the magnetic Hamiltonian can no longer be treated as a perturbation to the spin-orbit Hamiltonian, $\mathcal{H}_{\rm fs}$. In this case, the energy levels have to be found by diagonalizing the total Hamiltonian $\mathcal{H}$ given by

$$\mathcal{H} = \mathcal{H}_{\rm fs} + \mathcal{H}_B \; . \tag{5.5}$$

The quantization axis (z-axis) is taken to be along the applied magnetic field so that the total Hamiltonian can be diagonalized in the energy eigenvector basis $|L_kSJ_k\mu_k\rangle$. However, in the PB regime, the magnetic field produces a mixing of the J states belonging to a given term. Thus, the eigenvectors of the total Hamiltonian are of the form

$$|L_kSj_k\mu_k\rangle = \sum_{J_k} C^{j_k}_{J_k}(L_kS,\mu_k)|L_kSJ_k\mu_k\rangle \; , \tag{5.6}$$

where the symbol j_k labels the states spanned by the quantum numbers (L_k, S, μ_k) and $C^{j_k}_{J_k}(L_kS,\mu_k)$ are the expansion coefficients. In order to determine the PB regime eigenvectors $|L_kSj_k\mu_k\rangle$ and the corresponding eigenvalues, we have to diagonalize a set of matrices of the form

$$\langle L_kSJ_k\mu_k|\mathcal{H}_{\rm fs} + \mathcal{H}_B|L_kSJ_{k'}\mu_k\rangle \; . \tag{5.7}$$

The above expression indicates that a given μ_k can be assigned to both J_k and $J_{k'}$ as a result of level interference. Since the spin-orbit Hamiltonian is diagonal in J_k, we have

$$\langle L_kSJ_k\mu_k|\mathcal{H}_{\rm fs}|L_kSJ_k\mu_k\rangle = E_{L_kS}(J_k) \; , \tag{5.8}$$

where $E_{L_kS}(J_k)$ is given by Equation (5.3). The magnetic Hamiltonian can be written in the energy eigenvector basis as

$$\langle L_kSJ_k\mu_k|\mathcal{H}_B|L_kSJ_{k'}\mu_{k'}\rangle = \delta_{\mu_k\mu_{k'}}\mu_0 B\Bigg[\mu_k\delta_{J_kJ_{k'}} + (-1)^{J_k+J_{k'}+L_k+S+\mu_k}$$
$$\times\sqrt{(2J_k+1)(2J_{k'}+1)S(S+1)(2S+1)}\begin{pmatrix} J_k & J_{k'} & 1 \\ -\mu_k & \mu_k & 0\end{pmatrix}\begin{Bmatrix} J_k & J_{k'} & 1 \\ S & S & L_k\end{Bmatrix}\Bigg]. \quad (5.9)$$

The diagonalization of the total Hamiltonian gives the energy eigenvalues and the energy eigenvectors (see Landi Degl'Innocenti, 1978). For simplicity, we consider the PBE only in the upper term and neglect the crossing of magnetic substates belonging to different fine structure states in the lower term.

5.3 RM for PBE on Fine Structure States

The step we follow in deriving the RM are the same as those presented in Chapter 4 for the case of PBE in hyperfine structure states (see Sowmya et al., 2014c). The resulting RM for J-state interference in the presence of magnetic fields of arbitrary strengths can also be obtained from the corresponding RM for the F-state interference phenomenon in Equation (4.16) by the following quantum number replacement:

$$F \to J, \quad J \to L, \quad I_s \to S, \quad i \to j\,, \quad (5.10)$$

in Equation (4.16). Here, i and j label different states spanned by the quantum numbers (J, I_s, μ_F) and (L, S, μ_J) respectively. μ_F and μ_J are the projections of F and J onto the quantization axis. Thus, the RM for J-state interference in the presence of a magnetic field of arbitrary strength can be written as

$$\boldsymbol{R}^{\rm II}_{ij}(x,\boldsymbol{n},x',\boldsymbol{n}';\boldsymbol{B}) = \frac{3(2L_b+1)}{(2S+1)}\sum_{KK'Q}\sum_{j_a\mu_a j_f\mu_f j_b\mu_b j_{b'}\mu_{b'}}\sum_{J_aJ_{a'}J_fJ_{f'}J_bJ_{b'}J_{b''}J_{b'''}}$$
$$\times\sum_{qq'q''q'''}(-1)^{q-q'''+Q}\sqrt{(2K+1)(2K'+1)}\cos\beta_{j_{b'}\mu_{b'}j_b\mu_b}\mathrm{e}^{\mathrm{i}\beta_{j_{b'}\mu_{b'}j_b\mu_b}}$$
$$\times[(h^{\rm II}_{j_b\mu_b,j_{b'}\mu_{b'}})_{j_a\mu_aj_f\mu_f} + \mathrm{i}(f^{\rm II}_{j_b\mu_b,j_{b'}\mu_{b'}})_{j_a\mu_aj_f\mu_f}]C^{j_f}_{J_f}(L_aS,\mu_f)C^{j_a}_{J_a}(L_aS,\mu_a)C^{j_b}_{J_b}(L_bS,\mu_b)$$
$$\times C^{j_b}_{J_{b''}}(L_bS,\mu_b)C^{j_f}_{J_{f'}}(L_aS,\mu_f)C^{j_a}_{J_{a'}}(L_aS,\mu_a)C^{j_{b'}}_{J_{b'}}(L_bS,\mu_{b'})C^{j_{b'}}_{J_{b'''}}(L_bS,\mu_{b'})$$
$$\times\sqrt{(2J_a+1)(2J_{a'}+1)(2J_f+1)(2J_{f'}+1)(2J_b+1)(2J_{b'}+1)(2J_{b''}+1)(2J_{b'''}+1)}$$

$$\times \begin{pmatrix} J_b & J_f & 1 \\ -\mu_b & \mu_f & -q \end{pmatrix} \begin{pmatrix} J_{b'} & J_{f'} & 1 \\ -\mu_{b'} & \mu_f & -q' \end{pmatrix} \begin{pmatrix} J_{b''} & J_a & 1 \\ -\mu_b & \mu_a & -q'' \end{pmatrix} \begin{pmatrix} J_{b'''} & J_{a'} & 1 \\ -\mu_{b'} & \mu_a & -q''' \end{pmatrix}$$
$$\times \begin{pmatrix} 1 & 1 & K \\ q & -q' & -Q \end{pmatrix} \begin{pmatrix} 1 & 1 & K' \\ q''' & -q'' & Q \end{pmatrix} \begin{Bmatrix} L_a & L_b & 1 \\ J_b & J_f & S \end{Bmatrix} \begin{Bmatrix} L_a & L_b & 1 \\ J_{b'} & J_{f'} & S \end{Bmatrix}$$
$$\times \begin{Bmatrix} L_a & L_b & 1 \\ J_{b''} & J_a & S \end{Bmatrix} \begin{Bmatrix} L_a & L_b & 1 \\ J_{b'''} & J_{a'} & S \end{Bmatrix} (-1)^Q \mathcal{T}^K_{-Q}(i, \boldsymbol{n}) \mathcal{T}^{K'}_Q(j, \boldsymbol{n}') \, . \tag{5.11}$$

The assumptions underlying the derivation of Equation (5.11) are that the lower levels are unpolarized and infinitely sharp; see Chapter 4 for details on the terminology and the derivation.

5.4 Single Scattering Polarization with PBE

As an example to study PBE in the fine structure states, we consider the $L = 0$ and $L = 1$ terms of the two stable isotopes of neutral lithium, namely, ^{7}Li and ^{6}Li. The isotope shifts are measured with respect to the reference isotope ^{7}Li. In our calculations, we use the isotope shift values given in Table 1 of Belluzzi et al. (2009). The abundances for the two isotopes are also read from the same table. See Asplund et al. (2009) for more details on the calculation of abundances.The total electron spin is $S = 1/2$. The coupling between $\boldsymbol{L}$ and $\boldsymbol{S}$ results in $J = 3/2$ and $1/2$ for the $L = 1$ term and $J = 1/2$ for the $L = 0$ term. The transitions between these J states in the absence of magnetic fields results in the D_1 and D_2 lines (obeying the selection rules $\Delta S = 0$ and $\Delta J = 0, \pm 1$). The wavelengths of these transitions are listed in Table 5.1. In the presence of a magnetic field, the non-degenerate magnetic substates give rise to 10 allowed transitions (according to the selection rule $\Delta\mu = 0, \pm 1$) in each of the two isotopes. Among these 10 transitions, 6 are between the magnetic substates of the upper $J = 3/2$ and the lower $J = 1/2$ states and the rest are between those of the upper $J = 1/2$ and the lower $J = 1/2$ states. These transitions can be classified into three groups: $\sigma_{\rm r}$ ($\Delta\mu = -1$), π ($\Delta\mu = 0$), and $\sigma_{\rm b}$ ($\Delta\mu = +1$). Note that $\Delta\mu = \mu_b - \mu_a$, where μ_b are the magnetic substates of the upper J state and μ_a are the magnetic substates of the lower J state. The magnetic (π and σ) components of the D_1 lines will be denoted with a prime in the following discussions for the sake of clarity and distinction. As per this classification, the D_2 line gives rise to two $\sigma_{\rm r}$, two π, and two $\sigma_{\rm b}$ components while the D_1 line gives rise to one $\sigma'_{\rm r}$, two π', and one $\sigma'_{\rm b}$ components in each of the two isotopes. These are tabulated in Table 5.2. The magnetic components of the two isotopes will be distinguished by their mass numbers, indicated in the superscripts to the π and σ components. For the computation of the Stokes profiles presented in Figures 5.2–5.4,

we assume that an unpolarized radiation is incident on the atom at an angle $\cos\theta' = 1$ and is scattered in a direction $\cos\theta = 0$, where θ' and θ are the colatitudes. The values of the azimuths χ and χ' for scattered and incident rays, respectively, are assumed to be zero in this single $90°$ scattering event. The scattered ray thus obtained is given by the first column of the RM, which is then integrated over the incoming frequencies to obtain the singly scattered Stokes profiles. For the Li I D line system, the Stokes parameters are obtained by linearly combining the Stokes parameters computed for the individual isotopes weighted by their respective abundances. Such a linear superposition is allowed because the lines are optically thin. Following Belluzzi et al. (2009), we use a Doppler width of 60 mÅ for all of the components.

Isotope	Line	λ (Å)	A (s^{-1})
^{6}Li	D_1	6708.05534	3.689×10^7
^{6}Li	D_2	6707.90232	3.689×10^7
^{7}Li	D_1	6707.89719	3.689×10^7
^{7}Li	D_2	6707.74416	3.689×10^7

Table 5.1: Wavelengths and Einstein A coefficients for the D line transitions of neutral Li isotopes.

$J_a \diagdown J_b$		$1/2$	$1/2$	$3/2$	$3/2$	$3/2$	$3/2$
	$\mu_a \diagdown \mu_b$	$-1/2$	$+1/2$	$-3/2$	$-1/2$	$+1/2$	$+3/2$
$1/2$	$-1/2$	π'	$\sigma'_{\rm b}$	$\sigma_{\rm r}$	π	$\sigma_{\rm b}$	NA
$1/2$	$+1/2$	$\sigma'_{\rm r}$	π'	NA	$\sigma_{\rm r}$	π	$\sigma_{\rm b}$

Table 5.2: The list of transitions between the magnetic substates of the upper and the lower J states. NA: Not Allowed. In the discussions, the magnetic components of the two isotopes are distinguished by their atomic masses indicated in the superscripts.

5.4.1 The Diagonalization Procedure

The non-zero matrix elements of the total Hamiltonian defined in Equation (5.7) are of the form given by Equations (3.61a) and (3.61b) of Landi Degl'Innocenti & Landolfi (2004). Following Landi Degl'Innocenti (1978), we write a program to diagonalize the total Hamiltonian in Equation (5.5). The numerical diagonalization is performed using the Givens–Householder method. We obtain the eigenvalues in terms of the energy shifts from the parent L state and the eigenvectors in terms of the C coefficients. By making use of these energy shifts, we determine the energies of the $L_a = 0$ and $L_b = 1$ terms. Since J is not

a good quantum number in the PB regime, we cannot use either D_1 or D_2 wavelengths. For the atomic system we have considered, the line center wavelengths correspond to the transitions ${}^7L_a = 0 \rightarrow {}^7L_b = 1$ and ${}^6L_a = 0 \rightarrow {}^6L_b = 1$, which are, respectively, 6707.79517 Å and 6707.95333 Å.

In the presence of a magnetic field, the degeneracy of the magnetic substates is lifted and the spectral lines split into magnetic components. It is possible to obtain the magnetic shifts and strengths of these components by making use of the C coefficients and the energy eigenvalues. The normalized strengths of the transitions which connect the magnetic substates of the lower term (L_aS) with those of the upper term (L_bS) are given by

$$\begin{aligned}\mathcal{S}_q^{j_a\mu_a,j_b\mu_b} &= \alpha \sum_{J_a J_{a'} J_b J_{b'}} \frac{3}{2S+1} C^{j_a}_{J_a}(L_aS,\mu_a) C^{j_a}_{J_{a'}}(L_aS,\mu_a) \\ &\times C^{j_b}_{J_b}(L_bS,\mu_b) C^{j_b}_{J_{b'}}(L_bS,\mu_b) \sqrt{(2J_a+1)(2J_{a'}+1)(2J_b+1)(2J_{b'}+1)} \\ &\times \begin{pmatrix} J_b & J_a & 1 \\ -\mu_b & \mu_a & -q \end{pmatrix} \begin{pmatrix} J_{b'} & J_{a'} & 1 \\ -\mu_b & \mu_a & -q \end{pmatrix} \begin{Bmatrix} L_a & L_b & 1 \\ J_b & J_a & S \end{Bmatrix} \begin{Bmatrix} L_a & L_b & 1 \\ J_{b'} & J_{a'} & S \end{Bmatrix} . \quad (5.12)\end{aligned}$$

Here, α represents the percentage abundance of the isotope. The magnetic shifts are given by

$$\Delta^{j_a j_b}_{\mu_a \mu_b} = \frac{E_{j_b}(L_bS,\mu_b) - E_{j_a}(L_aS,\mu_a)}{h} + \delta E_{\rm iso} \, , \quad (5.13)$$

where E_j are the energy eigenvalues. h is the Planck constant. $\delta E_{\rm iso}$ is the isotope shift measured with respect to the reference isotope ^{7}Li. Note that $\delta E_{\rm iso}$ is zero for the reference isotope ^{7}Li. Δs are given in frequency units. Figure 5.1 shows the behavior of the energy eigenvalues of the magnetic substates belonging to upper J states as a function of the magnetic field strength B. As described in Landi Degl'Innocenti & Landolfi (2004), we define a parameter γ as

$$\gamma = \frac{\mu_0 B}{\zeta} \, , \quad (5.14)$$

which is the ratio of the magnetic energy to the fine structure energy. The energy eigenvalues diverge linearly with increasing magnetic field strength for $\gamma \ll 1$. This regime is called the linear Zeeman regime. For intermediate values of γ, nonlinearity sets in and the eigenvalues start to cross. This regime is called the incomplete PB regime. For $\gamma \gg 1$, the eigenvalues again vary linearly with B and this regime is called the complete PB regime. For the atomic system considered, we see two level-crossings. The values of γ and B for which these crossings occur are listed in Table 5.3.

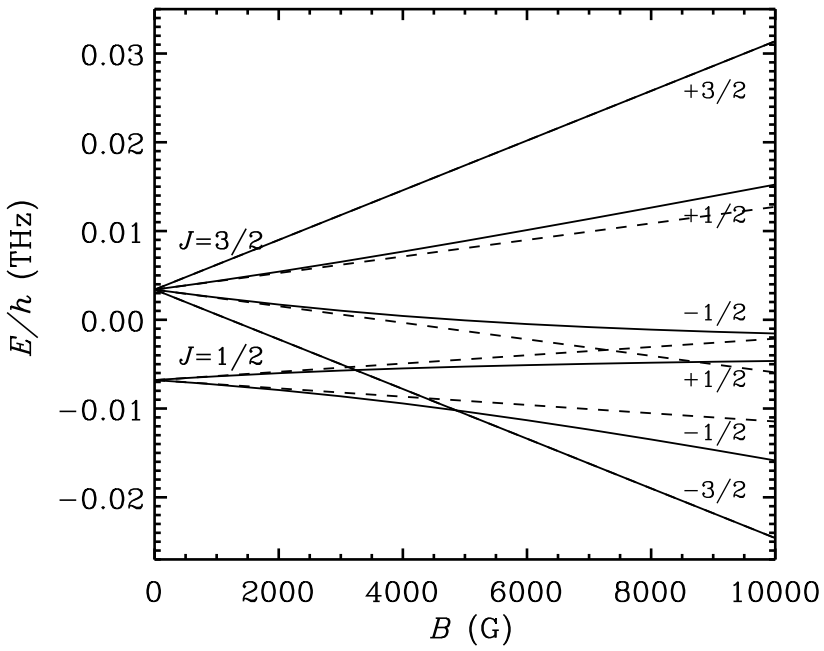

Figure 5.1: Level-crossings between the magnetic substates belonging to the $^2\mathrm{P}$ term of the ^{7}Li isotope in the presence of a magnetic field. A comparison between the splittings produced by including (solid lines) and neglecting (dashed lines) PBE. The $^2\mathrm{P}$ term of the ^{6}Li isotope gives a similar diagram except for the isotopic shift.

$\mu_{b'}$	μ_b	γ	B (G)
$-3/2$	$+1/2$	0.667	3238
$-3/2$	$-1/2$	1.0	4855

Table 5.3: The values of γ and approximate values of B at level-crossings for the $^2\mathrm{P}$ term of ^{7}Li for which the diagram shown in Figure 5.1 is made. The same table holds good for the $^2\mathrm{P}$ term of ^{6}Li.

The solid lines in Figure 5.1 are computed by taking into account the non-zero non-diagonal elements of the total Hamiltonian, while the dashed lines are computed by neglecting them (see Equation (3.61b) of Landi Degl'Innocenti & Landolfi, 2004). This means that for the dashed lines, the splitting produced by the magnetic field is simply given by the expression $\mu_0 B \mathrm{g}_{J_b} \mu_b$ (where g_{J_b} is the Landé factor). From this diagram, we can clearly see the differences that PBE makes to the energy eigenvalues. The substates with $\mu_b = +3/2$ and $-3/2$ show the same behavior irrespective of whether or not PBE is included. This is because the contribution from the non-diagonal elements for these μ_bs are zero, as these μ_bs can be assigned to only $J_b = 3/2$ state. For the other magnetic substates, the splitting becomes nonlinear because of the contribution from the non-diagonal elements to the total splitting caused by the magnetic field. In particular, we note that the magnetic substates

which cross in the case of Zeeman effect avoid crossing one another in the case of PBE. For example, the $\mu_{b'} = +1/2$ belonging to $J_{b'} = 1/2$ and $\mu_b = -1/2$ belonging to $J_b = 3/2$ cross at $B \sim 7300\,\mathrm{G}$ when MS is computed using the Zeeman effect. On the other hand, when PBE is included to compute MS, these substates do not cross. This is known as avoided crossing (also known as anti-level-crossing). Consequently, we find that the polarization in the asymptotic limit of $B \to \infty$ is larger than that when $B \to 0$; see Bommier (1980) and Landi Degl'Innocenti & Landolfi (2004) for more details on this effect.

5.4.2 Comparison of the Stokes Profiles

In the linear Zeeman regime, the RM presented in Section 5.3 reduces to Equation (25) of Smitha et al. (2011b). In order to show the effects of level-crossing, we compare the results of our code which programs Equation (5.11, hereafter referred to as PB-FS code) with the results of Smitha et al. (2011b, hereafter referred to as the Zeeman-FS code). This comparison is shown in Figures 5.2 and 5.3. The Stokes profiles from the two codes match very well up to $500\,\mathrm{G}$ for which $\gamma = 0.1029$. According to the classification scheme discussed in the previous section, we are still in the linear Zeeman regime for this field strength. For field strengths greater than $500\,\mathrm{G}$, the differences start to appear as we already enter the nonlinear regime in which the linear Zeeman approximation (Zeeman-FS code) breaks down. The separation between the magnetic components (which increases with an increase in B) is no longer given by $\mu_0 B \mathrm{g}_{J_b} \mu_b$. Hence, there is a difference in the line center positions of the magnetic components computed from the two codes. These small differences can clearly be seen in intensity (I) profiles (see right panels of Figure 5.2). For level-crossing field strengths ($3238\,\mathrm{G}$ and $4855\,\mathrm{G}$), the Stokes profiles computed from the Zeeman-FS and PB-FS codes differ drastically. The Zeeman-FS code therefore does not cover all the field strength ranges that we can expect on the Sun.

5.4.3 Stokes Profiles in the PB Regime

By making use of the strengths and shifts of the PB components obtained from the diagonalization code, we have made line splitting diagrams where the logarithm of the PB component strengths ($\mathcal{S}$) given in Equation (5.12) are plotted against their wavelength shifts from the line center computed using Equation (5.13). These are shown in Figures 5.2 and 5.3 along with the Stokes profiles for different values of B. The zero on the x-axis of the line splitting diagram corresponds to the line center wavelength of the $L = 0 \to 1$ transition in ^{7}Li.

For $B = 500\,\mathrm{G}$ (linear regime), the magnetic components are separated into two

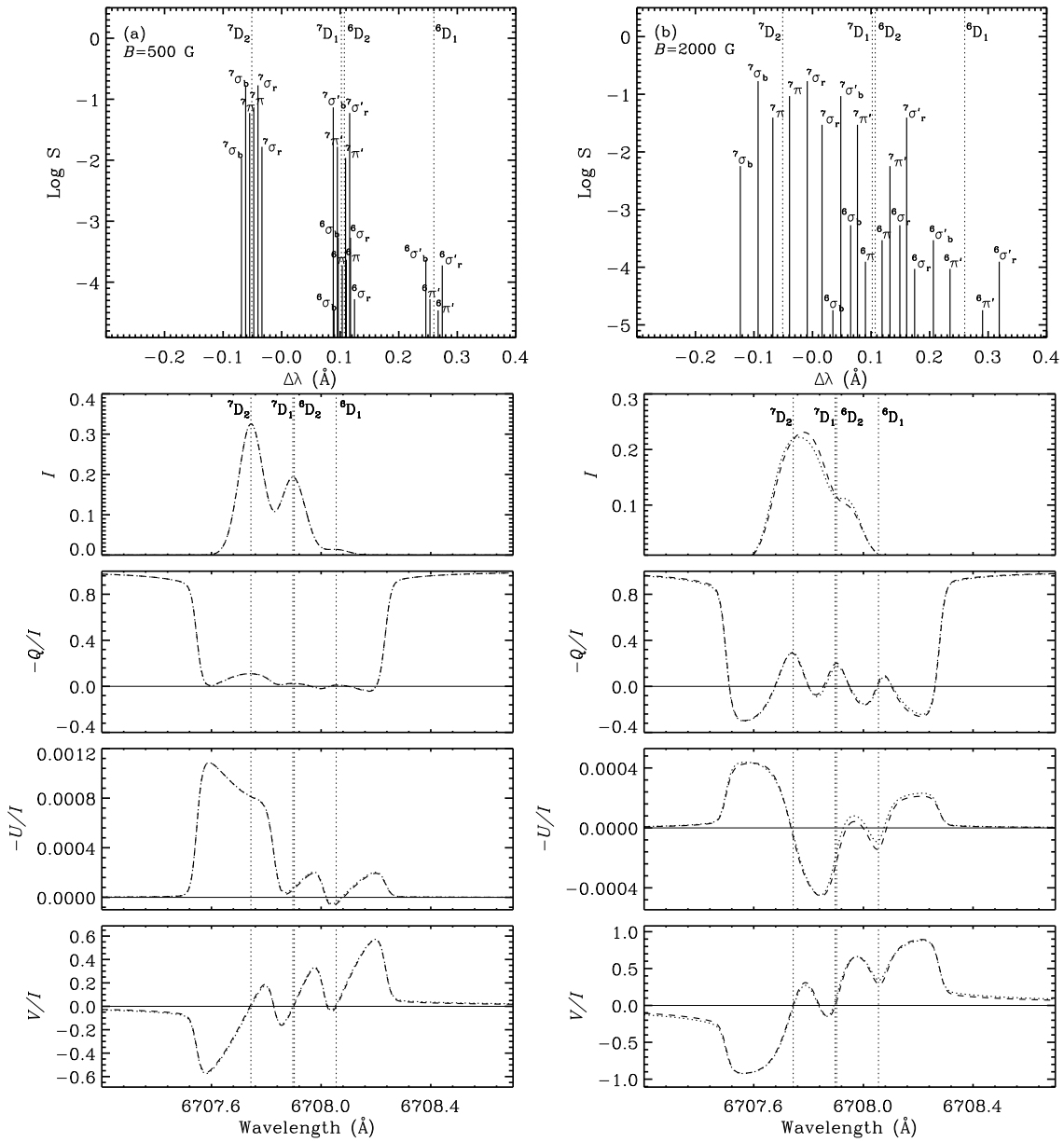

Figure 5.2: Top panels refer to the line splitting diagrams (line strength $\mathcal{S}$ vs. wavelength shift). The other panels show the comparison of the Stokes profiles computed using the PB-FS code (dashed lines) with the Zeeman-FS code (dotted lines). The two columns correspond to different field strengths, as indicated in the line splitting diagrams. The vertical dotted lines indicate the positions of the ^{7}Li and ^{6}Li D lines. The orientation of the magnetic field is given by $(\theta_B, \phi_B) = (90°, 45°)$.

bunches of six and four each in both isotopes. The magnetic components of the $^7D_1$ and $^6D_2$ lines are superposed due to their proximity in wavelength. The splitting is more or less symmetric about the line centers of the D_1 and D_2 lines, but the strengths of the components

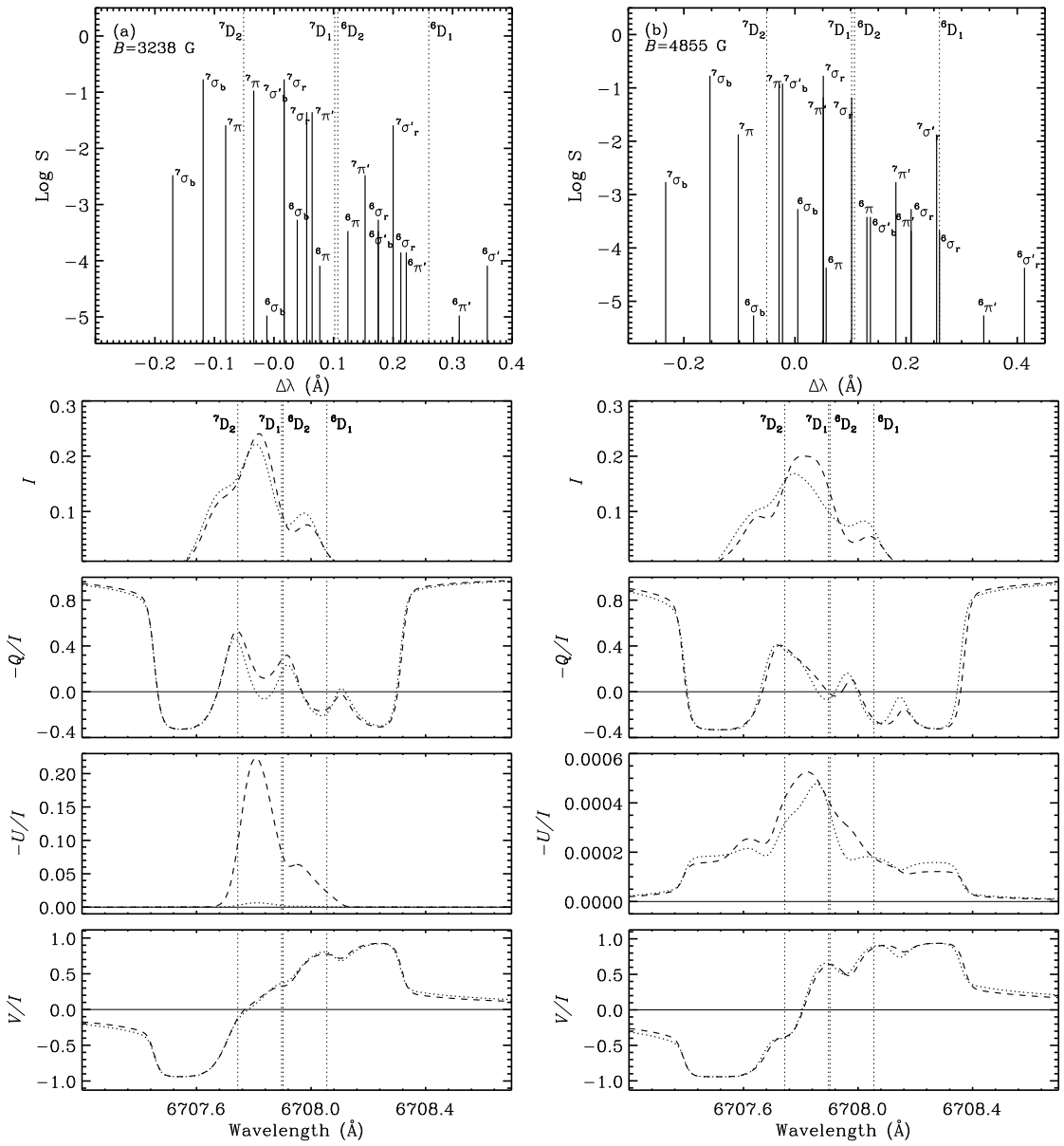

Figure 5.3: Same as Figure 5.2, except for field strengths.

vary depending on the values of the magnetic quantum numbers μ_a and μ_b (see the left top panel of Figure 5.2). The same is reflected in the intensity profiles. The three observed peaks in intensity correspond to the three bunches of magnetic components with the amplitudes of the peaks being proportional to the relative abundances of the two isotopes. The Q/I and U/I profiles show typical signatures of the Hanle effect, especially at the position of the ^{7}D$_2$ line, namely, a depolarization of the Q/I with respect to the non-magnetic value (0.428 in the line core) and a generation of the U/I signal. The ^{7}D$_1$ and ^{6}D$_1$ lines are non-polarizing, and hence are unaffected by Hanle effect. The ^{6}D$_2$ line, although affected by

Hanle effect, produces insignificant signatures due to its small abundance. In spite of these, we see U/I peaks at the positions corresponding to (^{7}D$_1$,^{6}D$_2$) and ^{6}D$_1$, the origin of which is not clear. They may be due to the interference between the D lines. Note, however, that these U/I signatures are about three orders of magnitude smaller than the corresponding Q/I signatures, and are therefore much too weak to be observable. The V/I arises due to the longitudinal component of the magnetic field.

For $B = 2000\,\mathrm{G}$ (see panels (b) of Figure 5.2), the components are well separated and their strengths change because of the dependence on the C coefficients, which vary with B. The components cannot be resolved in intensity as their Doppler width is larger than the separation between them. The decrease in intensity is due to an increased separation between the magnetic components with increasing magnetic field strength. In Q/I, a three-lobed Zeeman-like pattern is seen; U/I is very small because of the geometry. The V/I profiles become broader, as expected. The σ_b components show the opposite behavior to those of σ_r, again as expected. Positive peaks appear at the positions of the σ_r components while negative peaks occur at the positions corresponding to σ_b.

For $B = 3238\,\mathrm{G}$ (see panels (a) of Figure 5.3), at which the first level-crossing occurs, we see the interference between the σ_r and σ'_b components in the two isotopes. Their positions overlap, as can be seen from the line splitting diagram. Interestingly, at these positions, we see a generation of U/I signal due to interference between the magnetic substates (Hanle effect). The V/I signals of the D lines overlap giving rise to a broader profile.

For $B = 4855\,\mathrm{G}$ (see panels (b) of Figure 5.3), where the second level-crossing occurs, there is interference between the σ_r and π' components in the two isotopes. The U/I signal is generated due to the Hanle effect.

In Figure 5.4, we show the Stokes profiles obtained from the PB-FS code in the presence of a weakly polarized background continuum. The contribution from the continuum is included in the same way as in Stenflo (1998). For the sake of clarity, we recall his Equations (58) and (61):

$$I'/I'_c = 1 - \beta + \frac{a}{I+a}\beta\,, \tag{5.15}$$

$$p' = \frac{I}{I+a}p + \frac{a}{I+a}b\,. \tag{5.16}$$

In the above equations, I and p are the intensity and fractional polarization given by $-Q/I, -U/I$, and V/I in the absence of the continuum. The corresponding quantities

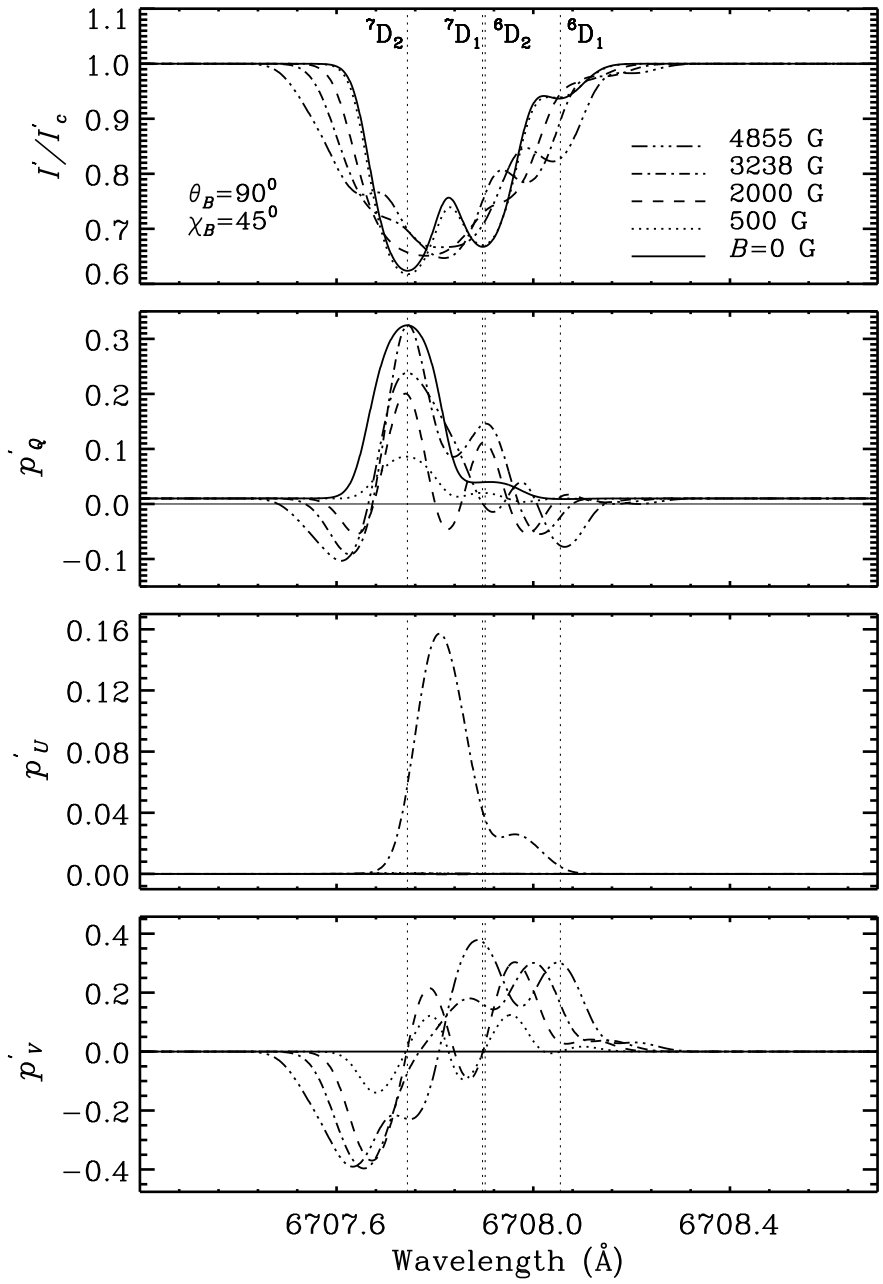

Figure 5.4: Stokes profiles computed using PB-FS code by including the contribution from the polarized continuum. The line types and the orientation of the magnetic field are indicated in the intensity panel. The vertical dotted lines correspond to the line center wavelengths of the Li I D lines; see text for more details.

in the presence of the continuum are I' and p'. The limb darkening parameter, β, and the continuum strength parameter, a, are chosen as 0.5 and 0.1, respectively. Such a large value of a is chosen to make the Stokes profiles closely resemble the profiles presented for the non-magnetic case in Belluzzi et al. (2009). The continuum polarization parameter, b, is

chosen to be 0.01 for Q and 0 for U and V. With this choice, we obtain profile shapes of the kind that we expect in the Sun's spectrum. In particular, our non-magnetic $p'_Q(= -Q'/I')$ profile (solid line) resembles the shape of the corresponding profile observed with ZIMPOL (Stenflo, 2011). The intensity profiles appear as broad absorption lines. The fractional linear polarization p'_Q approaches the continuum polarization value ($b = 0.01$) away from the line center. The $p'_U(= -U'/I')$ and $p'_V(= V'/I')$ profiles retain their overall shape compared to the pure line case without continuum, although their amplitudes decrease because of the contribution from the continuum strength parameter a to I'. As can be seen from the figure, the shape of the p'_Q profile for the zero field case (solid line) compares well with the corresponding profiles presented in Belluzzi et al. (2009). Note that since the Stokes profiles are computed here for a single scattering event, only the shape and not the amplitude is comparable to the corresponding profiles presented by Belluzzi et al. (2009).

5.4.4 Polarization Diagrams

The geometry considered for the results presented in this section is shown in Figure 4.2. Polarization diagrams are shown for the line center wavelengths of the Li I D lines in Figure 5.5. For the geometry considered, only the level-crossings with $|\Delta\mu = \mu_{b'} - \mu_b| = 2$ are effective. Therefore, in the following, we will only see the effects due to the first level-crossing at $3238\,\mathrm{G}$.

At the $^7\mathrm{D}_2$ line center ($\lambda = 6707.74416\,\text{Å}$), we see a decrease in Q/I up to a few hundred gauss (Hanle regime) with an initial increase followed by a decrease in U/I (see Figure 5.5(a)). This is due to the Hanle effect which operates in the line core. As we approach the level-crossing field strength ($B = 3238\,\mathrm{G}$), we see an increase in the value of Q/I and the formation of a loop. Indeed, the level-crossing occurs over a narrow range of field strengths around $3238\,\mathrm{G}$. Within this narrow range, if the field strength is varied by organizing a fine grid, we get a strong variation in Q/I and U/I, producing the polarization diagram shown in Figure 5.5(a). This behavior is generic to all of the polarization diagrams shown in Figure 5.5. Further discussion on the formation of loops around the level-crossing field strengths can be found in Landi Degl'Innocenti & Landolfi (2004). Basically, at the level-crossing field strengths, the coherence between the overlapping magnetic substates increases, resulting in the scattered Q/I tending toward the non-magnetic value. U/I becomes zero for fields having a strength of a few thousand gauss because of the geometry considered. For fields stronger than $10000\,\mathrm{G}$ (see Figure 5.5(b)), Q/I arises due to Rayleigh scattering in strong magnetic fields, as discussed by Bommier (1997b, Section 6, Figure 14). The author states that in this case, for the geometry considered (magnetic

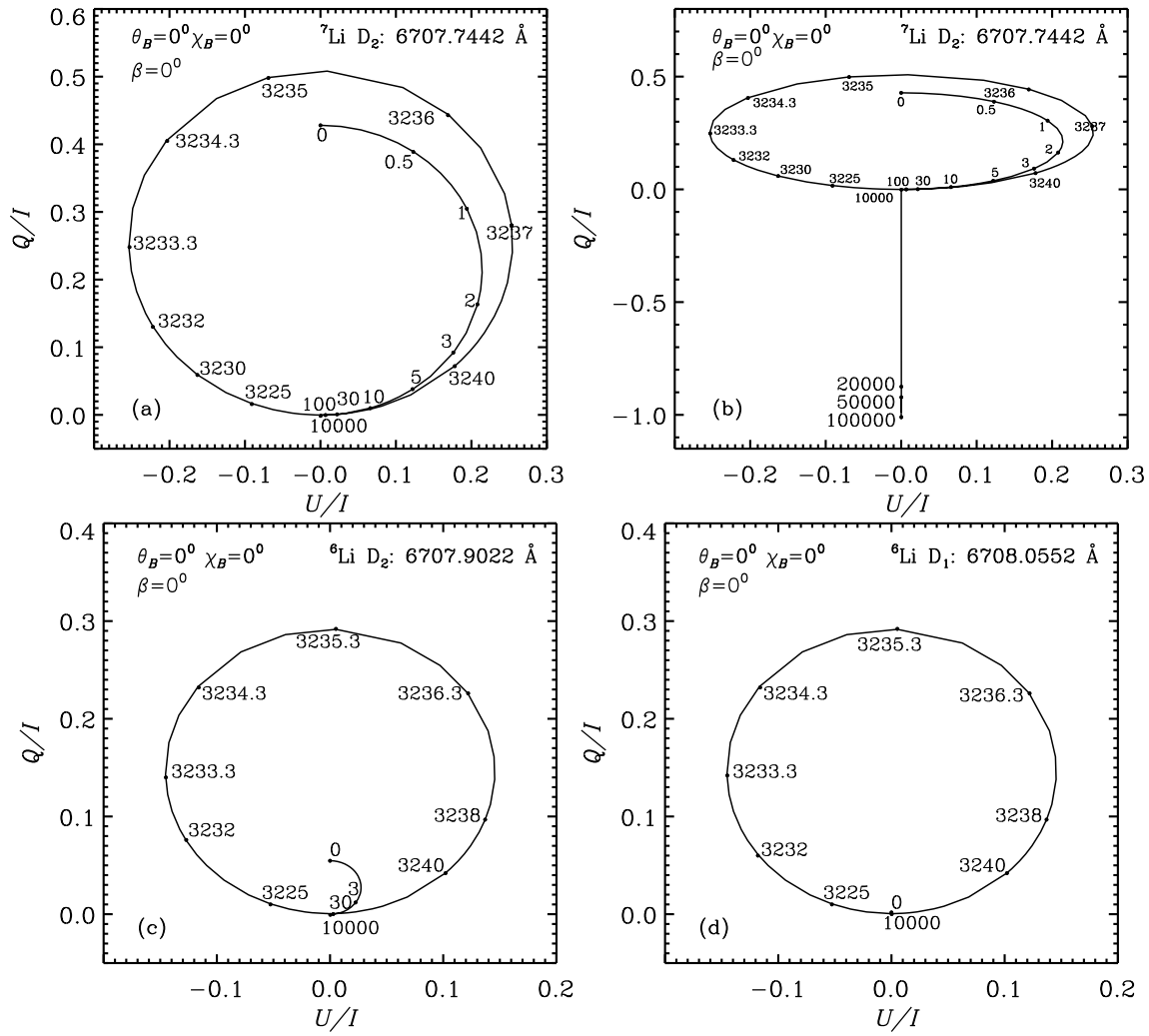

Figure 5.5: Polarization diagrams computed using the PB-FS code at the line center wavelengths of the ^{7}Li and ^{6}Li D lines. The curves are marked by the values of the magnetic field strength B in G.

field along the line of sight) and for a $90°$ scattering, only the σ components are scattered if the atomic system considered is a normal Zeeman triplet ($J = 0 \rightarrow 1 \rightarrow 0$). Incidentally, we note the same behavior in the case of $L = 0 \rightarrow 1 \rightarrow 0$ transition (which is not a normal Zeeman triplet). It is interesting to note that the π components are not scattered in this case also. The Q/I changes sign and increases for fields up to 100000 G.

At the ^{6}D$_2$ line center ($\lambda = 6707.90232$ Å; see Figure 5.5(c)), the Q/I for zero magnetic field case is approximately 10 times smaller than the Q/I at the ^{7}D$_2$ line center. This is due to the relatively small abundance of ^{6}Li. Due to an increased separation between the magnetic components with the field strength, the Q/I value decreases. As in the case of ^{7}D$_2$, we note the formation of a loop near the level-crossing field strength. When the

field strength is increased beyond $10000\,\mathrm{G}$, we again note Rayleigh scattering in the strong magnetic fields (not shown in the figure).

The $^6\mathrm{D}_1$ line ($\lambda = 6708.05534\,\text{Å}$; see Figure 5.5(d)) is intrinsically unpolarizable as it has $W_2 = 0$. Therefore, the polarization remains zero until the level-crossing field strength ($B = 3238\,\mathrm{G}$) is reached. A further increase in the field strength results in the formation of a loop and Rayleigh scattering as already described for the $^7\mathrm{D}_2$ and $^6\mathrm{D}_2$ line center positions.

5.5 Conclusions

Landi Degl'Innocenti & Landolfi (2004) developed the theory of Hanle effect in a two-term atom assuming a flat-spectrum for the incident unpolarized radiation using the density matrix formalism. Though this theory is applicable to the entire range of magnetic fields, it does not take into account the effects of PRD. Smitha et al. (2011b) included the effects of PRD by taking the RM approach, but their treatment was limited to the linear Zeeman regime. In this chapter, we have generalized the approach of Smitha et al. (2011b) for magnetic fields of arbitrary strengths to include the PB regime. However, our treatment ignores the effects of collisions. Furthermore, the lower term is assumed to be unpolarized. The frequency dependence of the incident radiation field is taken into account in our theory which is essentially a relaxation of the flat-spectrum approximation of Landi Degl'Innocenti & Landolfi (2004). This enables us to properly calculate the scattered Stokes profile shapes, which was otherwise not possible with the theory presented in Landi Degl'Innocenti & Landolfi (2004).

An example where the present theory has observable effects on the Sun is for the lithium $6708\,\text{Å}$ doublet. Since the FS in this line system is small ($0.15\,\text{Å}$), PBE in scattering polarization becomes prominent for magnetic fields which occur on the Sun (in sunspots, see Maltby, 1971). We have therefore tested our theory by applying it to this lithium doublet and demonstrated the correctness of the formalism by reproducing available benchmarks. We have explored the properties of the RM for the single scattering case, and clarified the effects of Rayleigh scattering in strong fields when the magnetic field is along the line of sight. This has given us an overview of the behavior of the polarization effects that can occur as a result of PRD in the PB regime.

6

PBE IN A TWO-TERM ATOM WITH HYPERFINE STRUCTURE

This chapter is based on:
Sowmya, K., Nagendra, K. N., Sampoorna, M., & Stenflo J. O. 2015, ApJ, 814, 127

Outline

We studied the F-state interference process in Chapter 4 and showed how this formalism can be used to study the J-state interference process in Chapter 5. In this chapter, we study the combined effects of J- and F-state interference processes. It is now established that the interference between magnetic substates of the hyperfine structure states belonging to different fine structure states of the same term influences the polarization for some of the diagnostically important lines of the Sun's spectrum, like the sodium and lithium doublets. The polarization signatures of this combined interference contain information on the properties of the solar magnetic fields. Motivated by this, in this chapter, we study the problem of polarized scattering on a two-term atom with hyperfine structure (Section 1.4.3) by accounting for the partial redistribution in the photon frequencies arising due to the Doppler motions of the atoms. We consider the scattering atoms to be under the influence of a magnetic field of arbitrary strength and develop a formalism based on the Kramers–Heisenberg approach to calculate the scattering cross section for this process. We explore the rich polarization effects that arise from various level-crossings in the PB regime in a single scattering case using the lithium atomic system as a concrete example that is relevant to the Sun.

6.1 Introduction

In this chapter, we address the problem of quantum interference between the magnetic substates of the F states pertaining to different J states of a given term, in the presence of magnetic fields of arbitrary strength covering the Hanle, Zeeman, and PB effect regimes. We will refer to this as "combined interference" or the "$F + J$-state interference". We develop the necessary theory including the effects of PRD in the absence of collisions, assuming the lower levels to be unpolarized and infinitely sharp. We refer to this theory as the "combined theory".

We consider a two-term atom with hyperfine structure under the assumption that the lower term is unpolarized. In the absence of a magnetic field, the atomic transitions in a two-term atom take place between the degenerate magnetic substates belonging to the F states. An applied magnetic field lifts the degeneracies and modifies the energies of these magnetic substates. The amount of splitting (or the energy change) produced by the magnetic field defines the regimes in which Zeeman and PB effects act. Depending on the relative magnitudes of the FS, HFS, and MS, we characterize the magnetic field strength into five regimes. These regimes are illustrated schematically in Figure 6.1. In the approach presented in this chapter, we account for the interference between the magnetic substates pertaining to the same F state, the magnetic substates belonging to different F states of the same J state, and the magnetic substates belonging to different F states pertaining to different J states. Although all three types of interference are always present, depending on the field strength one or two of them would dominate as depicted in the different panels of Figure 6.1.

Casini & Manso Sainz (2005) formulated a theory, within the framework of the non-relativistic quantum electrodynamics, for polarized scattering on a multi-term atom with hyperfine structure in the presence of an arbitrary strength magnetic field under the approximation of CRD. In this chapter, we restrict our treatment to a two-term atom with hyperfine structure and consider the limit of coherent scattering in the atomic frame with Doppler frequency redistribution in the observer's frame. We base our formalism on the Kramers–Heisenberg coherency matrix approach of Stenflo (1994). In our combined theory, we do not account for the coherences among the states in the lower term. In a recent paper, Stenflo (2015b) indicated how they may be included by extending the coherency matrix approach to the multi-level case.

Based on the concept of "metalevels", Landi Degl'Innocenti et al. (1997) formulated a theory that is able to treat coherent scattering in the atomic rest frame for a two-term atom with hyperfine structure. Recently, Casini et al. (2014) presented a generalized frequency

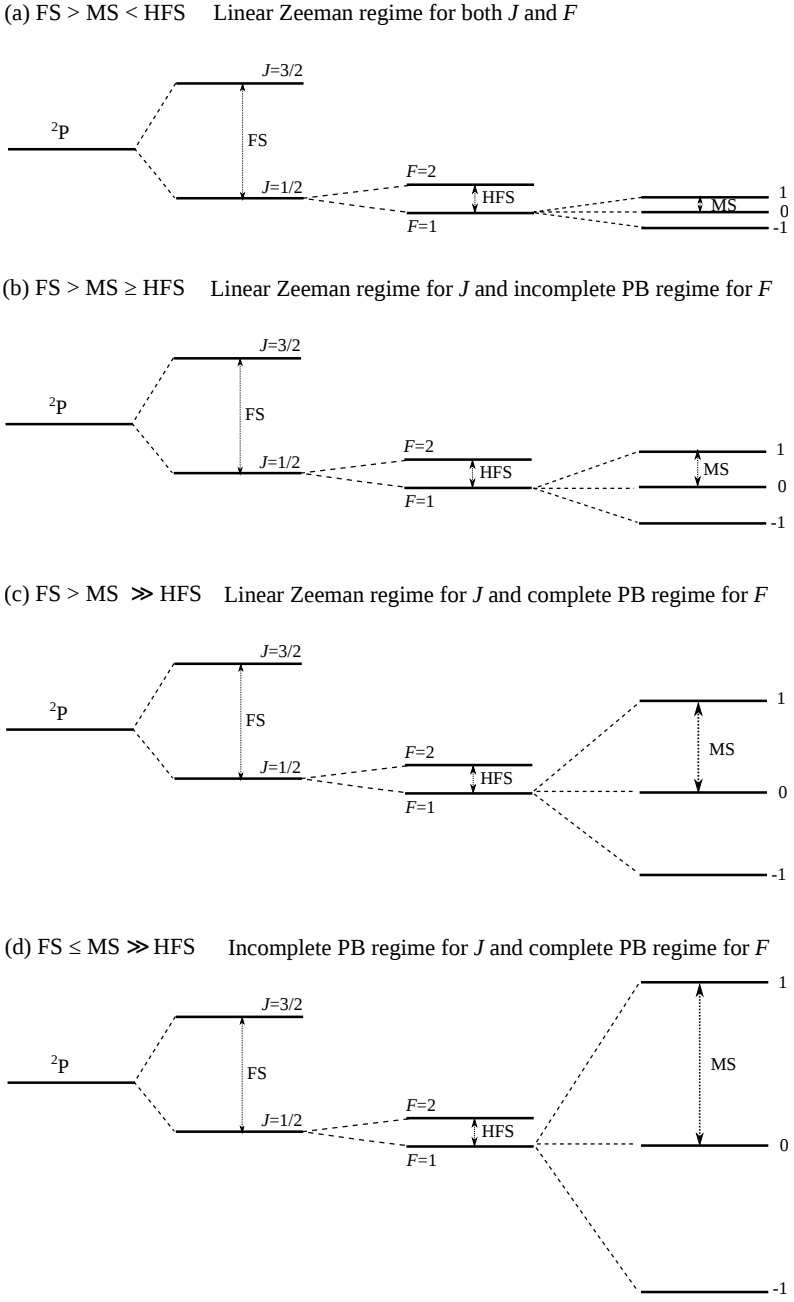

Figure 6.1: Illustration of the magnetic field strength regimes in the combined theory. For illustration purpose, a ^{2}P term with nuclear spin $3/2$ is considered. The various splittings indicated are not to scale. Panels (a)–(d) show the first four regimes of the field strength. When MS is much greater than FS, we have a complete PB regime for both J and F, which we call the fifth regime (not illustrated in the figure).

redistribution function for the polarized two-term atom in arbitrary fields, based on a new formulation of the quantum scattering theory. Our approach is an alternative approach to

the same problem and is conceptually more transparent, although limited to infinitely sharp and unpolarized lower levels.

Belluzzi et al. (2009) studied the linear polarization produced due to scattering on the D lines of neutral lithium isotopes. They employed the density matrix formalism presented in Landi Degl'Innocenti & Landolfi (2004), together with the approximation of CRD, to treat the quantum interference between the fine and hyperfine structure states. They restricted their study to the non-magnetic case. However, they explored the sensitivity of the Stokes profiles to the microturbulent magnetic fields. For our study, we consider the same D lines of lithium isotopes and present in detail the effects of a deterministic magnetic field of arbitrary strength. For this atomic line system, the PB effect in both the fine and the hyperfine structure states occurs for the magnetic field strengths encountered on the Sun. We restrict our treatment to the single scattering case, since our aim here is to explore the basic physical effects of the combined theory.

6.2 The Atomic Model

In this section, we describe the structure of the model atom considered for our studies and its interaction with an external magnetic field. We consider a two-term atom, each state of which is designated by the quantum numbers L, S, J, I_s, F, and μ (projection of F onto the quantization axis).

6.2.1 The Atomic Hamiltonian

Under the $L-S$ coupling scheme, the atomic Hamiltonian for a two-term atom with hyperfine structure is given by

$$\mathcal{H}_A = \zeta(LS)\boldsymbol{L}\cdot\boldsymbol{S} + \mathcal{A}_J\boldsymbol{I}_s\cdot\boldsymbol{J} + \frac{\mathcal{B}_J}{2I_s(2I_s-1)J(2J-1)} \times\left\{3(\boldsymbol{I}_s\cdot\boldsymbol{J})^2+\frac{3}{2}(\boldsymbol{I}_s\cdot\boldsymbol{J})-I_s(I_s+1)J(J+1)\right\}. \tag{6.1}$$

The first term in the above equation is a measure of the FS while the second and the third terms provide a measure of the HFS (see Sections 1.5.1 and 1.5.2). The eigenvalues of the atomic Hamiltonian represent the energies of the F states, calculated with respect to the energy of the corresponding term.

6.2.2 The Magnetic and the Total Hamiltonians

An external magnetic field lifts the degeneracies of the magnetic substates of the F states and changes their energies by an amount given by the eigenvalues of the magnetic Hamiltonian

$$\mathcal{H}_B = \mu_0(\boldsymbol{J} + \boldsymbol{S}) \cdot \boldsymbol{B} \,. \tag{6.2}$$

Assuming the quantization axis to be along the magnetic field (z-axis of the reference system), the matrix elements of the total Hamiltonian, $\mathcal{H}_T = \mathcal{H}_A + \mathcal{H}_B$, can be written as

$$\begin{aligned}
&\langle LSJI_sF\mu|\mathcal{H}_T|LSJ'I_sF'\mu\rangle = \delta_{JJ'}\delta_{FF'}\left[\frac{1}{2}\zeta(LS)\{J(J+1) - L(L+1) - S(S+1)\}\right.\\
&\left.+\frac{1}{2}\mathcal{A}_J\mathcal{K} + \frac{\mathcal{B}_J}{8I_s(2I_s-1)J(2J-1)}\{3\mathcal{K}(\mathcal{K}+1) - 4J(J+1)I_s(I_s+1)\}\right]\\
&+\mu_0 B(-1)^{L+S+J+J'+I_s-\mu+1}\sqrt{(2J+1)(2J'+1)(2F+1)(2F'+1)}\\
&\times\begin{pmatrix} F & F' & 1\\ -\mu & \mu & 0\end{pmatrix}\begin{Bmatrix} J & J' & 1\\ F' & F & I_s\end{Bmatrix}\left[\delta_{JJ'}(-1)^{L+S+J+1}\frac{\sqrt{J(J+1)}}{\sqrt{2J+1}}\right.\\
&\left.+(-1)^{J-J'}\sqrt{S(S+1)(2S+1)}\begin{Bmatrix} J & J' & 1\\ S & S & L\end{Bmatrix}\right],
\end{aligned} \tag{6.3}$$

where $\mathcal{K} = F(F+1) - I_s(I_s+1) - J(J+1)$. The total Hamiltonian matrix in the combined theory is no longer a symmetric tridiagonal matrix, unlike the case of the PB effect in fine or hyperfine structure states. Instead, it is a full symmetric matrix and we diagonalize it using the Givens–Householder method described in Ortega (1968). We test the diagonalization code written for the problem at hand using the principle of spectroscopic stability (PSS) presented in Appendix C.

6.2.3 Eigenvalues and Eigenvectors

The diagonalization of the total Hamiltonian gives the energy eigenvectors in terms of the linear Zeeman effect regime basis $|LSJI_sF\mu\rangle$ through the expansion coefficients C^k_{JF} as

$$|LSI_s, k\mu\rangle = \sum_{JF} C^k_{JF}(LSI_s, \mu)\,|LSJI_sF\mu\rangle \,. \tag{6.4}$$

The symbol k labels different states corresponding to the given values of (L, S, I_s, μ) and its dimension is given by

$$N_k = \sum_{d=|L-S|}^{L+S} 1 + d + I_s - \max(|\mu|, |d - I_s|) \; . \tag{6.5}$$

We assume the C coefficients appearing in Equation (6.4) to be real because the total Hamiltonian is real. We obtain the C coefficients and the corresponding eigenvalues denoted here as $E_k(LSI_s, \mu)$ after diagonalizing the atomic and magnetic Hamiltonians presented in Sections 6.2.1 and 6.2.2.

6.3 RM for the Combined Theory

The methodology followed to derive the RM for the $F+J$-state interference in the presence of a magnetic field is similar to that presented in Chapter 4 for F-state interference alone. For the sake of clarity, we only present the important equations involved in the derivation.

Using Equation (6.4) for the states $|a\rangle, |b\rangle$, and $|f\rangle$ in the Kramers–Heisenberg formula given by Equation (4.7), and noting that $L_f = L_a$ and using the Wigner–Eckart theorem (refer to Equations (2.96) and (2.108) of Landi Degl'Innocenti & Landolfi, 2004), we arrive at

$$\begin{aligned}
w_{\alpha\beta} \sim\; & (2L_a+1) \sum_{k_b \mu_b} \sum_{J_a J_f J_b J_{b''} F_a F_f F_b F_{b''}} \sum_{q q''} (-1)^{q-q''} (-1)^{J_f + J_a + J_b + J_{b''}} \\
& \times C^{k_f}_{J_f F_f}(L_a S I_s, \mu_f) C^{k_a}_{J_a F_a}(L_a S I_s, \mu_a) C^{k_b}_{J_b F_b}(L_b S I_s, \mu_b) C^{k_b}_{J_{b''} F_{b''}}(L_b S I_s, \mu_b) \\
& \times \sqrt{(2F_a+1)(2F_f+1)(2F_b+1)(2F_{b''}+1)(2J_a+1)(2J_f+1)(2J_b+1)(2J_{b''}+1)} \\
& \times \begin{pmatrix} F_b & F_f & 1 \\ -\mu_b & \mu_f & -q \end{pmatrix} \begin{pmatrix} F_{b''} & F_a & 1 \\ -\mu_b & \mu_a & -q'' \end{pmatrix} \begin{Bmatrix} J_f & J_b & 1 \\ F_b & F_f & I_s \end{Bmatrix} \begin{Bmatrix} J_a & J_{b''} & 1 \\ F_{b''} & F_a & I_s \end{Bmatrix} \\
& \times \begin{Bmatrix} L_a & L_b & 1 \\ J_b & J_f & S \end{Bmatrix} \begin{Bmatrix} L_a & L_b & 1 \\ J_{b''} & J_a & S \end{Bmatrix} \varepsilon^{\alpha^*}_{q} \varepsilon^{\beta}_{q''} \; \Phi_\gamma(\nu_{k_b \mu_b k_f \mu_f} - \xi) \; .
\end{aligned} \tag{6.6}$$

Here, ε are the spherical vector components of the polarization unit vectors ($\mathbf{e}_\alpha$ and $\mathbf{e}_\beta$) with α and β referring to the scattered and incident rays, respectively. $\Phi_\gamma(\nu_{k_b \mu_b k_f \mu_f} - \xi)$ is the frequency-normalized profile function defined as

$$\Phi_\gamma(\nu_{k_b \mu_b k_f \mu_f} - \xi) = \frac{1/\pi \mathrm{i}}{\nu_{k_b \mu_b k_f \mu_f} - \xi - \mathrm{i}\gamma/4\pi} \; , \tag{6.7}$$

where we have used an abbreviation

$$\nu_{k_b\mu_b k_f\mu_f} = \nu_{L_bSI_sk_b\mu_b,L_aSI_sk_f\mu_f} = \nu_{L_bL_a} + \frac{E_{k_b}(L_bSI_s,\mu_b) - E_{k_f}(L_aSI_s,\mu_f)}{h}\,, \tag{6.8}$$

with h being the Planck constant.

Inserting Equation (6.6) into the expression for the coherency matrix given in Equation (4.8), and after elaborate algebra (see for example Sowmya et al., 2014c), we obtain the normalized RM, $\boldsymbol{R}^{\rm II}_{ij}$, for type II scattering in the laboratory frame as

$$\begin{aligned}
&\boldsymbol{R}^{\rm II}_{ij}(x,\boldsymbol{n},x',\boldsymbol{n}';\boldsymbol{B}) = \frac{3(2L_b+1)}{(2S+1)(2I_s+1)}\sum_{KK'Q}\sum_{k_a\mu_a k_f\mu_f k_b\mu_b k_{b'}\mu_{b'}}\\
&\times\sum_{qq'q''q'''}(-1)^{q-q'''+Q}\sqrt{(2K+1)(2K'+1)}\cos\beta_{k_{b'}\mu_{b'}k_b\mu_b}\,{\rm e}^{{\rm i}\beta_{k_{b'}\mu_{b'}k_b\mu_b}}\\
&\times[(h^{\rm II}_{k_b\mu_b,k_{b'}\mu_{b'}})_{k_a\mu_a k_f\mu_f} + {\rm i}(f^{\rm II}_{k_b\mu_b,k_{b'}\mu_{b'}})_{k_a\mu_a k_f\mu_f}]\sum_{J_aJ_{a'}J_fJ_{f'}J_bJ_{b'}J_{b''}J_{b'''}}\sum_{F_aF_{a'}F_fF_{f'}F_bF_{b'}F_{b''}F_{b'''}}\\
&\times C^{k_f}_{J_fF_f}(L_aSI_s,\mu_f)C^{k_a}_{J_aF_a}(L_aSI_s,\mu_a)C^{k_b}_{J_bF_b}(L_bSI_s,\mu_b)C^{k_b}_{J_{b''}F_{b''}}(L_bSI_s,\mu_b)\\
&\times C^{k_f}_{J_{f'}F_{f'}}(L_aSI_s,\mu_f)C^{k_a}_{J_{a'}F_{a'}}(L_aSI_s,\mu_a)C^{k_{b'}}_{J_{b'}F_{b'}}(L_bSI_s,\mu_{b'})C^{k_{b'}}_{J_{b'''}F_{b'''}}(L_bSI_s,\mu_{b'})\\
&\times(-1)^{J_a+J_{a'}+J_f+J_{f'}+J_b+J_{b'}+J_{b''}+J_{b'''}}\\
&\times\sqrt{(2J_a+1)(2J_f+1)(2J_{a'}+1)(2J_{f'}+1)(2J_b+1)(2J_{b'}+1)(2J_{b''}+1)(2J_{b'''}+1)}\\
&\times\sqrt{(2F_a+1)(2F_f+1)(2F_{a'}+1)(2F_{f'}+1)(2F_b+1)(2F_{b'}+1)(2F_{b''}+1)(2F_{b'''}+1)}\\
&\times\begin{pmatrix}F_b & F_f & 1\\ -\mu_b & \mu_f & -q\end{pmatrix}\begin{pmatrix}F_{b'} & F_{f'} & 1\\ -\mu_{b'} & \mu_f & -q'\end{pmatrix}\begin{pmatrix}F_{b''} & F_a & 1\\ -\mu_b & \mu_a & -q''\end{pmatrix}\\
&\times\begin{pmatrix}F_{b'''} & F_{a'} & 1\\ -\mu_{b'} & \mu_a & -q'''\end{pmatrix}\begin{pmatrix}1 & 1 & K\\ q & -q' & -Q\end{pmatrix}\begin{pmatrix}1 & 1 & K'\\ q''' & -q'' & Q\end{pmatrix}\\
&\times\begin{Bmatrix}J_f & J_b & 1\\ F_b & F_f & I_s\end{Bmatrix}\begin{Bmatrix}J_{f'} & J_{b'} & 1\\ F_{b'} & F_{f'} & I_s\end{Bmatrix}\begin{Bmatrix}J_a & J_{b''} & 1\\ F_{b''} & F_a & I_s\end{Bmatrix}\begin{Bmatrix}J_{a'} & J_{b'''} & 1\\ F_{b'''} & F_{a'} & I_s\end{Bmatrix}\\
&\times\begin{Bmatrix}L_a & L_b & 1\\ J_b & J_f & S\end{Bmatrix}\begin{Bmatrix}L_a & L_b & 1\\ J_{b'} & J_{f'} & S\end{Bmatrix}\begin{Bmatrix}L_a & L_b & 1\\ J_{b''} & J_a & S\end{Bmatrix}\begin{Bmatrix}L_a & L_b & 1\\ J_{b'''} & J_{a'} & S\end{Bmatrix}\\
&\times(-1)^Q\mathcal{T}^K_{-Q}(i,\boldsymbol{n})\mathcal{T}^{K'}_{Q}(j,\boldsymbol{n}')\,.
\end{aligned} \tag{6.9}$$

The non-dimensional frequencies x' and x are given in Doppler width units (see Ap-

pendix D for their definitions). The Hanle angle $\beta_{k_{b'}\mu_{b'}k_b\mu_b}$ is given by

$$\tan\beta_{k_{b'}\mu_{b'}k_b\mu_b} = \frac{\nu_{k_{b'}\mu_{b'}k_a\mu_a} - \nu_{k_b\mu_b k_a\mu_a}}{\gamma/2\pi} \,. \tag{6.10}$$

The explicit forms of the auxiliary functions $h^{\rm II}$ and $f^{\rm II}$ appearing in Equation (6.9) are given in Appendix D. When $I_s = 0$, Equation (6.9) reduces to Equation (5.11). When FS is neglected, Equation (6.9) reduces to Equation (4.16). When we neglect both FS and HFS, we recover RM for $L_a \rightarrow L_b \rightarrow L_a$ transition (analogous to a two-level atom case) in the presence of a magnetic field.

6.4 Results

In this section, we present the results obtained from the combined theory for the case of the single scattering of an unpolarized, spectrally flat incident radiation beam by an atom with both non-zero electron and nuclear spins. Considering the relevance to solar applications, we choose the D line system at $6708\,$Å from neutral ^{6}Li and ^{7}Li isotopes as an example to test the formalism developed (the atomic level diagrams for the D line transitions in these two isotopes are given in Figures 1.4 and 1.5, respectively). We take the values of the atomic parameters and isotope abundances for this system from Table 1 of Belluzzi et al. (2009).

6.4.1 Level-Crossings and Avoided Crossings

In Figures 6.2 and 6.3, we show the dependence of the energies of the levels in the ^{2}P terms of the ^{6}Li and ^{7}Li isotopes on the magnetic field strength. Such figures provide us with the information on the field strength regimes in which processes like the Zeeman effect, incomplete PB effect, and complete PB effect operate. They help us to choose the magnetic field strength values for studying the effects of level-crossing on the Stokes profiles. We choose different scales for the x-axes in different panels to bring out the level-crossings which occur at different field strengths due to the difference in the magnitudes of FS and HFS. The y-axes in all of the panels in both figures denote the energy shift of the levels from the parent $L = 1$ level.

In panels (a) and (c) of Figure 6.2, we plot the energies of the magnetic substates of the F states belonging to the $^2\mathrm{P}_{3/2}$ and $^2\mathrm{P}_{1/2}$ levels of ^{6}Li, respectively, as a function of the field strength. Since the nuclear spin of ^{6}Li is 1, we have half-integer values for F. In these panels, we see that the magnetic substates of the F states of $^2\mathrm{P}_{3/2}$ cross at nine points while

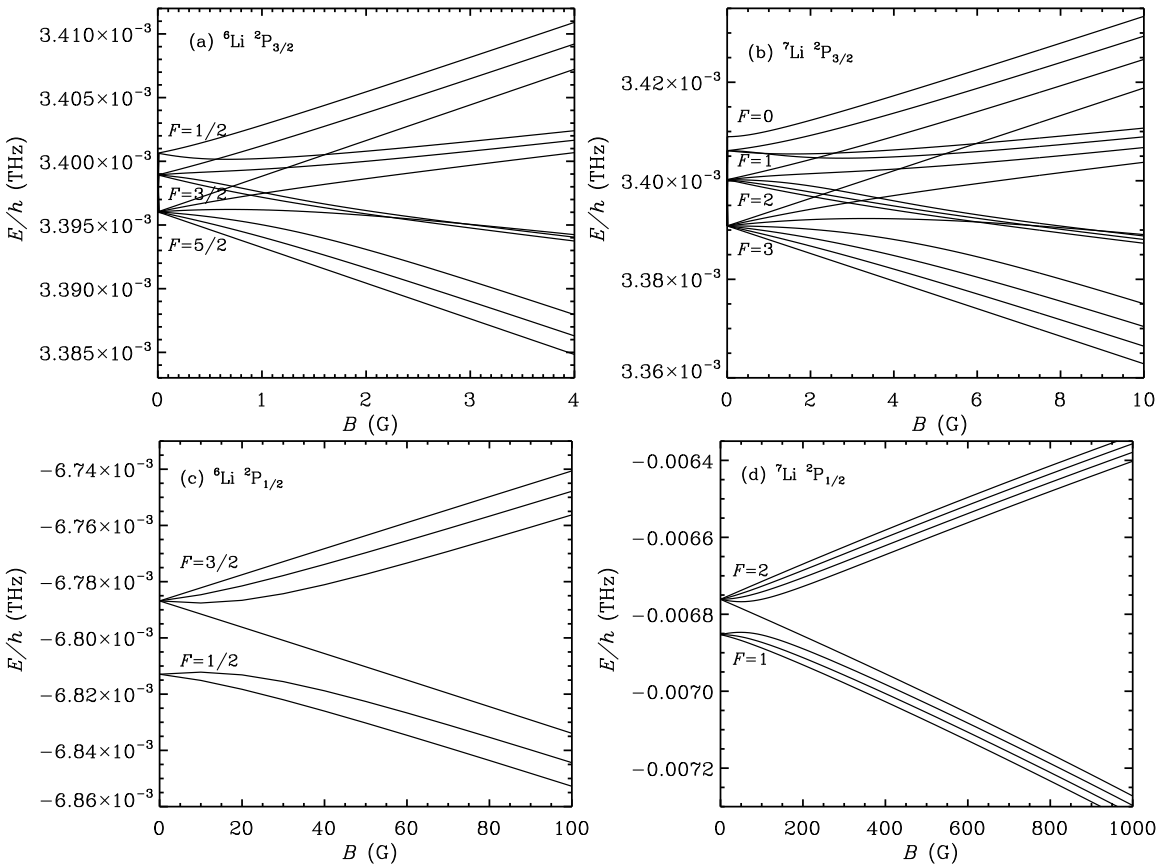

Figure 6.2: Energies of the HFS magnetic substates as a function of the magnetic field strength for ^{6}Li (left column) and ^{7}Li (right column). Panels (a) and (b) correspond, respectively, to the $^2\mathrm{P}_{3/2}$ levels of ^{6}Li and ^{7}Li, while panels (c) and (d) correspond to the $^2\mathrm{P}_{1/2}$ levels of ^{6}Li and ^{7}Li, respectively. The nuclear spins of ^{6}Li and ^{7}Li are 1 and $3/2$, respectively.

those of $^2\mathrm{P}_{1/2}$ do not cross. We note a similar behavior in the case of the F states belonging to the $^2\mathrm{P}_{3/2}$ and $^2\mathrm{P}_{1/2}$ levels of ^{7}Li (see panels (b) and (d), respectively). The magnetic substates of the F states of $^2\mathrm{P}_{1/2}$ do not cross while those of $^2\mathrm{P}_{3/2}$ cross at 14 points. In the weak field regime (e.g., $0 - 60\,\mathrm{G}$), we see PB effect for the F states, and in the strong field regime (for thousand gauss fields) we see PB effect for the J states. In Tables 6.1 and 6.2, we list the quantum numbers of the levels which cross along with their corresponding field strengths for the weak field regime. The numbers indicated in boldface in these tables correspond to those crossings which satisfy $\Delta\mu = \mu_{b'} - \mu_b = \pm 2$. We discuss the effects of these level-crossings on the polarization in later sections.

In panels (a) and (d) of Figure 6.3, we plot the energies of the magnetic substates of the ^{2}P terms of ^{6}Li and ^{7}Li as a function of the magnetic field strength. In these panels, the

$F_b \diagdown F_{b'}$		$1/2$	$3/2$	$3/2$	$3/2$
	$\mu_b \diagdown \mu_{b'}$	$+1/2$	$-1/2$	$+1/2$	$+3/2$
$3/2$	$-3/2$	$\mathbf{0.57}$	...	...	...
$5/2$	$-5/2$	1.61	$\mathbf{1.26}$	0.72	0.63
$5/2$	$-3/2$	...	...	$\mathbf{1.3}$	0.9
$5/2$	$-1/2$	...	...	2.93	$\mathbf{2.25}$

Table 6.1: Magnetic field strengths (approximate values in G) for which the magnetic substates of the F states cross in the ^{6}Li isotope. For instance, the crossing between $(\mu_b = -3/2, F_b = 3/2)$ and $(\mu_{b'} = 1/2, F_{b'} = 1/2)$ occurs at $B \sim 0.57\,\mathrm{G}$. The numbers highlighted in boldface represent the field strength values for which the level-crossings corresponding to $\Delta\mu = \mu_{b'} - \mu_b = \pm 2$ occur.

$F_b \diagdown F_{b'}$		1	1	2	2	2	2
	$\mu_b \diagdown \mu_{b'}$	0	$+1$	-1	0	$+1$	$+2$
2	-2	$\mathbf{2.2}$	2.6	...	...	...	...
3	-3	5.2	5.95	$\mathbf{4.15}$	2.65	2.35	2.1
3	-2	...	...	...	$\mathbf{3.7}$	3.25	2.95
3	-1	...	...	...	8.8	$\mathbf{7.25}$	6.0

Table 6.2: Magnetic field strengths (approximate values in G) for which the magnetic substates of the F states cross in the ^{7}Li isotope. For instance, the crossing between $(\mu_b = -2, F_b = 2)$ and $(\mu_{b'} = 0, F_{b'} = 1)$ occurs at $B \sim 2.2\,\mathrm{G}$. The numbers highlighted in boldface represent the field strength values for which the level-crossings corresponding to $\Delta\mu = \mu_{b'} - \mu_b = \pm 2$ occur.

points where the levels cross are denoted as c1 and c2 for ^{6}Li and as c$'1$ and c$'2$ for ^{7}Li. When we zoom into these crossing points, we see other interesting phenomena (see panels (b), (c), (e), and (f)). For example, at c1, we see a crossing of the bunch of lowermost three levels going downward in Figure 6.2(a) with the three levels going upward in Figure 6.2(c). Although the magnetic substates of the F states appear to be degenerate in Figure 6.3(a), they are not fully degenerate, as can be seen in Figure 6.3(b). Similar behavior can be seen in Figures 6.3(c), (e), and (f), and the levels correspond to the magnetic substates of the F states shown in Figure 6.2.

In addition to the usual level-crossings, we see several avoided crossings in Figures 6.3, in panels (b), (c), (e), and (f). For example, in panel (b), we see one avoided crossing marked a1, two in panel (c) marked a2 and a3, two in panel (e) marked a$'1$ and a$'2$, and three in panel (f) marked a$'3$, a$'4$, and a$'5$. As we can see from the figure, these avoided crossings take place between the magnetic substates with the same μ values ($-1/2$ in panel (b), $-3/2$ and $-1/2$ in panel (c), 0 and -1 in panel (e), and -2, -1, and 0 in panel (f)). The levels with the same μ cannot cross owing to the small interaction that takes place between

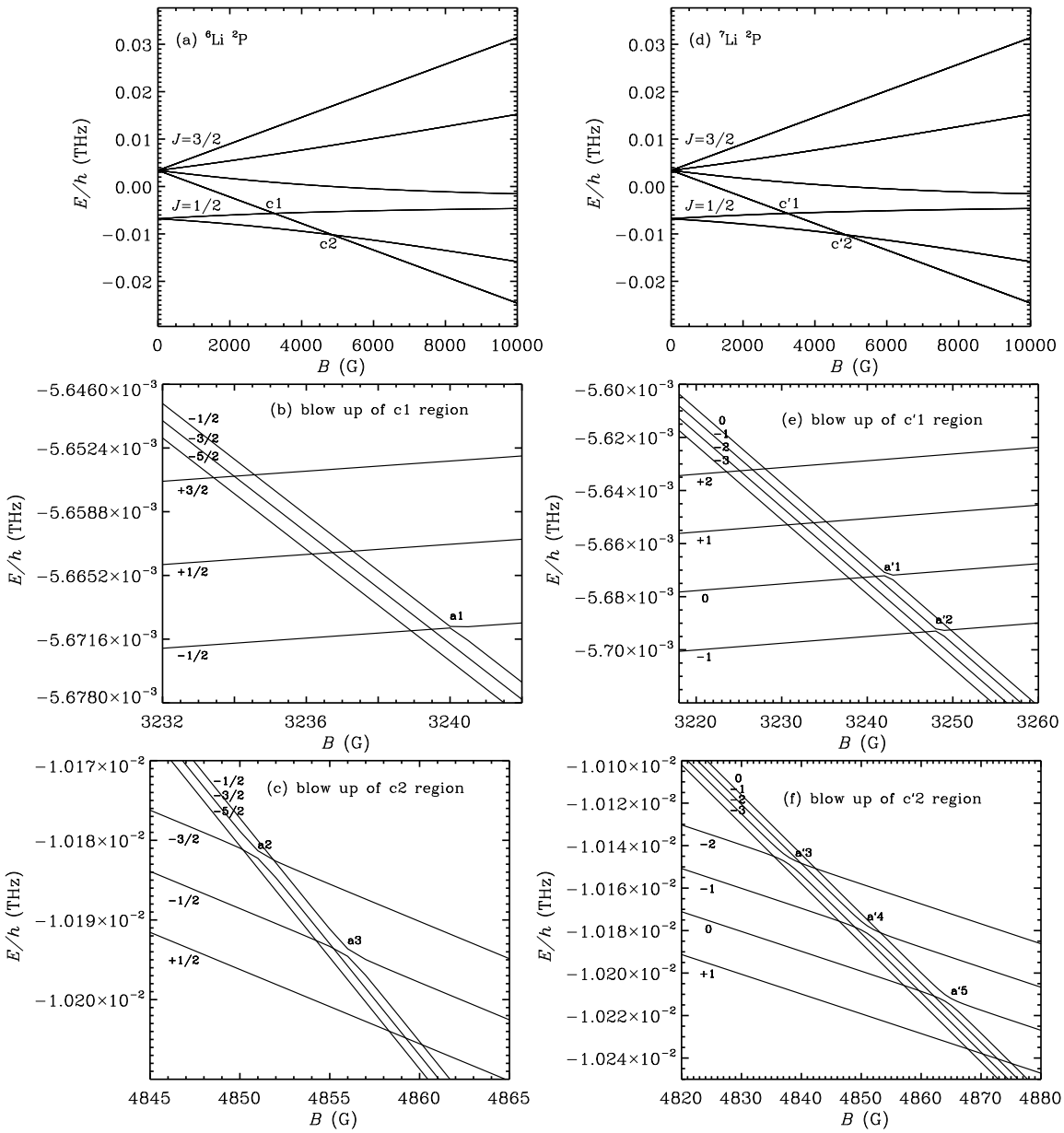

Figure 6.3: Energies of the magnetic substates belonging to the ^{2}P terms as a function of the magnetic field strength for ^{6}Li (a) and ^{7}Li (d). Blow up of the crossing regions c1 (b) and c2 (c) in ^{6}Li and c′1 (e) and c′2 (f) in ^{7}Li. In the panels (b), (c), (e), and (f) the levels are identified by their magnetic quantum number values μ.

them. This interaction is determined by the off-diagonal elements of the magnetic hyperfine interaction Hamiltonian which couple the states with different J values (Brog et al., 1967; Wieder & Eck, 1967; Arimondo et al., 1977). A rapid transformation in the eigenvector basis takes place around the region of avoided crossing. This is described in Bommier (1980) and in Landi Degl'Innocenti & Landolfi (2004, see also Sowmya et al. 2014b,c).

6.4.2 Line Splitting Diagrams

The line splitting diagram shows the displacement of the magnetic components from the line center (corresponding to the wavelength of the $L = 0 \rightarrow 1 \rightarrow 0$ transition in the reference isotope ^{7}Li) and the strengths of these components for a given field strength. In Figure 6.4, we show the line splitting diagrams for different B values. We take into account the isotope shift and the solar abundances of the two isotopes while computing the strengths and magnetic shifts. As mentioned earlier, the components arising for $B = 0$ correspond to the transitions between the unperturbed F states. We see that the hyperfine structure components of the D lines are well separated when $B = 0$ due to the relatively large FS. When the magnetic field is applied, the degeneracy of the magnetic substates is lifted. As a result, 70 allowed transitions take place in ^{6}Li and 106 in ^{7}Li. This explains why the diagrams become crowded as the field strength increases. We see that the magnetic displacements increase with an increase in B as expected. In the diagrams shown, we note that the MS is nonlinear and is a characteristic of the incomplete PB regime.

6.4.3 Single Scattered Stokes Profiles

In this section, we present the Stokes profiles for various B values computed using the combined theory for the single scattering case. We choose a coordinate system (see Figure 6.5) in which the magnetic field lies in the horizontal (xy) plane making angles $\theta_B = 90°$ and $\chi_B = 45°$. We make this choice following Stenflo (1998) in order to bring out clearly the effects of the magnetic field. We assume the unpolarized incident ray to be along the vertical (z-axis) and the scattered ray (or the line of sight) to lie in the horizontal plane along the x-axis. Thus, the angles for the incident and the scattered rays become $\mu' = 1$, $\chi' = 0°$, $\mu = 0$, and $\chi = 0°$. We use the fact that the lithium lines are optically thin and only single scattering is considered here to add the Stokes profiles computed for the individual isotopes after weighting them by their respective abundances. In Figures 6.6–6.9, we compare the single scattered Stokes profiles for three cases: the cases of pure F-state interference (dotted lines) represented by a two-level atom with hyperfine structure, pure J-state interference (dashed lines) represented by a two-term atom without hyperfine structure, and the combined theory (solid lines) represented by a two-term atom with hyperfine structure. We choose a Doppler width of 60 mÅ for all of the components of the multiplet when computing the Stokes profiles. For this particular value of the Doppler width, the theoretical Q/I profile closely resembles the observed Q/I profile (see Belluzzi et al., 2009). We use the Einstein A coefficient of 3.689×10^7 s^{-1} for all of the components.

In Figure 6.6, we show the Stokes profiles computed in the absence of magnetic fields

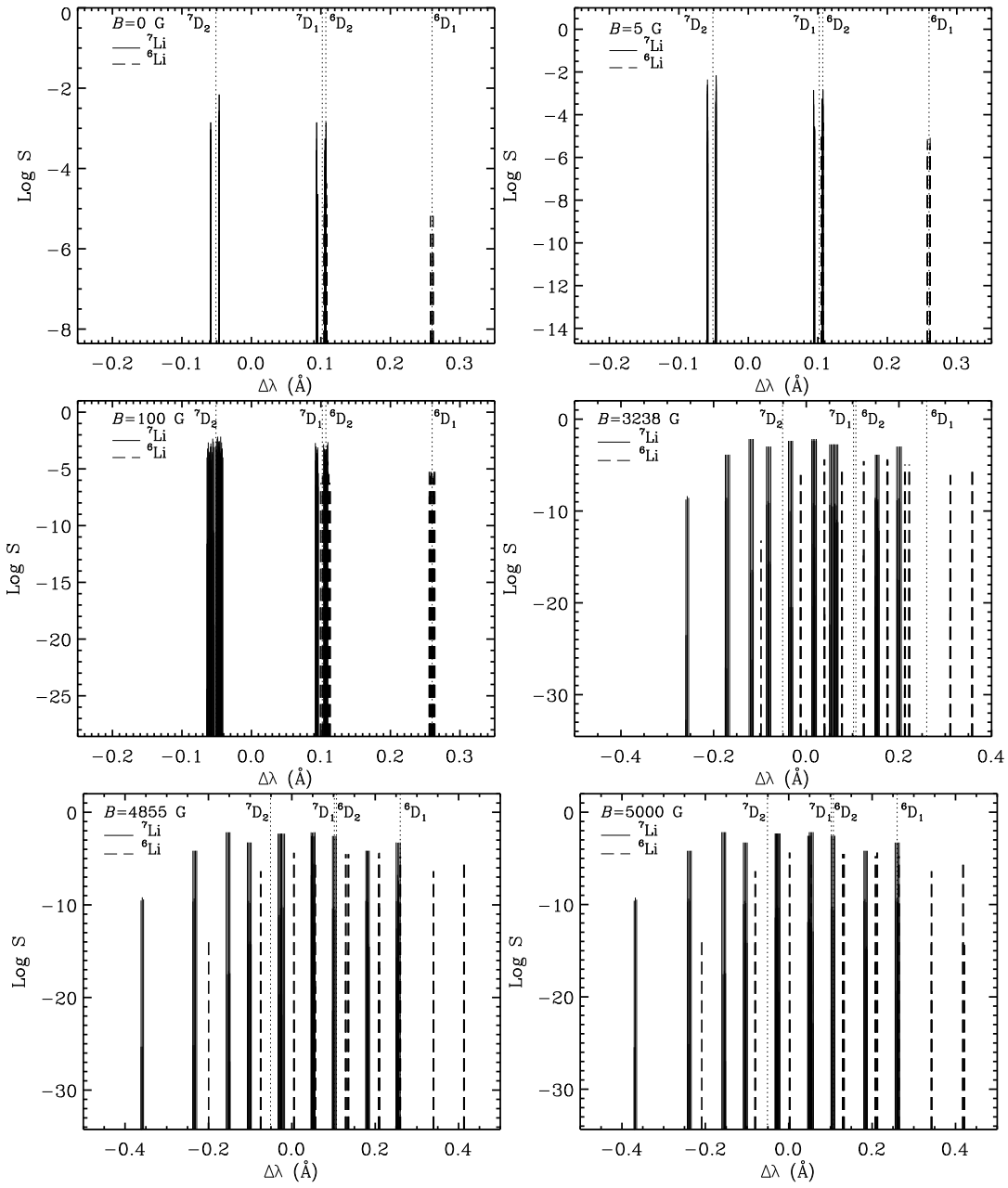

Figure 6.4: Line splitting diagrams for the two lithium isotopes for the field strengths indicated. The solid lines represent the magnetic components of ^{7}Li while the dashed lines represent those of ^{6}Li. Vertical dotted lines mark the positions of the D lines of the two isotopes. $\Delta\lambda = 0$ corresponds to the line center wavelength of $L = 0 \rightarrow 1 \rightarrow 0$ transition in ^{7}Li.

for $100\,\%$ ^{7}Li in panel (a), for $100\,\%$ ^{6}Li in panel (b), and for both the isotopes combined according to their percentage abundance in panel (c). In panels (a) and (b), we see two peaks corresponding to the D lines of the two isotopes in intensity. The intensities of the D

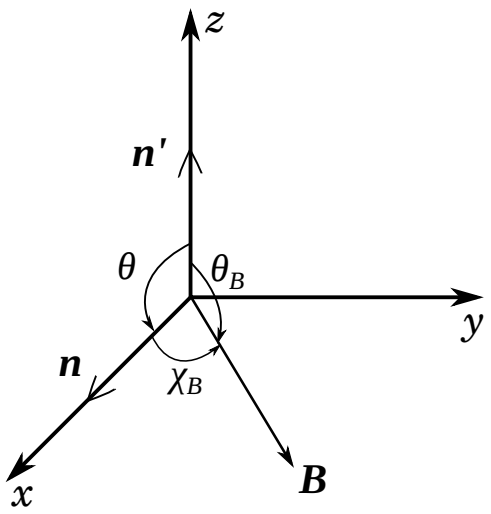

Figure 6.5: Scattering geometry considered for the results presented in Section 6.4.3.

lines in both the isotopes are of similar magnitude since we have assumed $100\,\%$ abundance for the two isotopes. We also note that the wavelength positions of the D lines of ^{6}Li are different from those of ^{7}Li owing to the isotope shift. In panel (c), we see two distinct peaks in intensity. The first peak to the left is due to the ^{7}Li D_2 line. The second peak falls at the line center positions of ^{7}Li D_1 and ^{6}Li D_2. However, the dominant contribution comes from the ^{7}Li D_1 due to its relatively larger abundance. A small bump to the right of the second peak is due to the ^{6}Li D_1 line. A small difference in the intensity at the ^{7}Li D_2 peak between the dashed lines and the other two cases is seen in panels (a) and (c). It is clear from the figure that this discrepancy is caused by ^{7}Li. Comparing the solid, dotted, and dashed profiles, we come to the conclusion that the HFS is at the origin of this discrepancy. This is because the solid and dotted lines computed by including HFS perfectly match and only the dashed lines computed without HFS differ from the other two cases. The discrepancy is very small in the case of ^{6}Li because of smaller HFS in ^{6}Li compared to that in ^{7}Li. The reason for this discrepancy is due to the asymmetric splitting of the hyperfine structure components about the given J state and also due to finite widths of the components. This difference decreases (graphically indistinguishable) when a magnetic field is applied (for example, when $B = 5\,\mathrm{G}$ as seen in Figure 6.7) because of the superposition of a large number of magnetic components. In contrast, this difference is about an order of magnitude larger in the non-magnetic case. As we increase the field strength, the intensity profiles broaden due to an increased separation between the magnetic components.

When $B = 0$, the Q/I profiles exhibit a multi-step behavior around the line center po-

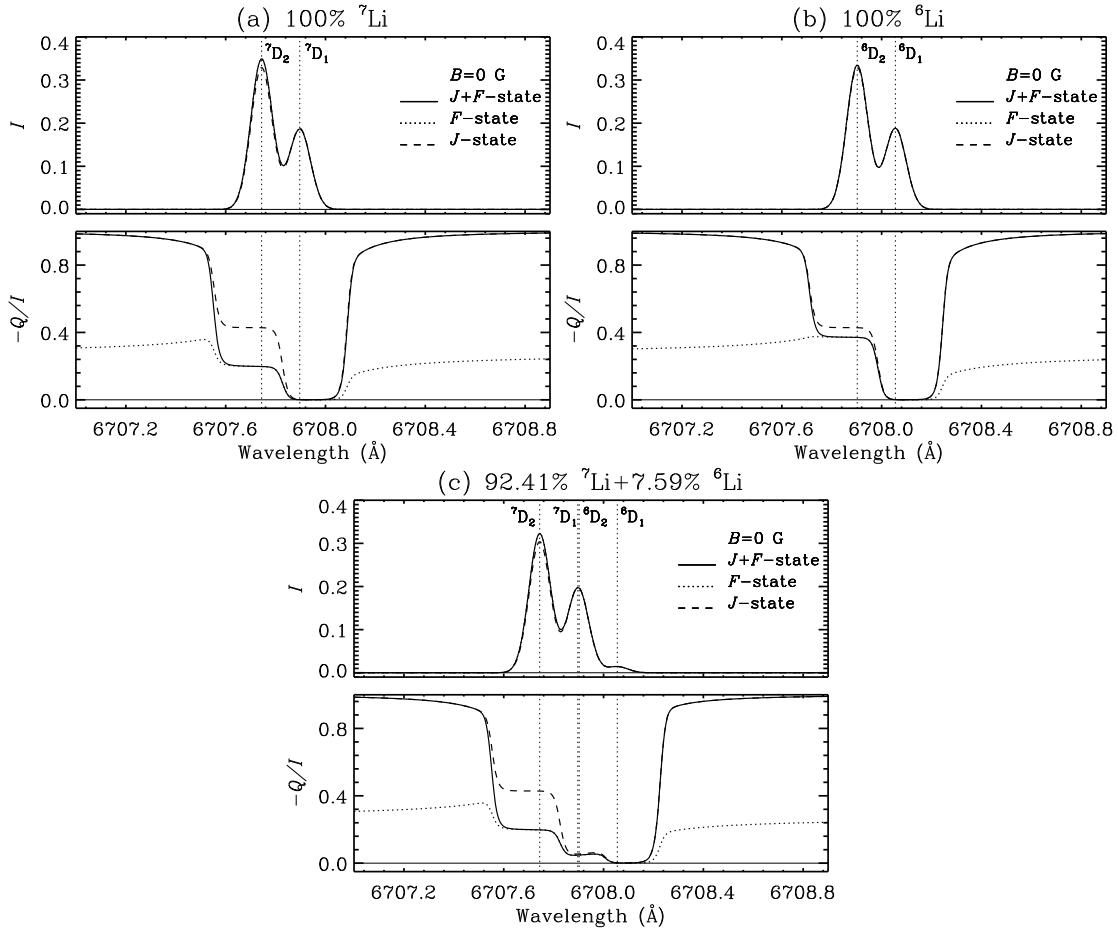

Figure 6.6: Single scattered Stokes profiles for the lithium D line system in the absence of a magnetic field: (a) $100\,\%$ ^{7}Li, (b) $100\,\%$ ^{6}Li, and (c) ^{7}Li and ^{6}Li combined according to their percentage abundance. The line types are indicated in the intensity panels. The geometry considered for scattering is $\mu = 0$, $\mu' = 1$, $\chi = 0°$, and $\chi' = 0°$. The vertical dotted lines represent the line center wavelength positions of the ^{7}Li D_2, ^{7}Li D_1, ^{6}Li D_2, and ^{6}Li D_1 lines in the absence of magnetic fields.

sitions of the D_1 and D_2 lines of both isotopes. We see the effects of quantum interference clearly in Q/I. In the ^{7}Li D_2 core, significant depolarization is caused by the HFS compared to the case where this splitting is neglected (compare the solid and dashed lines in panels (a) and (c)). A similar depolarization is also exhibited by the core of the ^{6}Li D_2 line (see panels (b) and (c)). However, in the scale adopted, the solid and dashed lines appear to merge around the core of ^{6}Li D_2 in panels (c), as the Q/I values of ^{6}Li D_2 are an order of magnitude smaller than those of ^{7}Li D_2 because of their relative abundances. The D_1 lines remain upolarized. As expected, the solid lines merge with the dotted lines in the cores of lithium lines while they coincide with the dashed lines in the wings. When a magnetic field

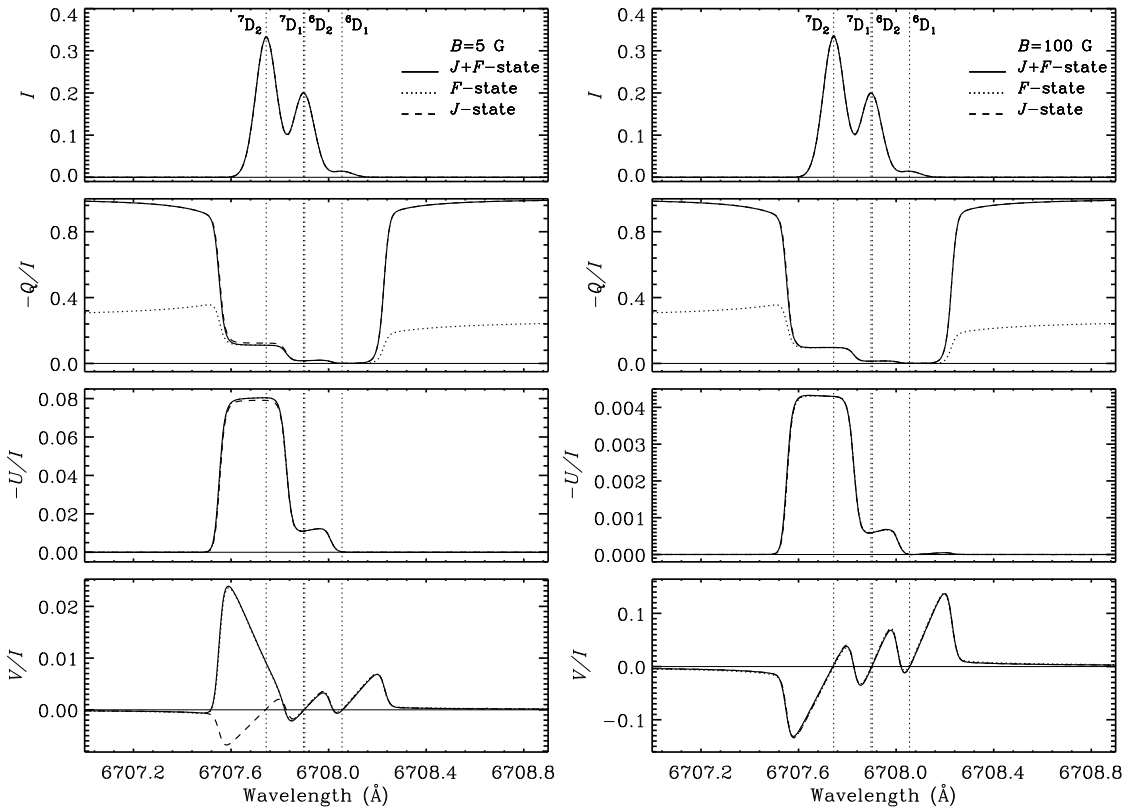

Figure 6.7: Same as Figure 6.6 but in the presence of a magnetic field. The left and the right panels correspond to different field strength values. The field orientation ($\theta_B = 90°$, $\chi_B = 45°$) is the same in both the panels. Refer to Section 6.4.3 for the scattering geometry.

is applied, we see a depolarization in Q/I and a generation of U/I signal in the cores of the lithium lines due to the Hanle effect. We note that the combined theory results match more closely the pure J-state interference results for fields of the order of $100\,\mathrm{G}$. This behavior continues until the level-crossing field strength of $B = 3238\,\mathrm{G}$ for fine structure is reached.

When the field strength is of the order of a few thousand gauss, we are by far in the complete PB regime for the F states. In this regime, the J and I_s couple strongly to the magnetic field and the interaction between J and I_s becomes negligible. Therefore, one would expect the magnetic substates of the F states to be fully degenerate, and therefore the solid and dashed lines should match closely for fields of this order. However, for the level-crossing field strengths, we see considerable differences between the solid and the dashed lines, especially in U/I. In order to understand this, we compare the Stokes profiles for ^{7}Li and ^{6}Li separately in panel (a) and (b) of Figure 6.8 with the combined profiles in panel (c). We do this to check whether a particular isotope is giving rise to this difference. We note that this difference between the solid and dashed lines prevails in all three

panels (i.e., in both isotopes). We attribute this difference in the shape and amplitude between the solid and the dashed lines to HFS, the level-crossings, and avoided crossings between the magnetic substates of the F states. When we look at Figure 6.3, we find that the magnetic substates of the F states have finite energy differences and are not fully degenerate in the complete PB regime for the F states. We see several crossings as well as a few avoided crossings. These level-crossings and avoided crossings between the non-degenerate magnetic substates of the F states lead to a modification of the coherence and significant Hanle rotation, thereby affecting the shape and amplitude of the U/I profiles. The HFS effects show more prominently in the polarization diagrams which will be discussed in Section 6.4.5. For the geometry under consideration, this effect is significantly seen for $B = 3238\,\mathrm{G}$. For a level-crossing field strength of $4855\,\mathrm{G}$, the Stokes profiles show somewhat different behavior.

We also note that for fields of the order of a few thousand gauss, differences between the solid and dashed lines remain only in the far left wing (see Figures 6.8 and 6.9). From Figure 6.8 it is clear that this difference in the far blue wings is only due to the ^{7}Li isotope (compare panels (a)–(c)). This can be understood with the help of the line splitting diagrams for level-crossing fields in Figure 6.4 in comparison with the corresponding diagrams in Figure 5.3 (a direct comparison of the displacements can be made as the zero points in the two figures are the same). In a two-term atom without hyperfine structure, when a magnetic field is applied, the various fine structure magnetic components are either blue or redshifted from the line center depending on their energies. When HFS is included, the hyperfine structure magnetic components are distributed around the positions of the fine structure magnetic components in the absence of HFS. We find that the positions of the hyperfine structure magnetic components in Figure 6.4 correspond well with the wavelength positions of the fine structure magnetic components in Figure 5.3, except for the bunch of magnetic components to the extreme left represented by solid lines. The magnetic field leads to a large blue shift of this bunch, which consists of three σ_b ($\Delta\mu = \mu_b - \mu_a = +1$), two π ($\Delta\mu = 0$) and one σ_r ($\Delta\mu = -1$) components. These components (otherwise not present at this wavelength position when HFS is neglected) give rise to the systematic difference in $Q/I, U/I,$ and V/I in the far blue wing of the D_2 line of ^{7}Li. However, they do not affect the intensity.

The V/I profiles remain somewhat indistinguishable between the three cases considered, except for very weak fields like $5\,\mathrm{G}$ as in Figure 6.7. F-state interference significantly changes the V/I profile at the ^{7}Li D_2 wavelength position. This is a signature of the alignment-to-orientation (A-O) conversion mechanism (for more details, see Landi Degl'Innocenti, 1982; Landi Degl'Innocenti & Landolfi, 2004) acting in the incom-

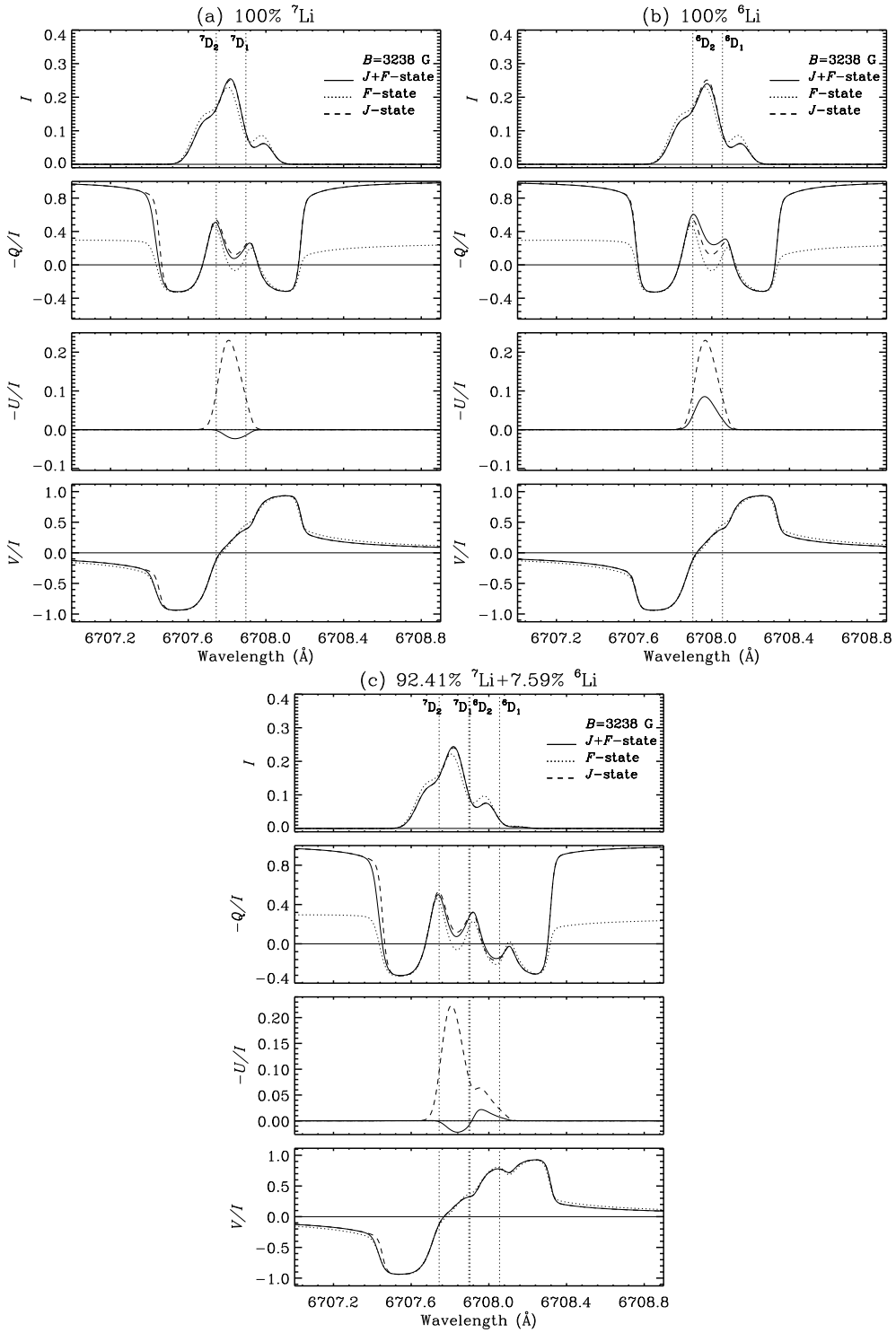

Figure 6.8: Stokes profiles obtained for $B = 3238\,\mathrm{G}$: (a) $100\,\%$ ^{7}Li, (b) $100\,\%$ ^{6}Li, and (c) ^{7}Li and ^{6}Li combined according to their percentage abundance. Refer to Section 6.4.3 for the scattering geometry. When $B = 3238\,\mathrm{G}$, the U/I values are so small for the dotted line case that they become indistinguishable from the zero line.

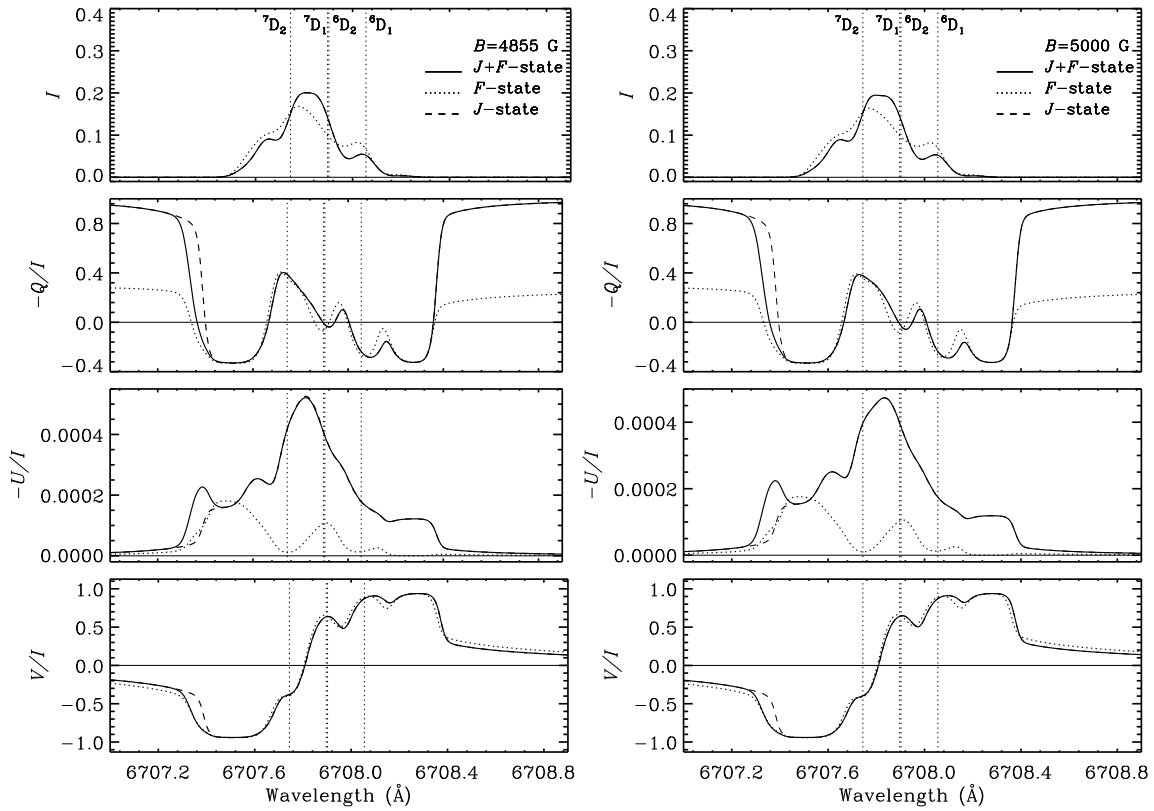

Figure 6.9: Stokes profiles obtained for $B = 4855\,\mathrm{G}$ and $B = 5000\,\mathrm{G}$. Refer to Section 6.4.3 for the scattering geometry.

plete PB regime for the F states. As described in Landi Degl'Innocenti & Landolfi (2004), this occurs because of the double summation over K and K' appearing in Equation (6.9) and because the spherical tensor $\mathcal{T}^K_Q(3,\boldsymbol{n})$ is non-zero only when $K = 1$ (see Equation (E.6) of Appendix E). This means that circular polarization can be generated by resonance scattering even if the atom is not exposed to circularly polarized light. The alignment present in the radiation field is converted to the orientation in the upper term. This orientation in the upper F states gives rise to circularly polarized light. As discussed earlier, small differences appear in the far blue wings for fields equal to or larger than the level-crossing field strengths.

Finally, we remark that the discussion presented above concerning the comparison of the single scattered Stokes profiles between the three cases (namely, the pure J-state, pure F-state, and $F + J$-state interference) also remains valid for other scattering geometries.

In Figure 6.10, we show the Stokes profiles obtained after including a weakly polarized background continuum. The continuum is added in the same way as described in Section 5.4.3. The parameters used for the continuum are same as the ones given in Sec-

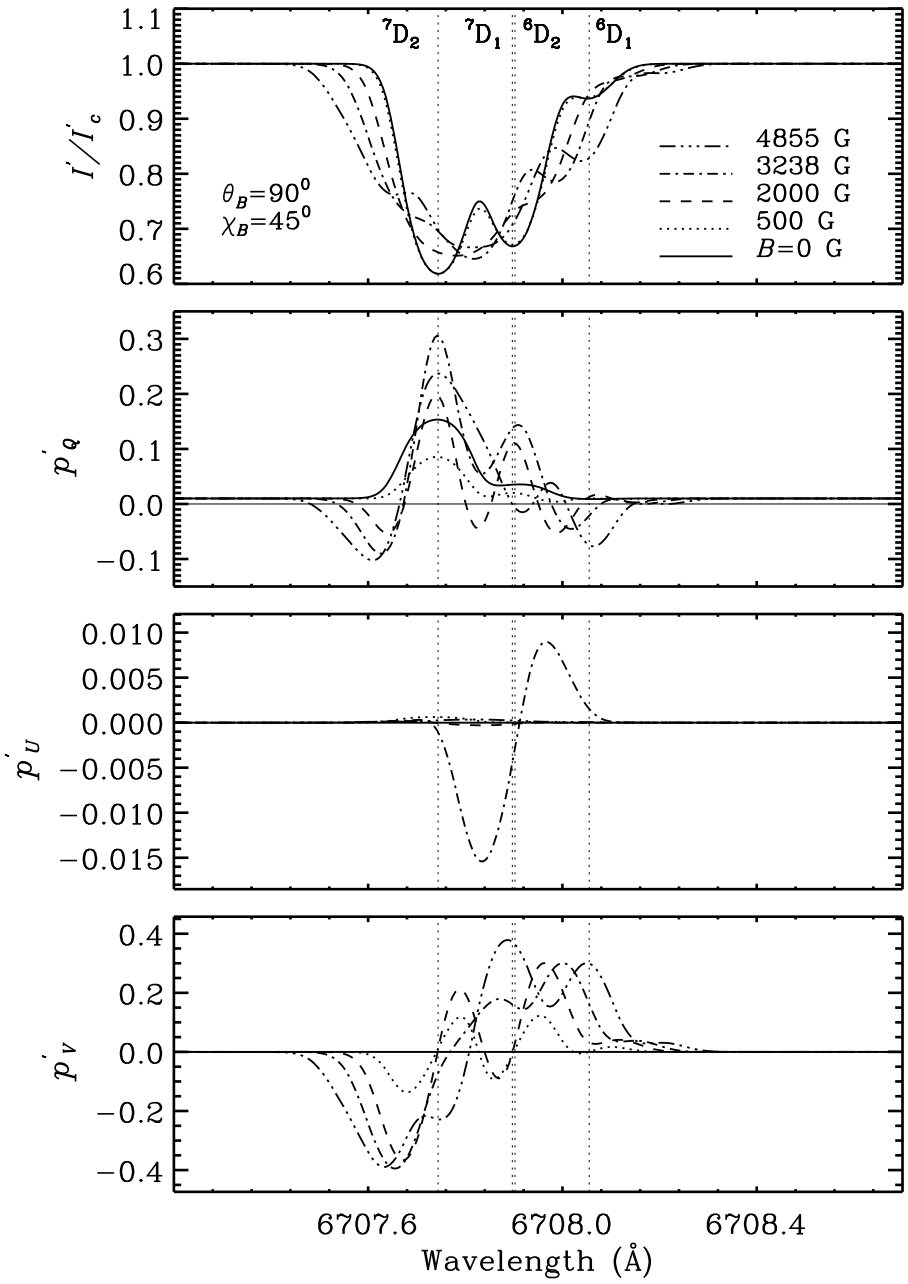

Figure 6.10: Stokes profiles obtained by including the contribution from the continuum for different values of B. Refer to Section 6.4.3 for the scattering geometry. The vertical dotted lines represent the positions of the D lines.

tion 5.4.3. We compare Figure 6.10 with Figure 5.4 and find that the HFS does not cause any change in the intensities. When $B = 0$ the HFS causes a depolarization in the core of Q/I without affecting the shape of the profile. For other field strengths, there is only a slight difference in the amplitude of the profiles as compared to the case without HFS,

although their shapes remain the same. The U/I profiles differ both in amplitude and shape for $B = 3238$ G. This difference is due to HFS. When HFS is neglected, there is only one level-crossing at this field strength. On the other hand, when HFS is included, there are several level-crossings around this field strength (see Figures 6.3(b) and (e)). V/I profiles have the same shapes and amplitudes as compared to the case without hyperfine structure.

6.4.4 NCP in the Combined Theory

In this section, we present the plots NCP as a function of B. Since the PBE causes nonlinear splitting of the magnetic components with respect to the line center, the Stokes V profiles become asymmetric. As a result of this asymmetry, the integration of the Stokes V over the full line profile yields a non-zero value. In the linear Zeeman and complete PB regimes, the V profiles show perfect antisymmetry which causes the NCP to become zero. The A-O conversion mechanism discussed in Section 6.4.3 further enhances the asymmetry in Stokes V profiles already caused by nonlinear MS, and thereby contributes to the NCP. This mechanism is particularly efficient when the level-crossings satisfy $\Delta\mu = \mu_{b'} - \mu_b = 1$.

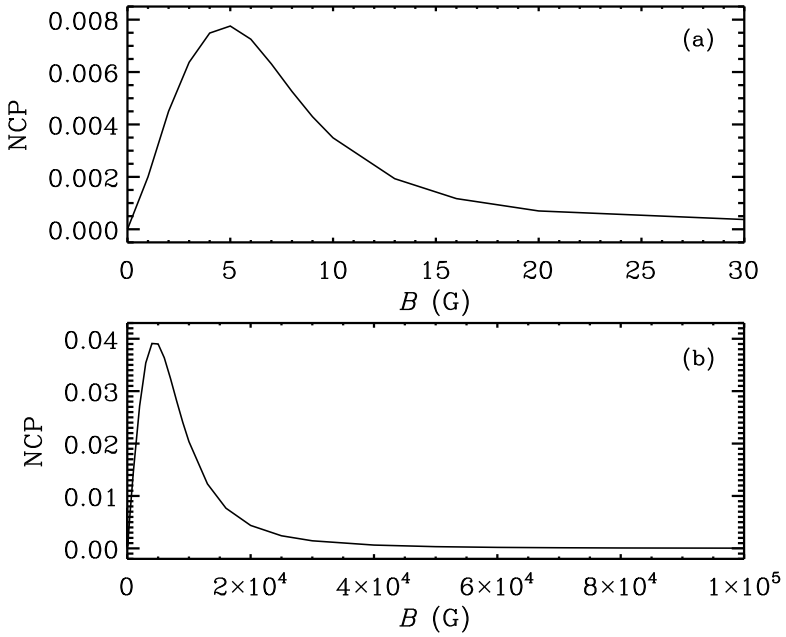

Figure 6.11: NCP as a function of the magnetic field strength B. The scattering geometry is characterized by: $\mu' = 0$, $\chi' = 0°$, $\mu = 1$, $\chi = 90^{\circ}$, $\theta_B = 0°$, and $\chi_B = 0°$.

In Figure 6.11, we show the behavior of NCP in different field strength ranges for the scattering geometry: $\mu' = 0$, $\chi' = 0°$, $\mu = 1$, $\chi = 90°$, $\theta_B = 0°$, and $\chi_B = 0°$. This choice of the field geometry is made in order to obtain larger values for Stokes V. In panel (a),

we show the weak field behavior of NCP. We attribute the non-zero NCP in this regime to the PBE in the F states and the A-O conversion mechanism taking place in the incomplete PB regime for the F states. We find that the NCP increases with increasing field strength, peaking around the level-crossing field strength (see Tables 6.1 and 6.2), and decreases with further increase in B. When the fields are as strong as a few thousand gauss we see a second peak in NCP whose magnitude is larger than the first peak by an order. This is due to the PBE in the J states and the A-O conversion mechanism occurring in the incomplete PB regime for the J states. With a further increase in the field strength, we enter the complete PB regime for the J states where the NCP becomes zero.

See Landi Degl'Innocenti & Landolfi (2004) for detailed discussions on the various mechanisms producing NCP.

6.4.5 Polarization Diagrams

In Figure 6.12, we present the polarization diagrams for a given B and θ_B and for the full range of χ_B. Refer to the figure caption for the incident and scattered ray directions. θ_B takes values $0°, 70°, 90°$, and $110°$. We find that the $\theta_B = 70°$ and $110°$ curves perfectly coincide in all four panels. They take same values for Q/I and U/I at $\chi_B = 0°$ and $\chi_B = 180°$. However, we see that the dependence on χ_B of the $\theta_B = 70°$ curve is somewhat different from that of the $\theta_B = 110°$ curve. By this, we mean that for the $\theta_B = 70°$ case, the Q/I value changes in an anti-clockwise direction from the $\chi_B = 0°$ point while it changes in a clockwise direction from the $\chi_B = 0°$ point for the $\theta_B = 110°$ case. The Q/I value increases with increasing χ_B, reaches a maximum and then decreases till $\chi_B = 180°$. U/I makes a gradual transition from being positive to negative. Q/I again increases with an increase in χ_B and at $\chi_B = 360°$ it resumes the same value it had at $\chi_B = 0°$. U/I now makes a transition from being negative to positive. When $\theta_B = 0°$ the magnetic field is along the z-axis and exhibits azimuthal symmetry. Hence, $\theta_B = 0°$ is just a point in the polarization diagram. For $\theta_B = 90°$ the diagram is symmetric with respect to the $U/I = 0$ line.

In Figure 6.13, we compare the polarization diagrams obtained at different wavelength points by varying B for a two-term atom without hyperfine structure (dashed curves) and a two-term atom with hyperfine structure (solid curves). The geometry considered is described in the caption to the figure. In panel (a), we see a decrease in Q/I with increasing field strength due to the Hanle effect. For fields greater than $100\,\mathrm{G}$, we enter the Hanle saturation regime. Q/I starts to increase as we approach the level-crossing field strength (around $3000\,\mathrm{G}$). Loops (i.e., a single circular loop for the dashed line and multiple small

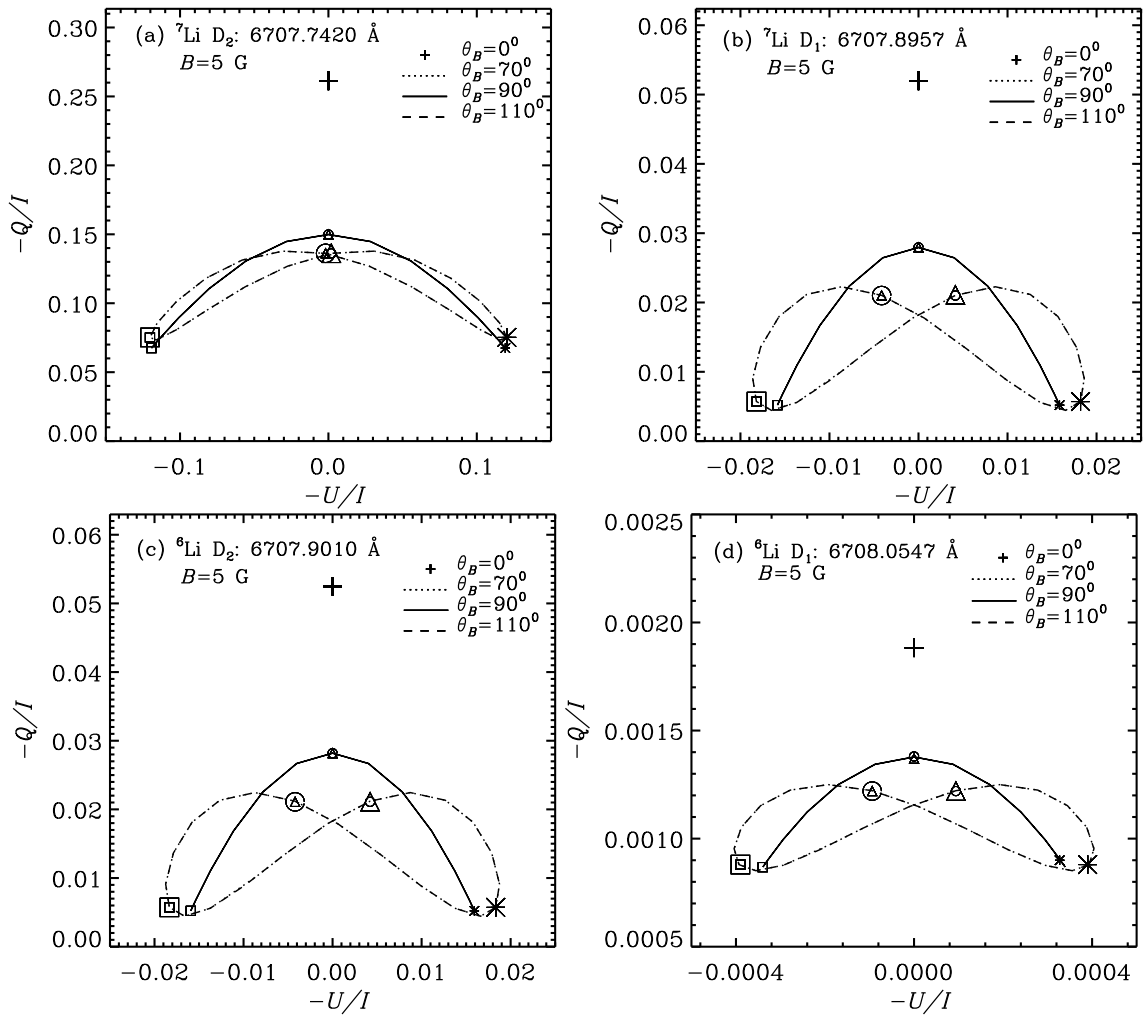

Figure 6.12: Polarization diagrams obtained at the D line positions for $B = 5\,\mathrm{G}$ and different θ_B as indicated in the panels. The azimuth χ_B of the magnetic field is varied from $0°$ to $360°$. The symbols on the curves mark the χ_B values: $* - 0°$, $\circ - 70°$, $\square - 180°$, and $\triangle\ -270°$. Since the curves for the $\theta_B = 70°$ and $110°$ coincide, we use symbols that are bigger in size for the $\theta_B = 110°$ case to distinguish it from the $\theta_B = 70°$ curve. The geometry considered is $\mu = 0$, $\mu' = 1$, $\chi = 0°$, and $\chi' = 0°$.

loops for the solid line) arise due to several level-crossings (see Figure 6.3) where the coherence increases and Q/I tends to approach its non-magnetic value. Comparing the solid and dashed curves in Figure 6.13, the effects of HFS can be clearly seen. First, due to the depolarization caused by HFS, the polarization diagram shrinks in size. Second, multiple small loops are formed (see the solid lines in Figure 6.13). These multiple loops arise due to several level-crossings that occur only when HFS is included (see Figure 6.3(b), (c), (e), and (f)). For field strengths larger than the level-crossing field strengths, the Q/I value decreases again and becomes zero around $10000\,\mathrm{G}$. We see the effects due to Rayleigh

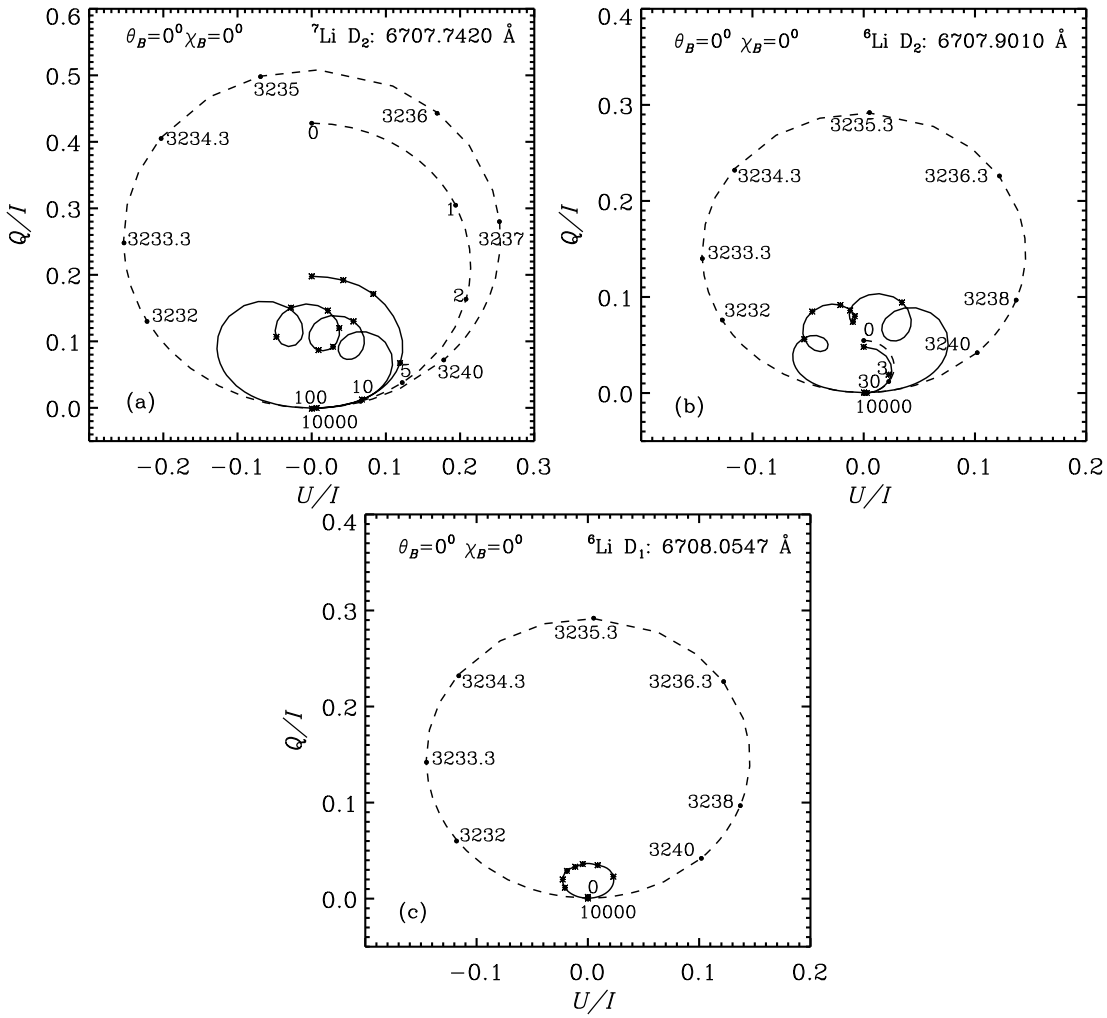

Figure 6.13: Polarization diagrams obtained at the D line positions for a given orientation of the magnetic field. The dashed lines correspond to the pure J-state interference case without HFS while the solid lines correspond to the combined theory case (including HFS). The magnetic field strength values are marked along the dashed curves in G. The asterisks on the solid curves represent the same field strength values as indicated for the dashed curves. The scattering geometry considered is $\mu = 1$, $\mu' = 0$, $\chi = 90°$, and $\chi' = 0°$.

scattering in strong magnetic fields when we increase the field strength beyond $10000\,\mathrm{G}$ (similar to Figure 5.5(b)). In panel (b), we show the polarization diagram computed at the ^{6}Li D_2 wavelength position. Since the ^{7}Li D_1 position nearly coincides with that of ^{6}Li D_2, we see the combined effect of both lines. However, due to the large abundance of ^{7}Li, the behavior of the polarization diagram is dominated by contribution from ^{7}Li D_1. Since ^{7}Li D_1 is unpolarized, the small arcs seen for weak fields are due to the ^{6}Li D_2 line. After the Hanle saturation field strength ($30\,\mathrm{G}$), the polarization diagrams essentially show behavior similar to the corresponding polarization diagrams in panel (a). In panel (c), we show the

polarization diagram for ^{6}Li D_1 position. The D_1 line remains unpolarized till the level-crossing field strength (around 3000 G) is reached. Around the level-crossing field strength, we see a bigger loop for the case without HFS (dashed line) and a smaller loop for the case with HFS (solid line).

6.5 Conclusions

In this chapter, we presented a formalism to treat the interferences between the magnetic substates of the hyperfine structure states pertaining to different fine structure states of the same term including the effects of PRD in scattering. Using the Kramers–Heisenberg approach, we calculated the polarized scattering cross section (i.e., the RM) for this process. We also demonstrated the behavior of the RM in a single scattering of the incident unpolarized radiation by the lithium atoms. In the solar case, the combined theory finds applications in modeling of spectral lines like lithium 6708 Å for which the effects of both fine and hyperfine structure are significant.

We illustrated the effects of a deterministic magnetic field on the Stokes profiles of the lithium D line system. We covered the entire field strength regime from a weak field Hanle regime to incomplete and complete PB regimes. When the fields are weak, the Stokes profiles exhibit the well known Hanle signatures at the centers of the lithium D lines, namely, depolarization of Q/I and rotation of polarization plane. We noted that there are Zeeman-like signatures for stronger fields. We identified the signatures of level-crossings and avoided crossings in Stokes profiles and polarization diagrams. Unlike the pure J-state or F-state interferences, when J- and F-state interferences are treated together, a multitude of level-crossings and avoided crossings occur which produce multiple loops in the polarization diagrams and interesting signatures in the U/I profiles. Non-zero NCP is seen for fields in the incomplete PB regime which arises not only due to nonlinear MS but also due to the A-O conversion mechanism as already described in Landi Degl'Innocenti & Landolfi (2004). However, its diagnostic potential needs to be explored. We performed all the calculations including the effects of PRD. However, its effect manifests itself only when one considers the transfer of the line radiation in the solar atmospheric conditions.

7

MODELING THE LI I D_1 AND D_2 LINES

Outline

In this chapter, we present our efforts towards modeling the Stokes profiles of the Li I D lines at $6708\,$Å using the LSA and the combined theory for arbitrary magnetic field strengths described in Chapter 6. These lines are optically very thin and weakly polarized. They can be observed in the quiet Sun with the existing spectropolarimeters. The magnetic field reduces the polarization already present in these lines and their observations in magnetized regions are currently unavailable due to the lack of polarimeters with a sensitivity beyond 10^{-5} which is necessary to measure the weak polarization of these lines. Therefore, we aim at only computing the theoretical profiles for various geometry and strengths of the magnetic field in order to explore the diagnostic potential of these lines.

7.1 Introduction

In Chapter 6, we derived the RM for the $F + J$- state interference process and studied its characteristics in a single $90°$ scattering of the incident unpolarized light. To model the lines in the second solar spectrum which are sensitive to this combined interference for the field strengths encountered on the Sun, we need to compute theoretical Stokes profiles through detailed radiative transfer calculations using the RM derived and the realistic solar model atmospheres. These profiles can then be compared with the observations and attempts be made to infer and constrain the magnetic field parameters. This task, however, is computationally very expensive for the magnetic field parameter domains that one need to consider for such a study. Therefore, we opt for the LSA method which is based on

the concept that the polarization information contained in the scattered light is generated in the last scattering event and is determined by the anisotropy of the medium at the place of the last scattering. Since the amount of polarization contained in the emergent radiation is very small (less than a few percent), the polarization of the incident radiation can be neglected. This method is computationally fast and allows one to determine the polarization from Stokes I, without the need to solve the full polarized radiative transfer equation for multiple scattering.

LSA concept has proven to be a useful tool in modeling the polarization profiles of molecular and atomic lines. Stenflo (1980) used this concept to model the polarization profiles of the Ca II H and K lines, which exhibited the signatures of quantum mechanical interference. Stenflo (1982) used the LSA concept to elucidate the physics of the Hanle effect and diagnose the turbulent magnetic fields in the solar atmosphere (see also Stenflo, 1994). Faurobert & Arnaud (2002) applied this method to model the scattering polarization of molecular emission lines in the quiet solar chromosphere. In order to study the polarization of the Sun's continuous spectrum, Stenflo (2005) used LSA. Belluzzi et al. (2007); Belluzzi (2009) and Belluzzi et al. (2009) used a variant of the LSA method to understand the origin of the polarization in Ba II D_1 and D_2, Sc II, and Li I D lines, respectively. The single scattering approximation proposed in Frisch et al. (2009) is another variant of the LSA method to study the Hanle effect in random magnetic fields.

In this chapter, we will work with the LSA methods proposed by Sampoorna et al. (2009) and Anusha et al. (2010). Sampoorna et al. (2009) extended the approach of Stenflo (1982) to deal with the Hanle effect for resolved magnetic fields. They determined the radiation field anisotropy at the place where the last scattering occurs from the observed limb darkening and used it in combination with the PRD matrices (either of the form given in Domke & Hubeny 1988 or the ones presented in Sampoorna et al. 2007a,b) to obtain the Stokes profiles. With this method, Sampoorna et al. (2009) could successfully reproduce most of the features in the limb observations of the Ca I 4227 Å line. This modeling effort led them to rule out the magnetic origin for the spatial variation of the scattering polarization in the wings of this line. In this chapter, we will refer to this approach as LSA-0 method. We use this method to compute the Li I D line profiles for various magnetic field strengths.

Anusha et al. (2010) presented three different LSA methods, namely, LSA-1, LSA-2, and LSA-3 (see also Anusha et al., 2011a) for the non-magnetic case. In LSA-1 method, the anisotropy factor is determined from the observed center to limb variation (CLV) of the intensity. It is very similar to the LSA-0 method and makes use of the angle averaged forms of the Domke & Hubeny (1988) PRD matrices. LSA-2 and LSA-3 methods

take into account the radiative transfer effects. In these two approximations, Stokes I is calculated by solving the scalar transfer equation at all depth points in a given model of the solar atmosphere, neglecting contributions from polarization. Then the total polarized source vector for the line and the continuum are obtained. In LSA-2, Eddington–Barbier relation (Mihalas, 1978) is employed to calculate the Q and I values using this source vector whereas in LSA-3, a simple formal solution of the radiative transfer equation gives the emergent Stokes Q. The authors model the Ca I 4227 Å line profiles using LSA-3 and compare the modeled profiles with the observations taken at different limb (μ) positions. They show that LSA-3 gives a reasonably good fit to the observed profile that are comparable to the ones obtained by solving the full polarized radiative transfer equation.

In this chapter, our aim is to model the Li I D lines using LSA in order to avoid the computationally difficult radiative transfer calculations. Here, we describe the developments made so far in this regard. This work is in progress. In Section 7.2, we present the outcome of our efforts to compute the Li I D line profiles using the LSA-0 method. We derive the required anisotropy factor, absorption matrix including the effects of PBE, and present the Stokes profiles obtained using the RM derived for the combined theory. We compare the non-magnetic profiles with the quiet Sun observations given in Stenflo (2011). In Section 7.3, we present an extension of the LSA-3 method of Anusha et al. (2010) to include arbitrarily strong magnetic fields. We call this as the extended LSA-3 method.

7.2 The LSA-0 Method

In this section, we describe our attempts to model the Li I D lines using the LSA-0 method of Sampoorna et al. (2009). This method assumes that the polarization of the emergent radiation is determined by the anisotropy of the incident radiation field at the last scattering event. The anisotropy factor is then determined as a function of the wavelength by fitting the limb darkening function obtained from the observed data with a parabolic function and using the limb darkening coefficients from Pierce (2000). This empirical anisotropy profile is then used along with the polarized continuum, the line absorption matrix, and the RM for the single scattering case (which contains all the PRD, collisional, fine and hyperfine structure, isotope shifts, and magnetic field effects) to calculate the Stokes profiles.

7.2.1 CLV of the Li I D Line Intensity

Since the Li I D lines are optically very thin, their intensities can be approximated to the intensities of the continuum at their line center wavelengths (i.e., $I_\lambda(\mu) \backsimeq I_c(\mu)$, where

$\mu = \cos\theta$, with θ being the colatitude). To obtain the CLV of the continuum at Li I D line wavelengths we use the limb darkening function of Neckel (1996) who present the wavelength dependency of the limb darkening coefficients by fitting the continuum data of Neckel & Labs (1994). The limb darkening function is defined as

$$c_\lambda(\mu) = \frac{I_c(\mu)}{I_c(\mu = 1)} \, . \tag{7.1}$$

An IDL program provided by Stenflo, J. O. (through private communication) computes the limb darkening function for a given μ using the wavelength dependent limb darkening coefficients. We use this IDL program to obtain the CLV of the Li I D line intensities. In

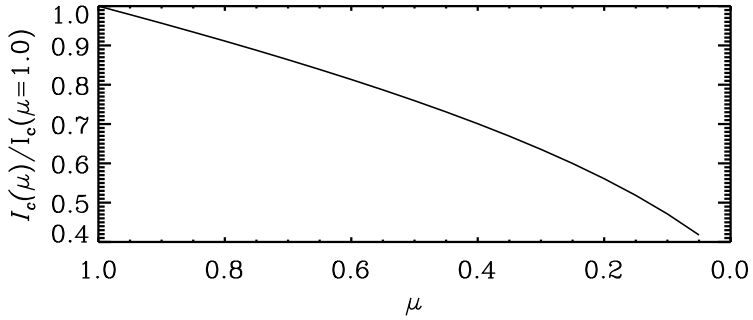

Figure 7.1: CLV of the continuum at $\sim 6708\,$Å.

Figure 7.1 we show the CLV of the continuum at $\sim 6708\,$Å. We use the intensity values obtained in this step for the computation of the anisotropy factor $k_{\mathrm{G},\lambda}(\mu)$ discussed in the next section.

7.2.2 The Anisotropy Factor

The anisotropy factor $k_{\mathrm{G},\lambda}(\mu)$, is obtained by multiplying the Rayleigh phase matrix with an unpolarized Stokes vector of the form $(I, 0, 0, 0)^T$ and integrating it over all incoming angles as

$$k_{\mathrm{G},\lambda}(\mu) = \frac{\mathrm{G}_\lambda(1-\mu^2)}{I_\lambda(\mu)} \, , \tag{7.2}$$

where

$$\mathrm{G}_\lambda = \frac{3}{16}\int_{-1}^{+1}(3\mu'^2 - 1) I_\lambda(\mu')\mathrm{d}\mu' \, . \tag{7.3}$$

Since the limb darkening function is defined only for positive μ, we carry out the integration in the above equation in the limit $0 \leq \mu \leq 1$. The anisotropy factor is flat in the wavelength range that covers the Li I D lines. It has a value of ~ 0.0575 at $\mu = 0.1$.

7.2.3 The Absorption Matrix

In the LSA method, to compute the fractional polarization, we need to take into account the contribution from the absorption probability for the Li I D lines. The Li I D line system can well be represented by a two-term atom model and we need to derive the corresponding absorption matrix in the presence of arbitrary strength fields. In this section, we present this derivation of the PB absorption matrix in the combined theory following Landi Degl'Innocenti & Landolfi (2004). Most of the symbols and notations used carry the same meaning as in Chapter 6, unless indicated otherwise.

We start from the set of Equations (6.88) given in Landi Degl'Innocenti & Landolfi (2004) which are listed below

$$\eta_i^{\rm A}(\nu,\boldsymbol{n}) = \frac{8\pi^3\nu}{ch}\mathcal{N}\sum_{mnn'}\sum_{qq'}(-1)^{q+q'} \times{\rm Re}[(d_{-q})_{mn}(d_{-q'})^*_{mn'}\mathcal{T}_{qq'}(i,\boldsymbol{n})\rho_{nn'}\Phi(\nu_{mn}-\nu)]\ , \tag{7.4}$$

where $\eta_i^{\rm A}(\nu,\boldsymbol{n})$ is the absorption coefficient with the symbol $i = (1,2,3,4)$ representing the Stokes parameters (I,Q,U,V). ν is the frequency and $\boldsymbol{n}$ is the direction of the ray. c is the speed of light, h is the Planck constant, and $\mathcal{N}$ is the total number density of atoms. d_q are the spherical components of the dipole moment operator, $\mathcal{T}_{qq'}$ are the reducible spherical tensors, and $\rho_{nn'}$ are the matrix elements of the density operator. m, n, n' represent a set of eigenvectors which will be defined below, and Φ is the complex profile function with ν_{mn} being the frequency of the transition between the states with eigenvectors m and n. The dispersion coefficient $\rho_i^{\rm A}(\nu,\boldsymbol{n})$ is given by

$$\rho_i^{\rm A}(\nu,\boldsymbol{n}) = \eta_i^{\rm A}(\nu,\boldsymbol{n})\{{\rm Re}\rightarrow{\rm Im}\}\ , \tag{7.5}$$

with $\{{\rm Re}\rightarrow{\rm Im}\}$ meaning that the ${\rm Re}$ (for real part) in last line of Equation (7.4) should be replaced with ${\rm Im}$ (for imaginary part). Substituting in the above equations,

$$m\rightarrow L_bSI_sk_b\mu_b;\quad n\rightarrow L_aSI_sk_a\mu_a;\quad n'\rightarrow L_aSI_sk_{a'}\mu_{a'}\ ,$$

where a and b represent the lower and upper terms, respectively, μ the quantum number of the magnetic substates, and k the subspace spanned by μ (see Chapter 6, also Sowmya et al., 2015b). Making use of the expression for the Wigner–Eckart theorem,

Equations (7.31) and (7.32) of Landi Degl'Innocenti & Landolfi (2004), we arrive at

$$\eta_i^{\rm A}(\nu,\boldsymbol{n}) = \mathcal{N}\frac{h\nu}{4\pi}(2L_a+1)B(L_aSI_s\rightarrow L_bSI_s)\sum_{k_ak_{a'}k_b}\sum_{\mu_a\mu_{a'}\mu_b}\sum_{qq'}3(-1)^{q+q'}$$
$$\times\sum_{J_aJ_{a'}F_aF_{a'}J_bJ_{b'}F_bF_{b'}}(-1)^{J_b+J_{b'}+J_a+J_{a'}}\sqrt{(2J_a+1)(2J_{a'}+1)(2F_a+1)(2F_{a'}+1)}$$
$$\times\sqrt{(2J_b+1)(2J_{b'}+1)(2F_b+1)(2F_{b'}+1)}C^{k_a}_{J_aF_a}(L_aSI_s,\mu_a)C^{k_{a'}}_{J_{a'}F_{a'}}(L_aSI_s,\mu_{a'})$$
$$\times C^{k_b}_{J_bF_b}(L_bSI_s,\mu_b)C^{k_b}_{J_{b'}F_{b'}}(L_bSI_s,\mu_b)\begin{pmatrix}F_b & F_a & 1\\ -\mu_b & \mu_a & -q\end{pmatrix}\begin{pmatrix}F_{b'} & F_{a'} & 1\\ -\mu_b & \mu_{a'} & -q'\end{pmatrix}$$
$$\times\begin{Bmatrix}L_a & L_b & 1\\ J_b & J_a & S\end{Bmatrix}\begin{Bmatrix}L_a & L_b & 1\\ J_{b'} & J_{a'} & S\end{Bmatrix}\begin{Bmatrix}J_a & J_b & 1\\ F_b & F_a & I_s\end{Bmatrix}\begin{Bmatrix}J_{a'} & J_{b'} & 1\\ F_{b'} & F_{a'} & I_s\end{Bmatrix}$$
$$\times{\rm Re}[\mathcal{T}_{qq'}(i,\boldsymbol{n})\rho_{L_aSI_s}(k_a\mu_a,k_{a'}\mu_{a'})\Phi(\nu_{L_bSI_sk_b\mu_b,L_aSI_sk_a\mu_a}-\nu)]\,, \tag{7.6}$$

$$\rho_i^{\rm A}(\nu,\boldsymbol{n}) = \eta_i^{\rm A}(\nu,\boldsymbol{n})\{{\rm Re}\rightarrow{\rm Im}\}\,. \tag{7.7}$$

Here, $B(L_aSI_s\rightarrow L_bSI_s)$ is the Einstein B coefficient. We expand the density matrix elements in the above equations using Equation (7.36) of Landi Degl'Innocenti & Landolfi (2004) as

$$\rho_{L_aSI_s}(k_a\mu_a,k_{a'}\mu_{a'}) = \sum_{K_aQ_a}\sum_{J_{a'''}F_{a'''}}\sum_{J_{a''}F_{a''}}(-1)^{F_{a''}-\mu_a}\sqrt{2K_a+1}$$
$$\times C^{k_{a'}}_{J_{a'''}F_{a'''}}(L_aSI_s,\mu_{a'})C^{k_a}_{J_{a''}F_{a''}}(L_aSI_s,\mu_a)$$
$$\times\begin{pmatrix}F_{a''} & F_{a'''} & K_a\\ \mu_a & -\mu_{a'} & -Q_a\end{pmatrix}{}^{L_aSI_s}\rho^{K_a}_{Q_a}(J_{a''}F_{a''},J_{a'''}F_{a'''})\,. \tag{7.8}$$

where $\rho^{K_a}_{Q_a}$ are the multipolar components of the density matrix. Using the relation (5.156) of Landi Degl'Innocenti & Landolfi (2004) which is

$$\mathcal{T}_{qq'}(i,\boldsymbol{n}) = \sum_{KQ}(-1)^{1+q}\sqrt{\frac{2K+1}{3}}\begin{pmatrix}1 & 1 & K\\ q & -q' & -Q\end{pmatrix}\mathcal{T}^K_Q(i,\boldsymbol{n})\,, \tag{7.9}$$

and the orthogonality relations (5a) and (5b) of Casini & Manso Sainz (2005), we can rewrite Equations (7.6) and (7.7) as

$$\eta_i^{\rm A}(\nu,\boldsymbol{n}) = \mathcal{N}\frac{h\nu}{4\pi}(2L_a+1)B(L_aSI_s\rightarrow L_bSI_s)\sum_{KQ}\sum_{K_aQ_a}\sqrt{3(2K+1)(2K_a+1)}$$

$$
\begin{aligned}
&\times \sum_{k_a k_b} \sum_{J_a J_{a'} J_{a''} F_a F_{a'} F_{a''}} \sum_{J_b J_{b'} F_b F_{b'}} \sum_{\mu_a \mu_{a'} \mu_b} \sum_{q q'} (-1)^{J_b + J_{b'} + J_a + J_{a'} + F_{a''} - \mu_a + q' + 1} \\
&\times \sqrt{(2J_a+1)(2J_{a'}+1)(2F_a+1)(2F_{a'}+1)(2J_b+1)(2J_{b'}+1)(2F_b+1)(2F_{b'}+1)} \\
&\quad \times C^{k_a}_{J_a F_a}(L_a S I_s, \mu_a) C^{k_a}_{J_{a''} F_{a''}}(L_a S I_s, \mu_a) C^{k_b}_{J_b F_b}(L_b S I_s, \mu_b) C^{k_b}_{J_{b'} F_{b'}}(L_b S I_s, \mu_b) \\
&\times \left\{ \begin{array}{ccc} L_a & L_b & 1 \\ J_b & J_a & S \end{array} \right\} \left\{ \begin{array}{ccc} L_a & L_b & 1 \\ J_{b'} & J_{a'} & S \end{array} \right\} \left\{ \begin{array}{ccc} J_a & J_b & 1 \\ F_b & F_a & I_s \end{array} \right\} \left\{ \begin{array}{ccc} J_{a'} & J_{b'} & 1 \\ F_{b'} & F_{a'} & I_s \end{array} \right\} \\
&\times \left(\begin{array}{ccc} F_b & F_a & 1 \\ -\mu_b & \mu_a & -q \end{array} \right) \left(\begin{array}{ccc} F_{b'} & F_{a'} & 1 \\ -\mu_b & \mu_{a'} & -q' \end{array} \right) \left(\begin{array}{ccc} 1 & 1 & K \\ q & -q' & -Q \end{array} \right) \left(\begin{array}{ccc} F_{a''} & F_{a'} & K_a \\ \mu_a & -\mu_{a'} & -Q_a \end{array} \right) \\
&\times \mathrm{Re}[\mathcal{T}^K_Q(i, \boldsymbol{n})\, {}^{L_a S I_s}\rho^{K_a}_{Q_a}(J_{a''} F_{a''}, J_{a'} F_{a'}) \Phi(\nu_{L_b S I_s k_b \mu_b, L_a S I_s k_a \mu_a} - \nu)] \,, \qquad (7.10)
\end{aligned}
$$

$$
\rho^{\mathrm{A}}_i(\nu, \boldsymbol{n}) = \eta^{\mathrm{A}}_i(\nu, \boldsymbol{n}) \{\mathrm{Re} \rightarrow \mathrm{Im}\} \,. \qquad (7.11)
$$

Equations (7.10) and (7.11) represent the general expressions for the absorption coefficients which include polarization intrinsic to the lower term. In order to evaluate these coefficients we need to compute $\rho^{K_a}_{Q_a}$. This can be done by solving the statistical equilibrium equations of the lower term. To be consistent with Chapter 6 wherein we neglect the lower term polarization, we neglect it in this chapter also. This means that the absorption takes place from the equally populated lower states. Following Equations (10.120) and (10.121) of Landi Degl'Innocenti & Landolfi (2004), we represent this approximation mathematically as

$$
\rho_{L_a S I_s}(k_a \mu_a, k_{a'} \mu_{a'}) = \delta_{k_a k_{a'}} \delta_{\mu_a \mu_{a'}} C \,, \qquad (7.12)
$$

and

$$
{}^{L S I_s}\rho^{K_a}_{Q_a}(J_a F_a, J_{a'} F_{a'}) = \delta_{K_a 0} \delta_{Q_a 0} \delta_{J_a J_{a'}} \delta_{F_a F_{a'}} \sqrt{2F_a + 1}\, C \,, \qquad (7.13)
$$

with

$$
C = \frac{1}{(2S+1)(2I_s+1)(2L_a+1)} \frac{N_a}{\mathcal{N}} \,, \qquad (7.14)
$$

where N_a is the population of the lower term. Using this approximation we finally obtain

$$
\begin{aligned}
\eta^{\mathrm{A}}_i(\nu, \boldsymbol{n}) &= N_a \frac{h\nu}{4\pi} \frac{B(L_a S I_s \rightarrow L_b S I_s)}{(2S+1)(2I_s+1)} \sum_{KQ} \sqrt{3(2K+1)} \sum_{k_a k_b} \sum_{J_a J_{a'} F_a F_{a'} J_b J_{b'} F_b F_{b'}} \\
&\times \sum_{\mu_a \mu_b q} (-1)^{J_b + J_{b'} + J_a + J_{a'} + q + 1} \sqrt{(2J_a+1)(2J_{a'}+1)(2F_a+1)(2F_{a'}+1)} \\
&\times \sqrt{(2J_b+1)(2J_{b'}+1)(2F_b+1)(2F_{b'}+1)} \\
&\times C^{k_a}_{J_a F_a}(L_a S I_s, \mu_a) C^{k_a}_{J_{a'} F_{a'}}(L_a S I_s, \mu_a) C^{k_b}_{J_b F_b}(L_b S I_s, \mu_b) C^{k_b}_{J_{b'} F_{b'}}(L_b S I_s, \mu_b)
\end{aligned}
$$

$$\times \left\{ \begin{array}{ccc} L_a & L_b & 1 \\ J_b & J_a & S \end{array} \right\} \left\{ \begin{array}{ccc} L_a & L_b & 1 \\ J_{b'} & J_{a'} & S \end{array} \right\} \left\{ \begin{array}{ccc} J_a & J_b & 1 \\ F_b & F_a & I_s \end{array} \right\} \left\{ \begin{array}{ccc} J_{a'} & J_{b'} & 1 \\ F_{b'} & F_{a'} & I_s \end{array} \right\}$$
$$\times \left(\begin{array}{ccc} F_b & F_a & 1 \\ -\mu_b & \mu_a & -q \end{array} \right) \left(\begin{array}{ccc} F_{b'} & F_{a'} & 1 \\ -\mu_b & \mu_a & -q \end{array} \right) \left(\begin{array}{ccc} 1 & 1 & K \\ q & -q & -Q \end{array} \right)$$
$$\times \mathrm{Re}[\mathcal{T}^K_Q(i,\boldsymbol{n})\Phi(\nu_{L_bSI_sk_b\mu_b,L_aSI_sk_a\mu_a} - \nu)] \,, \tag{7.15}$$

$$\rho^{\mathrm{A}}_i(\nu,\boldsymbol{n}) = \eta^{\mathrm{A}}_i(\nu,\boldsymbol{n})\{\mathrm{Re} \rightarrow \mathrm{Im}\} \,. \tag{7.16}$$

With the help of Equations (7.15) and (7.16), we can write the PB line absorption matrix as

$$\boldsymbol{\Phi}(\nu,\boldsymbol{n}) = \left(\begin{array}{cccc} \eta^{\mathrm{A}}_I & \eta^{\mathrm{A}}_Q & \eta^{\mathrm{A}}_U & \eta^{\mathrm{A}}_V \\ \eta^{\mathrm{A}}_Q & \eta^{\mathrm{A}}_I & \rho^{\mathrm{A}}_V & -\rho^{\mathrm{A}}_U \\ \eta^{\mathrm{A}}_U & -\rho^{\mathrm{A}}_V & \eta^{\mathrm{A}}_I & \rho^{\mathrm{A}}_Q \\ \eta^{\mathrm{A}}_V & \rho^{\mathrm{A}}_U & -\rho^{\mathrm{A}}_Q & \eta^{\mathrm{A}}_I \end{array} \right) \,. \tag{7.17}$$

7.2.3.1 The Absorption Coefficient in the Non-Magnetic Case

In the absence of a magnetic field, the absorption matrix reduces to a scalar function which forms the diagonal element, and is given by the expression

$$\eta^{\mathrm{A}}_I(\nu) = \frac{k_M}{(2S+1)(2I_s+1)} \sum_{J_aF_aJ_bF_b} \sqrt{(2J_a+1)(2F_a+1)(2J_b+1)(2F_b+1)}$$
$$\times \left\{ \begin{array}{ccc} J_a & J_b & 1 \\ F_b & F_a & I_s \end{array} \right\}^2 \left\{ \begin{array}{ccc} L_a & L_b & 1 \\ J_b & J_a & S \end{array} \right\}^2 \phi(\nu_{J_bF_b,J_aF_a} - \nu) \,, \tag{7.18}$$

with

$$k_M = N_a \frac{h\nu}{4\pi} B(L_aSI_s \rightarrow L_bSI_s) \,, \tag{7.19}$$

and

$$\phi(\nu_{J_bF_b,J_aF_a} - \nu) = \mathrm{Re}[\Phi(\nu_{L_bSJ_bI_sF_b,L_aSJ_aI_sF_a} - \nu)] \,, \tag{7.20}$$

where ϕ is the Voigt profile function with line center at $\nu_{J_bF_b,J_aF_a}$. This line center frequency actually corresponds to $\nu_{F_bF_a}$. The indices J_b and J_a are used to label the fine structure states to which the F states belong. We expand Equation (7.18) for the allowed transitions between the F states in ^{6}Li and ^{7}Li isotopes and arrive at

$${}^6\eta^{\mathrm{A}}_I(\nu) = k^6_M \Bigg[\frac{1}{81}\phi(\nu_{\frac{1}{2}\frac{1}{2},\frac{1}{2}\frac{1}{2}} - \nu) + \frac{8}{81}\phi(\nu_{\frac{1}{2}\frac{3}{2},\frac{1}{2}\frac{1}{2}} - \nu) + \frac{8}{81}\phi(\nu_{\frac{1}{2}\frac{1}{2},\frac{1}{2}\frac{3}{2}} - \nu)$$

$$+\frac{10}{81}\phi(\nu_{\frac{1}{2}\frac{3}{2},\frac{1}{2}\frac{3}{2}}-\nu)+\frac{8}{81}\phi(\nu_{\frac{3}{2}\frac{1}{2},\frac{1}{2}\frac{1}{2}}-\nu)+\frac{10}{81}\phi(\nu_{\frac{3}{2}\frac{3}{2},\frac{1}{2}\frac{1}{2}}-\nu)$$
$$+\frac{1}{81}\phi(\nu_{\frac{3}{2}\frac{1}{2},\frac{1}{2}\frac{3}{2}}-\nu)+\frac{8}{81}\phi(\nu_{\frac{3}{2}\frac{3}{2},\frac{1}{2}\frac{3}{2}}-\nu)+\frac{3}{9}\phi(\nu_{\frac{3}{2}\frac{5}{2},\frac{1}{2}\frac{3}{2}}-\nu)\Bigg], \tag{7.21}$$

and

$$^7\eta_I^{\rm A}(\nu)=k_M^7\Bigg[\frac{1}{48}\phi(\nu_{\frac{1}{2}1,\frac{1}{2}1}-\nu)+\frac{5}{48}\phi(\nu_{\frac{1}{2}2,\frac{1}{2}1}-\nu)+\frac{15}{144}\phi(\nu_{\frac{1}{2}1,\frac{1}{2}2}-\nu)$$
$$+\frac{5}{48}\phi(\nu_{\frac{1}{2}2,\frac{1}{2}2}-\nu)+\frac{1}{24}\phi(\nu_{\frac{3}{2}0,\frac{1}{2}1}-\nu)+\frac{15}{144}\phi(\nu_{\frac{3}{2}1,\frac{1}{2}1}-\nu)+\frac{5}{48}\phi(\nu_{\frac{3}{2}2,\frac{1}{2}1}-\nu)$$
$$+\frac{5}{240}\phi(\nu_{\frac{3}{2}1,\frac{1}{2}2}-\nu)+\frac{5}{48}\phi(\nu_{\frac{3}{2}2,\frac{1}{2}2}-\nu)+\frac{7}{24}\phi(\nu_{\frac{3}{2}3,\frac{1}{2}2}-\nu)\Bigg]. \tag{7.22}$$

Here, k_M^6 and k_M^7 are given by Equation (7.19) where the respective lower term populations of ^{6}Li and ^{7}Li are used.

7.2.4 Stokes Profiles Computed Using the LSA-0 Method

Following Sampoorna et al. (2009) we write the polarization in line as

$$P_{Q,\rm line}=\frac{\int R_{21}(\lambda,\lambda',\Theta)k_{{\rm G},\lambda'}(\mu)I_{\lambda'}(\mu=1)d\lambda'}{\int R_{11}(\lambda,\lambda',\Theta)I_{\lambda'}(\mu=1)d\lambda'}, \tag{7.23}$$

$$P_{U,\rm line}=\frac{\int R_{31}(\lambda,\lambda',\Theta)k_{{\rm G},\lambda'}(\mu)I_{\lambda'}(\mu=1)d\lambda'}{\int R_{11}(\lambda,\lambda',\Theta)I_{\lambda'}(\mu=1)d\lambda'}, \tag{7.24}$$

and

$$P_{V,\rm line}=\frac{\int R_{41}(\lambda,\lambda',\Theta)k_{{\rm G},\lambda'}(\mu)I_{\lambda'}(\mu=1)d\lambda'}{\int R_{11}(\lambda,\lambda',\Theta)I_{\lambda'}(\mu=1)d\lambda'}. \tag{7.25}$$

Here, Θ is the scattering angle, and $R_{i1}(\lambda,\lambda',\Theta)$ with $i=1,2,3,4$ are the elements of the first column of the RM computed using the combined theory presented in Chapter 6 (see also Sowmya et al., 2015b).

When modeling the Li I D lines with the LSA method, we have to account for the contribution from the continuum in addition to the contribution from the line. The expressions for the fractional polarization in the presence of continuum then take the form

$$\frac{Q}{I}=S\left[P_{Q,\rm line}\frac{\eta_I^{\rm A}(\lambda,\boldsymbol{n})}{\eta_I^{\rm A}(\lambda,\boldsymbol{n})+C_c}+P_c\frac{C_c}{\eta_I^{\rm A}(\lambda,\boldsymbol{n})+C_c}\right], \tag{7.26}$$

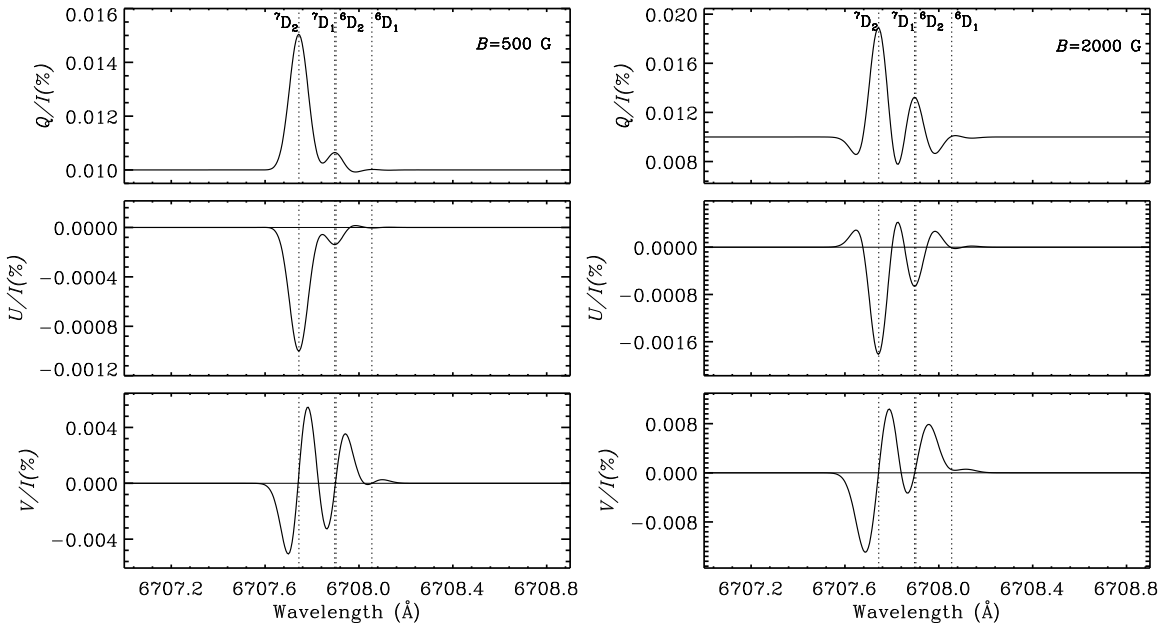

Figure 7.2: Combined Stokes profiles for the Li I D lines for $B = 500\,\mathrm{G}$ (left) and $B = 2000\,\mathrm{G}$ (right). The model parameters used are $S = 1$, $C_c = 40$ and $P_c = 0.009\,\%$.

$$\frac{U}{I} = SP_{U,\mathrm{line}} \frac{\eta_I^{\mathrm{A}}(\lambda, \boldsymbol{n})}{\eta_I^{\mathrm{A}}(\lambda, \boldsymbol{n}) + C_c} \,, \tag{7.27}$$

and

$$\frac{V}{I} = SP_{V,\mathrm{line}} \frac{\eta_I^{\mathrm{A}}(\lambda, \boldsymbol{n})}{\eta_I^{\mathrm{A}}(\lambda, \boldsymbol{n}) + C_c} \,, \tag{7.28}$$

where η_I^{A} is now written in terms of λ. S is the global scaling parameter, C_c is the continuum opacity, and P_c is the continuum polarization.

The Stokes profiles computed using the LSA-0 method, assuming the scattering to be frequency coherent, is presented in Figures 7.2 and 7.3. The contributions from the two isotopes are combined considering their percentage abundances. For the calculation of the Stokes profiles we have used $\mu = 0.1, \chi = 0°, \cos\theta' = \mu' = 1.0$, and $\chi' = 0°$. The magnetic field orientation is given by $(\theta_B, \chi_B) = (90°, 45°)$. The model parameter values used are mentioned in the figure captions. We fix $P_c = 0.009\,\%$ based on Stenflo (2005) and choose a Doppler width of $60\,\mathrm{m\AA}$ (corresponding to $3000\,\mathrm{K}$) following Belluzzi et al. (2009). Since the Li I D lines are optically very thin and produce almost no feature in the intensity spectrum, we assume the continuum to dominate over the line and choose $C_c = 40$. This high value of C_c is needed to obtain the fractional polarization values that are similar to the observed values (see for example Stenflo et al., 2000; Stenflo, 2011; Belluzzi et al., 2009). We expect the radiative transfer calculations to not affect the results

much as the Li I D lines are very weak and hence use the global scaling parameter value as unity.

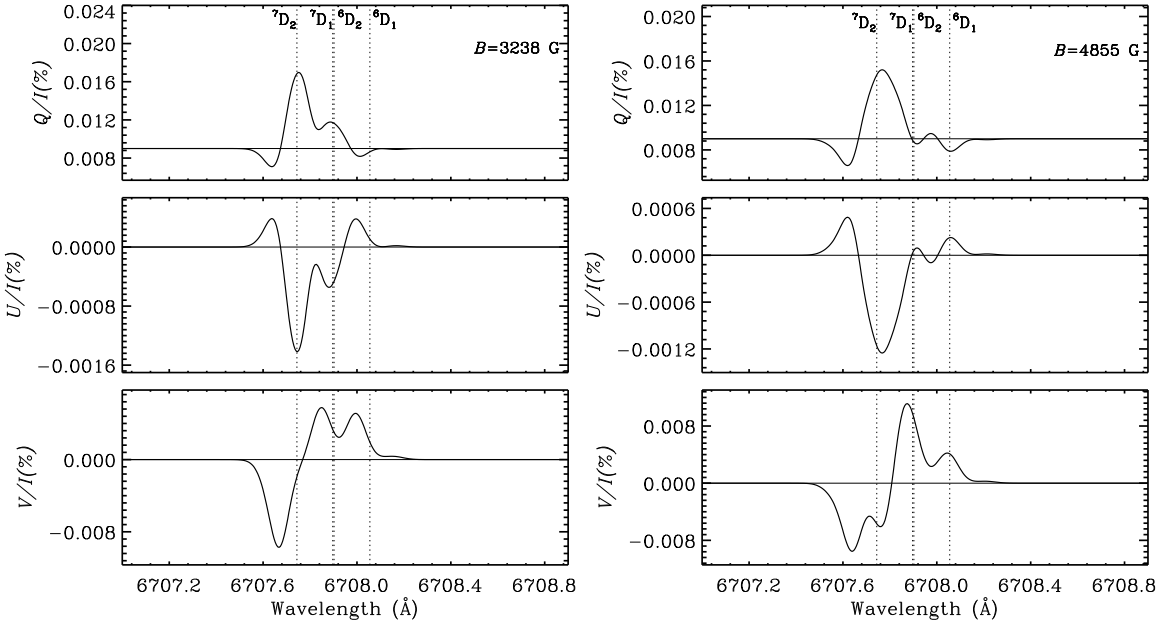

Figure 7.3: Combined Stokes profiles for the Li I D lines for $B = 3238\,\mathrm{G}$ (left) and $B = 4855\,\mathrm{G}$ (right). The model parameters used are $S = 1$, $C_c = 40$ and $P_c = 0.009\,\%$.

We notice that the profiles computed with the LSA-0 method are similar to the ones obtained in a single scattering event shown in Figure 6.10. If we examine Equations (7.26)–(7.28) for the LSA-0 method and Equations (5.15)–(5.16) for the single scattering case, we see that they depend on similar free parameters, namely, the parameters representing the radiation anisotropy, continuum strength and its polarization. The only difference being the global scaling parameter S (that may differ from unity) in the LSA-0 method which is introduced to obtain a match with the profiles obtained by solving the radiative transfer equation fully. Also, the Li D lines are optically thin and therefore, $k_{\mathrm{G},\lambda}$ is spectrally flat across these lines (which is equivalent to using a constant value for β in Equation (5.15)). Therefore, the profiles computed using the LSA-0 method do not differ much from their counterparts for the single scattering case.

7.2.5 Comparison with the Observations

In Figure 7.4 we show the comparison between the non-magnetic theoretical Q/I profile and the observed Q/I profile. Since the observations were recorded in the quiet Sun region, we have first tried to fit it by considering $B = 0\,\mathrm{G}$. The model parameters used in comput-

ing the theoretical profiles using the LSA-0 method of Sampoorna et al. (2009) are given in the figure caption. These values are different from the ones used in Section 7.2.4. We have used a Doppler width of 85 mÅ in order to achieve the required broadening. This Doppler width corresponds to a temperature of about 6000 K. As we can see from the figure, the LSA-0 method gives a reasonable fit to the non-magnetic observations of the Li I D lines.

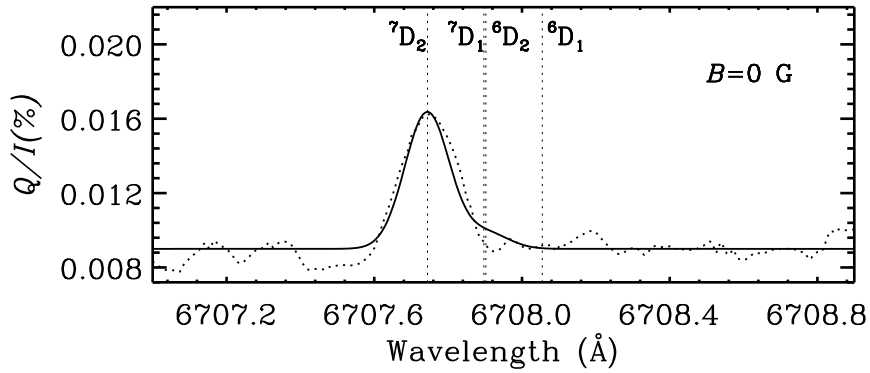

Figure 7.4: Comparison between the observed (dotted) and theoretical (solid) Q/I for the Li I D lines. Observations were taken with ZIMPOL at THEMIS, 5 arcsec inside the E limb of the quiet Sun on June 7, 2008 by Stenflo (see Stenflo, 2011, for more details). The model parameters used to compute the theoretical profile are $S = 1$, $C_c = 55$, $P_c = 0.009$ %, and $B = 0$ G. We have used a Doppler width of 85 mÅ to obtain a match with the observed profile.

LSA-0 method, however, does not take into account the depth dependence of the physical quantities. We saw in the previous section that this method needs free parameters and empirical $k_{\mathrm{G},\lambda}$ as input. In order to eliminate these free parameters, while still being significantly less computationally expensive as compared with a full polarized radiative transfer solution, we use the LSA-3 method of Anusha et al. (2010) which we will discuss in the next section. In LSA-3, the depth dependence of various physical quantities is taken into consideration.

7.3 The LSA-3 Method

In this method, the radiation anisotropy is calculated by solving the scalar radiative transfer equation using a realistic model atmosphere (see Fontenla et al., 1993; Avrett, 1995). PRD-capable multi-level ALI code of Uitenbroek (2001) is used to compute the Stokes I, in the absence of magnetic fields, at all depth points by neglecting the contribution from Q to I. This code is based on the methods described in the papers Rybicki & Hummer (1991, 1992, 1994). The mean intensity and the anisotropy are then calculated using the Stokes

I, from which the source vector is constructed under the LSA (see Anusha et al., 2010, for more details). The emergent Q/I is obtained from this source vector using a formal solver.

7.3.1 Extended LSA-3 Method

The LSA-3 method described in Anusha et al. (2010) considers the case of resonance scattering in the presence of microturbulent magnetic fields. Our aim in this chapter is to develop a method to compute the Stokes profiles of Li I D lines by including the effects of arbitrarily strong deterministic magnetic fields. Therefore we modify the LSA-3 equations of Anusha et al. (2010) to include the effects of deterministic magnetic fields.

The 1D polarized radiative transfer equation in the presence of magnetic fields (see Section 1.8.1) is written as (see also Sampoorna et al., 2008b)

$$\mu \frac{\partial}{\partial \tau} \boldsymbol{I}(\tau, \lambda, \boldsymbol{n}) = (\boldsymbol{\Phi} + r\mathbf{E})\boldsymbol{I}(\tau, \lambda, \boldsymbol{n}) \\ -[(r\mathbf{E} + \epsilon\boldsymbol{\Phi})B_\lambda(\tau)\mathbf{U} + \boldsymbol{S}_{\rm scat}(\tau, \lambda, \boldsymbol{n}) + \beta_c \boldsymbol{S}_c(\tau, \lambda, \boldsymbol{n})] \ . \quad (7.29)$$

Here, $\boldsymbol{I} = [I, Q, U, V]^T$, $\boldsymbol{\Phi}$ is the depth dependent 4×4 line absorption matrix (see Equation (7.17)), $\mathbf{E}$ is the 4×4 unity matrix, $\mathbf{K} = (\boldsymbol{\Phi} + r\mathbf{E})$ is the total absorption matrix where r is the ratio of continuum to line averaged opacity. $B_\lambda(\tau)$ is the Planck function, $\mathbf{U} = [1, 0, 0, 0]^T$ and ϵ is the thermalization parameter. β_c denotes the ratio of continuum scattering coefficient to the line averaged absorption coefficient. The scattering integral $\boldsymbol{S}_{\rm scat}(\tau, \lambda, \boldsymbol{n})$ is given by

$$\boldsymbol{S}_{\rm scat}(\tau, \lambda, \boldsymbol{n}) = \oint \frac{d\boldsymbol{n}'}{4\pi} \int_0^\infty d\lambda' \boldsymbol{R}(\lambda, \lambda', \boldsymbol{n}, \boldsymbol{n}', \tau, \boldsymbol{B}) \boldsymbol{I}(\tau, \lambda', \boldsymbol{n}') \ , \quad (7.30)$$

where $\boldsymbol{R}$ is the RM for the combined theory including PBE. $\boldsymbol{S}_c$ is the continuum source vector scattering according to Rayleigh's law given by

$$\boldsymbol{S}_c(\tau, \lambda, \boldsymbol{n}) = \oint \frac{d\boldsymbol{n}'}{4\pi} \boldsymbol{P}(\boldsymbol{n}, \boldsymbol{n}') \boldsymbol{I}(\tau, \lambda', \boldsymbol{n}') \ , \quad (7.31)$$

where $\boldsymbol{P}(\boldsymbol{n}, \boldsymbol{n}')$ is the well known Rayleigh phase matrix (see Chandrasekhar, 1950). Defining the total optical depth as

$$d\tau^{\rm tot} = d\tau(\eta_I^{\rm A} + r + \beta_c)/\mu \ , \quad (7.32)$$

and using $d\tau$ instead of $d\tau^{\rm tot}$ for simplicity of notation, we rewrite the transfer equation

(7.29) as

$$\frac{\partial}{\partial\tau}\boldsymbol{I}(\tau,\lambda,\boldsymbol{n}) = \frac{(\boldsymbol{\Phi}+r\mathbf{E})}{(\eta_I^{\mathrm{A}}+r+\beta_c)}\boldsymbol{I}(\tau,\lambda,\boldsymbol{n}) - \boldsymbol{S}_{\mathrm{tot}}(\tau,\lambda,\boldsymbol{n})\;, \tag{7.33}$$

where the total source vector $\boldsymbol{S}_{\mathrm{tot}}$ is given by

$$\boldsymbol{S}_{\mathrm{tot}}(\tau,\lambda,\boldsymbol{n}) = \frac{1}{(\eta_I^{\mathrm{A}}+r+\beta_c)}[(r\mathbf{E}+\epsilon\boldsymbol{\Phi})B_\lambda(\tau)\mathbf{U} + \boldsymbol{S}_{\mathrm{scat}}(\tau,\lambda,\boldsymbol{n}) + \beta_c\boldsymbol{S}_c(\tau,\lambda,\boldsymbol{n})]\;. \tag{7.34}$$

The dominant contribution to $\boldsymbol{S}_{\mathrm{scat}}$ comes from $I(\tau,\lambda,\boldsymbol{n})$. Therefore we neglect the contributions from (Q,U,V). In other words, in the integral in Equation (7.30) we replace the incident Stokes vector $\boldsymbol{I}$ by $[I,0,0,0]^T$. With this replacement, only the contribution from the first column of the $\boldsymbol{R}$ matrix becomes relevant. Thus the expressions for the total source vector components including the contribution from the polarized continuum take the following simple form under LSA-3

$$\begin{aligned}[S_I(\tau,\lambda,\boldsymbol{n})]_{\mathrm{LSA-3}} &= \frac{[r(\tau,\lambda)+\epsilon(\tau)\eta_I^{\mathrm{A}}(\tau,\lambda)]}{[\eta_I^{\mathrm{A}}(\tau,\lambda)+r(\tau,\lambda)+\beta_c(\tau,\lambda)]}B_\lambda(\tau)\\ &+ \oint\frac{d\boldsymbol{n}'}{4\pi}\int_0^\infty d\lambda'\frac{R_{11}(\lambda,\lambda',\boldsymbol{n},\boldsymbol{n}',\tau,\boldsymbol{B})}{[\eta_I^{\mathrm{A}}(\tau,\lambda)+r(\tau,\lambda)+\beta_c(\tau,\lambda)]}I(\tau,\lambda',\boldsymbol{n}')\\ &+ \oint\frac{d\boldsymbol{n}'}{4\pi}\frac{\beta_c(\tau,\lambda)P_{11}(\boldsymbol{n},\boldsymbol{n}')}{[\eta_I^{\mathrm{A}}(\tau,\lambda)+r(\tau,\lambda)+\beta_c(\tau,\lambda)]}I(\tau,\lambda',\boldsymbol{n}')\;,\end{aligned} \tag{7.35}$$

$$\begin{aligned}[S_Q(\tau,\lambda,\boldsymbol{n})]_{\mathrm{LSA-3}} &= \frac{\epsilon(\tau)\eta_Q^{\mathrm{A}}(\tau,\lambda)B_\lambda(\tau)}{[\eta_I^{\mathrm{A}}(\tau,\lambda)+r(\tau,\lambda)+\beta_c(\tau,\lambda)]}\\ &+ \oint\frac{d\boldsymbol{n}'}{4\pi}\int_0^\infty d\lambda'\frac{R_{21}(\lambda,\lambda',\boldsymbol{n},\boldsymbol{n}',\tau,\boldsymbol{B})}{[\eta_I^{\mathrm{A}}(\tau,\lambda)+r(\tau,\lambda)+\beta_c(\tau,\lambda)]}I(\tau,\lambda',\boldsymbol{n}')\\ &+ \oint\frac{d\boldsymbol{n}'}{4\pi}\frac{\beta_c(\tau,\lambda)P_{21}(\boldsymbol{n},\boldsymbol{n}')}{[\eta_I^{\mathrm{A}}(\tau,\lambda)+r(\tau,\lambda)+\beta_c(\tau,\lambda)]}I(\tau,\lambda',\boldsymbol{n}')\;,\end{aligned} \tag{7.36}$$

$$\begin{aligned}[S_U(\tau,\lambda,\boldsymbol{n})]_{\mathrm{LSA-3}} &= \frac{\epsilon(\tau)\eta_U^{\mathrm{A}}(\tau,\lambda)B_\lambda(\tau)}{[\eta_I^{\mathrm{A}}(\tau,\lambda)+r(\tau,\lambda)+\beta_c(\tau,\lambda)]}\\ &+ \oint\frac{d\boldsymbol{n}'}{4\pi}\int_0^\infty d\lambda'\frac{R_{31}(\lambda,\lambda',\boldsymbol{n},\boldsymbol{n}',\tau,\boldsymbol{B})}{[\eta_I^{\mathrm{A}}(\tau,\lambda)+r(\tau,\lambda)+\beta_c(\tau,\lambda)]}I(\tau,\lambda',\boldsymbol{n}')\;,\end{aligned} \tag{7.37}$$

and

$$[S_V(\tau,\lambda,\boldsymbol{n})]_{\mathrm{LSA-3}} = \frac{\epsilon(\tau)\eta_V^{\mathrm{A}}(\tau,\lambda)B_\lambda(\tau)}{[\eta_I^{\mathrm{A}}(\tau,\lambda)+r(\tau,\lambda)+\beta_c(\tau,\lambda)]}$$

$$+ \oint \frac{d\boldsymbol{n}'}{4\pi} \int_0^\infty d\lambda' \frac{R_{41}(\lambda, \lambda', \boldsymbol{n}, \boldsymbol{n}', \tau, \boldsymbol{B})}{[\eta_I^{\rm A}(\tau, \lambda) + r(\tau, \lambda) + \beta_c(\tau, \lambda)]} I(\tau, \lambda', \boldsymbol{n}') \; . \tag{7.38}$$

Here, $P_{\rm ij}$ are the elements of the Rayleigh phase matrix. The emergent $Q/I, U/I$, and V/I profiles can be obtained by using the source terms constructed above, in the formal solution of the transfer equation. The Stokes profiles can then be calculated for various magnetic field strengths and orientations, in order to understand the influence of the magnetic field.

However, this is a challenging task because of the complications related to the computation of the elements of the RM. If we treat only the frequency coherent scattering processes in the atom's rest frame, neglecting collisions, then we can replace $R_{ij}(\lambda, \lambda', \boldsymbol{n}, \boldsymbol{n}', \tau, \boldsymbol{B})$ with $R_{ij}^{\rm II}(\lambda, \lambda', \boldsymbol{n}, \boldsymbol{n}', \tau, \boldsymbol{B})$. In that case, for a given combination of the magnetic field parameters, incoming and outgoing radiation angles, the time take taken for the computation of the RM for a single depth point is ~ 29 hrs. It becomes computationally very difficult to calculate the RM elements over grids of depth, radiation angles and magnetic field variables. Because of this practical difficulty, we are unable to compute the Stokes profiles using the LSA-3 method. We are currently trying to devise numerical methods with reasonable approximations which will help us overcome this problem to an extent. These methods can be tested by applying them to reproduce the known benchmarks. This work is in progress.

7.4 Conclusions

In this chapter, we have tried to model the Li I D lines at 6807 Å using the last scattering approximation to avoid numerical complications which arise while performing detailed radiative transfer calculations. We first used the LSA-0 method of Sampoorna et al. (2009) to compute the polarization profiles of these lines. We found that the LSA-0 method gives results which are nearly indistinguishable from the results obtained in a single scattering event (see for e.g., Chapter 6). A comparison of the Q/I profile obtained from the LSA-0 method with the non-magnetic observations shows that the observations are reproduced reasonably well by this method.

However, the LSA-0 method uses free parameters. In order to get rid of these free parameters and to consider the effects due to the atmosphere, we chose to use the LSA-3 method of Anusha et al. (2010) which is computationally less expensive (as compared to the full transfer computations) as only the scalar radiative transfer equation is solved instead of the full polarized radiative transfer equation. We extended this method of Anusha et al. (2010) to include the effects due to deterministic magnetic fields of arbitrary strengths.

We have not yet succeeded in computing the Stokes profiles using the extended LSA-3 method because of the challenges discussed in the previous section. We are now working at developing the numerical methods to surpass these problems. This project forms an extension of the thesis work in the future.

8

SUMMARY AND FUTURE PROSPECTS

The study of solar magnetic fields is of profound importance as they dictate the structural evolution of the Sun. They also directly influence the space weather which has direct implications for the Earth. Several methods are employed in order to measure their strength and distribution in the solar atmosphere. One such method involves extracting the magnetic field parameters from the polarization of the light emitted by the Sun, via the Zeeman and Hanle effects. Zeeman effect is the most popular measurement technique in use. It uses the fact that the lines formed in the magnetic regions are split by the magnetic field and the amount of splitting is directly proportional to the field strength B. The limitation of the Zeeman effect is that it is insensitive to weak and turbulent fields. To explore weak magnetic fields, Hanle effect was proposed as a tool for the field measurements. Hanle effect is sensitive to weak fields which are inaccessible to the Zeeman effect. However, these tools are not sufficient to encompass the field strength regimes observationally detected on the Sun. This is because the Zeeman and Hanle effects do not fully account for various interference phenomena occurring between the magnetic sustates belonging to different fine or hyperfine structure states. For many atomic lines, this type of interference occurs for the field strengths prevailing on the Sun. This effect of the magnetic field, called the Paschen–Back effect, can serve as a diagnostic tool complementary to the Hanle and Zeeman effects.

8.1 Summary

In Chapter 1, we introduced some of the basic concepts which were necessary for understanding the contents of the rest of the thesis. In the first part of the thesis, we focused

our attention on understanding the influence of blend lines on the main line of interest. Modeling any spectral line in the second solar spectrum for determining the physical quantities like magnetic field, abundances etc., requires a proper treatment of the blend lines. Blend lines are generally treated to be formed in local thermodynamic equilibrium conditions and are assumed to possess no intrinsic polarization of their own. We proposed a formalism where, in addition to the main line, the blend lines are also treated in non-local thermodynamic equilibrium conditions. Our formalism allows the blend lines to have intrinsic polarization. It is also capable of treating any number of blend lines that lie in the wavelength range of interest. By considering the lines formed in an isothermal atmosphere, we showed that the effects of polarized blend lines are significant when they are relatively strong and lie very close to the main line.

With a motivation to explore the usefulness of Paschen–Back effect in atomic states for extracting the information on distribution of solar magnetic fields, we developed the necessary primary theoretical framework, namely, the derivation of the redistribution matrix. We formulated the theory of Paschen–Back effect in atomic states accounting for the effects of partial frequency redistribution. We first dealt with Paschen–Back effect in a two-level atom with hyperfine structure and developed the formulation for this process by following the Kramers–Heisenberg scattering matrix approach. For simplicity, we assumed the lower levels to be unpolarized and accounted for Paschen–Back effect in only the upper levels. We checked the correctness of the formulation by reproducing the known and available theoretical benchmarks on the Na I D_2 line polarization. We identified the signatures of Paschen–Back effect on polarization in the case where the incident unpolarized light is singly scattered in a direction perpendicular to the direction of incidence.

The next logical step was to explore the influence of Paschen–Back effect in fine structure states on the Stokes parameters. Therefore, we took up the problem of Paschen–Back effect in a two-term atom without hyperfine structure and derived the required redistribution matrix following the Kramers–Heisenberg approach. We studied its properties in a single $90°$ scattering of the incident unpolarized radiation. We used Li I D lines at $6708\,\text{Å}$ for this purpose because it is only for this system that one can expect to see Paschen–Back effect in fine structure states for the magnetic field strengths that one encounters on the Sun. For this atomic system, the fine structure splitting in the ^{2}P term is about $0.15\,\text{Å}$ and Paschen–Back effect sets in for fields stronger than $2000\,\text{G}$. Such strong fields are known to be present in sunspots.

The polarization of some of the diagnostically important spectral lines in the second solar spectrum is a result of the combined effects of fine and hyperfine structure. Therefore, we developed a more general theory which treats the F- and J-state interference

processes together, considering a two-term atom with hyperfine structure. We followed the same procedure that we employed for the cases discussed above and arrived at a general expression for the redistribution matrix, which reduces to the expressions for the redistribution matrices derived in Chapters 4 and 5, when fine and hyperfine structure respectively, are neglected. Keeping in mind the relevance to solar applications, we again used Li I D lines at $6708\,\text{Å}$ for testing the redistribution matrix. We identified a multitude of effects, such as level-crossing, avoided crossing, quantum interference, alignment-to-orientation conversion mechanism etc., caused by the magnetic field in the Paschen–Back regime.

The radiation field undergoes multiple scattering before it escapes from the solar atmosphere. When modeling the lines in the second solar spectrum, one has to account for the radiative transfer effects in the atmosphere. This can be done by using the redistribution matrix (in the Paschen–Back regime), in the polarized radiative transfer equation, and solving it using the available models which closely mimic the solar atmosphere. However, it takes huge computational resources to perform this task, as a large number of transitions are involved in the Paschen–Back regime. Also, the radiation and magnetic field parameter domains that one has to consider while solving the transfer equation are large. Devising the numerical methods to solve the transfer equation in the presence of arbitrary magnetic fields is challenging. To avoid the numerical complications, a simple approach, called the last scattering approximation (LSA) method is proposed.

As the Li I D lines are weak and optically very thin, the transfer effects are not expected to play a major role in shaping these line profiles. Hence we used different levels of LSA method to model these lines. We found that the LSA-0 method nearly reproduces the observed profiles in the quiet Sun. We presented the theoretical Stokes profiles obtained using the LSA-0 method for various values of B. We also presented the extended LSA-3 method which can be used to generate Stokes profiles and later compare them with the observations when they are available.

8.2 Future Work

In this section, we briefly discuss the possible ways to expand the work already carried out in this thesis and its application to better understand the Sun with a particular interest in the surface magnetic fields.

For the radiative transfer calculations carried out in Chapters 2 and 3 with blend lines, we used isothermal atmospheres. The real solar atmosphere, however, is not a constant property medium and is not isothermal. Therefore, the computations in Part I can be extended for realistic solar model atmospheres. This enables us to decipher the effects of

blend lines on main line polarization in a more transparent manner. We can then attempt to model some of the observations recorded in the solar spectrum using these new computations with blend lines. For example, we can apply this theory to extend the efforts by Anusha et al. (2010, 2011b) and Supriya et al. (2014, 2015) to model the observations of Ca I 4227 Å line which exhibits the highest degree of polarization in the second solar spectrum.

In Chapters 4, 5, and 6, we identified the signatures of Paschen–Back effect such as nonlinear splitting, level-crossing, anti-level-crossing, non-zero net circular polarization etc., considering various atomic systems. Our ultimate goal is to use Paschen–Back effect, like the Hanle and Zeeman effects, to diagnose solar or stellar magnetic fields. We know that in the case of Zeeman effect, the fact that the wavelength shift produced by the magnetic field is directly proportional to its strength, is used to obtain information about the field strength in the line of sight. Through the analysis carried out in this thesis, we know that the nonlinear wavelength shift produced by the magnetic field gives rise to asymmetric Stokes V profiles. In addition to this, the alignment-to-orientation conversion mechanism also contributes to the asymmetry. Using this information, an attempt can be made to quantitatively express the relation between the amount of net circular polarization and the field strength B. Polarization diagrams presented by us along with those of the similar kind shown in Anusha et al. (2011b) can also be used in this regard. This will then enable one to ascertain the use of Paschen–Back effect as a tool to diagnose the magnetic structuring of the solar atmosphere.

While formulating the theory of quantum interference between the atomic states in the presence of a magnetic field, in Part II, we assumed the lower levels to be unpolarized and infinitely sharp. This assumption is valid in cases where the lower levels have the quantum numbers $J = 0$ or $1/2$, as the lower level polarization becomes zero due to equally populated magnetic substates and also due to symmetry considerations. Moreover, if the $J = 1/2$ state undergoes hyperfine structure splitting, then the resulting hyperfine structure states can get polarized. We also neglected Paschen–Back effect occurring in the lower levels. Another possible future task is to extend the Kramers–Heisenberg formalism used in this thesis to account for the polarization of the lower levels following the foundations laid by Stenflo (2015b) and Landi Degl'Innocenti & Landolfi (2004, see also Supriya et al. 2016).

In Chapter 7, we have presented the Stokes profiles computed using the LSA-0 method for a given magnetic field configuration. We have also developed the extended LSA-3 method, but have not presented results obtained with this method. The immediate plan of action is to develop a numerical method to handle the modified LSA-3 equations and com-

pute the Stokes parameters using the solar model atmospheres for a set of magnetic field strengths and orientations. Due to the lack of magnetic observations of Li I line polarization we cannot compare our results with the observations. A possibility is to record magnetic observations of other spectral lines which are sensitive to Paschen–Back effect and apply the formulation of Part II, and the extended LSA-3 method to model those observations.

For some of the strong resonance lines, the radiative transfer effects are important. The magnetic field diagnostics using these lines require a proper solution of the polarized radiative transfer equation in the presence of magnetic fields. In such cases, the LSA-3 method may not suffice (the results from the LSA-3 method may greatly deviate from what is observed). One has to carry out detailed transfer calculations which are computationally expensive. Therefore, faster numerical methods have to be devised in order to overcome the challenges of solving the full transfer equation in large parameter domains. This task, along with the others mentioned above, form important steps ahead in the modeling of spectral lines and gives an opportunity to explore a wide range of possibilities to map and study the magnetic field distribution.

APPENDICES

A

TRANSITION AMPLITUDE APPROACH

In this appendix, we present an alternate derivation of the RM for the F-state interference process derived in Chapter 4, following the approach given in Section 3 of Shapiro et al. (2007). In the presence of a magnetic field, F states undergo a mixing, because of which F no longer remains a good quantum number. However the projection of F on the magnetic axis, namely μ, is a good quantum number and the magnetic components can be classified into three groups characterized by $\Delta\mu = \mu_b - \mu_a = 0, \pm 1$. The symbols used have the same meaning as in Chapter 4.

To derive the coherency matrix, the starting point is to calculate the elements of the Jones matrix from the Kramers–Heisenberg formula

$$w_{\alpha\beta} \sim \sum_{i_b\mu_b} \frac{\langle J_f I_s i_f \mu_f | \mathbf{r}\cdot\mathbf{e}_\alpha | J_b I_s i_b \mu_b\rangle \langle J_b I_s i_b \mu_b | \mathbf{r}\cdot\mathbf{e}_\beta | J_a I_s i_a \mu_a\rangle}{\omega_{bf} - \omega - \mathrm{i}\gamma/2} \,. \tag{A.1}$$

We expand the dot product using spherical vectors, and rewrite the above equation as

$$\begin{aligned} w_{\alpha\beta} \sim \sum_{i_b\mu_b} \langle J_f I_s i_f \mu_f | \sum_q r_q \varepsilon_q^{\alpha^*} | J_b I_s i_b \mu_b\rangle \langle J_a I_s i_a \mu_a | \sum_{q'} r_{q'} \varepsilon_{q'}^{\beta^*} | J_b I_s i_b \mu_b\rangle^* \\ \times \Phi_\gamma(\nu_{i_b\mu_b i_f\mu_f} - \xi) \,. \end{aligned} \tag{A.2}$$

This can be further written as

$$w_{\alpha\beta} \sim \sum_{i_b\mu_b} \sum_{qq'} (-1)^{q-q'} \mathcal{Q}^{i_b\mu_b}_{i_f\mu_f} \mathcal{Q}^{i_b\mu_b}_{i_a\mu_a} \varepsilon_q^\alpha \varepsilon_{q'}^{\beta^*} \Phi_\gamma(\nu_{i_b\mu_b i_f\mu_f} - \xi) \,. \tag{A.3}$$

Here, $q = \mu_b - \mu_f$ and $q' = \mu_b - \mu_a$. $\mathcal{Q}$ is the amplitude of the transition between the upper and lower levels. In the atomic rest frame, we take the bilinear product of the Jones matrix

elements, and write the coherency matrix as

$$\mathbf{W} = \sum_{i_a\mu_a i_f\mu_f} \sum_{i_b\mu_b i_{b'}\mu_{b'}} A^{\mu_a\mu_f\mu_b\mu_{b'}}_{i_a i_f i_b i_{b'}} \Gamma(q,q',q'',q''') \cos\beta_{i_{b'}\mu_{b'} i_b\mu_b} \mathrm{e}^{\mathrm{i}\beta_{i_{b'}\mu_{b'} i_b\mu_b}} \times \Phi^{\gamma}_{i_b\mu_b i_{b'}\mu_{b'} i_a\mu_a}(\xi') \delta(\xi - \xi' - \nu_{i_a\mu_a i_f\mu_f}) \,. \tag{A.4}$$

Here, A contains all the four $\mathcal{Q}$s representing transition amplitudes. It is given by

$$A^{\mu_a\mu_f\mu_b\mu_{b'}}_{i_a i_f i_b i_{b'}} = \mathcal{Q}^{i_b\mu_b}_{i_f\mu_f} \mathcal{Q}^{i_b\mu_b}_{i_a\mu_a} \mathcal{Q}^{i'_b\mu'_b}_{i_f\mu_f} \mathcal{Q}^{i'_b\mu'_b}_{i_a\mu_a} \,. \tag{A.5}$$

$\Gamma(q,q',q'',q''')$ is a 4×4 matrix containing the bilinear product of the geometrical factors, expressed as

$$\Gamma(q,q',q'',q''') = \varepsilon^{\alpha}_{q} \varepsilon^{\beta^*}_{q'} \varepsilon^{\alpha'^*}_{q''} \varepsilon^{\beta'}_{q'''} \,. \tag{A.6}$$

To transform Equation (A.4) to the laboratory frame, we follow the steps described in Section 2.2 of Sampoorna et al. (2007a). In the laboratory frame, Equation (A.4) then takes the form

$$\mathbf{W} = \sum_{i_a\mu_a i_f\mu_f} \sum_{i_b\mu_b i_{b'}\mu_{b'}} A^{\mu_a\mu_f\mu_b\mu_{b'}}_{i_a i_f i_b i_{b'}} \Gamma(q,q',q'',q''') \cos\beta_{i_{b'}\mu_{b'} i_b\mu_b} \mathrm{e}^{\mathrm{i}\beta_{i_{b'}\mu_{b'} i_b\mu_b}} \times [(h^{\mathrm{II}}_{i_b\mu_b, i_{b'}\mu_{b'}})_{i_a\mu_a i_f\mu_f} + \mathrm{i}(f^{\mathrm{II}}_{i_b\mu_b, i_{b'}\mu_{b'}})_{i_a\mu_a i_f\mu_f}] \,. \tag{A.7}$$

Finally, the Mueller matrix $\mathbf{M}$ (Section 1.1) that relates the scattered Stokes vector to the incident Stokes vector is given by

$$\mathbf{M} = \mathbf{T}\mathbf{W}\mathbf{T}^{-1} \,, \tag{A.8}$$

where $\mathbf{T}$ and $\mathbf{T}^{-1}$ are purely mathematical transformation matrices (see Stenflo, 1998, and Section 1.1 for the forms of these matrices). The Mueller matrix $\mathbf{M}$ given in Equation (A.8) is obtained in the magnetic reference frame, and it needs to be transformed to the atmospheric reference frame for use in the radiative transfer equation. This is done following the steps given in Appendix D of Sampoorna et al. (2007b). The matrix $\mathbf{M}$ is related to the RM $\boldsymbol{R}$ through the relation

$$\boldsymbol{R} = \frac{1}{N}\mathbf{M} \,, \tag{A.9}$$

where N is the normalization constant.

B

PBE IN HYPERFINE STRUCTURE STATES OF LITHIUM

In this appendix, we apply the theory of PBE in hyperfine structure states developed in Chapter 4 including the effects of PRD to the case of Li I D_2 lines (see Sowmya et al., 2015a). We consider both the stable isotopes of Li, namely ^{6}Li and ^{7}Li. All the relevant atomic parameters for both the isotopes (including their abundance) are taken from Table 1 of Belluzzi et al. (2009). For the computation of Stokes profiles, we use the geometry given

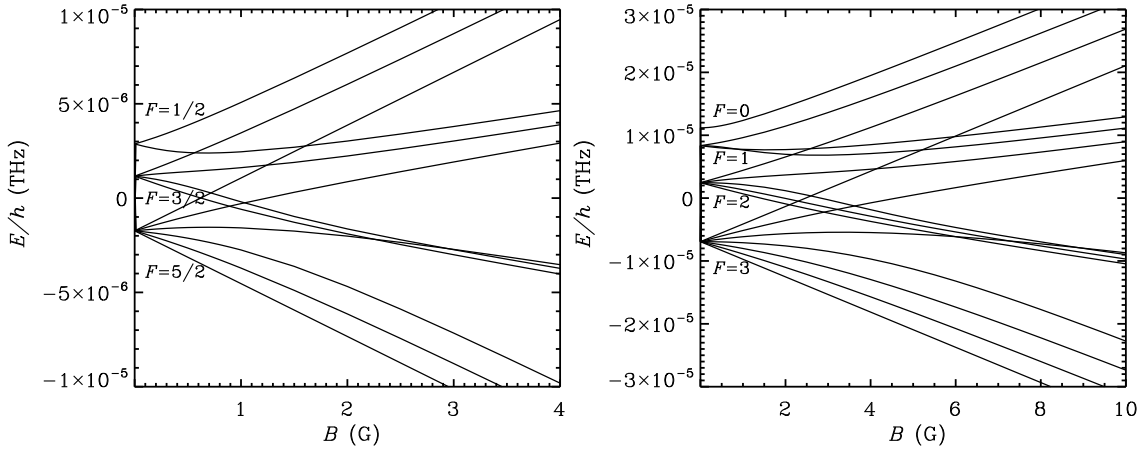

Figure B.1: Energies of the hyperfine structure states as a function of B for ^{6}Li (left panel) and ^{7}Li (right panel).

in Figure 4.2. Following Belluzzi et al. (2009) we choose the Doppler width as $60\,$mÅ. Because the lithium lines are optically thin and as only single scattering is considered here, the Stokes profiles computed for the two isotopes are added after weighting them with their

percentage abundances, to obtain the actual scattered Stokes profiles from both isotopes together.

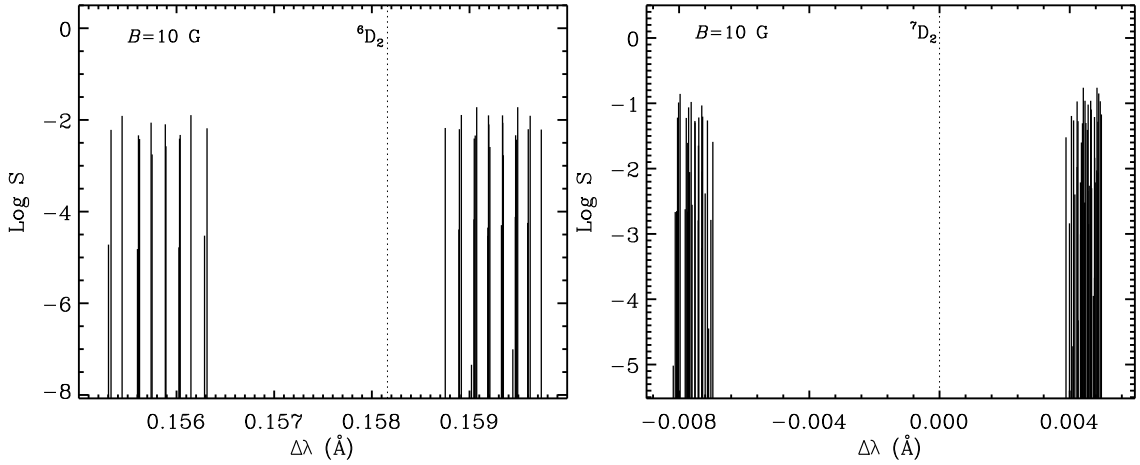

Figure B.2: Line splitting diagrams for D_2 lines of ^{6}Li (left panel) and ^{7}Li (right panel).

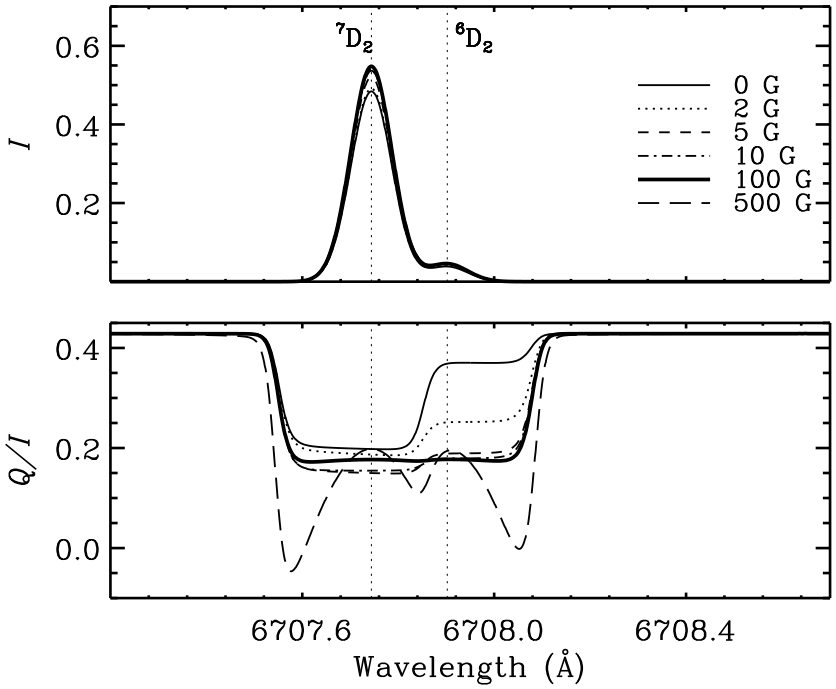

Figure B.3: The scattered Stokes profiles in the presence of a vertical magnetic field. The geometry for scattering is shown in Figure 4.2.

As described earlier, the PB regime is characterized by the crossing of magnetic substates belonging to different hyperfine structure states. The magnetic substates belonging

to hyperfine structure states of ^{6}Li (nuclear spin, $I_s = 1$) show 9 crossings corresponding to magnetic fields in the range $0 - 4\,$G (see left panel of Figure B.1) while those of ^{7}Li ($I_s = 3/2$) show 14 crossings in the range $0 - 10\,$G (see right panel of Figure B.1). Because of the relatively smaller HFS (in comparison to the FS), the fields required to enter the PB regime are much smaller in the case of hyperfine structure states.

Another characteristic of the PB regime is the nonlinearity of the MS. In the linear Zeeman regime, the magnetic components are symmetrically displaced about the line center position while in the PB regime, they are displaced asymmetrically. Line splitting diagrams for the magnetic components resulting from the transitions between the magnetic substates belonging to the hyperfine structure states of D_2 lines of ^{6}Li and ^{7}Li are respectively shown in left and right panels of Figure B.2. One can clearly notice the asymmetric splitting of the magnetic components caused by the PBE.

In Figure B.3, we present the Stokes profiles obtained in the presence of a vertical magnetic field ($\beta = 90°$, see Figure 4.2) for the hyperfine structure case involving only the D_2 lines of ^{6}Li and ^{7}Li weighted by their respective abundances. The intensity profiles remain almost unaffected as the MS is too small to produce any significant broadening. We see a decrease in Q/I with the increasing field strength followed by an increase. For stronger fields, signatures of the transverse Zeeman effect are seen. The Stokes U and V are zero owing to the chosen geometry.

C

THE PSS FOR THE COMBINED THEORY

PSS is a basic test for checking the correctness of the eigenvalues and eigenvectors obtained from a diagonalization procedure, for a given problem. Landi Degl'Innocenti & Landolfi (2004) provides a detailed description of the PSS. In Landi Degl'Innocenti & Landolfi (2004), the manifestations of PSS are given separately for (a) a two-level atom with hyperfine structure and (b) a two-term atom exhibiting only FS. In this appendix, we formulate the PSS for the case of a two-term atom exhibiting both FS and HFS. We basically follow the same procedure as described in Landi Degl'Innocenti & Landolfi (2004) to derive the expression for the centers of gravity in frequency of the magnetic components.

The strengths of the magnetic components are given by

$$\mathcal{S}_q^{k_a\mu_a,k_b\mu_b} = |\langle L_a S I_s, k_a\mu_a|\mathrm{r}_q|L_b S I_s, k_b\mu_b\rangle|^2 \,, \tag{C.1}$$

which are essentially the square of the complex amplitude of the transition between the lower term (quantities with subscripts a) and the upper term (quantities with subscripts b). r_q are the spherical components of the dipole moment operator. Using the basis expansion defined in Equation (6.4), the Wigner–Eckart theorem and its corollary, we expand the above equation as

$$\begin{aligned}
\mathcal{S}_q^{k_a\mu_a,k_b\mu_b} &= (2L_a+1) \sum_{J_a J_{a'} J_b J_{b'} F_a F_{a'} F_b F_{b'}} (-1)^{J_a+J_{a'}+J_b+J_{b'}} \\
&\times C^{k_a}_{J_a F_a}(L_a S I_s, \mu_a) C^{k_a}_{J_{a'} F_{a'}}(L_a S I_s, \mu_a) C^{k_b}_{J_b F_b}(L_b S I_s, \mu_b) C^{k_b}_{J_{b'} F_{b'}}(L_b S I_s, \mu_b) \\
&\times \sqrt{(2J_a+1)(2J_{a'}+1)(2J_b+1)(2J_{b'}+1)(2F_a+1)(2F_{a'}+1)(2F_b+1)(2F_{b'}+1)}
\end{aligned}$$

$$\times \left\{ \begin{array}{ccc} L_a & L_b & 1 \\ J_b & J_a & S \end{array} \right\} \left\{ \begin{array}{ccc} L_a & L_b & 1 \\ J_{b'} & J_{a'} & S \end{array} \right\} \left\{ \begin{array}{ccc} J_a & J_b & 1 \\ F_b & F_a & I_s \end{array} \right\} \left\{ \begin{array}{ccc} J_{a'} & J_{b'} & 1 \\ F_{b'} & F_{a'} & I_s \end{array} \right\}$$
$$\times \left(\begin{array}{ccc} F_b & F_a & 1 \\ -\mu_b & \mu_a & -q \end{array} \right) \left(\begin{array}{ccc} F_{b'} & F_{a'} & 1 \\ -\mu_b & \mu_a & -q \end{array} \right) |\langle L_a||\mathbf{r}||L_b\rangle|^2 \,, \tag{C.2}$$

with, $q = 0$ for π, $+1$ for σ_r, and -1 for the σ_b components. The transitions connecting the upper and the lower terms obey the selection rules $\Delta L = 0, \pm 1$, $\Delta S = 0$, $\Delta I_s = 0$, and $\Delta\mu = \mu_b - \mu_a = 0, \pm 1$. Summing the expression for the unnormalized strengths over all the possible transitions, making use of the orthogonality property of the C coefficients given in Equation (5a) of Casini & Manso Sainz (2005) and Equations (2.23a) and (2.39) of Landi Degl'Innocenti & Landolfi (2004), we obtain

$$\sum_{k_a k_b \mu_a \mu_b} \mathcal{S}_q^{k_a \mu_a, k_b \mu_b} = \frac{1}{3}(2L_a + 1)(2S + 1)(2I_s + 1)|\langle L_a||\mathbf{r}||L_b\rangle|^2 \,. \tag{C.3}$$

Making use of the condition that

$$\sum_{k_a k_b \mu_a \mu_b} \mathcal{S}_q^{k_a \mu_a, k_b \mu_b} = 1 \,, \tag{C.4}$$

we write the expression for the normalized strengths as

$$\begin{aligned} \mathcal{S}_q^{k_a \mu_a, k_b \mu_b} = {} & \frac{3}{(2S+1)(2I_s+1)} \sum_{J_a J_{a'} J_b J_{b'} F_a F_{a'} F_b F_{b'}} (-1)^{J_a + J_{a'} + J_b + J_{b'}} \\ & \times C^{k_a}_{J_a F_a}(L_a S I_s, \mu_a) C^{k_a}_{J_{a'} F_{a'}}(L_a S I_s, \mu_a) C^{k_b}_{J_b F_b}(L_b S I_s, \mu_b) C^{k_b}_{J_{b'} F_{b'}}(L_b S I_s, \mu_b) \\ & \times \sqrt{(2J_a+1)(2J_{a'}+1)(2J_b+1)(2J_{b'}+1)(2F_a+1)(2F_{a'}+1)(2F_b+1)(2F_{b'}+1)} \\ & \times \left\{ \begin{array}{ccc} L_a & L_b & 1 \\ J_b & J_a & S \end{array} \right\} \left\{ \begin{array}{ccc} L_a & L_b & 1 \\ J_{b'} & J_{a'} & S \end{array} \right\} \left\{ \begin{array}{ccc} J_a & J_b & 1 \\ F_b & F_a & I_s \end{array} \right\} \left\{ \begin{array}{ccc} J_{a'} & J_{b'} & 1 \\ F_{b'} & F_{a'} & I_s \end{array} \right\} \\ & \times \left(\begin{array}{ccc} F_b & F_a & 1 \\ -\mu_b & \mu_a & -q \end{array} \right) \left(\begin{array}{ccc} F_{b'} & F_{a'} & 1 \\ -\mu_b & \mu_a & -q \end{array} \right) \,. \end{aligned} \tag{C.5}$$

The centers of gravity in frequency of the magnetic components are defined as

$$\Delta\nu_q = \sum_{k_a k_b \mu_a \mu_b} \mathcal{S}_q^{k_a \mu_a, k_b \mu_b} \Delta\nu_{\mu_a \mu_b}^{k_a k_b} \,, \tag{C.6}$$

with

$$\Delta\nu^{k_a k_b}_{\mu_a\mu_b} = \frac{E_{k_b}(L_b S I_s, \mu_b) - E_{k_a}(L_a S I_s, \mu_a)}{h} \,. \tag{C.7}$$

Using Equations (C.5) and (C.7) in Equation (C.6), and performing sums over k_a and k_b with the help of Equations (5a) and (7) of Casini & Manso Sainz (2005), we obtain

$$\begin{aligned}
\Delta\nu_q = {} & \frac{1}{h}\frac{3}{(2S+1)(2I_s+1)} \sum_{J_a J_{a'} J_b J_{b'} F_a F_{a'} F_b F_{b'}} \sum_{\mu_a\mu_b} (-1)^{J_a+J_{a'}+J_b+J_{b'}} \\
& \times\sqrt{(2J_a+1)(2J_{a'}+1)(2J_b+1)(2J_{b'}+1)(2F_a+1)(2F_{a'}+1)(2F_b+1)(2F_{b'}+1)} \\
& \times \left\{ \begin{array}{ccc} L_a & L_b & 1 \\ J_b & J_a & S \end{array} \right\} \left\{ \begin{array}{ccc} L_a & L_b & 1 \\ J_{b'} & J_{a'} & S \end{array} \right\} \left\{ \begin{array}{ccc} J_a & J_b & 1 \\ F_b & F_a & I_s \end{array} \right\} \left\{ \begin{array}{ccc} J_{a'} & J_{b'} & 1 \\ F_{b'} & F_{a'} & I_s \end{array} \right\} \\
& \times \left(\begin{array}{ccc} F_b & F_a & 1 \\ -\mu_b & \mu_a & -q \end{array} \right) \left(\begin{array}{ccc} F_{b'} & F_{a'} & 1 \\ -\mu_b & \mu_a & -q \end{array} \right) \\
& \times [\delta_{J_a J_{a'}} \delta_{F_a F_{a'}} \langle L_b S J_b I_s F_b \mu_b | \mathcal{H}_T | L_b S J_{b'} I_s F_{b'} \mu_b \rangle \\
& - \delta_{J_b J_{b'}} \delta_{F_b F_{b'}} \langle L_a S J_a I_s F_a \mu_a | \mathcal{H}_T | L_a S J_{a'} I_s F_{a'} \mu_a \rangle] \,.
\end{aligned} \tag{C.8}$$

We separate the atomic and magnetic Hamiltonians in the above expression. It can be shown that the atomic part does not contribute to the centers of gravity. Using Equations (2.42), (2.41), (2.36d), (2.26d), and (2.39) of Landi Degl'Innocenti & Landolfi (2004), we simplify the magnetic Hamiltonian part and find that

$$\Delta\nu_q = -q\nu_{\rm L} \,, \tag{C.9}$$

where $\nu_{\rm L}$ is the Larmor frequency associated with the applied magnetic field. This result is the same as Equation (3.66) of Landi Degl'Innocenti & Landolfi (2004) which one would expect for a two-term atom without any fine or hyperfine structure. This means that the centers of gravity of the magnetic components in the PB regime have the same frequencies as the individual components due to Zeeman effect that would arise from the transitions between spinless lower and upper terms. In situations where the electron and nuclear spins are negligible, this is expected from the PSS.

We then verify that the eigenvalues and eigenvectors obtained by diagonalizing $\mathcal{H}_T$, when used in Equation (C.6), give the same value for $\Delta\nu_q$ as that calculated from Equation (C.9).

D

THE MAGNETIC REDISTRIBUTION FUNCTIONS FOR THE COMBINED THEORY

The magnetic redistribution functions of type II in the case of combined J and F state interferences have the same form as those in cases where only the interferences between fine structure or hyperfine structure states are considered, except for the increase in the dimension of the quantum number space. For our problem of interest, they take the forms given by

$$R^{\mathrm{II,H}}_{k_b\mu_b k_a\mu_a k_f\mu_f}(x_{ba}, x'_{ba}, \Theta) = \frac{1}{\pi \sin\Theta}\exp\left\{ -\left[\frac{x_{ba} - x'_{ba} + x_{k_a\mu_a k_f\mu_f}}{2\sin(\Theta/2)}\right]^2\right\} \times H\left(\frac{a}{\cos(\Theta/2)}, \frac{x_{ba} + x'_{ba} + x_{k_a\mu_a k_f\mu_f}}{2\cos(\Theta/2)}\right), \quad \text{(D.1)}$$

and

$$R^{\mathrm{II,F}}_{k_b\mu_b k_a\mu_a k_f\mu_f}(x_{ba}, x'_{ba}, \Theta) = \frac{1}{\pi \sin\Theta}\exp\left\{ -\left[\frac{x_{ba} - x'_{ba} + x_{k_a\mu_a k_f\mu_f}}{2\sin(\Theta/2)}\right]^2\right\} \times 2F\left(\frac{a}{\cos(\Theta/2)}, \frac{x_{ba} + x'_{ba} + x_{k_a\mu_a k_f\mu_f}}{2\cos(\Theta/2)}\right). \quad \text{(D.2)}$$

Here, Θ is the scattering angle, and the functions H and F are the Voigt and Faraday-Voigt functions (see Equation (18) of Smitha et al., 2011b). The quantities appearing in the

expressions for the type II redistribution functions have the following definitions:

$$x_{ba} = \frac{\nu_{k_b\mu_b k_a\mu_a} - \nu}{\Delta\nu_{\mathrm{D}}} \; ; \;\; x'_{ba} = \frac{\nu_{k_b\mu_b k_a\mu_a} - \nu'}{\Delta\nu_{\mathrm{D}}} \, ,$$
$$x_{k_a\mu_a k_f\mu_f} = \frac{\nu_{k_a\mu_a k_f\mu_f}}{\Delta\nu_{\mathrm{D}}} \; ; \;\; a = \frac{\gamma}{4\pi\Delta\nu_{\mathrm{D}}} \, , \tag{D.3}$$

where x_{ba} is the emission frequency, x'_{ba} is the absorption frequency, a is the damping parameter, and $\Delta\nu_{\mathrm{D}}$ is the Doppler width.

The auxiliary functions h^{II} and f^{II} appearing in Equation (6.9) can be constructed by making use of Equations (D.1) and (D.2) as

$$(h^{\mathrm{II}}_{k_b\mu_b,k_{b'}\mu_{b'}})_{k_a\mu_a k_f\mu_f} = \frac{1}{2}\left[R^{\mathrm{II,H}}_{k_b\mu_b k_a\mu_a k_f\mu_f} + R^{\mathrm{II,H}}_{k_{b'}\mu_{b'} k_a\mu_a k_f\mu_f}\right] , \tag{D.4}$$

$$(f^{\mathrm{II}}_{k_b\mu_b,k_{b'}\mu_{b'}})_{k_a\mu_a k_f\mu_f} = \frac{1}{2}\left[R^{\mathrm{II,F}}_{k_{b'}\mu_{b'} k_a\mu_a k_f\mu_f} - R^{\mathrm{II,F}}_{k_b\mu_b k_a\mu_a k_f\mu_f}\right] . \tag{D.5}$$

These auxiliary functions contain the information regarding the Doppler redistribution of photon frequencies.

E

A-O CONVERSION MECHANISM

The RM presented in Equation (6.9) can be reduced to the phase matrix by integrating the auxiliary functions over the incoming and outgoing frequencies. The phase matrix will then take the form given by

$$\boldsymbol{P}_{ij}(\boldsymbol{n},\boldsymbol{n}';\boldsymbol{B}) = \sum_{KK'Q} W_{KK'Q}(\boldsymbol{B})(-1)^{Q}\mathcal{T}^{K}_{Q}(i,\boldsymbol{n})\mathcal{T}^{K'}_{-Q}(j,\boldsymbol{n}') \,, \tag{E.1}$$

where

$$\begin{aligned}
W_{KK'Q}(\boldsymbol{B}) &= \frac{3(2L_b+1)}{(2S+1)(2I_s+1)} \left\{ \begin{array}{ccc} 1 & 1 & K \\ L_b & L_b & L_a \end{array} \right\} \left\{ \begin{array}{ccc} 1 & 1 & K' \\ L_b & L_b & L_a \end{array} \right\} \\
&\times \sum_{J_b J_{b'} J_{b''} J_{b'''}} \sum_{F_b F_{b'} F_{b''} F_{b'''}} \sum_{\mu_b \mu_{b'}} (-1)^{J_b+J_{b'}+J_{b''}+J_{b'''}} (-1)^{K+K'} \\
&\times \sqrt{(2J_b+1)(2J_{b'}+1)(2J_{b''}+1)(2J_{b'''}+1)} \\
&\times \sqrt{(2F_b+1)(2F_{b'}+1)(2F_{b''}+1)(2F_{b'''}+1)} \\
&\times \left\{ \begin{array}{ccc} L_b & L_b & K \\ J_b & J_{b'} & S \end{array} \right\} \left\{ \begin{array}{ccc} L_b & L_b & K' \\ J_{b''} & J_{b'''} & S \end{array} \right\} \left\{ \begin{array}{ccc} J_{b'} & J_b & K \\ F_b & F_{b'} & I_s \end{array} \right\} \left\{ \begin{array}{ccc} J_{b'''} & J_{b''} & K' \\ F_{b''} & F_{b'''} & I_s \end{array} \right\} \\
&\times \left(\begin{array}{ccc} F_b & F_{b'} & K \\ -\mu_b & \mu_{b'} & -Q \end{array} \right) \left(\begin{array}{ccc} F_{b''} & F_{b'''} & K' \\ -\mu_b & \mu_{b'} & -Q \end{array} \right) \sqrt{(2K+1)(2K'+1)} \\
&\times \sum_{k_b k_{b'}} C^{k_b}_{J_b F_b}(L_b S I_s, \mu_b) C^{k_b}_{J_{b''} F_{b''}}(L_b S I_s, \mu_b) C^{k_{b'}}_{J_{b'} F_{b'}}(L_b S I_s, \mu_{b'}) C^{k_{b'}}_{J_{b'''} F_{b'''}}(L_b S I_s, \mu_{b'}) \\
&\times \frac{1}{1 + 2\pi \mathrm{i} \nu(k_{b'}\mu_{b'}, k_b \mu_b)/A(L_a S I_s \rightarrow L_b S I_s)} \,.
\end{aligned} \tag{E.2}$$

Here, A is the Einstein coefficient for the $L_a \rightarrow L_b$ transition and $\nu(k_{b'}\mu_{b'}, k_b\mu_b) = (E_{k_{b'}\mu_{b'}} - E_{k_b\mu_b})/h$. We compute the $\mathcal{T}_Q^K$s for the geometry considered in Section 6.4.3 so that we can obtain an expression for the frequency integrated fractional circular polarization, $\tilde{p}_V$ (see Section 10.20 of Landi Degl'Innocenti & Landolfi, 2004). The explicit expressions for the $\mathcal{T}_Q^K(i,\boldsymbol{n})$ in the atmospheric reference frame for a rotation of the form $R \equiv (0, -\theta, -\chi) \times (\chi_B, \theta_B, 0)$ are given by

$$
\begin{aligned}
&\mathcal{T}_0^0(0,\boldsymbol{n}) = 1 \,, \\
&\mathcal{T}_0^1(0,\boldsymbol{n}) = 0 \,, \\
&\mathcal{T}_1^1(0,\boldsymbol{n}) = 0 \,, \\
&\mathcal{T}_0^2(0,\boldsymbol{n}) = \frac{1}{\sqrt{2}} \left[\frac{1}{4} \left(3\cos^2\theta - 1\right) \left(3\cos^2\theta_B - 1\right) \right. \\
&\qquad \left. +3 \sin\theta \cos\theta \sin\theta_B \cos\theta_B \cos(\chi - \chi_B) + \frac{3}{4} \sin^2\theta \sin^2\theta_B \cos 2(\chi - \chi_B) \right] \,, \\
&\mathcal{T}_1^2(0,\boldsymbol{n}) = \frac{1}{\sqrt{2}} \left[\frac{\sqrt{3}}{2\sqrt{2}} \left(3\cos^2\theta - 1\right) \sin\theta_B \cos\theta_B \right. \\
&\qquad -\frac{\sqrt{3}}{\sqrt{2}} \sin\theta \cos\theta \left[\mathrm{e}^{\mathrm{i}(\chi-\chi_B)} \left(\cos\theta_B - \frac{1}{2} \right) \left(\cos\theta_B + 1\right) \right. \\
&\qquad \left. -\mathrm{e}^{-\mathrm{i}(\chi-\chi_B)} \left(\cos\theta_B + \frac{1}{2} \right) \left(1 - \cos\theta_B\right) \right] \\
&\qquad \left. -\frac{\sqrt{3}}{2\sqrt{8}} \sin^2\theta \sin\theta_B \left[\mathrm{e}^{2\mathrm{i}(\chi-\chi_B)} (1 + \cos\theta_B) - \mathrm{e}^{-2\mathrm{i}(\chi-\chi_B)} (1 - \cos\theta_B) \right] \right] \,, \\
&\mathcal{T}_2^2(0,\boldsymbol{n}) = \frac{1}{\sqrt{2}} \left[\frac{\sqrt{3}}{4\sqrt{2}} \left(3\cos^2\theta - 1\right) \sin^2\theta_B \right. \\
&\qquad -\frac{\sqrt{3}}{2\sqrt{2}} \sin\theta \cos\theta \sin\theta_B \left[\mathrm{e}^{\mathrm{i}(\chi-\chi_B)} (1 + \cos\theta_B) - \mathrm{e}^{-\mathrm{i}(\chi-\chi_B)} (1 - \cos\theta_B) \right] \\
&\qquad \left. +\frac{\sqrt{3}}{8\sqrt{2}} \sin^2\theta \left[\mathrm{e}^{2\mathrm{i}(\chi-\chi_B)} (1 + \cos\theta_B)^2 + \mathrm{e}^{-2\mathrm{i}(\chi-\chi_B)} (1 - \cos\theta_B)^2 \right] \right] \,, \qquad \text{(E.3)}
\end{aligned}
$$

$$
\begin{aligned}
&\mathcal{T}_0^0(1,\boldsymbol{n}) = 0 \,, \\
&\mathcal{T}_0^1(1,\boldsymbol{n}) = 0 \,, \\
&\mathcal{T}_1^1(1,\boldsymbol{n}) = 0 \,, \\
&\mathcal{T}_0^2(1,\boldsymbol{n}) = -\frac{\sqrt{3}}{2} \left[\frac{\sqrt{3}}{\sqrt{8}} \sin^2\theta \left(3\cos^2\theta_B - 1\right) \right. \\
&\qquad \left. -\frac{2\sqrt{3}}{\sqrt{2}} \sin\theta \cos\theta \sin\theta_B \cos\theta_B \cos(\chi - \chi_B) \right.
\end{aligned}
$$

$$
\begin{aligned}
&+\frac{\sqrt{3}}{\sqrt{8}}\,(1+\cos^2\theta)\,\sin^2\theta_B\,\cos2(\chi-\chi_B)\Big]\,,\\
\mathcal{T}_1^2(1,\boldsymbol{n}) &= -\frac{\sqrt{3}}{2}\Big[\frac{3}{2}\,\sin^2\theta\,\sin\theta_B\,\cos\theta_B\\
&\quad+\sin\theta\,\cos\theta\Big[\mathrm{e}^{\mathrm{i}(\chi-\chi_B)}\Big(\cos\theta_B-\frac{1}{2}\Big)(\cos\theta_B+1)\\
&\quad-\mathrm{e}^{-\mathrm{i}(\chi-\chi_B)}\Big(\cos\theta_B+\frac{1}{2}\Big)(1-\cos\theta_B)\Big]\\
&\quad-\frac{1}{4}\,(1+\cos^2\theta)\,\sin\theta_B\big[\mathrm{e}^{2\mathrm{i}(\chi-\chi_B)}(1+\cos\theta_B)-\mathrm{e}^{-2\mathrm{i}(\chi-\chi_B)}(1-\cos\theta_B)\big]\Big]\,,\\
\mathcal{T}_2^2(1,\boldsymbol{n}) &= -\frac{\sqrt{3}}{2}\Big[\frac{3}{4}\,\sin^2\theta\,\sin^2\theta_B\\
&\quad+\frac{1}{2}\,\sin\theta\,\cos\theta\,\sin\theta_B\big[\mathrm{e}^{\mathrm{i}(\chi-\chi_B)}(1+\cos\theta_B)-\mathrm{e}^{-\mathrm{i}(\chi-\chi_B)}(1-\cos\theta_B)\big]\\
&\quad+\frac{1}{8}(1+\cos^2\theta)\big[\mathrm{e}^{2\mathrm{i}(\chi-\chi_B)}(1+\cos\theta_B)^2+\mathrm{e}^{-2\mathrm{i}(\chi-\chi_B)}(1-\cos\theta_B)^2\big]\Big]\,, \qquad \text{(E.4)}
\end{aligned}
$$

$$
\begin{aligned}
&\mathcal{T}_0^0(2,\boldsymbol{n}) = 0\,,\\
&\mathcal{T}_0^1(2,\boldsymbol{n}) = 0\,,\\
&\mathcal{T}_1^1(2,\boldsymbol{n}) = 0\,,\\
&\mathcal{T}_0^2(2,\boldsymbol{n}) = \frac{\sqrt{3}}{2}\Big[-\sqrt{6}\,\sin\theta\,\sin\theta_B\,\cos\theta_B\,\sin(\chi-\chi_B)\\
&\qquad+\frac{\sqrt{3}}{\sqrt{2}}\,\cos\theta\,\sin^2\theta_B\,\sin2(\chi-\chi_B)\Big]\,,\\
&\mathcal{T}_1^2(2,\boldsymbol{n}) = -\mathrm{i}\frac{\sqrt{3}}{2}\Big[\sin\theta\Big[\mathrm{e}^{\mathrm{i}(\chi-\chi_B)}\Big(\cos\theta_B-\frac{1}{2}\Big)(\cos\theta_B+1)\\
&\qquad+\mathrm{e}^{-\mathrm{i}(\chi-\chi_B)}\Big(\cos\theta_B+\frac{1}{2}\Big)(1-\cos\theta_B)\Big]\\
&\qquad-\frac{1}{2}\,\cos\theta\,\sin\theta_B\big[\mathrm{e}^{2\mathrm{i}(\chi-\chi_B)}(1+\cos\theta_B)+\mathrm{e}^{-2\mathrm{i}(\chi-\chi_B)}(1-\cos\theta_B)\big]\Big]\,,\\
&\mathcal{T}_2^2(2,\boldsymbol{n}) = -\mathrm{i}\frac{\sqrt{3}}{2}\Big[\frac{1}{2}\,\sin\theta\,\sin\theta_B\big[\mathrm{e}^{\mathrm{i}(\chi-\chi_B)}(1+\cos\theta_B)+\mathrm{e}^{-\mathrm{i}(\chi-\chi_B)}(1-\cos\theta_B)\big]\\
&\qquad+\frac{1}{4}\,\cos\theta\big[\mathrm{e}^{2\mathrm{i}(\chi-\chi_B)}(1+\cos\theta_B)^2-\mathrm{e}^{-2\mathrm{i}(\chi-\chi_B)}(1-\cos\theta_B)^2\big]\Big]\,, \qquad \text{(E.5)}
\end{aligned}
$$

and

$$
\mathcal{T}_0^0(3,\boldsymbol{n}) = 0\,,
$$

$$
\begin{aligned}
\mathcal{T}^1_0(3,\boldsymbol{n}) &= \frac{\sqrt{3}}{\sqrt{2}}[\cos\theta\,\cos\theta_B + \sin\theta\,\sin\theta_B\,\cos(\chi-\chi_B)]\,,\\
\mathcal{T}^1_1(3,\boldsymbol{n}) &= \frac{\sqrt{3}}{\sqrt{2}}\Bigg[\frac{1}{\sqrt{2}}\cos\theta\,\sin\theta_B\\
&\qquad -\frac{1}{2\sqrt{2}}\sin\theta\big[\mathrm{e}^{\mathrm{i}(\chi-\chi_B)}(1+\cos\theta_B) - \mathrm{e}^{-\mathrm{i}(\chi-\chi_B)}(1-\cos\theta_B)\big]\Bigg]\,,\\
\mathcal{T}^2_0(3,\boldsymbol{n}) &= 0\,,\\
\mathcal{T}^2_1(3,\boldsymbol{n}) &= 0\,,\\
\mathcal{T}^2_2(3,\boldsymbol{n}) &= 0\,.
\end{aligned}
\tag{E.6}
$$

We then expand the summations over K, K', and Q in Equation (E.1) and write down the expressions for the P_{00} and P_{30}[1] elements. We substitute in the expressions for P_{00} and P_{30} the $\mathcal{T}^K_Q$s evaluated for the incoming and the outgoing rays by making use of Equations (E.3) and (E.6) for the geometry considered in Section 6.4.3. After elaborate algebra, we finally arrive at an expression for the frequency integrated fractional circular polarization given by

$$
\tilde{p}_V = \frac{P_{30}}{P_{00}} = \frac{-2\sqrt{6}W_{120}}{16 - W_{220} - 3\mathrm{Re}(W_{222})}\,. \tag{E.7}
$$

As discussed in Section 6.4.3 and in Section 10.20 of Landi Degl'Innocenti & Landolfi (2004), due to the double summations over K and K' in Equation (E.1) and due to the fact that the spherical tensor $\mathcal{T}^K_Q(3,\boldsymbol{n})$ are non-zero only when $K=1$, orientation can be produced in the upper term even when the circular polarization is not present in the incident radiation. This mechanism is therefore called the A-O conversion mechanism. We identify that the term with $K=1$ in the numerator of Equation (E.7) is responsible for the A-O conversion mechanism. We have discussed the signatures of this mechanism in the Stokes V parameter in Section 6.4.

[1]Note that we consider P_{30} element to calculate the frequency integrated fractional circular polarization and not P_{33} as erroneously mentioned in Appendix C of Sowmya et al. (2015b).

BIBLIOGRAPHY

Anusha, L. S., Nagendra, K. N., Stenflo, J. O., et al. 2010, ApJ, 718, 988

Anusha, L. S., Stenflo, J. O., Frisch, H., et al. 2011a, in Astronomical Society of the Pacific Conference Series, Vol. 437, Solar Polarization 6, ed. J. R. Kuhn, D. M. Harrington, H. Lin, S. V. Berdyugina, J. Trujillo-Bueno, S. L. Keil, & T. Rimmele, 57

Anusha, L. S., Nagendra, K. N., Bianda, M., et al. 2011b, ApJ, 737, 95

Arimondo, E., Inguscio, M., & Violino, P. 1977, Reviews of Modern Physics, 49, 31

Asensio Ramos, A. 2006, in Astronomical Society of the Pacific Conference Series, Vol. 358, Astronomical Society of the Pacific Conference Series, ed. R. Casini & B. W. Lites, 301

Asensio Ramos, A., & Trujillo Bueno, J. 2006, ApJ, 636, 548

Asensio Ramos, A., Trujillo Bueno, J., & Collados, M. 2005, ApJL, 623, L57

Asplund, M., Grevesse, N., Sauval, A. J., & Scott, P. 2009, Ann.Rev. Astron. Astrophys., 47, 481

Auer, L. H., Heasley, J. N., & House, L. L. 1977, ApJ, 216, 531

Avrett, E. H. 1995, in Infrared tools for solar astrophysics: What's next?, ed. J. R. Kuhn & M. J. Penn

Beckers, J. M. 1971, in IAU Symposium, Vol. 43, Solar Magnetic Fields, ed. R. Howard, 3

Belluzzi, L. 2009, A&A, 508, 933

Belluzzi, L., Landi Degl'Innocenti, E., & Trujillo Bueno, J. 2009, ApJ, 705, 218

Belluzzi, L., Trujillo Bueno, J., & Landi Degl'Innocenti, E. 2007, ApJ, 666, 588

Berdyugina, S. V., Braun, P. A., Fluri, D. M., & Solanki, S. K. 2005, A&A, 444, 947

Berdyugina, S. V., Fluri, D. M., Ramelli, R., et al. 2006a, ApJL, 649, L49

Berdyugina, S. V., Fluri, D. M., & Solanki, S. K. 2006b, in Astronomical Society of the Pacific Conference Series, Vol. 358, Astronomical Society of the Pacific Conference Series, ed. R. Casini & B. W. Lites, 329

Bommier, V. 1980, A&A, 87, 109

—. 1997a, A&A, 328, 706

—. 1997b, A&A, 328, 726

Bommier, V., Leroy, J. L., & Sahal-Bréchot, S. 1985, in NASA Conference Publication, Vol. 2374, NASA Conference Publication, 375–378

Bommier, V., & Stenflo, J. O. 1999, A&A, 350, 327

Brog, K. C., Eck, T. G., & Wieder, H. 1967, Physical Review, 153, 91

Cannon, C. J. 1985, The transfer of spectral line radiation

Casini, R., Landi Degl'Innocenti, M., Manso Sainz, R., Landi Degl'Innocenti, E., & Landolfi, M. 2014, ApJ, 791, 94

Casini, R., & Manso Sainz, R. 2005, ApJ, 624, 1025

—. 2016, ArXiv e-prints, arXiv:1602.07173

Chandrasekhar, S. 1950, Radiative Transfer (New York: Dover Press)

Clarke, D. 2010, Stellar Polarimetry (Weinheim: WILEY-VCH Verlag GmbH & Co. KGaA)

Collett, E. 1993, Polarized Light: Fundamentals and Applications (New York/Basel: Marcel Dekker, Inc.)

Condon, E. U., & Shortley, G. H. 1935, The Theory of Atomic Spectra

Corney, A. 1977, Atomic and Laser Spectroscopy (Oxford: Oxford Univ. Press)

del Toro Iniesta, J. C. 2004, Introduction to Spectropolarimetry (Cambridge, UK: Cambridge University Press)

Dirac, P. A. M. 1927a, Proceedings of the Royal Society of London Series A, 114, 710

—. 1927b, Proceedings of the Royal Society of London Series A, 114, 243

Domke, H., & Hubeny, I. 1988, ApJ, 334, 527

Faurobert, M. 1987, A&A, 178, 269

—. 1988, A&A, 194, 268

Faurobert, M. 2000, in Astronomical Society of the Pacific Conference Series, Vol. 205, Last Total Solar Eclipse of the Millennium, ed. W. Livingston & A. Özgüç, 156

Faurobert, M. 2003, in EAS Publications Series, Vol. 9, EAS Publications Series, ed. J. Arnaud & N. Meunier, 77

—. 2012, IAU Special Session, 6, E3.01

Faurobert, M., & Arnaud, J. 2002, A&A, 382, L17

Faurobert-Scholl, M. 1996, Solar Phys., 164, 79

Faurobert-Scholl, M., Feautrier, N., Machefert, F., Petrovay, K., & Spielfiedel, A. 1995, A&A, 298, 289

Faurobert-Scholl, M., Frisch, H., & Nagendra, K. N. 1997, A&A, 322, 896

Feautrier, P. 1964, Comptes Rendus Academie des Sciences (serie non specifiee), 258

Fluri, D. M., Nagendra, K. N., & Frisch, H. 2003, A&A, 400, 303

Fluri, D. M., & Stenflo, J. O. 1999, in Astrophysics and Space Science Library, Vol. 243, Polarization, ed. K. N. Nagendra & J. O. Stenflo, 171–178

Fluri, D. M., & Stenflo, J. O. 2001, in Astronomical Society of the Pacific Conference Series, Vol. 236, Advanced Solar Polarimetry – Theory, Observation, and Instrumentation, ed. M. Sigwarth, 205

Fluri, D. M., & Stenflo, J. O. 2003, A&A, 398, 763

Fontenla, J. M., Avrett, E. H., & Loeser, R. 1990, ApJ, 355, 700

—. 1991, ApJ, 377, 712

—. 1993, ApJ, 406, 319

Frisch, H. 1996, Solar Phys., 164, 49

—. 2007, A&A, 476, 665

Frisch, H. 2009, in Astronomical Society of the Pacific Conference Series, Vol. 405, Solar Polarization 5: In Honor of Jan Stenflo, ed. S. V. Berdyugina, K. N. Nagendra, & R. Ramelli, 87

—. 2010, A&A, 522, A41

Frisch, H., Anusha, L. S., Sampoorna, M., & Nagendra, K. N. 2009, A&A, 501, 335

Gandorfer, A. 2000, The Second Solar Spectrum: A High Spectral Resolution Polarimetric Survey of Scattering Polarization at the Solar Limb in Graphical Representation. Volume I: 4625 Å to 6995 Å

—. 2002, The Second Solar Spectrum: A High Spectral Resolution Polarimetric Survey of Scattering Polarization at the Solar Limb in Graphical Representation. Volume II: 3910 Å to 4630 Å

—. 2005a, The Second Solar Spectrum: A High Spectral Resolution Polarimetric Survey of Scattering Polarization at the Solar Limb in Graphical Representation. Volume III: 3160 Å to 3915 Å

Gandorfer, A. 2005b, in ESA Special Publication, Vol. 596, Chromospheric and Coronal Magnetic Fields, ed. D. E. Innes, A. Lagg, & S. A. Solanki, 5.1

Hale, G. E. 1908a, ApJ, 28, 315

—. 1908b, Pub. Astron. Soc. Pac., 20, 287

Hanle, W. 1923, Naturwissenschaften, 11, 690

—. 1924, Zeitschrift fur Physik, 30, 93

Heinzel, P. 1981, JQSRT, 25, 483

Heinzel, P., & Hubený, I. 1982, JQSRT, 27, 1

Howard, R., ed. 1971, IAU Symposium, Vol. 43, Solar magnetic fields. Symposium no. 43, held at the College de France Paris, France, August 31 to September 4, 1970.

Hubený, I. 1982, JQSRT, 27, 593

Hubeny, I. 1992, in Lecture Notes in Physics, Berlin Springer Verlag, Vol. 401, The Atmospheres of Early-Type Stars, ed. U. Heber & C. S. Jeffery, 377

Hubeny, I. 2003, in Astronomical Society of the Pacific Conference Series, Vol. 288, Stellar Atmosphere Modeling, ed. I. Hubeny, D. Mihalas, & K. Werner, 17

Hubeny, I., & Mihalas, D. 2015, Theory of Stellar Atmospheres (Princeton and Oxford: Princeton University Press)

Hummer, D. G. 1962, MNRAS, 125, 21

Ivanov, V. V. 1991, in NATO Advanced Science Institutes (ASI) Series C, Vol. 341, NATO Advanced Science Institutes (ASI) Series C, ed. L. Crivellari, I. Hubeny, & D. G. Hummer, 81

Khalack, V., & Landstreet, J. D. 2012, MNRAS, 427, 569

Kramers, H. A., & Heisenberg, W. 1925, Zeitschrift fur Physik, 31, 681

Kunasz, P., & Auer, L. H. 1988, JQSRT, 39, 67

Kundu, M. R., Woodgate, B., & Schmahl, E. J., eds. 1989, Astrophysics and Space Science Library, Vol. 153, Energetic Phenomena on the Sun

Kuzmychov, O., & Berdyugina, S. V. 2013, A&A, 558, A120

Landi Degl'Innocenti, E. 1975, A&A, 45, 269

—. 1978, Astron. Astrophys. Suppl., 33, 157

—. 1982, Solar Phys., 79, 291

—. 1984, Solar Phys., 91, 1

Landi Degl'Innocenti, E. 1985, in NASA Conference Publication, Vol. 2374, NASA Conference Publication, 279–299

—. 1992, Magnetic field measurements, ed. F. Sanchez, M. Collados, & M. Vazquez, 71

Landi Degl'Innocenti, E., Landi Degl'Innocenti, M., & Landolfi, M. 1997, in Proc. Forum THEMIS, Science with THEMIS, ed. N. Mein and S. Sahal Bréchot (Paris: Obs. Paris-Meudon), 59

Landi Degl'Innocenti, E., & Landolfi, M. 2004, Polarization in Spectral Lines (Dordrecht: Kluwer)

Landi Degl'Innocenti, M., & Landi Degl'Innocenti, E. 1988, A&A, 192, 374

Leroy, J. L. 1985, in NASA Conference Publication, Vol. 2374, NASA Conference Publication, 121–140

Leroy, J. L., Ratier, G., & Bommier, V. 1977, A&A, 54, 811

López Ariste, A., Tomczyk, S., & Casini, R. 2002, ApJ, 580, 519

López Ariste, A., Tomczyk, S., & Casini, R. 2003, in Astronomical Society of the Pacific Conference Series, Vol. 307, Solar Polarization, ed. J. Trujillo-Bueno & J. Sanchez Almeida, 115

Maltby, P. 1971, in IAU Symposium, Vol. 43, Solar Magnetic Fields, ed. R. Howard, 141

Mihalas, D. 1978, Stellar Atmospheres, 2nd edn. (USA: W. H. Freeman and Company)

Moruzzi, G., & Strumia, F., eds. 1991, The Hanle Effect and Level-Crossing Spectroscopy

Nagendra, K. N. 2003, in Astronomical Society of the Pacific Conference Series, Vol. 288, Stellar Atmosphere Modeling, ed. I. Hubeny, D. Mihalas, & K. Werner, 583

Nagendra, K. N. 2014, in Astronomical Society of the Pacific Conference Series, Vol. 489, Solar Polarization 7, ed. K. N. Nagendra, J. O. Stenflo, Q. Qu, & M. Samooprna, 179

Nagendra, K. N. 2015, in IAU Symposium, Vol. 305, Polarimetry, ed. K. N. Nagendra, S. Bagnulo, R. Centeno, & M. Jesús Martínez González, 351–359

Nagendra, K. N., Frisch, H., & Faurobert, M. 2002, A&A, 395, 305

Nagendra, K. N., Frisch, H., & Faurobert-Scholl, M. 1998, A&A, 332, 610

Nagendra, K. N., Frisch, H., Faurobert-Scholl, M., & Paletou, F. 2000, Journal of Astrophysics and Astronomy, 21, 255

Nagendra, K. N., Frisch, H., & Fluri, D. M. 2003, in Astronomical Society of the Pacific Conference Series, Vol. 307, Solar Polarization, ed. J. Trujillo-Bueno & J. Sanchez Almeida, 227

Nagendra, K. N., Paletou, F., Frisch, H., & Faurobert-Scholl, M. 1999, in Astrophysics and Space Science Library, Vol. 243, Polarization, ed. K. N. Nagendra & J. O. Stenflo, 127–142

Nagendra, K. N., & Peraiah, A. 1985a, MNRAS, 214, 203

—. 1985b, Astrophys. Spa. Sci., 117, 121

Nagendra, K. N., & Sampoorna, M. 2009, in Astronomical Society of the Pacific Conference Series, Vol. 405, Solar Polarization 5: In Honor of Jan Stenflo, ed. S. V. Berdyugina, K. N. Nagendra, & R. Ramelli, 261

Nagendra, K. N., & Sampoorna, M. 2011, A&A, 535, A88

Neckel, H. 1996, Solar Phys., 167, 9

Neckel, H., & Labs, D. 1994, Solar Phys., 153, 91

Olson, G. L., Auer, L. H., & Buchler, J. R. 1986, JQSRT, 35, 431

Omont, A., Smith, E. W., & Cooper, J. 1972, ApJ, 175, 185

—. 1973, ApJ, 182, 283

Ortega, J. 1968, in Mathematical Methods for Digital Computers, ed. A. Ralston & H. S. Wilf (New York: Wiley), 94

Paletou, F., & Auer, L. H. 1995, A&A, 297, 771

Paletou, F., & Faurobert-Scholl, M. 1997, A&A, 328, 343

Paschen, F., & Back, E. 1912, Annalen der Physik, 344, 897

Pauli, W. 1924, Naturwissenschaften, 12, 741

Pierce, K. 2000, in Allen's Astrophysical Quantities, 4th edn., ed. A. N. Cox (New York: Springer), 355

Povel, H. P. 1995, Optical Engineering, 34, 1870

Rayleigh. 1922, Proc. R. Soc., 102, 190

Rees, D. E., Durrant, C. J., & Murphy, G. A. 1989, ApJ, 339, 1093

Rees, D. E., & Saliba, G. J. 1982, A&A, 115, 1

Rybicki, G. B., & Hummer, D. G. 1991, A&A, 245, 171

—. 1992, A&A, 262, 209

—. 1994, A&A, 290, astro-ph/9404019

Sampoorna, M. 2011a, ApJ, 731, 114

—. 2011b, A&A, 532, A52

Sampoorna, M. 2014, in Astronomical Society of the Pacific Conference Series, Vol. 489, Solar Polarization 7, ed. K. N. Nagendra, J. O. Stenflo, Q. Qu, & M. Samooprna, 197

Sampoorna, M., Nagendra, K. N., & Frisch, H. 2008a, JQSRT, 109, 2349

—. 2011, A&A, 527, A89

Sampoorna, M., Nagendra, K. N., & Stenflo, J. O. 2007a, ApJ, 663, 625

—. 2007b, ApJ, 670, 1485

—. 2008b, ApJ, 679, 889

—. 2013, ApJ, 770, 92

Sampoorna, M., Stenflo, J. O., Nagendra, K. N., et al. 2009, ApJ, 699, 1650

Sasso, C., Lagg, A., & Solanki, S. K. 2006, A&A, 456, 367

Shapiro, A. I., Fluri, D. M., Berdyugina, S. V., & Stenflo, J. O. 2006, in Astronomical Society of the Pacific Conference Series, Vol. 358, Astronomical Society of the Pacific Conference Series, ed. R. Casini & B. W. Lites, 311

Shapiro, A. I., Fluri, D. M., Berdyugina, S. V., & Stenflo, J. O. 2007, A&A, 461, 339

Shurcliff, W. A. 1961, Polarized Light: Production and Use (Cambridge: Harvard Univeristy Press)

Smitha, H. N., Nagendra, K. N., Sampoorna, M., & Stenflo, J. O. 2011a, A&A, 535, A35

—. 2013a, JQSRT, 115, 46

Smitha, H. N., Nagendra, K. N., Stenflo, J. O., Bianda, M., & Ramelli, R. 2014, ApJ, 794, 30

Smitha, H. N., Nagendra, K. N., Stenflo, J. O., et al. 2012a, A&A, 541, A24

Smitha, H. N., Nagendra, K. N., Stenflo, J. O., & Sampoorna, M. 2013b, ApJ, 768, 163

Smitha, H. N., Sampoorna, M., Nagendra, K. N., & Stenflo, J. O. 2011b, ApJ, 733, 4

Smitha, H. N., Sowmya, K., Nagendra, K. N., Sampoorna, M., & Stenflo, J. O. 2012b, ApJ, 758, 112

Socas-Navarro, H., Trujillo Bueno, J., & Landi Degl'Innocenti, E. 2004, ApJ, 612, 1175

Sowmya, K., Nagendra, K. N., & Sampoorna, M. 2012, MNRAS, 423, 2949

Sowmya, K., Nagendra, K. N., & Sampoorna, M. 2014a, in Astronomical Society of the Pacific Conference Series, Vol. 489, Solar Polarization 7, ed. K. N. Nagendra, J. O. Stenflo, Q. Qu, & M. Samooprna, 125

Sowmya, K., Nagendra, K. N., Sampoorna, M., & Stenflo, J. O. 2014b, ApJ, 793, 71

Sowmya, K., Nagendra, K. N., Sampoorna, M., & Stenflo, J. O. 2015a, in IAU Symposium, Vol. 305, IAU Symposium, ed. K. N. Nagendra, S. Bagnulo, R. Centeno, & M. Jesús Martínez González, 154–158

—. 2015b, ApJ, 814, 127

Sowmya, K., Nagendra, K. N., Stenflo, J. O., & Sampoorna, M. 2014c, ApJ, 786, 150

Steck, D. A. 2003, Sodium D Line Data, `http://steck.us/alkalidata/`

Stenflo, J. O. 1978a, A&A, 66, 241

—. 1978b, Reports on Progress in Physics, 41, 865

—. 1980, A&A, 84, 68

—. 1982, Solar Phys., 80, 209

Stenflo, J. O. 1994, Solar Magnetic Fields: Polarized Radiation Diagnostics (Dordrecht: Kluwer)

Stenflo, J. O. 1997, A&A, 324, 344

—. 1998, A&A, 338, 301

Stenflo, J. O. 2002, in Astrophysical Spectropolarimetry, ed. J. Trujillo-Bueno, F. Moreno-Insertis, & F. Sánchez, 55–100

—. 2005, A&A, 429, 713

—. 2009a, Central European Astrophysical Bulletin, 33, 1

Stenflo, J. O. 2009b, in Astronomical Society of the Pacific Conference Series, Vol. 405, Solar Polarization 5: In Honor of Jan Stenflo, ed. S. V. Berdyugina, K. N. Nagendra, & R. Ramelli, 3

Stenflo, J. O. 2011, in Astronomical Society of the Pacific Conference Series, Vol. 437, Solar Polarization 6, ed. J. R. Kuhn, D. M. Harrington, H. Lin, S. V. Berdyugina, J. Trujillo-Bueno, S. L. Keil, & T. Rimmele, 3

—. 2015a, Space Sci. Rev., arXiv:1508.03312

—. 2015b, ApJ, 801, 70

Stenflo, J. O., & Keller, C. U. 1996, Nature, 382, 588

—. 1997, A&A, 321, 927

Stenflo, J. O., Keller, C. U., & Gandorfer, A. 1998, A&A, 329, 319

—. 2000, A&A, 355, 789

Stenflo, J. O., Twerenbold, D., & Harvey, J. W. 1983, Astron. Astrophys. Suppl., 52, 161

Stift, M. J., & Leone, F. 2008, Contributions of the Astronomical Observatory Skalnate Pleso, 38, 185

Stift, M. J., Leone, F., & Landi Degl'Innocenti, E. 2008, MNRAS, 385, 1813

Supriya, H. D., Sampoorna, M., Nagendra, K. N., Ravindra, B., & Anusha, L. S. 2013a, JQSRT, 119, 67

Supriya, H. D., Sampoorna, M., Nagendra, K. N., Stenflo, J. O., & Ravindra, B. 2016, under review

Supriya, H. D., Smitha, H. N., Nagendra, K. N., Ravindra, B., & Sampoorna, M. 2013b, MNRAS, 429, 275

Supriya, H. D., Smitha, H. N., Nagendra, K. N., et al. 2014, ApJ, 793, 42

Supriya, H. D., Smitha, H. N., Nagendra, K. N., et al. 2015, in IAU Symposium, Vol. 305, Polarimetry, ed. K. N. Nagendra, S. Bagnulo, R. Centeno, & M. Jesús Martínez González, 381–386

Trujillo Bueno, J. 2001, in Astronomical Society of the Pacific Conference Series, Vol. 236, Advanced Solar Polarimetry – Theory, Observation, and Instrumentation, ed. M. Sigwarth, 161

Trujillo Bueno, J. 2003a, in Cambridge Workshop on Cool Stars, Stellar Systems, and the Sun, Vol. 12, The Future of Cool-Star Astrophysics: 12th Cambridge Workshop on Cool Stars, Stellar Systems, and the Sun, ed. A. Brown, G. M. Harper, & T. R. Ayres, 196–209

Trujillo Bueno, J. 2003b, in Astronomical Society of the Pacific Conference Series, Vol. 288, Stellar Atmosphere Modeling, ed. I. Hubeny, D. Mihalas, & K. Werner, 551

Trujillo Bueno, J., Asensio Ramos, A., & Shchukina, N. 2006, in Astronomical Society of the Pacific Conference Series, Vol. 358, Astronomical Society of the Pacific Conference Series, ed. R. Casini & B. W. Lites, 269

Trujillo Bueno, J., Casini, R., Landolfi, M., & Landi Degl'Innocenti, E. 2002, ApJL, 566, L53

Trujillo Bueno, J., Merenda, L., Centeno, R., Collados, M., & Landi Degl'Innocenti, E. 2005, ApJL, 619, L191

Uitenbroek, H. 2001, ApJ, 557, 389

Wieder, H., & Eck, T. G. 1967, Physical Review, 153, 103

Wilson, A., ed. 1999, ESA Special Publication, Vol. 448, Magnetic Fields and Solar Processes

Wood, R. W., & Ellet, A. 1923, Nature, 111, 255

Woodgate, G. K. 1992, Elementary Atomic Structure, 2nd edn. (Oxford: Oxford Univ. Press)

Zanstra, H. 1941a, MNRAS, 101, 273

—. 1941b, MNRAS, 101, 250

Zeeman, P. 1897, Phil. Mag., 43, 226